Charles University in Prague

Faculty of Science

Department of Biochemistry

Ľubica Škultétyová, MSc.

Hydrolasy závislé na zinku: Studium struktury a funkce glutamátkarboxypeptidasy II a histondeacetylasy 6

Zinc-Dependent Hydrolases: Structure-Function Study of Glutamate Carboxypeptidase II and Histone Deacetylase 6

Ph.D. THESIS

Supervisor: RNDr. Cyril Bařinka, Ph.D.

Prague 2018

Prohlášení:

Prohlašuji, že jsem závěrečnou práci zpracovala samostatně a že jsem uvedla všechny použité informační zdroje a literaturu. Tato práce ani její podstatná část nebyla předložena k získání jiného nebo stejného akademického titulu.

V Praze, 20.2.2018

Podpis

Declaration of co-authors:

The thesis contains four original publications co-authored by Lubica Skultetyova and all the work presented here was performed under my supervision. Hence I am authorized to confirm that Lubica Skultetyova contributed substantially to the projects forming basis of the dissertation thesis. In more detail, she:

1. Solved, refined and analyzed the structure of the complex of GCPII with a newly identified NAAM (N-acetyl-aspartyl-methionine) substrate (PDB code 3SJX). Published in "**Novel Substrate-Based Inhibitors of Human Glutamate Carboxypeptidase II with Enhanced Lipophilicity.** Plechanovová, A., Byun, Y., Alquicer, G., Škultétyová, Ľ., Mlčochová, P., Němcová, A., Kim, H.-J., Navrátil, M., Mease, R., Lubkowski J., Pomper, M. G., Konvalinka, J., Rulíšek, L., and Bařinka, C. Journal of Medicinal Chemistry (2011), 54 (21), 7535-7546"

2. Solved, refined and analyzed the structures of complexes GCPII/**3** (PDB code 4OC0) and GCPII/**4** (PDB code 4OC4). Published in "**Structural characterization of P1'-diversified urea-based inhibitors of glutamate carboxypeptidase II.** Pavlicek, J., Ptacek, J., Cerny, J., Byun, Y., Skultetyova, L., Pomper, M. G., Lubkowski J., and Barinka, C. Bioorganic & Medicinal Chemistry Letters (2014), 24(10), 2340–2345."

3. Solved, refined and analyzed the structure of the GCPII/4 complex (PDB code 4LQG). Published in "**Structure-Activity Relationship of ¹⁸F-Labeled Phosphoramidate Peptidomimetic Prostate-Specific Membrane Antigen (PSMA)-Targeted Inhibitor Analogues for PET Imaging of Prostate Cancer.** Dannoon, S., Ganguly, T., Cahaya, H., Geruntho, J. J., Galliher, M. S., Beyer, S. K., Choy, C. J., Hopkins, M. R., Regan, M., Blecha, J. E., Skultetyova, L., Drake, C. R., Jivan, S., Barinka, C., Jones, E. F., Berkman, C. E., and VanBrocklin, H. F. Journal of Medicinal Chemistry (2016), 59 (12), 5684-5694"

4. Cloned variants of human HDAC6, identified the optimal expression system, heterologously expressed and purified HDAC6 variants and established experimental protocols for HDAC6 activity measurements on tubulin-derived substrates. Contributed substantially to writing of the article. Published in "**Human histone deacetylase 6 shows strong preference for tubulin dimers over assembled microtubules.** Skultetyova, L., Ustinova, K., Kutil, Z., Novakova, Z., Pavlicek, J., Mikesova, J., Trapl, D., Baranova, P., Havlinova, B., Hubalek, M., Lansky, Z., and Barinka, C. Scientific Reports (2017), 14;7(1):11547."

5. Determined substrate specificity of human HDAC6 using human acetylome microarrays – developed assay conditions, analyzed microarray data. The manuscript is in preparation.

Prague, February 20, 2018

………………………………..

RNDr. Cyril Bařinka, Ph.D.

ABSTRACT

Zinc-binding proteins represent approximately one tenth of the proteome and a good portion of them are zinc-dependent hydrolases. This thesis focuses on biochemical and structural characterization of glutamate carboxypeptidase II (GCPII) and histone deacetylase 6 (HDAC6), two members of the zinc-dependent metallohydrolase superfamily. We describe here their interactions with natural substrates and inhibitors.

GCPII is a homodimeric membrane protease catalyzing hydrolytic cleavage of glutamate from the neurotransmitter N-acetylaspartylglutamate (NAAG) and dietary folates in the central and peripheral nervous systems and small intestine, respectively. This enzyme is associated with several neurological disorders and also presents an ideal target for imaging and treatment of prostate cancer. GCPII inhibitors typically consist of a zinc-binding group (ZBG) linked to an S1' docking moiety (a glutamate moiety or its isostere). As such, these compounds are highly hydrophilic molecules therefore unable to cross the blood-brain barrier and this hampers targeting GCPII to the central nervous system. Different approaches are adopted to alter the S1' docking moiety of the existing inhibitors. As a part of this thesis, we present different strategies relying on replacement of the canonical P1' glutamate residue with unbranched non-natural amino acids and glutamate bioisosteres. We also study the effect of introduction of an aminohexanoate linker on affinity and biological properties of phosphoramidate-based inhibitors. Analysis of crystal structures of GCPII in the complex with these novel inhibitors identified unprecedented plasticity of the S1' site that enables GCPII to accommodate bulky residues. We have succeeded in identifying compounds with increased hydrophobicity. These molecules, although not strong inhibitors, represent promising scaffolds for further rational design of new inhibitors.

Acetylation of Lys40 of α-tubulin protects the microtubules from mechanical ageing and plays role in cell motility, axonal branching, and growth and maintenance of neuronal processes. HDAC6 is the major tubulin deacetylase and it is emerging as a possible treatment target in cancer and neurodegenerative diseases. A better understanding of its interaction with the tubulin substrate is therefore needed. We show here that HDAC6 deacetylates the tubulin dimers at a rate 1500-fold higher than the microtubules. Our data indicates that amino acids beyond the P_1 and P_{-1} within the Lys40 loop contribute minimally to the substrate recognition and that efficient deacetylation requires complex longitudinal and lateral interactions with tubulin dimer.

ABSTRAKT

Proteiny vázající zinek představují přibližně desetinu proteomu a významnou část z nich tvoří hydrolasy závislé na zinku. Tato disertační práce se zaměřuje na biochemickou a strukturní charakterizaci glutamátkarboxypeptidasy II (GCPII) a histondeacetylasy 6 (HDAC6), které jsou členy rodiny metalohydrolas závislých na zinku, a popisuje interakce s jejich přirozenými substráty a inhibitory.

GCPII je homodimerní membránová proteasa, která v centrální a periferní nervové soustavě katalyzuje odštěpení glutamátu z neuropřenašeče N-acetyl-aspartyl glutamátu (NAAG) a v tenkém střevě z folátů přijatých v potravě. Tento enzym je spojován s několika neurologickými poruchami a představuje také ideální cíl pro diagnostiku a léčbu rakoviny prostaty. Inhibitory GCPII obvykle nesou skupinu vázající zinek a dále obsahují funkční skupinu specificky rozpoznávanou v S1' místě enzymu (tvořenou glutamátovým zbytkem nebo jeho isosterem). Tyto sloučeniny jsou přirozeně hydrofilní molekuly, což brání jejich průniku přes hematoencefalickou bariéru a znemožňuje inhibici GCPII v centrální nervové soustavě. V této disertační práci představujeme různé strategie zaměřené na záměnu tradičního P1' glutamátového zbytku nevětvenými neproteinogenními aminokyselinami a bioisostery glutamátu. Dále pak sledujeme vliv zavedení aminohexanového linkeru na afinitu a biologické vlastnosti inhibitorů na bázi fosforamidátů. Analýza krystalových struktur komplexů GCPII s těmito novými inhibitory odhalila dosud nepopsanou flexibilitu S1' místa, která umožňuje proteinu GCPII vázat objemné zbytky. Identifikovali jsme nové inhibitory se zvýšenou lipofilicitou, které i když nejsou silnými inhibitory, mohou složit jako prekursory pro následní racionální návrh nových léčiv.

Acetylace lysinu 40 v α-tubulinu chrání mikrotubuly před následky mechanického stárnutí a hraje i roli v pohybu buněk, větvení axonů a růstu a udržováni výběžků neuronů. HDAC6 je hlavní deacetylasou tubulinu a jeho význam jakožto možného cíle pro léčbu rakoviny a neurodegenerativních onemocnění stále roste. Tím pádem vzrůstá i potřeba hlubšího pochopení jeho interakce s tubulinovým substrátem. V této práci ukazujeme, že HDAC6 deacetyluje dimery tubulinu 1500 krát vyšší rychlostí než mikrotubuly. Naše data naznačují, že s výjimkou aminokyselin na pozicích P_1 a P_{-1} přispívají aminokyseliny obklopující Lys40 k rozpoznávání substrátu minimálně, a že účinná deacetylace vyžaduje komplexní interakce s tubulinovým dimerem.

Table of Contents

1. INTRODUCTION

1.1. ZINC-DEPENDENT HYDROLASES

Zinc, either catalytic or structural, is found in approximately 10% of the proteome. Zinc metalloproteins belong to each of the six enzyme classes but hydrolases are prevailing [1]. Zinc-dependent hydrolases are a class of metalloenzymes, where zinc ions catalyze hydrolytic reactions. In them, the zinc ions are usually coordinated by the side chains of His, Glu, Asp, and Cys, and water. The family encompasses peptidases, lipases, phosphatases, carbonic anhydrases, β-lactamases, and deacetylases.

The physiological function of zinc was recognized in 1940 when it was identified as an element crucial for activity of carbonic anhydrase. This bluish-white diamagnetic metal exists, within the organism, in both free and bound form. Cellular levels of free zinc need to be strictly regulated as decreased concentrations result in cell growth arrest and higher concentrations lead to zinc toxicity. Zinc is exported from cytosol by zinc transporters, imported into the cell by ZRT/IRT-like proteins (Zips), and stored by metallothioneins. A mutation in the gene for the zinc transporter ZIP4 causes zinc deficiency that could manifest as acrodermatitis enteropathica [2]. This disease illustrates the importance of zinc for human organism as it was lethal before the era of zinc supplements.

Based on the number of zinc ions required for their catalytic activity, the zinc metalloenzymes can be either mononuclear or binuclear. In zinc-dependent hydrolases both types of metal center were described. Interestingly, the mononuclear enzymes often have another zinc binding site but binding of an additional zinc into this site usually results in an inhibition of enzymatic activity [3]. In proteins, there are four types of zinc-binding site: catalytic, co-catalytic, protein interface, and structural. In the **catalytic** site the zinc ion is usually bound to at least one water molecule and three to four additional amino acid ligands. The metal ion is required for water activation that in turn is necessary for the nucleophilic attack, polarization of the scissile bond carbonyl, and stabilization of the negative charge in the transition state. **Co-catalytic** site contains additional one or two zincs or other transition metals bridged by water or an amino acid. These metals lie in close proximity to one another, act synchronously as a catalytic unit and are important for proper folding as well. **Protein interface** site zincs lie on the interaction interface of subunits of a protein or two adjacent

proteins and are important for quaternary structure. The **structural** site zinc stabilizes tertiary structure of the protein [4].

Zinc is an ideal enzyme cofactor for three reasons. Firstly, while a strong Lewis acid, it lacks redox properties. It does not cause oxidative damage because its d-orbital is full. Secondly, the full d orbital also means that ligand binding does not have stabilizing effects. Therefore, zinc enzymes can easily bind ligands as zinc can be, without preference, four-, five-, or six-coordinated (see Figure 1). The coordination number is determined by bonding between metal and donor and repulsion between ligands. To transition between tetrahedral, trigonal bipyramidal and octahedral coordinations, the zinc complexes need to overcome just a minor energy barrier. Lastly, in zinc enzymes the coordinated water is easily exchangeable due to kinetic instability of zinc complexes. Also the pKa of coordinated water is lower than that of free water, thus adding to the reactivity of zinc enzymes [5].
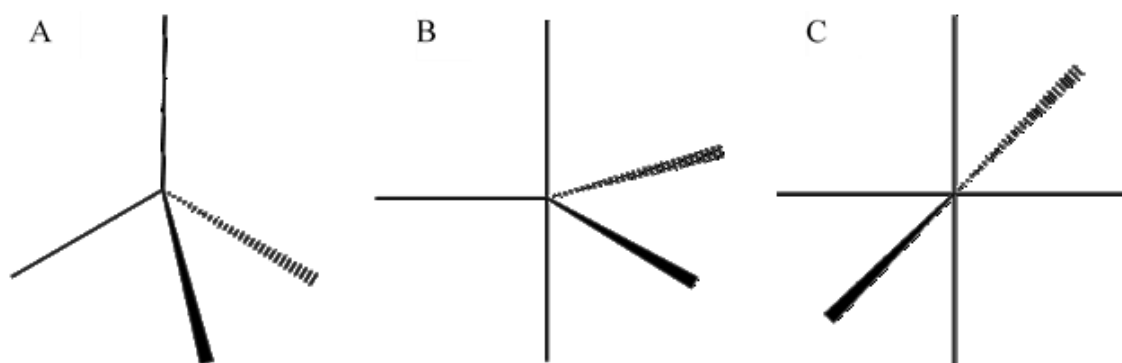
Figure 1: Zinc enzyme coordination
Zinc can exist in four-, five-, and six-coordinate state without any preference and assume A) slightly distorted tetrahedral, B) trigonal bipyramidal, or C) octahedral coordination.

Understanding of the exact mechanisms and specific roles of the individual zinc-dependent hydrolases might lead to identification of new highly specific inhibitors. Summarizing data collected on different hydrolases might help in rational design of inhibitors for hydrolases with yet unsolved crystal structures. In our laboratory we study histone deacetylases and carboxypeptidases. This thesis presents a detailed study of two of the zinc hydrolases: GCPII and HDAC6. We addressed structure-assisted design of new GCPII inhibitors and elucidated interactions between HDAC6 and tubulin, its natural substrate. We believe our work brings new data that adds to the understanding of the zinc hydrolase superfamily.

1.2.   GCPII

Human glutamate carboxypeptidase II (GCPII; E.C. 3.4.17.21) was independently identified by several research groups. As a result, it has different names based on either its physiological role or localization. It is the reason why it is also known as N-acetylated-α-linked acidic dipeptidase (NAALADase), prostate-specific membrane antigen (PSMA), and folate hydrolase (FOLH1). GCPII is now the name officially recognized by International Union of Biochemistry and Molecular Biology (IUBMB). It is a membrane bound zinc-dependent C-terminal exopeptidase that belongs to the M28 peptidase family [6,7].

The gene encoding human GCPII lies at the 11p11.2 locus. It consists of 19 exons and 18 introns [8] and translates into a 750 amino acids containing protein with molecular weight of 84 kDa. However, GCPII exists as a homodimer which undergoes posttranslational modifications and its actual molecular weight can therefore be up to 200 kDa.

GCPII was found to exist as a transmembrane protein localized to the apical plasma membrane of epithelial cells. It is expressed mainly in kidneys and brain, where its activity was reported to be the highest in cerebellum, midbrain, and at the boundary of medulla and pons [9]. High expression was also found in prostate cancer and neovasculature of majority of solid tumors [10,11].

1.2.1. GCPII DOMAINS

GCPII can be formally divided into 3 parts: a short intracellular N-terminal cytoplasmic tail (amino acids 1-18), a transmembrane helix (amino acids 19-43), and a large extracellular part (amino acids 44-750)[12,13].

The N-terminal tail mediates interaction with scaffold proteins such as clathrin, filamin A, or caveolin-1. It probably does not have any defined folds [14,15]. The transmembrane domain is predicted to have a canonical α-helical conformation and anchors the protein in the plasma membrane. The extracellular part is further subdivided into the protease-like domain (amino acids 57-116 and 352-590), the apical domain (amino acids 117-351), and the C-terminal domain (amino acids 591-750) (see Figure 2, page 4). The substrate binding cavity is formed by amino acid residues from all three of these domains. The protease-like

domain consists of the seven-stranded mixed β-sheet surrounded by 10 α-helices. The apical domain is formed by the central (3+4) stranded β-sheet sandwich flanked by 4 α-helices. It is wedged between the first and the second β-sheet of the protease-like domain. Helixes α15, α17, α18- α19, α20, organized in an Up-Down-Up-Down four helix bundle, form the C-terminal/helical domain [16,17].
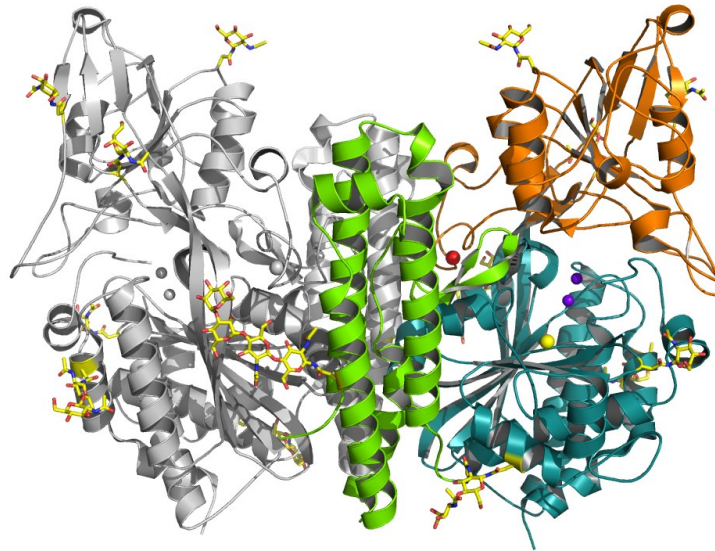
Figure 2: Extracellular part of GCPII
GCPII forms a dimer. Each of the monomers are consist of the N-terminal cytoplasmic tail, the transmembrane helix and the large extracellular part. The extracellular domain is further divided into the protease domain (blue), the apical domain (orange), and the C-terminal domain (green). Both monomers also contain two zinc ions (magenta), one calcium ion (red) and chloride ion (yellow). Pavlicek *et al*., 2012 [212] modified
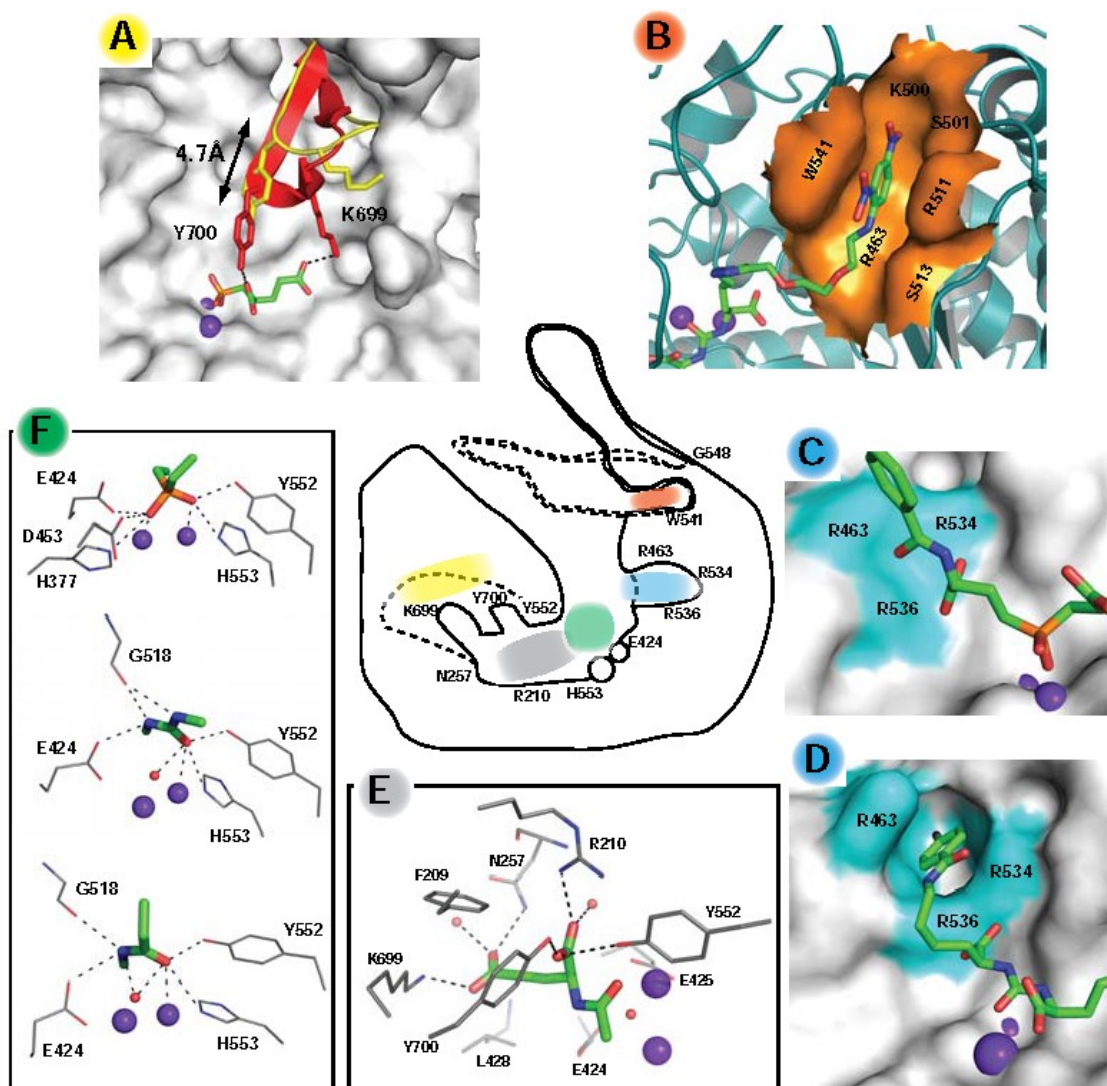
1.2.1.1.   ACTIVE SITE

The active site is shaped as a 20 Å deep substrate binding funnel with two active site Zn^{2+} ions at the bottom and this makes it a co-catalytic active site. The zinc cations are coordinated by water and Asp387. Zn_1 is additionally coordinated by His377 and Asp453 dietaryZn_2 by Glu425, and His553. The structure harbors two other inorganic ions. The Cl^- anion is responsible for orienting positively charged residues responsible for substrate or inhibitor binding. It is coordinated by the side chains of Arg534, Arg536, Asn451, and the main chains NH of Asp453 and lies in proximity of a P1 arginine patch. GCPII also contains Ca^{2+}, which although not a part of active site, is critical for activity. It is coordinated by Glu433, Glu436, Thr269, and Tyr272. The cation lies at the interface of the two monomers, 20 Å from

the active site and is thought to stabilize the loop Tyr272-Tyr279 involved in dimerization [16,18].

The pharmacophore (S1') pocket (Figure 3E, page 6) is a cavity occupying space of 8 x 8 x 8 Å and is delineated by Phe209, Arg210, Asn257, Glu424, Glu425, Gly427, Leu428, Gly518, Lys699, and Tyr700 [19]. The S1' site strongly favors L-amino acids and *(S)*-stereoisomeres of inhibitors [6,20]. The substrates bind into the S1' pharmacophore pocket via their C-termini. Generally, Gly518, Phe209, and Leu428 are engaged in Van der Waals interactions with a substrate/inhibitor functionality. The S1' pocket is optimized for binding of glutamate moiety (of a substrate or an inhibitor), and the GCPII specificity for glutamate-like groups is defined by a hydrogen-bonding pattern within this pocket. Here, the guanidinium group of Arg210 and the hydroxyl of Tyr552 engage the α-carboxylate of substrate, while the side chains of Asn257 and Lys699 form hydrogen bonds with its γ-carboxylate [21].

Several additional structural/functional features critical for the recognition of substrates/ligands by GCPII exist within the substrate-binding cavity. Residues Trp541–Gly548 form the so-called **entrance lid** (Figure 3, page 6). In its closed conformation it shields ligands in the active site from the exterior. On the other hand, in its open conformation, the lid can accommodate distal moieties of various inhibitors. A study using molecules containing dinitrophenyl with a long linker noted that the entrance lid remains open if needed. This led to identification of an **arene binding site** (Figure 3B, page 6) formed by three amino acids (Trp541, Arg511, and Arg463). Here, the arene ring is in the close contact with the indole group of Trp541 (3.1 Å) and the guanidinium group of Arg511 (3.9 Å) and the Arg463 side chain forms the bottom of the cleft. These interactions position the phenyl ring virtually parallel to both indole and guanidinium functional groups resulting in simultaneous π-cation (dinitrophenyl - Arg511) and π-stacking (dinitrophenyl - Trp541) interactions. It had been determined in a mutation study that only interaction with Trp541 is responsible for the affinity enhancement [22,23].

The GCPII active site contains flexible segments that allow the binding of ligands both similar and different from its natural substrates with high affinity. The S1 site contains so called **arginine patch** (Figure 3C, page 6) formed by Arg463, Arg534, and Arg536. This patch renders the S1 site more prone to bind substrates with acidic residues at the P1 position and its interaction with negatively charged moieties increases the enzyme's affinity towards

Figure 3: GCPII internal cavity

Central scheme represents glutarate sensor (yellow), arene binding site (red), arginine patch and S1/accessory hydrophobic patch (blue), S1'/pharmacophore pocket (gray), and active site (green). Alternative positions of the flexible elements (entrance lid, arginine patch, and glutarate sensor) are depicted by dashed lines. Zinc atoms are depicted as circles. **A)** Glutarate sensor position with pharmacophore pocket empty (yellow) or occupies by inhibitor or substrate (red) **B)** Arene binding site (orange) occupied by dinitrophenyl group of ARM-P2 (PDB code 2XEI **C)** Arginine patch (cyan) in the "stacking" position **D)** S1 accessory hydrophobic pocket (cyan) with DCIBzL (PDB code 3D7H). The S1 site is opened by simultaneous repositioning of the side chains of Arg463 and Arg536. **E)** hydrogen-bonding interactions between the S1' (pharmacophore) pocket-bound substrate and interacting GCPII residues. **F)** Interactions with phosphinate ZBG (top), urea ZBG (middle), and NAAG (bottom) in the vicinity of the active-site zinc ions. Zinc ions and water molecules are shown as purple and red spheres, respectively. Inhibitors/substrates bound are in stick representation with carbon atoms colored green, while GCPII residues are shown as lines with carbon atoms colored gray (panels E and F). Remaining atoms are colored blue (nitrogen), red (oxygen), and orange (phosphorus). Hydrogen-bonding interactions are shown as dashed lines. Pavlicek *et al.*, 2012 [212]

them. The position of Arg534 is invariant mainly thanks to the chloride anion bound to the S1 site which serves

as an anchor. The other two arginines are more flexible. Arg463 can alter between "up" and "down" positions and this transition allows the Arg536 side chain to alter between "stacking" and "binding" conformations. In the 'stacking' conformation Arg536 has its guanidinium group blocked between the guanidinium groups of Arg534 and Arg463 and is unable to bind a substrate. The transition into the 'binding' conformation requires a 4.5-Å shift of the guanidinium group [17].

Another important structural feature associated with the S1 site is an **accessory hydrophobic pocket** (Figure 3D, page 6) defined by Glu457, Arg463, Asp465, Arg534, and Arg536. Its bottom is formed in part by β-sheets of Arg463-Arg465 (β13) and Arg534-Arg536 (β14). Interaction of the long aliphatic chain of DCIBzL with this, relatively hard to reach, accessory hydrophobic binding site is believed to be behind the inhibitor's unique potency [21]. A **glutarate sensing** hairpin (Figure 3A, page 6) is an important structural feature formed by residues Lys699 and Tyr700 and wedged between helixes α18 and α19 along with the Leu679-Val690 loop. The glutarate sensor loop is directly involved in the specific binding of the glutarate. It is the only part of the S1' pharmacophore pocket that is not rigid as it can shift by 4 Å which results in the site's enlargement [16].

1.2.2. POSTTRANSLATIONAL MODIFICATIONS OF GCPII

Glycosylation of proteins is one of the most important posttranslational modifications that take place in the endoplasmic reticulum and the Golgi apparatus. There are 10 N-glycosylation sites in GCPII and N-glycosylation is a prerequisite for correct folding and secretion of human GCPII. Only glycosylation of residues distant from the putative catalytic domain are needed for GCPII activity. Among them the glycosylation of Asn638 is the only one considered indispensable. In all GCPII crystal structures four saccharide units at on the Asn638 are visible. However, only two saccharide units can be seen at the other glycosylation sites. This glycosylation has been identified as imperative for dimerization which in turn is essential for enzymatic activity of GCPII. It is unclear, however, if expression of the differently glycosylated variants is tissue specific nor what exactly is their role [24,25].

The only other reported posttranslational modification described for GCPII is acetylation. It has been shown that treatment of GCPII with the pan-HDAC inhibitor valproic acid (VPA) leads to 2-fold increase in acetylation. This posttranslational modification reportedly stabilizes the metallopeptidase by blocking its ubiquitination and thus degradation. Inhibition by selective HDAC6 inhibitor has the same effect as VPA treatment. Use of both inhibitors has cumulative inhibitory effects. Therefore, it stands to consider that the deacetylase involved in GCPII destabilization is HDAC6. Since the proof is indirect and the observation has not been confirmed by other groups the topic would require further examination [26].

1.2.3. REACTION MECHANISM
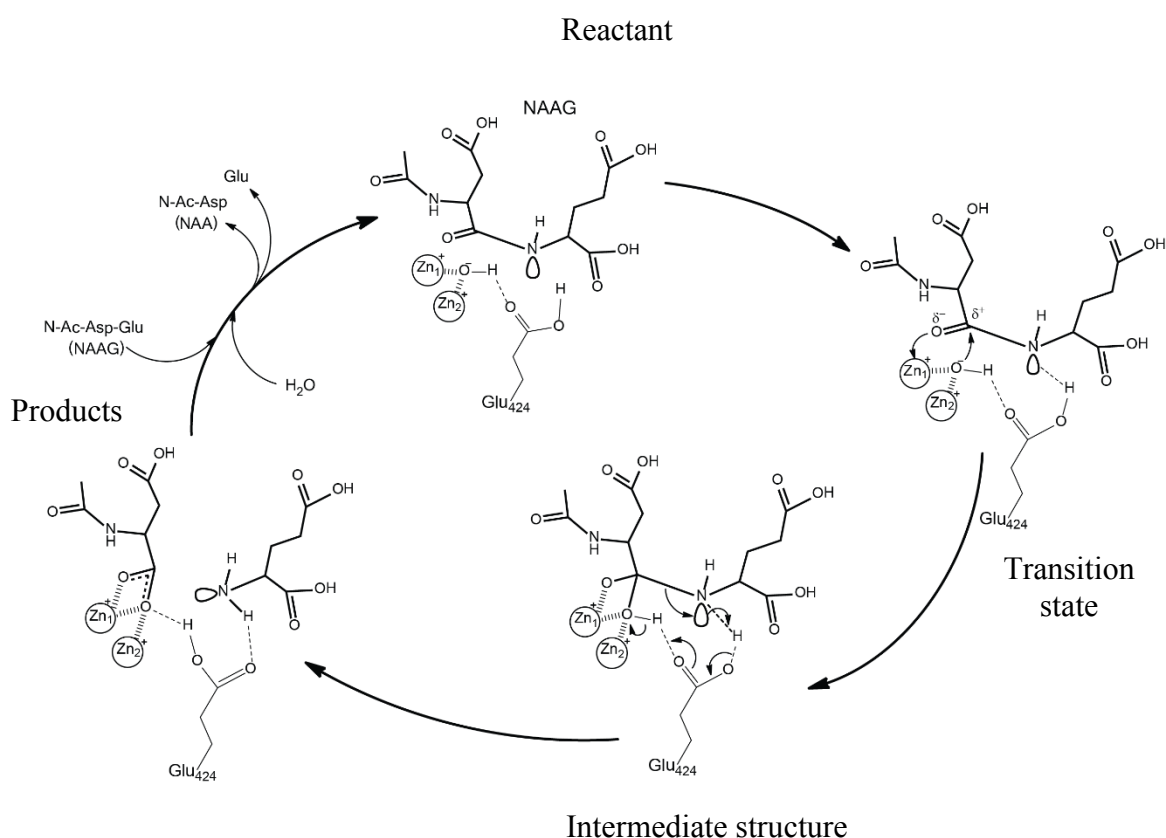
Figure 4: Reaction mechanism of NAAG hydrolysis by GCPII
Mechanism of NAAG hydrolysis catalyzed by GCPII. Substrate/products are depicted in bold lines. Catalytic (Zn_1) and co-catalytic (Zn_2) zinc ions are in circles. Small arrows indicate electron shifts. Klusak *et al.*, 2009 [27], modified

GCPII substrates recognition employs the induced fit mechanism. The substrate processing is exemplified here by the hydrolysis of N-acetyl-aspartyl-glutamate (NAAG), the natural GCPII substrate. Upon entering the substrate binding cavity the substrate Asp (via its β-carboxylate) forms an ionic bond with the guanidinium groups of Arg534 (2.9 Å) and Arg536 (3.1 Å) of the arginine patch, a hydrogen bond with Asn519 (Nδ2, 3.0 Å), and equidistant bonds with two water molecules (2.7 Å). The carbonyl oxygen of the acetyl group engages the side chains of Arg536 (Nη2, 2.7 Å), Asp453 (Oδ2, 3.0 Å), and Asn519 (Nδ2, 3.1 Å), while the methyl group extends into a pocket delineated by the side chains of Ile386, Asp387, Ser454, Glu457, and Tyr549. The carbonyl oxygen of the peptide bond forms a hydrogen bond with the hydroxyl group of Tyr552 and another weak bond with Zn_1^{2+} (both 2.6 Å). Additionally, the nitrogen atom of the secondary amide forms a hydrogen bond with the Gly518 carbonyl oxygen (2.9 Å). In the active site the catalytic Zn^{2+} ions are at 3.3 Å distance from each other bridged by equidistant interactions (2 Å) with oxygen of the hydroxide anion.

Formation of the tetrahedral reaction intermediate causes elongation of the distance between the two zinc ions to 3.5 Å. The oxygen of the hydroxide anion forms a C-O bond with the substrate's peptide bond carbon atom and the carbonyl oxygen of substrate is stabilized by interaction with Tyr552 and Zn_1^{2+}. The formation of the reaction intermediate is accompanied by a shift of the protonated hydroxyl group of Glu424 so that it can form a hydrogen bond with NAAG nitrogen thus stabilizing its pyramidal conformation. The reaction mechanism is completed when a proton is transferred from the Glu424 hydroxyl to the peptide bond nitrogen, and another proton is transferred from the OH- moiety to Glu424 and this culminates in the scissile bond cleavage. Resulting *N*-Ac-Asp dissociates and is released from the active site when the hydroxyl used in reaction is replaced by water while the glutamate part of the substrate remains tightly bound [27]. In the catalytic mechanism of GCPII, Glu424 plays a dual role as catalytic acid and base when it shuttles the proton from the zinc-bound catalytic water and transfers it to the amino moiety of the substrate. The activated water performs nucleophilic attack on the carbonyl group of the substrate (for example the aspartyl residue of NAAG) [16,27]. The summary of the reaction mechanism can be seen in Figure 4 on page 8.

1.2.4. ROLES OF GCPII

1.2.4.1. PHYSIOLOGICAL ROLE

Ideally a lot of information about the role of a protein can be gained from phenotype (if detectable) of model organisms with the relevant gene inactivated or deleted altogether. Four different studies had been published, describing the effects of GCPII knock out in mice. Bacich *et al.*, 2002, were the first to publish a study of GCPII KO mouse. Their strategy relied on deletion of exons 1 and 2. They were able to obtain GCPII$^{-/-}$ homozygotes who similarly to GCPII$^{+/-}$ heterozygotes bred and developed normally without any detectable phenotype [28]. A year later Tsai *et al.*, 2003 published a rather contradictory report. They chose an approach in which GCPII knock out was accomplished by deletion of exons 9 and 10 that lead to embryonic death of homozygous null mutants. The heterozygous mice developed apparently normally, but GCPII expression levels in wild type and heterozygous mutants indicated that GCPII expression was upregulated in the latter to compensate for the null allele [29]. Han *et al.*, 2009 obtained mice with deleted exons 1 and 2. In GCPII$^{+/-}$ heterozygous mice expression was reduced to 50%. The mice developed normally but the adults showed deficits in working memory, hyperactivity, and subnormal social skills. With this approach they were unable to breed the homozygous GCPII$^{-/-}$ mice, indicating that this approach to GCPII inactivation results in embryonic lethality suggesting that the enzyme plays a key role in embryogenesis [30]. Finally, Gao *et al.*, 2015 succeeded in preparing GCPII KO mice by removal of exons 3–5. The crossing of the GCPII$^{+/-}$ heterozygotes resulted in standard 25 % of homozygous GCPII null progeny and embryonic lethality was not observed. Western blots confirmed 50% decrease in GCPII expression in the heterozygous mice and no detectable GCPII in GCPII KO mice. The only difference observed was that the GCPII KO mice were more resistant to moderate traumatic brain injury [31]. These differing results are hard to reconcile at present and additional studies are warranted.

As mentioned before, GCPII has three major expression sites in the human organism. In healthy prostate GCPII exists as PSM', an N-terminally truncated form missing the first 56 amino acids of the intracellular and transmembrane domains, that is believed to be a product of posttranslational processing. This form is hydrolytically active on the NAAG substrate yet its function is unclear. It is localized to cytoplasm and apical side of the epithelium

surrounding prostatic ducts [32]. While the exact role of the carboxypeptidase in the prostate is yet to be identified, the substrates in the brain and the gut are identified and studied in depth. In the nervous system, GCPII is localized to the plasma membrane of astrocytes and Schwann cells [33,34]. There, the enzyme functions as NAALADase and hydrolyzes the neuropeptide *N*-acetyl-L-aspartyl-L-glutamate (NAAG). It is synthetized by the NAAG synthetase from NAA and glutamic acid which makes it different from other neuropeptides which arise from translation. This most abundant of mammalian neurotransmitters activates the group II metabotropic glutamate receptors. In particular, it is an mGluR3 agonist. GCPII inactivates NAAG by hydrolyzing it, resulting in N-acetyl-L-aspartate (NAA) and glutamic
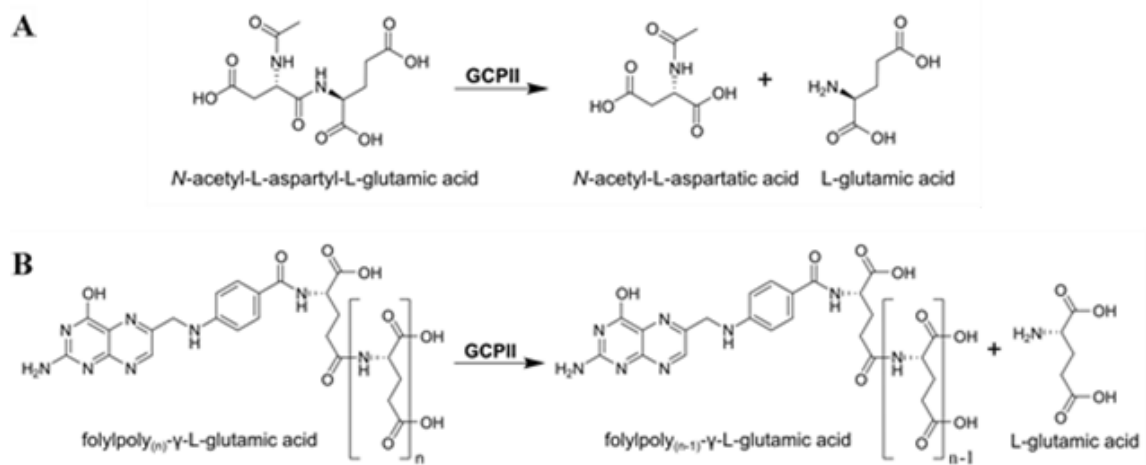
Figure 1: Scheme of reactions catalyzed by GCPII
A) GCPII cleaves the NAAG substrate into NAA and glutamic acid. B) GCPII hydrolyzes dietary folates thus enabling their absorption in small intestine (n=5-7)

acid release (Figure 5A) [9,28]. In the small intestine the enzyme cleaves the γ-linked glutamates from dietary folyl-poly-γ-glutamates, allowing thus their absorption into the blood stream (Figure 5B) [35]. GCPII also seems to play a role in vasculogenesis as the process is impaired in GCPII-null mice. The depletion of GCPII affects endothelial cell invasion through the extracellular matrix barrier and this is due to disturbance in a regulatory loop employing laminin-specific integrin and p21-activated kinase 1 [36].

1.2.4.2. PATHOLOGICAL ROLE

One of the highest expression levels observed for GCPII is in prostate cancer. In fact, GCPII/PSMA was found in more than 95% of prostate cancers. The exact role in oncogenesis is unknown but the vast difference in the expression levels between healthy and cancerous prostate tissue makes GCPII a great prostate cancer marker. As GCPII has been identified as a protein detected by the 7E11C-5 antibody, that was used for prostate cancer diagnostics, it was named prostate specific membrane antigen (PSMA) [37]. As prostate cancer is considered the second most common type of cancer in men worldwide, a plethora of molecules is being studied as possible tools for prostate cancer imaging. So far, the only FDA approved imaging molecule is ^{111}In-labeled capromab pendetide (also known as ProstaScint), a mouse monoclonal antibody against GCPII. This imaging agent was approved in 1996 by the US FDA for use in both newly diagnosed patients, potential or high risk patients, and patients suspected of having recurrent disease. It had been derived from 7E11-C5.3 antibody raised against the cytoplasmic portion of the enzyme and is currently used in diagnostics of prostate cancer. However, it has slow distribution and clearance and developing new imaging agents with better qualities would improve the diagnostics. The use of radiotracers brings along the usual dangers connected with introduction of radioactive matter into human organism so the research is aimed at minimizing the patients' exposure to them. Therefore, a lot of effort has been invested in generation of new diagnostic tools profiting of high levels of GCPII in prostate tumors and metastatic tissue derived from it yet with faster distribution and clearance [38].

Prostate cancer, however, is not the only malignancy with high GCPII expression. High levels of GCPII were observed in neovascular endothelium of lung, bladder, pancreas, skin, kidney, testes, brain, colon, skeletal muscle, and mesenchymal tissue (sarcoma) cancer. The expression was exclusively confined to the cancer tissue and did not occur in neovasculature of healthy organs and benign tumors [10,11,39]. These findings indicate that GCPII might be implicated in vasculogenesis and might be a valid target for cancer treatment by vasculogenesis inhibition.

Glutamate is the most potent excitatory neurotransmitter. Upregulation of GCPII activity leads to release of high amounts of glutamate into the synaptic space. This is considered neurotoxic and is associated with neurological disorders such as stroke, amyotrophic lateral

sclerosis, and Alzheimer's disease [40–43]. Administration of a potent GCPII inhibitor 2-MPPA shows a promise in treatment of schizophrenia [44]. Inhibition of GPII has a prophylactic effect against hyperalgesia, myelinated fiber degeneration and promotes nerve fiber regeneration in diabetic rats with longstanding diabetes, without affecting blood glucose levels. It alleviates hyperalgesia in rat models with preexisting neuropathy, improves nerve conduction velocity and myelinated fiber morphology and promotes nerve fiber regeneration and has neuroprotective effect in models of ischemic or traumatic brain injury and alleviates neuralgias. Inhibition of GCPII has a neuroprotective effect in rat model of middle cerebral artery occlusion potentially resulting in faciobrachial paralysis and damage to the dominant and/or non-dominant hemisphere [45–49]. These findings make inhibition of GCPII an intriguing approach for treatment of neurological diseases.
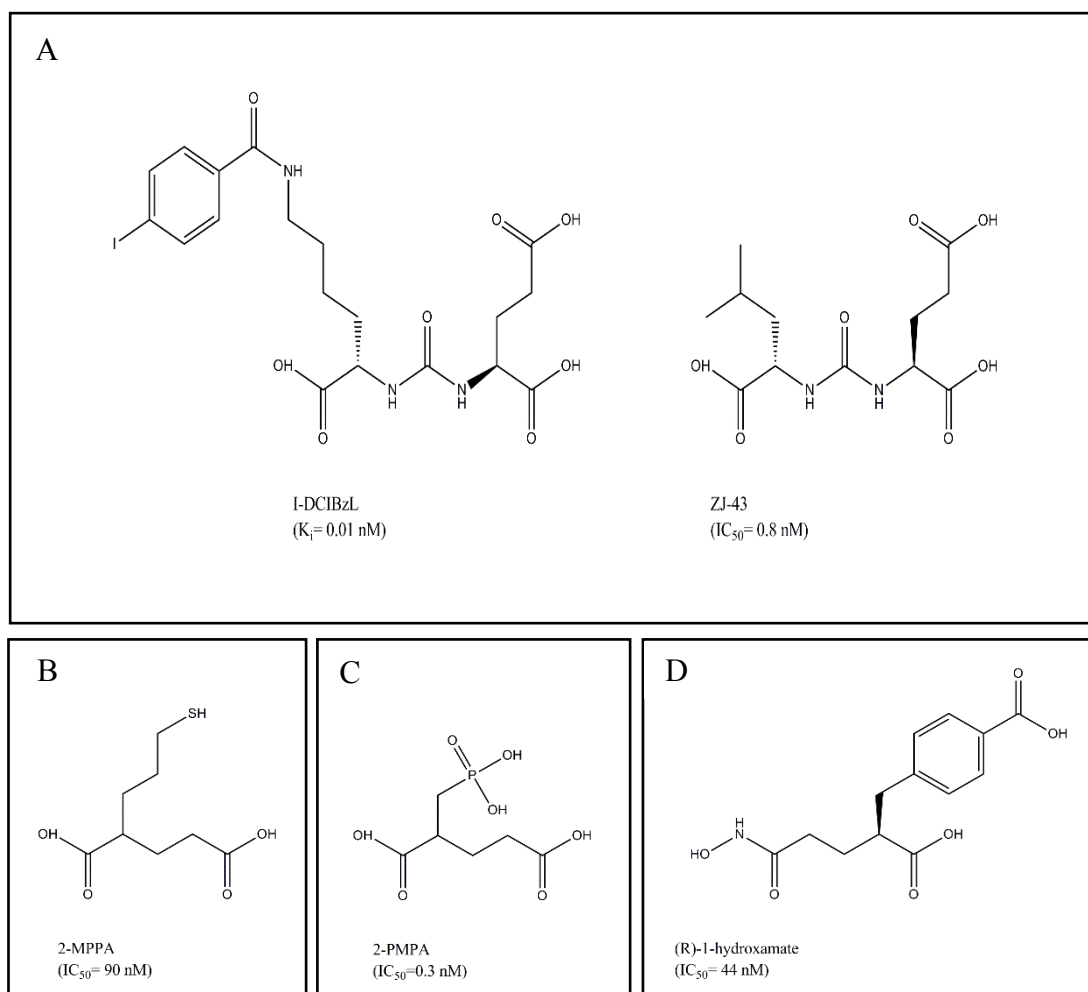
1.2.5. GCPII INHIBITORS

The role of GCPII in the CNS and prostate and its expression in neovasculature of almost exclusively malignant tissues makes it an interesting target of study. A lot of effort is nowadays invested into the design of new GCPII-specific inhibitors in order to find new compounds to block known functions of the enzyme. Therefore, use of new inhibitors as drugs in treatment of neurological disorders is conditioned by their ability to cross the blood-brain barrier. In case of prostate targeted inhibitors, they need to exhibit high specificity for the truncated PSM' form predominant in prostatic tumors. This is necessary for their use as scaffolds for imaging molecules for diagnostics and subsequently successful treatment. Potent specific inhibitors of prostate form of GCPII can also be used to generate highly selective PSMA binders that can serve as carriers of targeted cancerotoxic molecules.

In general, the GCPII inhibitors consist of a zinc-binding group (ZBG) and an S1' binding group (usually a glutamate moiety or glutamate isostere). Most of GCPII inhibitors are based on the NAAG molecule. The S1' pocket has evolved as a glutamate sensor and therefore GCPII has a high affinity for substrates and inhibitors bearing a glutamate moiety. The inhibitor's potency is affected by modifications at the P1' site such as shortening or lengthening of the aliphatic chain or removal of the carboxylic moiety. Analogously the S1 site has preference for negatively charged moieties and the loss of inhibitor potency after removal of α-carboxyl group indicates requirement of a third carboxylic acid for effective binding [22,50]. Crystal structures show that inhibitors derived from or similar to glutamic

acid bind exclusively to the pharmacophore S1' site, while dipeptide analogs with a non-hydrolysable peptide bond surrogate (such as the ureido linkage) or the tetrahedral transition state mimetics (phosphoramidates) occupy both S1' and S1 sites [21].

Inhibitors of GCPII can be divided into four groups based on the nature of the zinc-binding group present in their structure. These are: 1) phosphorous based inhibitors (phosphonate-, phosphate-, and phosphoramide-based), 2) urea based compounds, 3) thiols, and 4) hydroxamates. 2-phosphonomethylpentanedioic acid (2-PMPA) (Figure 6C, page 15) is an example of a potent phosphonate based GCPII inhibitor with the inhibition constant of 0.3 nM. Interestingly, the (*S*)-enantiomer of 2-PMPA inhibits GCPII with 300-fold higher affinity compared to the (*R*)-enantiomer. The high inhibitory potency results from the chelating effect of the phosphonate group combined with interaction of the glutarate (pentanedioic) part of inhibitor with the glutarate sensing site of the enzyme [51,52]. In phosphinate analogs of GCPII substrates, the planar peptide bond is replaced by the phosphinate functional group. These molecules resemble the unstable *gem*-diolate tetrahedral transition state formed during the course of substrate hydrolysis and are efficient inhibitors of the carboxypeptidase [17]. Among other potent GCPII inhibitors are phosphonate monoester derivatives of 2-PMPA and reverse phosphonate monoesters, with additional interactions with the S1 pocket, and phosphoramidates. The main problem with the phosphorous based inhibitors is the lack of oral bioavailability that limits their potential as therapeutic agents. This problem seems to have been resolved by the discovery of orally applicable fosinopril, a prodrug of fosinoprilat - a drug with disadvantageously poor absorption and distribution [53].

Urea based inhibitors have been widely used for prostate cancer imaging. They are easy to synthesize and modify. High potency of urea based inhibitors arises from the similarity in binding between these inhibitors and natural substrates. The binding of the C-terminal glutamate of the inhibitors into the S1' pocket is nearly indistinguishable from that of free glutamate and high similarity can be seen in binding mode of the urea group and the scissile peptide bond of NAAG. The ureido linkage of urea derived inhibitors mimics the planar peptide bond but the enzyme is unable to process it. Instead it binds via its carbonyl oxygen to Tyr552 (OH, 2.7 Å), His553 (Nε2, 3.2 Å), water molecule (2.8 Å), and the catalytic Zn^{2+} (2.6 Å). One of its nitrogens (N2) forms a hydrogen bond with γ-carboxylate of Glu424 (3 Å), carbonyl oxygen of Gly518 (2.9 Å), and activated water (3.1 Å) while the other (N1) binds solely to carbonyl group of Gly518 (3 Å) [21]. Additionally, interactions between

Figure 6: GCPII inhibitors
Urea based inhibitors I-DCIBzL and ZJ-43 B) thiol based inhibitor 2-MPPA C) Phosphonate based inhibitor 2-PMPA D) Hydroxamate inhibitor (R)-1-hydroxamate

the P1 carboxylate of the urea-based inhibitors and the side chains of Asn519, Arg534, and Arg536, mimic similar interaction pattern between GCPII and NAAG. Many urea based inhibitors are DCIBzL (IC_{50} = 0.06 nM) [54] (Figure 6a) derivatives, profiting from the unique interactions of its phenyl ring with the accessory hydrophobic pocket within the S1 site. A drawback of the urea-based inhibitors is their limited ability to cross the blood-brain barrier and therefore poor efficacy in the treatment of neurological disorders.

Thiol-based inhibitors stand out for their exceptional pharmacokinetic profiles. One of the most potent thiol inhibitors is 2-MPPA (2-(3-mercaptopropyl)pentanedioic acid, IC50 = 90 nM) (Figure 6B). This inhibitor is highly selective for GCPII and has 71% oral bioavailability in rats and is efficient in rat models of neuropathic pain [46]. Unfortunately, the thiol group is relatively nucleophilic and prone to oxidation that negatively affects its

metabolic stability and propensity to form immunogenic complexes with endogenous proteins.

Hydroxamates (Figure 6D, page 15) are inhibitors with nanomolar potency towards GCPII. These inhibitors have a unique binding mode in the internal cavity of GCPII. The hydroxamate head group a binds the active-site zinc ions with a distorted trigonal–bipyramidal geometry. The two zincs are bound asymmetrically, with Zn_1 bound in bidentate and Zn_2 in monodentate fashion. Unlike all other inhibitors that interact with the S1' site of GCPII, hydroxamate-based inhibitors bind selectively into the S1 site of the spacious entrance funnel. This conveys tolerance for bulky or hydrophobic groups as substituents of the canonical glutarate moiety and the absence of stereochemical preferences. Hydroxamates are effective in animal model of neuropathic pain and possess favorable pharmacokinetic properties [55]. It is interesting to note that hydroxamate-based compounds are also the major inhibitor class targeting HDAC6, the second hydrolase that is the focus of the thesis.

1.3.   HDAC6

HDAC6 belongs to the histone deacetylase family (EC 3.5.1.98, HDAC). HDACs are enzymes catalyzing removal of the acetyl group from the ε-amino group of lysine. The name, histone deacetylases, is historical and based on the ability to cause condensation of histones by removal the of acetyl group from their N-terminal tails resulting in transformation of the transcriptionally active euchromatin into heterochromatin and consequent decrease of transcription. Nowadays they are more accurately referred to as lysine deacetylases (KDACs) as they are active on many non-histone substrates. The HDAC family can be divided according to cofactor requirements into NAD^+-dependent Sirtuins and zinc-dependent histone deacetylases. The human histone deacetylase family consists of 18 members (Figure 7, page 17) which are further divided into four classes based on homology to their yeast counterparts. Class I, where HDACs 1, 2, 3, and 8 belong, is homologous to RPD3. Class II HDACs are homologous to HDA1 and are subdivided into 2 subclasses based on their domain organization. Class IIa consists of HDACs 4, 5, 7, and 9. Class IIb contains HDAC6 and HDAC10. In the sequence of these two deacetylases a duplication of the deacetylase domain occurred during the evolution. However, in the case of HDAC10 the second catalytic domain is incomplete and inactive. The NAD^+-dependent deacetylases encompassing Sirtuins 1-7 are grouped in class III and their yeast counterpart

is Sir2. Class IV has just one member HDAC11. This is the smallest histone deacetylase and it does not share homology with either RPD3 or Hda1 [56–58].

The coding sequence of human HDAC6 is mapped on the X-chromosome p11.22-23 locus. The HDAC6 gene is a single copy gene coded by 28 exons and spanning over nearly 22 000 bp and is translated into 1215 amino acid protein [59,60]. HDAC6 was identified in 1999 by two independent groups as a result of search for Hda1 homologues. The protein is expressed in high levels in testis, lower amounts were found in brain, heart, liver, kidneys, mammary gland, spleen, and pancreas. Although primarily localized in the cytoplasm, upon acetylation by CBP, HDAC6 translocates into the nucleus [61,62].
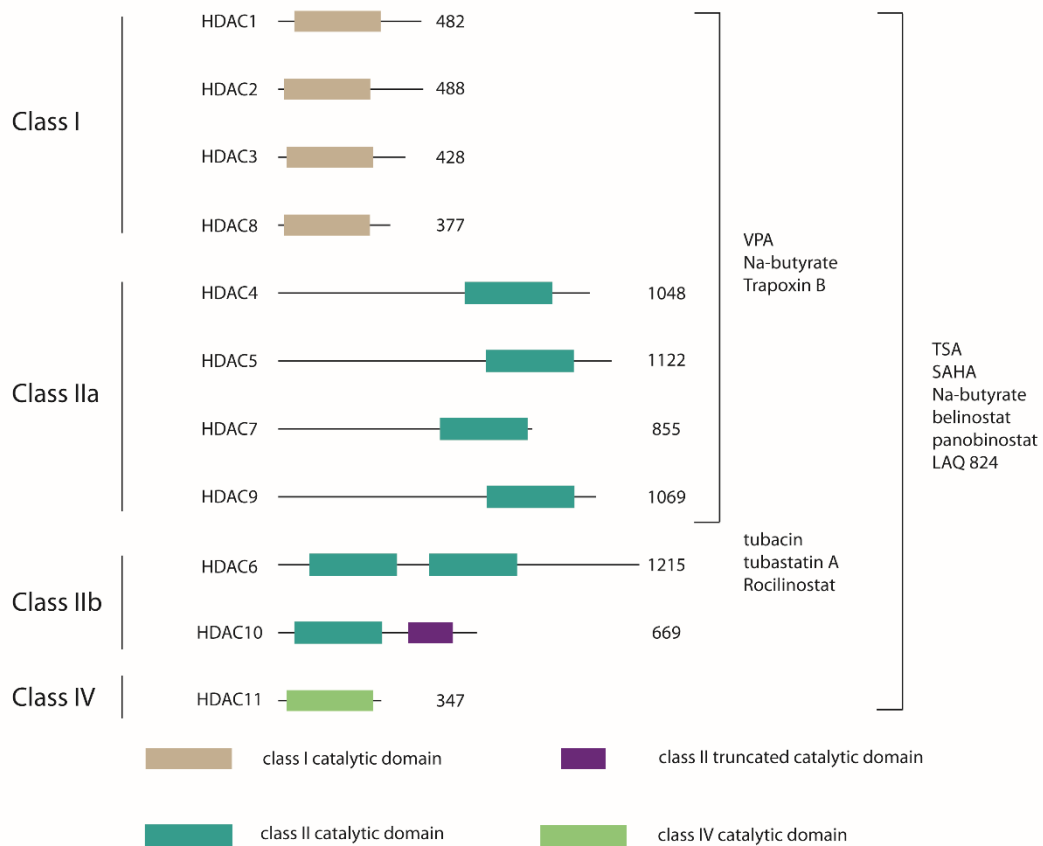
Figure 7: Zn-dependent histone deacetylases.
Zinc-dependent HDACs are divided into four classes according to homology with their yeast counterparts. Numbers following the domain scheme correspond to the size (number of amino acids) of the particular HDAC. Histone deacetylase inhibitors specificities indicated by brackets encompassing the classes they effectively inhibit.

1.3.1. HDAC6 DOMAINS

The domain organization (Figure 8) of HDAC6 makes it unique among zinc-dependent deacetylases as it is the only member to have a fully duplicated catalytically active deacetylase domains. The catalytic domains are highly structurally conserved and their amino acid sequences share 47% identity and 64% similarity. They are separated by a glutamate rich linker. Two sequences situated at the N-terminus regulate cellular localization of HDAC6. The first of them is nuclear localization sequence (NLS, 14-59 amino acids)

Figure 8: HDAC6 domain organization
Domain organization listed from the N-terminus: NLS (Nuclear Localization Sequence) by association to importin-α enables translocation to nucleus, NES (Nuclear Export Signal) targets HDAC6 for export from nucleus to the cytoplasm, DD1/DD2 (Deacetylase Domains) catalytic deacetylase domains, SE14 (Serine-Glutamate containing tetradecapeptide) cytoplasm retention signal, and BUZ (Binding of Ubiquitin Zinc finger) permits binding to ubiquitinated proteins. Numbers indicate positions of the individual domains within the amino acid sequence.

regulating HDAC6 import into the nucleus. The transport is mediated by importin-α and its interaction with HDAC6 is regulated by p300-mediated acetylation within the NLS sequence. Acetylation of a cluster of lysines in this domain results in the retention of HDAC6 in cytoplasm [63,64]. The shuttling of HDAC6 between the cytoplasm and the nucleus requires presence of the nuclear exclusion sequence (NES). Three short leucine rich NES-like sequences have been identified but only the N-terminal NES1 is critical for CRM1/exportin1 mediated transport [62].

The existence of two deacetylase domains (DD1, 84-440 amino acids and DD2, 479-835 amino acids) raises several questions. One of them is: How are the two domains organized within the protein? Recently solved structure of zebrafish DD1/DD2 tandem domains shows that they are closely attached in an ellipsoid-shaped complex in which the linker forms a symmetry axis and serves as a seal between the two catalytic domains with arginase-deacetylase fold [65,66]. The two active sites are located 50 Å apart. The importance of the linker region has been demonstrated by experiments in which addition or removal of as

little as 5 amino acids resulted in decrease of histone deacetylase activity and near complete abolishment of tubulin deacetylase activity [67].

Another question is: Are both of the domains catalytically active and if they are, do they have distinct roles? It seems that the activity of the domains differs depending on the substrate and origin of the particular HDAC6. Human and murine HDAC6 requires both domains for its histone and tubulin deacetylase activity [67,68] but only DD2 of human HDAC6 was necessary for survivin deacetylation [61,69]. A recently published report shows that human DD1 is highly active on C-terminally acetylated substrate only and exclusively in tandem domain assembly with both the linker and the DD2. This is thought to be due to the stabilizing effect of DD2 on the DD1 structure. The catalytic domains of *Danio rerio* Hdac6 share ~ 60% amino acid sequence identity and ~75% similarity with human HDAC6. Unlike in human however, both catalytic domains are active on peptide substrates even if tested as individual domains [70].

The SE14 (serine-glutamate tetradecapeptide, 884-1022 amino acids) domain is characteristic for the human isoform and not present in mouse Hdac6. The SE14 domain is dispensable for both the deacetylase and ubiquitin binding activity of HDAC6 and functions as cytoplasm retention signal [71].

BUZ (binding of ubiquitin zinc finger, 1131-1192 amino acids) domain bears homology to deubiquitinating enzymes. Thanks to the 11 conserved cysteine and 10 histidine residues the domain binds three molecules of zinc. The C-terminal domain binds equimolar amounts of ubiquitin and enables HDAC6 to bind to ubiquitinated proteins. This ability of HDAC6 is prerequisite for its pivotal role in polyubiquitin-positive aggresome formation. The BUZ domain is also necessary for recognition/binding of a subset of HDAC6 substrates such as Hsp90 and Tat [72–74].

1.3.2. POSTTRANSLATIONAL MODIFICATIONS OF HDAC6

As HDAC6 plays a role in so many processes it is understandable that its activity has to be finely regulated. Posttranslational modifications are a logical tool for the cell to achieve instantaneous change in HDAC6 enzymatic activity without affecting the overall amount of the protein. HDAC6 undergoes acetylation, phosphorylation, *S*-nitrosylation, and autoubiquitination (Table 1 on page 21 offers a detailed overview).

Phosphorylation is probably the most studied of HDAC6 modifications. It is highly diversified with different residues being phosphorylated by different kinases (Table 1). In mouse model, exposure to cigarette smoke leads to oxidative stress. As a result GSK-3β-mediated phosphorylation of Ser22 of HDAC6 causes increase in HDAC6 activity [75]. Phosphorylation of Ser458, localized outside DD1, by protein kinase CK2 is vital for dynein binding and formation of aggresome [76].

Phosphorylation of HDAC6 in response to EGF is an example of the already mentioned diversification. Binding of EGF into the EGFR receptor is a signal for phosphorylation of HDAC6 on Tyr570. The modification has inhibitory effects on its tubulin deacetylase activity. It leads to microtubule hyperacetylation and causes an increase in EGFR degradation. The active unphosphorylated form of HDAC6 deacetylates microtubules and slows down EGFR endosomal trafficking and degradation [77]. However, when EGF is a part of the EGFR-Ras-Raf-MEK-ERK signaling cascade, it mediates phosphorylation of Ser1035 by ERK1. This leads to upregulation of HDAC6 tubulin deacetylase activity. The resulting tubulin hypoacetylation induces cell migration [78]. So one signaling molecule activates two different kinases with two different results. Yet another kinase is utilized in regulation of cell motility by phosphorylation of HDAC6 as phosphorylation of HDAC6 by GRK2 at Ser1060, Ser1062, and Ser1069 enhances its tubulin deacetylase activity and promotes cell motility [79]. Lastly, phosphorylation of yet unknown residues by PKCζ and Aurora A resulting in upregulation of HDAC6 tubulin deacetylase activity have been reported. In the case of Aurora A, the phosphorylation negatively affects ciliary axoneme

Modification	Residue modified	Function	Enzyme involved	Source
Acetylation	Lys51, Lys52, Lys53,Lys 55, Lys 57, Lys 58	Decreases TDAC activity, decreases HDAC6 mediated cell motility, anchors HDAC6 within cytoplasm	p300	Liu *et al*., 2012 [63]
phosphorylation	Ser22	Increase of TDAC activity Depolymerization of MT	GSK-3β	Borgas *et al*., 2015 [75]
	Ser458	Necessary for interaction with dynein and aggresome formation	CK2	Watabe and Nakaki 2011 [76]
	Tyr570	Inhibits TDAC activity	EGFR	Deribe *et al*., 2009 [77]
	Thr1031	NA	ERK1	Williams, Zhang *et al*., 2013 [78]
	Ser1035	Increases TDAC activity Stimulates cell migration	ERK1	Williams, Zhang *et al*., 2013 [78]
	Ser1060 Ser1062 Ser1069	Increase in TDAC activity Promotes cell motility	GRK 2	Lafarga *et al*., 2012 [79]
S-nitrosylation	Ala549	Suppresses TDAC activity	NA	Okuda, Ito *et al*., 2015 [82]
Ubiquitination	NA		HDAC6	Riolo *et al*., 2012 [61]

Table 1: Overview of HDAC6 posttranslational modifications
The type, location, effect and modifying enzyme are listed, along with the publications describing the given modification. HDAC (histone deacetylase)/TDAC(tubulin deacetylase) activity

stability and leads to ciliary resorption during cell cycle [80,81]. Interestingly, the only inhibitory phosphorylation, the Tyr570 phosphorylation by EGFR, also happens to be the only phosphorylation within deacetylase domains.

Acetylation of HDAC6 regulates its activity and localization. Acetylation of HDAC6 by CBP on a yet unidentified lysine residue results in its transport into nucleus [61]. On the other hand, acetylation of a cluster of lysines (K51, 52, 53, 55, 57, and 58) within the N-terminal NLS by p300 acetyl transferase anchors HDAC6 in the cytoplasm by blocking its interaction with importin-α. This acetylation also causes a decrease of tubulin deacetylase activity, and results in decrease of cell motility [63,64].

Very little is known about HDAC6 *S*-nitrosylation and ubiquitination. The *S*-nitrosylation causes suppression of α-tubulin deacetylation. It can be induced by treatment with inflammatory cytokines TNF-α, IL-1β, and IFN-γ. This supports the presumed role of HDAC6 in immune system management. Nevertheless, the role of this modification needs to be studied further [82]. In accord with HDAC6 being an E3 ubiquitin ligase the enzyme undergoes autoubiquitination. It has been shown that ubiquitination of HDAC6 does not markedly affect its stability [73,83].

1.3.3. REACTION MECHANISM OF HDAC6

The current HDAC6 catalytic mechanism scheme is based on crystal structure of DD2 catalytic domain from *D. rerio* co-crystalized with trichostatin A. There is minimal structural difference between human and zebrafish DD2. This difference lies at the outer rim of the active site distant from bound inhibitors and all the amino acids critical for catalysis are strictly conserved across the species so this scheme should accurately represent the catalytic mechanism of human DD2 as well. In the absence of a substrate, the active site Zn2+ is coordinated by Asp612, His614, Asp705, and a water molecule thus assuming distorted tetrahedral coordination with the seemingly vacant coordination site (Figure 8a). Upon the substrate entering the catalytic pocket a precatalytic intermediate is formed. Here the substrate carbonyl of the N^ε-acetyl-L-lysine is coordinated to the previously vacant site on Zn^{2+} which then becomes a pentacoordinate metal ion as the substrate fails to displace the water molecule (Figure 8b). The nucleophilic attack of the metal-coordinated water molecule on the carbonyl group of N^ε-acetyl-L-lysine is initiated by the Zn^{2+} ion and H573 which serves as a general base. A tetrahedral intermediate forms and is stabilized by the coordinate
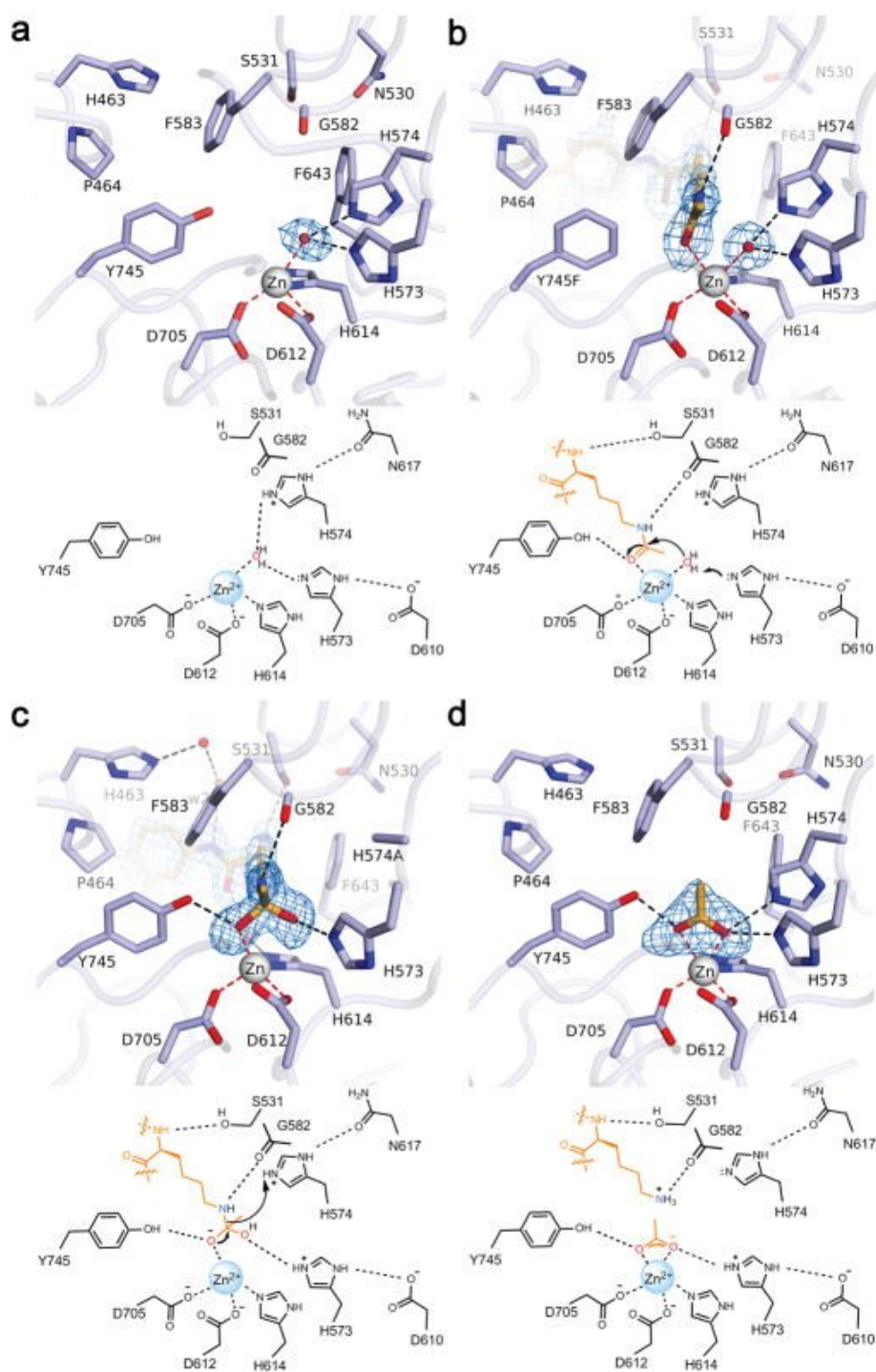
Figure 9: Reaction mechanism of deacetylation of tubulin derived substrate by DrHDAC6
(a) The active site of HDAC6 is empty. In the absence of a substrate, Zn^{2+} is coordinated by Asp612, His614, Asp705, and a water molecule and assumes distorted tetrahedral coordination. (b) Substrate binds to the active site. Upon substrate binding, Zn^{2+} becomes a pentacoordinate metal ion. (c) Nucleophilic attack of the metal coordinated water on the carbonyl group of Nε-acetyl-L-lysine results in tetrahedral intermediate. (d) Collapse of the tetrahedral intermediate yields products (lysine and acetate). (Hai & Christianson, 2016, [70])

bond with the Zn^{2+} ion and hydrogen bonds with Gly582, Tyr745, His573 and His574. In this HDAC6 differs from generally accepted HDAC8 catalytic mechanism where Zn^{2+} geometry is 5-coordinate square pyramidal and includes two water molecules, one of which is then replaced by the substrate carbonyl group [66]. The oxyanion atom of the tetrahedral intermediate is stabilized by coordination to Zn^{2+} and a hydrogen bond with Tyr745. Protonated His574 probably serves as a general acid and enables the collapse of the tetrahedral complex giving rise to acetate and L-lysine (Figure 9 Fc-d, page 23) [70].

The fact that the backbone amide group C-terminal to the acetyllysine is hydrogen-bonded to only a water molecule and makes no direct contacts with active site residues of HDAC6 means that there can be any amino acid at the P^{+1} position. The Ser531 and Ser538 of zebrafish and human DD2 domains, respectively, are conserved across all species as they are crucial for substrate recognition and acetyllysine positioning in the active site. The selectivity of DD1 for carboxy-terminal lysine acetylation is caused by restriction within its active site. The protruding Lys330 and in human HDAC6 also Tyr225 make the active site narrower and seem to function as gatekeepers [70].

1.3.4. ROLES OF HDAC6

1.3.4.1. PHYSIOLOGICAL ROLE

To date, at least twenty HDAC6 substrates have been identified. They are involved in various cellular processes and through them HDAC6 is implicated in apoptosis, cell signaling, cell motility, protein degradation, immune response and DNA repair. Role of HDAC6 in apoptosis is mediated via survivin and Ku70. Survivin, also called BIRC5 (baculoviral inhibitor of apoptosis repeat-containing 5), belongs to the IAP (Inhibitor of apoptosis protein) family. Its presence in the cytosol prevents caspases from inducing apoptosis. Opposing effects of histone acetyl transferase CBP and histone deacetylase HDAC6 regulate the acetylation state of survivin. The reversible acetylation of Lys129 serves as a mechanism for regulation of survivin localization. The deacetylation leads to its depletion from the nucleus. Estrogen induces CBP-mediated acetylation of HDAC6 and triggers its relocation from the cytoplasm to the nucleus. There HDAC6 binds directly to survivin and deacetylates it at Lys129. Acetylation of this amino acid marks it for export from the nucleus [61]. Ku-70

prevents the cell from entering apoptosis by inhibition of the pro-apoptotic Bax protein. The C-terminal tail of Ku70 contains Lys542 and Lys553. The deacetylation of these amino acids is critical for Ku70 to impede Bax induced apoptosis by sequestering Bax in the cytosol [84]. The role of reactive oxygen species and ensuing DNA damage in development is well studied. HDAC6 deacetylates peroxiredoxin I (PrxI; Lys197) and peroxiredoxin II (PrxII; Lys196). Acetylation of PrxI renders it more resistant to overoxidation caused by hydrogen peroxide. As a result, the hydrogen peroxide reducing activity, mediated by the thioredoxin system is rescued. Inhibition of HDAC6 and subsequent increase in PrxI and PrxII acetylation can save cells from ROS induced apoptosis [85].

HDAC6 in involved in DNA repair via the MutS protein homologue 2 (MSH2). In eukaryotic cells MSH2 and MSH6 form a heterodimer MutSα which scans DNA for mismatched pairs and short insertion deletion loops. When DNA damage is recognized, the MutSα repairs it in ATP-dependent manner or leads to cell cycle arrest and triggers apoptosis. HDAC6 first deacetylates MSH2 and then marks it for proteasomal degradation by functioning as the E3 ubiquitin ligase [83,86,87].

Via regulation of acetylation state of β-catenin, HDAC6 influences cell signaling. β-catenin is an important regulator of the Wnt signaling pathway that controls cellular differentiation and embryonic development. It also plays role in cell adhesion and gene transcription. In the absence of the Wnt ligand, β-catenin is phosphorylated, ubiquitinated, and finally it undergoes proteasomal degradation. β-catenin can be deacetylated by HDAC6 on Lys49. This deacetylation is under control of EGF and leads to inhibition of β-catenin phosphorylation on Ser45 by CK1. The phosphorylation otherwise serves as a signal for β-catenin degradation. The deacetylation results in c-Myc induction and is required for cell proliferation and nuclear localization of β-catenin [88,89]. HDAC6 has also been described as a MAPK activator as its overexpression activated ERK, JNK, and p38 MAP kinase in a dose-dependent manner [87,90].

HDAC6 mediated deacetylation of cortactin is critical for translocation of cortactin to cell periphery and cell migration. Eleven lysines within cortactin repeat regions are deacetylated, forming two distinct positively charged patches necessary for its interaction with F-actin [69]. Deacetylation of ciliary microtubules and cortactin by HDAC6 is an important step of ciliary disassembly. Ran et al., [91], reported that HDAC6 regulates ciliary disassembly by a process independent of known ciliary regulators. Deacetylation of microtubules of ciliary axoneme causes their destabilization. That causes ciliary disassembly, a mechanism that also

requires deacetylation of cortactin. This in turn stimulates interaction of cortactin with F-actin leading to resorption of cilia due to actin polymerization. This regulation process has implication in ciliopathies such as polycystic kidney disease, retinitis pigmentosa, Usher, Alstrom, and Bardet-Biedl syndromes. Myosin heavy chain 9 (MYH9 / myosin-9/ myosin IIA) is a cellular non-muscle myosin and a substrate of HDAC6. Opposing activities of MYH9 and MYH10 regulate lamellipodia extension at the leading edge and subsequent cell spreading. These two isoforms of myosin are also involved in focal adhesion of cells. Both lamellipodia extension and focal contact formation require reorganization of actin bundles. MYH9 associates with actin and the interaction decreases after MYH9 is deacetylated by HDAC6 [92–94].

There are three major pathways in which a cell can get rid of damaged or misfolded proteins: either lysosome mediated autophagy or the non-lysosomal pathways ending in proteasome or aggresome. HDAC6 binds misfolded proteins, marked for degradation by ubiquitination, via its C-terminal ubiquitin binding BUZ domain, HDAC6 is necessary for the formation of ubiquitin positive aggresome and mediates binding of misfolded polyubiquitinated proteins to dynein motor proteins. Along with the p97/VCP chaperone, HDAC6 determines the destiny of ubiquitinated proteins. In complex with HSF1 and HSP90 the deacetylase prevents a potentially cytotoxic accumulation of aggregated proteins [74,95,96]. If the ubiquitin-proteasome system is disabled, HDAC6 expression triggers autophagy and rescues degenerative phenotype in *D. melanogaster* model [97].

1.3.4.2. PATHOLOGICAL ROLE

HDAC6 is implicated in carcinogenic processes through several of its substrates. p53 is a tumor suppressor protein and tumors with mutated p53 tend to be more malignant and resistant to treatment by chemotherapeutics [98,99]. HDAC6 deacetylation of Lys 381/382 of p53 results in stabilization of the wild type protein and destabilization of the mutant p53 which accumulates in tumors. It has been shown that inhibition of HDAC6 results in disruption of the p53/Hsp90 complex. Thus a combinatorial treatment targeting p53 and HDAC6 might constitute a new anticancer strategy [100]. Hsp90 possibly implicates HDAC6 in tumor angiogenesis. Hyperacetylation of Hsp90, as a result of HDAC6 inhibition, triggers proteasomal degradation of VEGFR1 and VEGFR2 in cancer cells [101]. In neuroblastoma cell line, the inhibition of HDAC6 results in apoptosis. It leads to Ku70

hyperacetylation and renders the protein unable to sequester pro-apoptotic Bax, thus cancelling anti-apoptotic effect of Ku70 [102]. Blocking tumor angiogenesis and triggering apoptosis by inhibition of HDAC6 might present new cancer treatment strategy. Rocilinostat is currently the only selective inhibitor of HDAC6 considered for tumor treatment. Therefore, a lot of effort is invested in the development of new HDAC6-specific inhibitors. The role of HDAC6 in regulation of immune system response was brought up for the first time during analysis of HDAC6 KO mice. Their phenotype showed that apart from a mild change in bone density the only detectable defect was mild impact of the immune system. Results indicate that HDAC6 regulates IgG-mediated immune response to viral, bacterial, and fungal infections [103]. HDAC6 inhibits the ability of HIV1 virus to infect cells and can seriously hamper HIV1 amplification via deacetylation of Tat (transactivation protein). Deacetylation of Lys28 by HDAC6 decreases interaction between Tat and CDK9/P-TEFb kinase. The process reduces Tat transactivation activity and leads to reduction in HIV1 gene expression [104–106].

HDAC6 is necessary for branching and maintenance of neuronal processes and axon elongation. Therefore, deregulation of HDAC6 plays important role in neurodegeneration [107]. It is involved in neuronal diseases with plaque formation such as Alzheimer's, Huntington, Parkinson's, and prion disease but also plaque unrelated illnesses such as Charcot-Marie-Tooth disease. HDAC6 is involved in these pathologies mainly as tubulin deacetylase and regulator of misfolded protein degradation. In Alzheimer's disease a decrease in tubulin acetylation in brain was reported. The remaining acetylated tubulin resists degradation by an unknown mechanism [108]. Decrease in tubulin acetylation was also observed in patients with Huntington disease. Inhibition by pan-HDAC inhibitors TSA and SAHA, results in restoration of BDNF (Brain-derived neurotrophic factor) vesicle trafficking compromised in Huntington disease. Inhibition by HDAC6 selective inhibitor tubacin further increases the velocity of the renewed vesicle transport [109]. While the role in Parkinson's disease is not completely clear, HDAC6 has been found in aggresome-related Lewi bodies in brain samples of patients with Parkinson's and dementia [74]. In prion disease HDAC6 functions as an apoptosis regulator. Expression of HDAC6 alleviates effects of PrP106-126 (neurotoxic fragment of prion protein) induced cell death by engaging autophagy via Akt/mTor pathway [110]. In Charcot-Marie-Tooth (CMT), a peripheral nervous system disorder, inhibition of HDAC6 results in increase of αAcK40 levels in

peripheral nerves. Consequently the impaired microtubule transport along the dorsal root ganglion nerves is restored [111].

1.3.4.3.   HDAC6 AS TUBULIN DEACETYLASE

1.3.4.3.1.   TUBULIN

Tubulin stands out as the most abundant and the most important HDAC6 substrate although the exact role of tubulin acetylation is not completely understood. The tubulin family comprises of tubulin α, β, γ, δ, ε, ζ, and η. Only α-, β-, and γ- tubulin can be found in all eukaryotes and they are essential for tubulin polymerization [112].

There are 5 α- and 6 β- tubulin isoforms in mammals and they are highly conserved [113,114]. α- and β-tubulins are globular 55 000-Mw proteins that form a heterodimer. The dimer serves as the building block of tubulin polymers. Both tubulins have a single nucleotide binding site. The α-tubulin site binds strongly both GTP and GDP. This site is called GTPn because the nucleotide binding is non-exchangeable and GTP is restored by transphosphorylation. The β-subunit site is termed GTPe (exchangeable). Its lower binding affinity for GTP permits rapid nucleotide exchange. During polymerization, GTP is hydrolyzed [115,116]. Tubulin γ shares 33% amino-acid sequence identity with β-tubulin. It is necessary for timely progress through the cell cycle and it is a part of the microtubule-organizing center (MTOC), where along with other proteins it forms the γ- tubulin ring complex. The complex is involved in microtubule nucleation and functions as the minus-end cap [117–119]. δ-tubulin along with the ε-tubulin are a part of the centrosome and ε-tubulin is paramount for centriole duplication [120]. The roles of ζ- and η-tubulin are yet unknown although both were mapped to the basal body [121–123].

1.3.4.3.2.   TUBULIN POLYMERS

Under specific conditions tubulin can polymerize into macromolecules of different conformations. These include single or two walled rings, sheets, coiled-coils, ribbons, corkscrews, macrotubes, and the most common and the most important polymers - microtubules. α/β-subunits bind head to tail to form protofilaments. They then join side by side to form macrotubes, sheets, and microtubules. The different polymers are maintained

by lateral and longitudinal interactions between the subunits. Longitudinal are the bonds between two adjoining subunits, linking them into a linear protofilament. Lateral interactions unite protofilaments side by side to format a sheet or a microtubule.
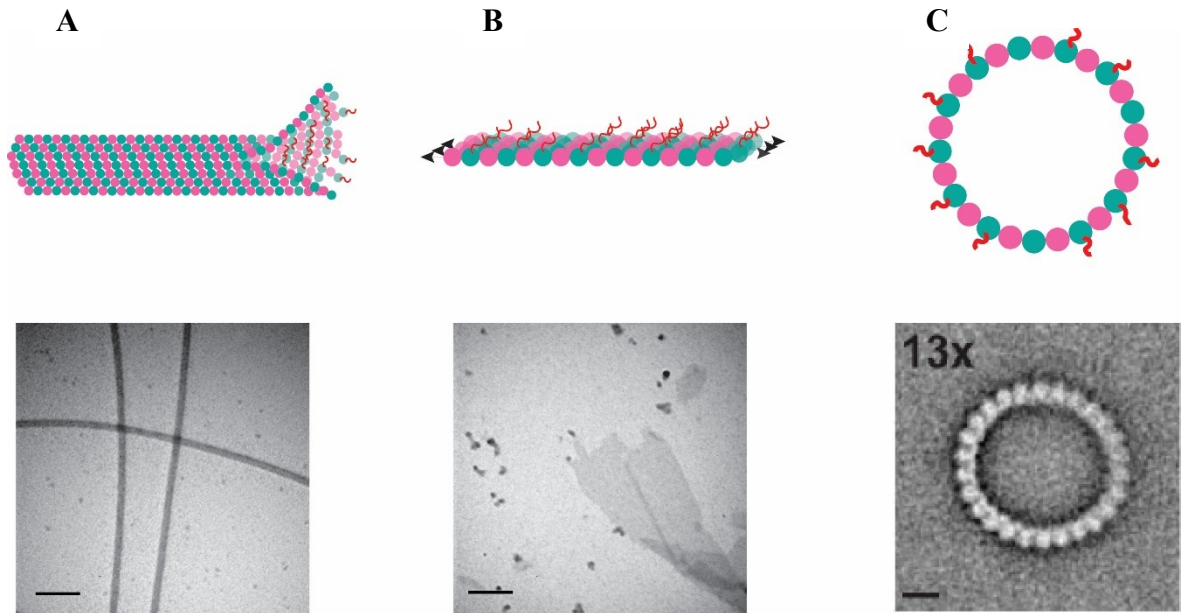
During depolymerization of microtubules, the lateral interactions between the protofilaments weaken and they start to curve outwardly. These curvatures either disassemble or close and form tubulin rings [124]. Addition of certain chemicals or proteins can cause the formation of single walled tubulin rings, mimicking these depolymerization products. In our work we used dolastatin-10 induced rings. Dolastatin-10 is a cytotoxic peptide isolated from *Dolabella auricularia* and inhibits formation of microtubules. Addition of dolastatin-10 to tubulin results in formation of single walled rings consisting of 13-15 tubulin heterodimers. The 14 dimer rings are the predominant species in the population [125,126]. These rings are formed so that the side of protofilament originally facing microtubule lumen becomes the outer side of the ring (Fig. 10C, page 30). Similar rings form in presence of kinesins or the HIV1-REV protein [125,127–129].

Zinc at concentrations higher than 50 μM and at pH 5.5-5.8 induces formation of zinc-sheets. These polymers are unlike microtubules resistant to cold and colchicine [130]. The macromolecules can have up to 2 μm in width. They consist, similarly to microtubules, of protofilaments but in an antiparallel orientation with twofold screw axis symmetry [131] (see Figure 10B, page 30).

Microtubules are the most common and the most important tubulin polymers. They are critical for cell division and intracellular transport, define the cell shape, organize the cytoplasm, play a role in touch sensing and reproduction, and enable cell movement. Inner and outer diameter of these hollow tubes is 15 and 25 nm, respectively (Figure 10A, page 30) [132]. Tubulin dimers polymerize into microtubules in a bidirectional head-to-tail manner. Microtubules are formed of 11-15 protofilaments of the same orientation, arranged side by side. As a result, microtubules are polarized with (+) and (-) ends. The polymers are dynamic structures. At physiological conditions, unless stabilized, microtubules undergo a treadmill addition of dimers at one end with a faster simultaneous dissociation of subunits at the other. The phenomenon is called dynamic instability and it is an intrinsic feature of microtubules. In the cell context, microtubules are associated to MTOC by their (-) termini. The (+) end can be protected from depolymerization by capping proteins and corresponds to the β-tubulin end. Thanks to the interchangeable GTPe site, it is characterized by a higher

polymerization rate. This is because the GTP hydrolysis on the β-subunit helps overcome the energetically unfavorable step of α/β-dimer addition [133].

Microtubules are not randomly distributed within the cell, but are organized in MTOCs

Figure 10: Tubulin polymers
Addition of various substances results in tubulin polymerization. Schemes supplemented with electron micrographs. (A) Addition of GTP induces formation of microtubules. (B) In high concentrations of zinc ions, tubulin polymerizes into zinc-sheets with protofilaments in antiparallel orientation. (C) Dolastatin-10 forces tubulin filaments to curve, resulting in rings formed of 13 - 15 tubulin dimers. Bars in (a) and (b) = 200 nm in (c) = 40 nm. α- and β- tubulin depicted as pink and green circle, respectively, acetylation as red curved line, black arrows indicate orientation of protofilaments. Scheme by LS, electron micrograph of dolastatin-10 ring by Moores & Milligan, 2008 [126].

(microtubule organizing centers) which coordinate microtubule nucleation, stabilization, and anchoring. The centrosome is the primary MTOC of most animal cells and serves to evenly distribute genetic material into daughter cells during cell division. Inside the centrosome microtubule triplets are organized radially around a central hub in two centrioles surrounded by pericentriolar material (PCM). Organizing microtubules along the length of axons in neurons and dendrites is the key element of transport, regeneration, and development. Higher plants and budding yeast lack the centrosome. The role of centrosome is in yeast taken over by the spindle pole body embedded into the nuclear envelope. In cilia and flagella, basal bodies play the role of MTOCs and they serve as the nucleation site for axoneme core structures. These structures are responsible for flagellar or ciliary beating permitting movement of sperms, bacteria, or bronchial cilia beating. Axonemes are formed by 9 doublet microtubules surrounding a central pair of singlet microtubules. This 9+2 arrangement

typical for axonemes is crosslinked together by proteins of inner sheath, nexin, and dynein [134,135].

While working with microtubules one has to keep in mind that dynamic microtubules depolymerize at low temperatures and low concentration. However, particular proteins and chemicals affecting the dynamic instability can be used as tools to study microtubules. Microtubule associated proteins (MAPs) are a group of proteins that bind to and regulate assembly and stability of microtubules. They also mediate microtubule interactions with cell structures. Their effect is either to stabilize (tau, MAP1, 2, 4) or to destabilize (katanin, stathmin, kinesin XKCM1) microtubules [136–141]. Drugs that are used to stabilize or destabilize microtubules or prevent their polymerization are used in treatment of cancer as they have anti-mitotic effect. Microtubules are most commonly stabilized by taxol (paclitaxel) or guanosine-5'-[(α,β)-methyleno]triphosphate (GMPCPP). Taxol is a triterpenoid isolated from yew tree. It stabilizes microtubules for days and makes them resistant to temperature changes [142]. GMPCPP is a non-hydrolysable GTP analog [143]. Drugs such as colchicine, its analog colcemid, or vinblastine are used as destabilizing agents. Colchicine is extracted from meadow saffron. It binds to β-tubulin at the α/β- tubulin interface and it inhibits tubulin polymerization. This compound is an example of an anti-mitotic drug [144].

1.3.4.3.3. POSTTRANSLATIONAL MODIFICATIONS (PTMs) OF TUBULIN

Microtubules play a role in diverse processes, assuring function and morphology of cells, but α- and β-tubulin variants exhibit high sequence homology. Therefore, PTMs are required to bestow different properties to the polymers. This enables them to fulfill their divergent roles. Collectively, tubulin PTMs are referred to as the tubulin code and comprise of palmitoylation, phosphorylation, (de)tyrosination, polyamination, polyglycylation, deglutamylation or polyglutamylation, and acetylation [114,145]. In microtubules the majority of the PTMs lay on the surface and they are freely accessible to the modifying enzymes – the writers and the readers – the MAPs. The sole exception is (de)acetylation as the loop containing αK40 lies inside microtubule lumen and harder to access.

Tyrosination and detyrosination are enzymatic attachment and removal of a tyrosine residue to α-tubulin. Detyrosination is a hallmark of stable long lived microtubules. It protects them

from depolymerizing activity of kinesin motor proteins and is catalyzed by a recently identified detyrosinase complex consisting of vasohibins [146]. Tubulin tyrosine ligase is known to prefer dimers as substrate [147–150]. Polyglutamylation is a progressive addition of glutamate residues onto γ-carboxyl group of Glu445 α- tubulin or Glu435 of β- tubulin. It is a reversible process and deglutamylation can lead to formation of Δ2-tubulin which accumulates in long lived microtubules of differentiated neurons and in axonemes. Polyglutamylation occurs during differentiation of neurons and in axonemes and centrioles. It serves to regulate ciliary beating [151–155]. Polyglycylation is an addition of polyglycine chains and it is believed to be restricted to cilia and flagella of mammals [156,157]. Polyamination decreases solubility of tubulin, it is irreversible and seems to contribute to microtubule stabilization [158]. Phosphorylation, palmitoylation, ubiquitination, methylation, sumoylation, arginylation, and glycosylation have also been reported, but very little is known about these alterations and their role [159–167].

The PTM studied in our manuscript [168] is acetylation of α-tubulin and as mentioned above, it stands out by its localization to the microtubule lumen. This makes it an intriguing research subject because it is unclear how it is accessed by modifying enzymes. Another unknown is how it can be sensed from the outer side by the proteins that it regulates. Acetylation of tubulin was first observed by L'Hernault and Rosenbaum in 1983 in flagella of Chlamydomonas reinhardtii. The acetylation site was later identified as the ε-amino group of lysine 40. Even nowadays it remains the best studied tubulin acetylation thanks to the discovery of an αAcK40-antibody by Piperno and Fuller. This antibody does not cross-react with the non-acetylated α-tubulin or β-tubulin [169–172]. Acetylated tubulin is present in stable and ordered microtubules such as sperm axoneme, primary cilia, kinetochores, spindles, and midbodies of mitotic cells. It does not influence morphology of microtubules. The increase in the K40 acetylation in the stable microtubules is considered to be the result of an accumulation of acetylated tubulin. Data indicates that the accumulation of tubulin acetylation is not directly responsible for microtubule stabilization. This is supported by the fact that although the addition of taxol does not increase acetylation or polymerization rates, it leads to increase in acetylation. Also, further experiments with soluble (dimeric) and insoluble (polymerized) tubulin show that acetylated tubulin exists in cells treated by taxol only in the form of microtubules [103,172–175].

Several enzymes have been found to be able to alter the acetylation state of lysine 40. These are: acetylases GCN5, ARD1-NAT1, ELP complex, MEC17/αTAT1 and deacetylases

HDAC6, SIRT2, HDAC5 [176–184]. However, αTAT1 (α-tubulin N-acetyltransferase) and HDAC6 are considered to be the major tubulin modifying enzymes in mammalian cells [103,179,180,185]. αTAT1, despite being identified 8 years later than HDAC6, is the better characterized of the two enzymes. In *C. elegans,* the αTAT1 homologue MEC-17 is responsible for touch reception and neuron maintenance. The tubulin acetyltransferase acetylates microtubules 4-6 times faster than tubulin dimers. The K_m for the acetylation of microtubules and free tubulin by αTAT1 was determined to be 1.6 ± 0.36 μM and 2.0 ± 0.16 μM respectively. The acetylation rate (defined by k_{cat}) was determined to be $615 \pm 34 \times 10^{-6}$ s^{-1} and $98 \pm 1.8 \times 10^{-6}$ s^{-1} for microtubules and free tubulin respectively. It has been shown that lateral lattice interactions are required for optimal transferase activity. αTAT1 scans microtubules bidirectionally via surface diffusion and enters the microtubule lumen in order to acetylate Lys40. Interestingly, a mutation of the conserved residues within the helix α2 of αTAT1 influences deacetylation of dimers and microtubules differently. This indicates that there exists a microtubule sensing structural element within αTAT1 [179,180,186,187].

HDAC6 is considered to be the major tubulin deacetylase because in HDAC6 KO mice all tubulin is acetylated [103]. Tubulin was identified as HDAC6 substrate in 2002 by two groups independently. Unfortunately, contradicting results in these two seminal works gave birth to a polemic about the preferred substrate. According to work of Matsuyama *et al*., 2002, murine HDAC6 failed to deacetylate microtubules. Contrarily, Hubbert *et al*., show that HDAC6 has no tubulin deacetylase activity on tubulin dimers [181,182]. There have been further attempts at elucidating the situation, but the data quantifying the substrate preference of the purified full length human HDAC6 is missing. Our report aims to fill this gap.

Tubulin acetylation serves as signal for MAPs. Microtubule severing, catalyzed by proteins like katanin and spastin, results in increase of microtubule number and generates new ends. This is important for processes such as cell motility, axonal branching, and growth and maintenance of neuronal processes [188,189]. It has been shown that tubulin acetylation regulates sensitivity of microtubules to katanin and breaks catalyzed by katanin coincide with acetylated regions of microtubules [190]. Deacetylation of αAcK40 results in decrease in kinesin-1 binding to microtubules, implying the role of tubulin acetylation in trafficking

within the cell [150]. *In vivo* acetylation enhances recruitment of dynein and kinesin-1 and promotes transport of their cargo vesicles [109,191,192].

HDAC6 localizes to the leading edge region and is implicated in cell motility regulation through its tubulin deacetylase activity. Its overexpression increases chemotaxis by 3.5-fold and tubulin hyperacetylation resulting from loss of HDAC6 activity leads to inhibition of cell motility by altering dynamics of focal adhesion. The adhesions area increases and adhesion turnover slows down. For a long time it was believed that acetylation does not affect the stability of microtubules directly, but that the acetylation might serve as a signal for microtubule associated proteins [182,193]. In 2017 two independent studies have shown that acetylation is involved in mechanical stabilization of microtubules and protects the microtubules from mechanical ageing [194,195].

Acetylation of αK40 also serves as a regulatory step for protofilament numbers in *C. elegans* touch sensor neurons. Mutation of acetyltransferase MEC-17 results in complete deacetylation of αK40, decrease in microtubule number and length, and increase in protofilament number variability in said neurons. Instead of 15 protofilaments, microtubules with 10-16 protofilaments can be seen upon MEC-17 depletion. αAcK40 might stabilize MT by promoting formation of salt bridges between adjacent protofilaments. In mec-17 KO nematodes microtubules exhibit lattice defects not detectable in MT from WT specimen [196].

Tubulin dimer might harbor more acetylation sites. A whole proteome study of lysine acetylations identified several new acetylation sites within the α-tubulins: TUBA1C (Lys60, Lys112, Lys326), TUBA4A (Lys163, Lys164, Lys311, Lys394, Lys370, and Lys401) as well as Lys58 in β-tubulins TUBB3, TUBB2C, and TUBB5 [197]. Only the acetylations Lys394 of α-tubulin and Lys58 of β-tubulin from this study were confirmed by further research. Additional acetylations of Lys154, Lys174, and Lys252 of β-tubulin were identified. San acetyl transferase is responsible for acetylation of β-tubulin at K252. The K252 acetylation appears only on dimers and inhibits microtubule polymerization probably due to destabilization of tubulin dimers [198,199]. Study of acetylation/deacetylation of these sites is hampered by the lack of a specific antibody.

1.3.5. HDAC6 INHIBITORS

Generally, HDAC inhibitors mimic acetyllysine and contain a peptoid-derived cap group. This group is connected by a linker to a zinc binding group, usually a hydroxamic acid moiety. The cap group, however, is not necessary for effective inhibition. HDAC6 is inhibited by the pan-HDAC inhibitors such as SAHA, trichostatin A, and valproic acid, but is resistant to trapoxin B and Na-butyrate (Figure 7, page 17) [200–202].

Until recently the design of HDAC6 specific inhibitors was hampered by a lack of structural information. Tubacin is a hydroxamate-based HDAC6 inhibitor with 4-fold selectivity over HDAC1 and HDAC4. It binds to DD2 only and affects HDAC6 ability to deacetylate α-tubulin *in vivo* at low micromolar concentration and causes decrease in cell motility without affecting microtubule stability. It has no effect on histone deacetylation [203,204]. Tubastatin A is a carbazole derivative of hydroxamic acid with IC50 = 15 nM. It has high selectivity for HDAC6 with 57-fold preference over HDAC8 and more than 1000-fold selectivity over the rest of HDACs and induces tubulin hyperacetylation [205].

The Food and Drug Administration (FDA) so far approved four HDAC inhibitors for cancer treatment: vorinostat (SAHA), romidepsin, belinostat (PXD101) and panobinostat. All of the inhibitors that passed clinical testing are nonselective and inhibit multiple HDAC isoforms. Rocilinostat (ACY-1215), also a hydroxamic acid derivative, is the only inhibitor selective for HDAC6 tested in phase II clinical trials. It is considered for the treatment of multiple myeloma and lymphoid malignancies. With IC_{50} = 5nM it is at least 10-fold less active against HDAC1-3 and 20-fold and 200-fold more selective over HDAC8 and the remaining HDACs respectively [206].

2. RESEARCH AIMS

•   Structure-assisted design of new lipophilic compounds binding to GCPII

•   Purification of full length HDAC6, characterization of HDAC6 as tubulin deacetylase, and quantification of its substrate preference

3. PUBLICATIONS

Publications included in the dissertation thesis

1. Plechanovova, A., Byun, Y., Alquicer, G., Skultetyova, L., Mlcochova, P., Nemcova, A., Kim, H. J., Navratil, M., Mease, R., Lubkowski, J., Pomper, M., Konvalinka, J., Rulisek, L., Barinka, C. 2011. Novel substrate-based inhibitors of human glutamate carboxypeptidase II with enhanced lipophilicity. J Med Chem 54:7535-7546.

2. Pavlicek, J., Ptacek, J., Cerny, J., Byun, Y., Skultetyova, L., Pomper, M. G., Lubkowski, J., Barinka. C. 2014. Structural characterization of P1'-diversified urea-based inhibitors of glutamate carboxypeptidase II. Bioorg Med Chem Lett 24:2340-2345.

3. Dannoon, S., Ganguly, T., Cahaya, H., Geruntho, J. J., Galliher, M. S., Beyer, S. K., Choy, C.J., Hopkins, M.R., Regan, M., Blecha, J. E., Skultetyova, L., Drake, C.R., Jivan, S., Barinka, C., Jones, E. F., Berkman, C. E., VanBrocklin, H. F. 2016. Structure-Activity Relationship of (18)F-Labeled Phosphoramidate Peptidomimetic Prostate-Specific Membrane Antigen (PSMA)-Targeted Inhibitor Analogues for PET Imaging of Prostate Cancer. J Med Chem 59:5684-5694.

4. Skultetyova, L., Ustinova, K., Kutil, Z., Novakova, Z., Pavlicek, J., Mikesova, J., Trapl, D., Baranova, P., Havlinova, B., Hubalek, M., Lansky, Z., Barinka, C. 2017. Human histone deacetylase 6 shows strong preference for tubulin dimers over assembled microtubules. Sci Rep 7:11547

Publication I: Novel substrate-based inhibitors of human glutamate carboxypeptidase II with enhanced lipophilicity.

BACKGROUND:

Glutamate carboxypeptidase II (GCPII) is exploited as an experimental target for treatment of several neuropathologies, including schizophrenia, traumatic brain injury, and peripheral neuropathy. However, currently used GCPII-specific inhibitors are highly polar and unable to effectively cross the blood-brain barrier, limiting thus their efficacy for the treatment of the nervous system related disorders. Our prior biochemical studies revealed that the charged glutamate at the P1' position of a GCPII substrate can be substituted by a less polar methionine residue and still being recognized and processed by the enzyme. We thus hypothesized that such substrates can be further modified by incorporating non-natural hydrophobic amino acids and these can be in turn used as a template for the design of GCPII-specific inhibitors with enhanced lipophilicity.

METHODS:

Human GCPII was heterologously expressed using Schneider's S2 cells and purified by the combination of affinity and size-exclusion chromatography. Kinetic constants on novel substrates were determined using the high-pressure liquid chromatography upon pre-column fluorescence derivatization and released products. The inactive mutant of GCPII was co-crystallized with the NAAM substrate and the X-ray structure of the complex solved by molecular replacement. A panel of substrate-based inhibitors was synthesized by the collaborating laboratory and their inhibition constants determined using 3H-NAAG as a substrate. Quantum mechanics/molecular mechanics calculations were used to quantify interaction energies between the enzyme and inhibitors.

RESULTS:

We designed and synthesized a panel of eight GCPII substrates bearing an unbranched, aliphatic side chain at the C-terminal moiety of 0 – 7 methyl groups. The kinetic analysis revealed the positive correlation between the length of the C-terminal side chain and catalytic

efficacy of hydrolysis by GCPII, with the kcat and KM values 0.62 s^{-1} and 10 μM, respectively, for the "best" dipeptidic substrate featuring aminononanoic acid at the C-terminus. The X-ray structure of the GCPII(E424A) inactive mutant in the complex with selected dipeptides revealed the importance of nonpolar interactions governing GCPII affinity toward novel substrates as well as formerly unnoticed plasticity of the S1' specificity pocket. The structural data were complemented with quantum mechanics/molecular mechanics calculations. On the basis of those results, we designed, synthesized, and evaluated a series of novel GCPII inhibitors with enhanced lipophilicity, with the best candidates having low nanomolar inhibition constants and ClogD > 0.3.

CONCLUSION:

Our findings offer new insights into the design of more lipophilic inhibitors targeting GCPII.

MY CONTRIBUTION:

I determined, refined and analyzed the structure of the GCPII(E242A) inactive mutant in complex with the N-acetylaspartylmethionine (NAAM) substrate and submitted it to the RCSB database under PDB code 3SJX.

Novel Substrate-Based Inhibitors of Human Glutamate Carboxypeptidase II with Enhanced Lipophilicity[†]

Anna Plechanovová,[‡,§,●] Youngjoo Byun,[∥,⊥,●] Glenda Alquicer,[#] L'ubica Škultétyová,[#] Petra Mlčochová,[‡,§] Adriana Němcová,[‡] Hyung-Joon Kim,[∥] Michal Navrátil,[‡,§] Ronnie Mease,[∥] Jacek Lubkowski,[∞] Martin Pomper,[∥] Jan Konvalinka,[‡,§] Lubomír Rulíšek,[‡] and Cyril Bařinka[*,#]

[†]Institute of Organic Chemistry and Biochemistry, Gilead Sciences Research Center at IOCB, Academy of Sciences of the Czech Republic, Flemingovo náměstí 2, 166 10 Praha 6, Czech Republic

[§]Department of Biochemistry, Faculty of Natural Science, Charles University in Prague, Hlavova 2030, Prague, Czech Republic

[∥]Russell H. Morgan Department of Radiology and Radiological Sciences, Johns Hopkins Medical Institutions, 1550 Orleans Street, Baltimore, Maryland 21231, United States

[⊥]College of Pharmacy, Korea University, Sejong-ro, Jochiwon-eup, Yeongi-gun, Chungnam 339-700, South Korea

[#]Institute of Biotechnology, Academy of Sciences of the Czech Republic, Videnska 1083, 14200 Praha 4, Czech Republic

[∞]Center for Cancer Research, National Cancer Institute at Frederick, Frederick, Maryland 21702, United States

Ⓢ Supporting Information

ABSTRACT: Virtually all low molecular weight inhibitors of human glutamate carboxypeptidase II (GCPII) are highly polar compounds that have limited use in settings where more lipophilic molecules are desired. Here we report the identification and characterization of GCPII inhibitors with enhanced lipophilicity that are derived from a series of newly identified dipeptidic GCPII substrates featuring nonpolar aliphatic side chains at the C-terminus. To analyze the interactions governing the substrate recognition by GCPII, we determined crystal structures of the inactive GCPII(E424A) mutant in complex with selected dipeptides and complemented the structural data with quantum mechanics/molecular mechanics calculations. Results reveal the importance of nonpolar interactions governing GCPII affinity toward novel substrates as well as formerly unnoticed plasticity of the S1′ specificity pocket. On the basis of those data, we designed, synthesized, and evaluated a series of novel GCPII inhibitors with enhanced lipophilicity, with the best candidates having low nanomolar inhibition constants and clogD > −0.3. Our findings offer new insights into the design of more lipophilic inhibitors targeting GCPII.
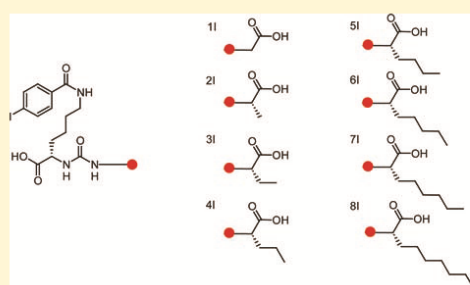
■ INTRODUCTION

Human glutamate carboxypeptidase II (GCPII) is a transmembrane metallopeptidase with the expression pattern restricted primarily to nervous and prostatic tissues.[1−3] As the expression levels of the prostate form of the enzyme are highly elevated in prostate carcinoma and its metastases, GCPII serves as a membrane-bound marker for prostate cancer imaging and experimental therapy.[4−8]

Within the nervous system, GCPII catabolizes N-Ac-Asp-Glu (NAAG), the dipeptidic neuropeptide, liberating glutamate into the extrasynaptic space.[1] Both NAAG and glutamate act as potent neurotransmitters, and their extracellular concentrations must be tightly regulated to secure normal brain functioning. Not surprisingly, dysregulated NAAG (and glutamate) metabolism and signaling are associated with a number of neurological disorders.[9] Given the intimate involvement of GCPII in NAAG (glutamate) metabolism, the modulation of its enzymatic activity

by small-molecule ligands is considered a viable option for the treatment and diagnosis of a variety of pathologies that involve glutamatergic transmission. Indeed, GCPII inhibitors have demonstrated efficacy in experimental models of stroke,[10] diabetic neuropathy,[11] amyotrophic lateral sclerosis,[12] neuropathic and inflammatory pain,[13−15] schizophrenia,[16] and drug addiction.[17,18] Additionally, radiolabeled GCPII-specific ligands were used to quantitatively visualize GCPII in rodent and human tissue ex vivo,[19,20] thus expanding their use into the diagnostic area.

Effective targeting of GCPII residing in nervous tissue requires inhibitors that can penetrate the neuronal compartment. That can be achieved by designing inhibitors that can leverage active transport mechanisms or by using liphophilic compounds with enhanced penetration across the blood−brain barrier. As the

Table 1. Formulas and Kinetic Parameters of Novel GCPII Dipeptidic Substrates[a]

compd	K_M (μM)	k_{cat} (s^{-1})	k_{cat}/K_M (L·mmol^{-1}·s^{-1})
1S	NA[b]	NA[b]	NA[b]
2S	85 ± 21	0.23 ± 0.05	2.7
3S	29 ± 8	0.25 ± 0.03	8.6
4S	31 ± 12	0.42 ± 0.05	13.5
5S	19 ± 4	0.24 ± 0.01	12.6
6S	12 ± 1	0.44 ± 0.04	36.7
7S	8 ± 2	0.60 ± 0.03	75.0
8S	10 ± 2	0.62 ± 0.10	62.0
NAAM	24.8 ± 2.9[c]	0.07 ± 0.002	2.9
NAAG	1.2 ± 0.5[d]	1.1 ± 0.2[d]	930[d]

[a] Ac-Asp-Glu (NAAG), natural GCPII substrate in mammalian nervous system; Ac-Asp-Met (NAAM), non-natural GCPII substrate from the dipeptidic library screen; 1S...8S, novel GCPII dipeptidic substrates featuring nonpolar aliphatic side chain at the P1' position. The kinetic parameters were determined by saturation kinetics employing precolumn derivatization of the reaction products (i.e., released C-terminal amino acids) with AccQ-Fluor, followed by HPLC separation on a C18(2) Luna column and fluorimetric detection. [b] Not analyzed, substrate hydrolysis below the detection limit. [c] From ref 21. [d] From ref 29.

early efforts in identifying low molecular weight GCPII inhibitors relied mainly on the knowledge of GCPII substrate specificity, the two major categories of GCPII-specific inhibitors that exist at present are either analogues of NAAG (the GCPII substrate) or derivatives of glutamic acid (the reaction product). Consequently, nearly all currently used GCPII inhibitors are highly polar with their total molecular charges under physiological pH conditions ranging typically between −2 and −3 and with lower likelihood of CNS penetration. The design of GCPII-specific inhibitors with increased liphophilicity/hydrophobicity is therefore highly desirable, with the ultimate goal of improving bioavailability and tissue penetration while maintaining potency and specificity for the use in clinical practice.

In our previous work, we reported the analysis of the substrate specificity of human GCPII, and in addition to the known GCPII substrates featuring C-terminal glutamate, we identified P1' methionine as a residue effectively recognized by the enzyme.[21] Taking into the account the substitution of the glutamate negatively charged side chain by the more hydrophobic side chain of methionine, we hypothesized that in addition to salt bridges and/or hydrogen bonds, nonpolar interactions at the S1' site of GCPII are likely to play an important role in the positioning of the C-terminal amino acid residue of GCPII substrates. These arguments are also consistent with our other findings concerning the importance of specific amino acid residues in the GCPII S1 and S1' sites,[22] the detailed study of GCPII reaction mechanism,[23] and previously reported series of GCPII-specific inhibitors.[7,24−28]

The aim of this work is to explore new directions in the rational design of GCPII inhibitors by increasing their lipophilicity and to explain in detail the observed nonpolar interaction patterns. To achieve this goal, we use a combination of experimental and theoretical approaches including X-ray crystallography, site-directed mutagenesis, and hybrid quantum mechanical and molecular mechanical (QM/MM) calculations. Starting from the detailed characterization of GCPII−methionine interactions within the S1' pocket, we designed and characterized novel GCPII substrates featuring aliphatic side chains at the C-terminal amino acid. Finally, on the basis of our kinetic data, we synthesized and evaluated a series of novel substrate-based GCPII inhibitors with enhanced lipophilicity.

■ RESULTS

Novel GCPII Substrates: Ac-Asp-Ala...Ac-Asp-Ano Series. Since dipeptides with the C-terminal methionine, but not with branched hydrophobic amino acids such as valine or leucine, are efficiently hydrolyzed by human GCPII,[21,29] we hypothesized that the enzyme might be able to process dipeptides bearing an unbranched, aliphatic side chain at the C-terminal moiety. To test this prediction, we analyzed the hydrolysis of a series of eight dipeptides by recombinant human GCPII (rhGCPII, Table 1). The series was chosen to examine systematically the effect of P1' aliphatic side chain length on the hydrolysis by rhGCPII. The substrate cleavage was followed by high-performance liquid

41
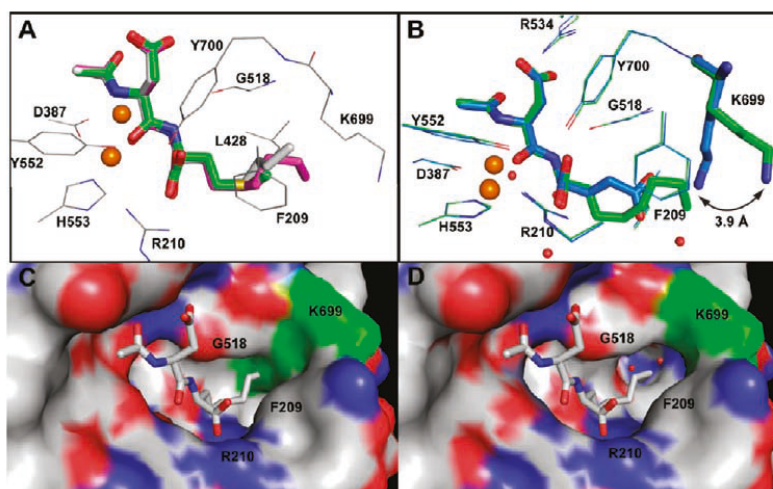
Figure 1. (A) Superposition of NAAM, 7S, and 8S substrates in the substrate binding pocket of GCPII(E424A). The substrates are shown in stick representation with carbon atoms colored green (NAAM), gray (7S), and magenta (8S). Selected GCPII residues surrounding the binding pocket are shown in line representation. The zinc ions are shown as orange spheres. (B) Superposition of NAAG (PDB code 3BXM) 8S substrate binding sites of GCPII. Substrates and the amino acids Lys699 are shown in stick representation, zinc ions and waters as orange and red spheres, respectively. Selected GCPII residues surrounding the binding pocket are shown in line representation. Atoms are colored as follows: cyan (NAAG carbon), green (8S carbon), blue (nitrogen), and red (oxygen). Note the displacement of the Lys699 side chain by 3.9 Å in the 8S complex (green) due to steric clash with the 8S side chain. (C, D) S1′ pocket plasticity defined by the "Lys699 swing". (C) Composite figure showing GCPII substrate binding site (surface representation) derived from the NAAG (PDB code 3BXM) complex and 8S (stick representation). Note the steric clash between the side chain of Lys699 (green) and the side chain of the C-terminal residue in 8S. (D) GCPII substrate binding site (surface representation) from the complex with 8S (stick representation). The swing-out of the Lys699 side chain (green) enlarges the S1′ pocket to accommodate longer (or more bulky) side chains of P1′ part of substrates/inhibitors. The figure was generated using The PyMOL Molecular Graphics System, version 0.99, Schrödinger, LLC.

chromatography (HPLC), and the results are summarized in Table 1. Except for **1S** (Ac-Asp-Gly), a substrate lacking a side chain at the C-terminal amino acid, all other dipeptidic substrates tested were hydrolyzed by rhGCPII. The least efficient substrate in this series was **2S** (Ac-Asp-Ala), i.e., the substrate with the shortest amino acid side chain, and gradual extension of the hydrocarbon side chain of the C-terminal amino acid resulted in the monotonic improvement of the overall catalytic efficiency. This trend is documented by the fact that compared to Ac-Asp-Ala, the rhGCPII hydrolysis of **8S** (Ac-Asp-Ano), the dipeptide with the longest (heptyl) C-terminal side chain, is approximately 20-fold more efficient (Table 1).

rhGCPII(E424A)/Substrate Complexes. To elucidate structural features that govern interactions between GCPII and nonpolar side chains of P1′ residues, we determined X-ray structures of the inactive rhGCPII(E424A) mutant[23] in complex with three of the biochemically characterized substrates Ac-Asp-Met (NAAM), **7S** (Ac-Asp-Aoc), and **8S** (Ac-Asp-Ano) at a resolution of 1.66, 1.65, and 1.70 Å, respectively. (Note: Glu424 acts as a proton shuttle during substrate hydrolysis by GCPII, and as such, it is indispensable for the enzymatic activity of the enzyme. By mutating Glu424 to alanine, we constructed the inactive GCPII(E424A) mutant that cannot hydrolyze cognate substrates and thus serves as an excellent tool for elucidating/approximating enzyme—substrate interactions.) All three structures were determined using difference Fourier methods, and the refinement statistics of the final models are summarized in the Supporting Information Table S1. The overall fold of the

rhGCPII(E424A) protein in individual complexes is nearly identical to the arrangement observed for the rhGCPII(E424A) complex with NAAG, a natural GCPII substrate reported earlier (PDB code 3BXM).[23] The only major structural deviations in the substrate binding cavity are observed for the Lys699 side chain that comes into contact with the side chains of C-terminal amino acids of novel substrates. The superposition of the active-site-bound substrates in the S1′ pocket and their comparison to the rhGCPII(E424A)/NAAG complex are depicted in Figure 1.

Substrate Orientation in the GCPII Binding Pocket. Positioning of all three dipeptides within the GCPII binding pocket can be unambiguously assigned from the electron density map and conforms to a canonical model, where the S1 pocket of GCPII is occupied by the acetyl-aspartyl moiety and the C-terminal part of a substrate extends into the S1′ site. Even though an equimolar mixture of (1′-R,S)-diastereomers was used in the cases of **7S** and **8S** dipeptides, only the 1′-S-stereoisomers are observed in the GCPII complexes (Figure 1). That observation is consistent with known preferences of GCPII toward L-amino acids in the P1′ position of substrates and (S)-stereoisomers of inhibitors.[1,30]
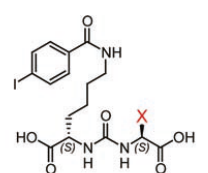
S1′ Pocket Interactions. The enzyme—substrate interactions within the S1′ site include both polar and nonpolar contacts. The arrangement of polar interactions is analogous to the polar contacts reported earlier for the rhGCPII(E424A) complex with NAAG[23] and includes direct hydrogen bonding/ionic interactions between the C-terminal α-carboxylate and side chains of Arg210, Tyr700, and Tyr552 as well as several water mediated

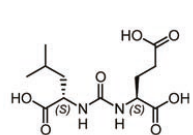**Table 2. Effects of the K699S Mutation on NAAG, NAAM, and 8S Hydrolysis**[a]

substrate	K_M (μM)		k_{cat} (s^{-1})		k_{cat}/K_M ($L \cdot mmol^{-1} \cdot s^{-1}$)	
	WT	K699S	WT	K699S	WT	K699S
NAAG	1.2 ± 0.5[b]	40.5 ± 22.7	1.1 ± 0.2[b]	0.34 ± 0.08	930[b]	8.4
NAAM	7.5 ± 1.6	2.6 ± 1.1	0.32 ± 0.07	0.25 ± 0.04	42.7	96.2
8S	10.4 ± 2.5	2.9 ± 0.7	0.62 ± 0.10	0.37 ± 0.05	59.6	127.6

[a] The kinetic parameters of wild-type (WT) and mutated (K699S) GCPII toward individual substrates were determined by saturation kinetics. The reaction products were derivatized with AccQ-Fluor and separated by HPLC on a C18(2) Luna column with fluorimetric detection. [b] The kinetic parameters of the NAAG hydrolysis by rhGCPII were taken from ref 29 and are included here for the purpose of comparison. These values were determined by the radioenzymatic assay using ^{3}H-NAAG as a substrate.

Table 3. Inhibition of GCPII by Novel Substrate-Based Inhibitors[a]

General inhibitor template

ZJ-43

inhibitor	X moiety	K_i (nM)	CI (95% confidence)	MW	ClogD
ZJ-43		1.08 (0.75[b])	0.85–1.36	304.13	6.13
1I	H	4390 (1320[b])	3344–5762	477.04	3.76
2I	CH_3	325	231–458	491.06	3.41
3I	CH_2CH_3	121	86–165	505.07	2.88
4I	$(CH_2)_2CH_3$	145 (52.3[b])	96–219	519.09	2.35
5I	$(CH_2)_3CH_3$	56	34–92	533.10	1.82
6I	$(CH_2)_4CH_3$	20	10–40	547.12	1.29
7I	$(CH_2)_5CH_3$	72	43–123	561.13	0.76
8I	$(CH_2)_6CH_3$	29	21–38	575.15	0.23
9I	Met	23	12–44	551.40	2.37
10I (DCIBzL)	Glu	0.01[b]	0.007–0.013	549.06	5.16

[a] Inhibitory properties of the novel compounds were determined using the Amplex Red assay, and the results are summarized in the table. [b] Values from ref 32.

contacts. On the other hand, two hydrogen-bonding interactions between the glutamate γ-carboxylate and the Asn257 and Lys699 side chains are lost in the case of dipeptides with P1′ nonpolar side chains. Instead, the positioning of the C-terminal aliphatic side chain relies mainly on nonpolar contacts with the side chains of Phe209, Asn257, Leu428, Lys699 and main chains of Gly427 and Gly517.

Flexibility of the Lys699 Side Chain Shapes the S1′ Pocket. Extended C-terminal side chains of several novel substrates (most prominently 7S and 8S) are too long (~8.5 Å from C_α to the terminal aminononanoic acid side chain carbon atom in the extended conformation) to fit conveniently into the standard-size S1′ pocket observed repeatedly for glutamate-like moieties. Instead, the S1′ pocket has to be reshaped to accommodate such residues. Our structural data show that the change in size and shape is realized by the out-swing of the Lys699 side chain with the positional shift of the N^ζ by 3.9 Å. Simultaneously, the C-terminal side chains adopt a bow-shaped conformation to fill in the S1′ pocket (Figure 1). Clearly, the flexibility of the Lys699 side chain is crucial for alleviating steric crowding imposed by the

presence of a bulkier substrate/inhibitor moiety, thus contributing prominently to the plasticity of the S1′ pocket.

To verify the "steric crowding" hypothesis, we constructed a GCPII(K699S) mutant, where Lys699 is mutated to serine. Compared to wild-type GCPII, the K699S mutation results in approximately 3-fold stronger binding of 8S as determined by the kinetic assay (Table 2). These data suggest that the short side chain of Ser699 is more accommodating toward the bulkier C-terminal side chains of a substrate than the long Lys699 side chain. On the other hand, a much lower affinity of NAAG toward the K699S mutant (~30-fold increase in the Michaelis constant compared to the wild-type enzyme) confirms the importance of the Lys699-Glu γ-carboxylate salt bridge for binding of compounds featuring C-terminal glutamate.

Substrate-Based Inhibitors. On the basis of our kinetic and structural data, we designed and evaluated a series of novel inhibitors, where the N-Ac-Asp moiety and the peptide bond of a substrate are replaced by the (4-iodobenzoylamino)hexanoyl functionality and the nonhydrolyzable urea surrogate, respectively. The rationale for the N-Ac-Asp to (4-iodobenzoylamino)hexanoyl
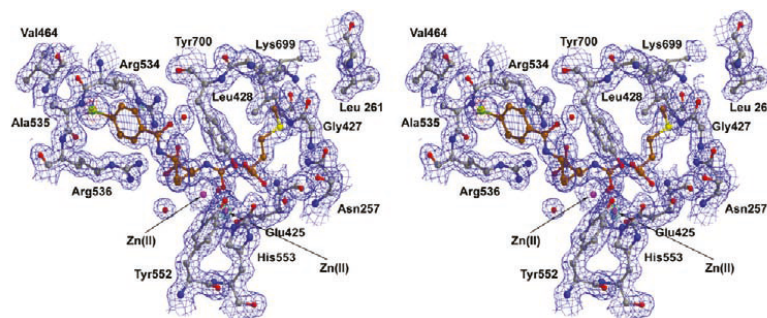
43

Figure 2. Stereoview of the electron density map of the GCPII/9I complex. The $2F_o - F_c$ map is contoured at 1σ (blue), and the $F_o - F_c$ electron density maps are contoured at -3σ (red) and $+3\sigma$ (green). Carbon atoms of the inhibitor and GCPII are colored brown and gray, respectively. The following coloring scheme was used for individual atoms: oxygen (red), nitrogen (blue), iodine (green), sulfur (yellow), zinc (pink).
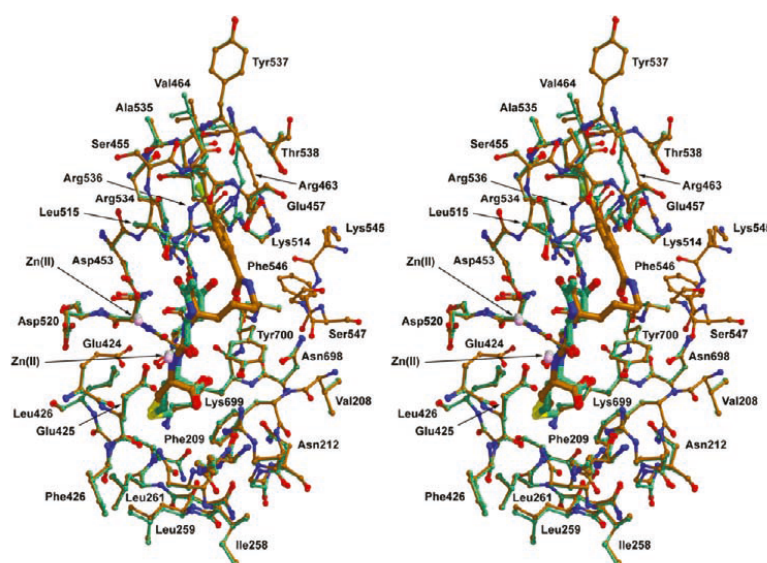

Figure 3. Stereoview of superimposed active site regions of GCPII/9I and GCPII(E424A)/NAAM complexes (inhibitor and its parent substrate). A fragment of the GCPII/9I (wild-type GCPII and 9I inhibitor) complex is shown in light-brown, and an equivalent fragment of the GCPII(E424A)/ NAAM (the inactive mutant and NAAM substrate) complex is shown in green. The following coloring scheme was used for individual atoms: oxygen (red), nitrogen (blue), iodine (green), sulfur (yellow). Two active site zinc atoms are shown as pink spheres, and the substrate/inhibitor is shown in a thick ball-and-stick representation.

substitution was driven by our prior observation that the incorporation of this functionality into the glutamate−urea scaffold increases the affinity of resulting compounds by several orders of magnitude.[24] Inhibitory properties of the novel compounds were determined using the Amplex Red assay, and the results are summarized in Table 3. The K_i values in the series follow the general trend observed for the parent substrates, with the inhibitor potency increasing with the elongation of the P1′ side chain. In this series, compound **1I** has the lowest affinity toward GCPII (K_i = 4390 nM), while the inhibition constants monotonically decrease from **1I** through **6I** and plateau for compounds **6I−8I**, reaching low nanomolar affinity (∼20 nM).

The "plateau effect" observed for the inhibitor series mirrors results from the kinetic measurements, pointing toward identical/similar positioning of P1′ moieties of substrates/inhibitors. As a result, structural/biochemical observations for one type of ligand, substrate or inhibitor, can likely be extrapolated to the corresponding counterpart and exploited for the design of substrate-based inhibitors in general.

GCPII/9I Complex: X-ray Structure. To confirm the assumption that binding modes to an inhibitor and its parent substrate by GCPII are similar, we determined an X-ray structure of GCPII in complex with **9I**, a urea-based inhibitor derived from NAAM, at 1.65 Å resolution. The binding mode of **9I** in the GCPII

44
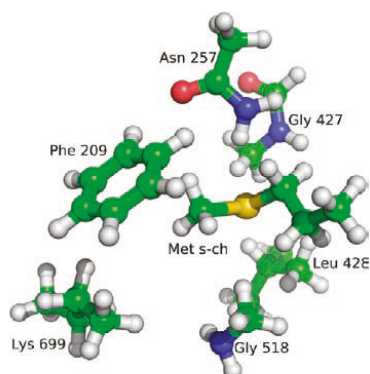
Figure 4. Model system used for the calculations of interaction energies, the S1′ residues (side chains of Phe209, Asn257, Leu428, backbone of Gly427 and Gly518, and nonpolar part of the Lys699 side chain) interacting with the nonpolar side chains of the substrates/inhibitors. The model system truncated from the GCPII(E424A)/NAAM complex (Met side chain and model functional groups representing the key interacting residues from the enzyme) is used in the figure.

specificity pockets is unambiguously defined by the $F_o - F_c$ omit map (Figure 2) and mirrors the orientation and positioning of **10I** (DCIBzL, a urea-based compound featuring C-terminal glutamate). More importantly, though, the C-terminal methionine in the GCPII/**9I** complex (together with surrounding GCPII side chains) spatially overlaps with the corresponding part of NAAM, its parent substrate (Figure 3). Taken together, these data suggest transferability of kinetic/enzymatic data into the inhibitory profiles of daughter compounds.

GCPII/Ligand Complexes: QM/MM Modeling. On the basis of the above-described crystallographic data, we carried out the QM/MM calculations to extend the experimental structural information over additional aspects of the ligand–GCPII binding such as the protonation equilibria between protein and ligand or energies associated with the enzyme···ligand interaction. In total, seven structures were modeled and examined, including complexes of NAAM, **7S**, and **8S** with both wild-type GCPII and the GCPII(E424A) mutant, as well as the complex of **8I** and **10I** with wild-type GCPII. Moreover, we have considered the protonation of the Glu424 residue (that acts as a proton shuttle in the GCPII catalytic cycle), which resulted in a total of 13 systems that were studied. A fairly large quantum region (~350 atoms) and a neighboring part of the protein optimized at the MM level (additional 110 amino acid residues) should allow for a sufficient degree of flexibility in the binding site.

The resulting optimized structures can be found in the Supporting Information (including partial charges on all atoms). The excellent structural agreement between the equilibrium QM/MM structures and their crystallographic counterparts allowed more detailed energy analysis of the interactions between substrates/inhibitors and GCPII (vide infra). Moreover, the QM/MM calculations yielded the equilibrium structures of the wild-type GCPII with NAAM, **7S**, **8S** and the model structure of the GCPII complex with **8I** (i.e., structures that have not been determined experimentally), which add to the already extensive structural information obtained in this study. The alignments of the calculated and experimental structures are depicted in

Table 4. Calculated Interaction Energies of the Model Ligands Representing S1′ Residues with the P1′ Side Chains of the Selected Substrates/Inhibitors Using B-LYP(+D)/TZVPP Method and QM/MM Optimized Geometries of GCPII/Ligand Complexes[a]

	Met	AOC	ANO
Phe209	1.4	2.4	2.2
Asn257	4.8	1.7	2.4
Gly427(bb)	1.3	1.9	2.1
Leu428	1.3	2	2.1
Gly518(bb)	2.1	2	1.4
Lys699(n-p)	0.3	1.4	1.6
ΣE_{ij}	11.2	11.4	11.5

[a] All values are in kcal·mol^{-1}.

Figure S1a–c (Supporting Information), whereas the newly predicted structures are depicted in Figure S2.

The most notable structural features of the QM/MM optimized structures not attainable from the X-ray crystallography can be summarized as follows:

(1) In wild-type complexes, a hydroxide anion, not a water molecule, bridges the two zinc ions in the active site, since the water molecule spontaneously deprotonates upon binding to the $(Zn)_2$ site. Most likely, the proton resides on the Glu424 moiety and is ready for the second step of the peptide bond cleavage as shown in the previous study.[23]

(2) In the complexes with the nonpolar side chains at the C-terminus, the charge of the Lys699 residue which is otherwise the key residue for the interaction with (and the recognition of) the C-terminal (P1′) glutamate in GCPII natural substrates is attenuated by a chain of three water molecules that are strongly polarized by the interaction with the charged NH_3^+ group with the O–H bonds elongated by 0.1–0.2 Å in comparison with their standard values.

(3) In QM/MM optimized structures, we have not observed any pronounced structural changes related to the protonation of the Glu424 residue, as the extra "catalytic" proton[23] is not directly involved in any hydrogen bond. Neither have we noticed any significant effect of the E424A mutation on the overall constitution of the GCPII active site and positioning of the substrate. The superpositions of the wild-type GCPII, GCPII(E424A), and protonated wild-type GCPII structures are given in the Supporting Information (Figures S3–S5).

Interaction Energies of Nonpolar Side Chains with the S1′ Site Residues. We utilized the results of the QM/MM calculations to provide semiquantitative arguments to the discussions concerning the origin of the nonpolar interactions between ligands and the S1′ site of GCPII. We have calculated interaction energies of the model ligands representing the side chains of Met, 2-aminooctanoic (AOC), and 2-aminononanoic (ANO) acids with the small models of interacting residues. The system is depicted in Figure 4, and the results are summarized in Table 4. It is emphasized that the results are only semiquantitative because of the simplicity of the model functional groups representing the residues, but a few observations can be made.

Concerning the overall value of the interaction energy, one may observe that for AOC and ANO side chains it is marginally higher (0.2–0.4 kcal·mol^{-1}) than for the Met side chain. It qualitatively correlates with the observed decrease in K_M values (NAAM vs **7S** and **8S**). However, these differences are very

45

small, and admittedly, the same correlation does not extend to the 7S vs 8S comparison.

In the case of methionine, more than 40% of the overall interaction energy $(-11.1 \text{ kcal} \cdot \text{mol}^{-1})$ with the neighboring residues comes from the interaction with Asn257 side chain $(-4.8 \text{ kcal} \cdot \text{mol}^{-1})$. Other nonpolar residues contribute by $\sim -1.5 \text{ kcal} \cdot \text{mol}^{-1}$ per residue with the exception of the nonpolar part of the Lys699 side chain (modeled as $CH_3(CH_2)_2CH_3$) that contributes negligibly. For the C-terminal AOC and ANO, there is a notable increase in the interaction of Phe209 and the nonpolar part of Lys699 (by $\sim 1 \text{ kcal/mol}^{-1}$) and a slight increase in the interaction energies of other nonpolar residues that more than compensates the energetic loss in the interaction of AOC/ANO with the Asn257. The same stabilizing role can be also postulated for several of our inhibitors previously published and highlights the importance of nonpolar and $\pi-\pi$ stacking interactions in biological systems.

Finally, we observed that the interaction energies between the P1′ side chain of the substrate/inhibitor and the S1′ residues are almost perfectly pairwise additive; i.e., the total interaction energy almost equals the sum of pair interaction energies. In summary, these calculations provide semiquantitative insight into the arguments about the origin of the hydrophobicity of the S1′ site, given in this study.

■ DISCUSSION

Glutamate-based functionalities are instrumental for selective targeting of human GCPII in applications ranging from prostate cancer (PCa) imaging to the experimental treatment of neurodegenerative conditions.[8] Since the GCPII pharmacophore (S1′) pocket is "optimized" for glutamate-like scaffolds, the presence of these functionalities ensures both high affinity and specificity of corresponding inhibitors.[31,32] Several groups reported structure–activity relationship (SAR) studies focusing on substituting the P1′ glutamate in GCPII inhibitors. Majer et al.[33] designed and tested a series of thiol-based inhibitors containing a benzyl moiety at the P1′ position to increase lipophilicity of 2-(3-mercaptopropyl)pentanedioic acid (2-MPPA), the first orally available GCPII inhibitor. In addition to higher lipophilicity, the best candidates were found to be more potent than the parent molecule and showed effectiveness in a rat chronic constriction injury model of neuropathic pain. The Kozikowski group[34] applied the SAR approach using N-[[[(1S)-1-carboxy-3-methyl-butyl]amino]carbonyl]-L-glutamic acid (ZJ-43, a urea-based NAAG analogue as a lead compound) to decrease polarity for more efficient targeting of GCPII in the nervous system, especially in the PNS. We evaluated a series of DCIBzL-based isosteres and identified several non-glutamate inhibitors with K_i values below 20 nM that exhibited selective binding to GCPII-expressing tumors by single photon emission computed tomography (SPECT-CT) imaging in mice.[32]

This report uses the rational design to extend and complement the above-mentioned SAR studies with the objective of preparing potent GCPII inhibitors with enhanced lipophilicity. On the basis of our earlier kinetic data, we first designed and characterized a set of novel dipeptidic GCPII substrates and provided the structural evidence for recognition of such dipeptides by GCPII. Next, we designed a series of inhibitors, where the P1′ moiety is derived from the dipeptidic substrates and the P1 part features 4-iodobenzoyl-ε-lysine, the functionality shown by us previously to augment interactions with GCPII;[24] the P1 and P1′ parts are

connected via a urea linker (Table 3). The most potent molecule (compound **8I**) has $K_i = 29$ nM and ClogD = -0.23. Although the binding affinity of **8I** is markedly lower compared to the parent glutamate-based compound (29 nM vs 10 pM, respectively), its affinity is sufficient for imaging PCa.[32] Furthermore, substantially increased lipophilicity (-0.23 vs -5.16) can be translated into a better pharmacokinetic profile in the periphery, with increased likelihood of the penetration into the CNS. Last but not least, in the phase I human clinical trial using N-[N-[(S)-1,3-dicarboxypropyl]carbamoyl]-4-[^{18}F]fluorobenzyl-L-cysteine ([^{18}F]DCFBC),[35] one of the glutamate-based PET agents targeting GCPII that was developed for prostate cancer imaging, we observed somewhat increased signal from the blood pool in human subjects, suggesting potential binding of the compound to an unidentified plasma protein. The prime suspect in the case is plasma glutamate carboxypeptidase, a circulating plasma protein with 27% overall sequence identity and overlapping substrate specificity to GCPII.[36,37] Given the substitution of glutamate by non-natural amino acids in novel inhibitors presented here, the likelihood of off-target interactions with endogenous proteins might be less pronounced in the latter. To prove these assumptions, however, additional in vivo studies are needed.

For both substrate and inhibitor synthesis, 2-amino acids with pentyl to heptyl side chains were used as a racemic mixture for both substrate and inhibitor synthesis. The corresponding products (substrates and inhibitors) are therefore equimolar mixtures of two diastereomers. In the case of inhibitors, the individual diastereomers were separated by HPLC and their inhibition potency was assayed. As expected, only compounds with the (S)-stereochemistry at the C-terminus were inhibitory, while their (R)-counterparts turned out to be inactive (data not shown). In the case of substrates, a mixture of diastereomers was used for kinetic studies. Following the substrate incubation with rhGCPII for 24 h at 37 °C, we analyzed the reaction mixture using HPLC with UV detection after precolumn derivatization of released C-terminal amino acids with Marfey's reagent (1-fluoro-2,4-dinitrophenyl-5-L-alanineamide), a chiral reagent used for distinguishing (S)- and (R)-amino acids. In all cases, we observed peaks corresponding to only a single, presumably (S), enantiomer (data not shown). Since previously reported data suggested that GCPII is inactive toward (R)-amino acids at the P1′ position, we concluded that only (S)-amino acid containing dipeptides serve as efficient substrates of rhGCPII.

The SAR studies suggest that the nonprime GCPII specificity pocket(s) are rather insensitive to structural changes of GCPII inhibitors and can accommodate (or at least tolerate) surprising diversity of functional groups of inhibitors.[4,7,24,26,28,34] On the contrary, the S1′ (or pharmacophore) pocket in GCPII is highly selective for glutamate and glutamate-like moieties. The selectivity is achieved via an intricate network of mostly polar interactions between GCPII and an inhibitor, with the most prominent being the Arg210-α-carboxylate and Lys699-γ-carboxylate ion pairing.[22,31] Structural data that characterize the S1′ pocket as fairly compact, small-sized, and unyielding, in contrast to the much larger and quite flexible nonprime site (the funnel emanating from the active site zinc to the surface of the protein), are in agreement with these observations.

This report expands the above concept in two ways: (i) it documents for the first time substantial plasticity of the GCPII pharmacophore pocket achieved by the relocation of the Lys699 side chain leading to the considerable enlargement (by 3.9 Å) of

46

the S1′ site. Furthermore, this work directly to S1′ site; (ii) it directly demonstrates the importance of nonpolar interactions, mediated by the side chains of Phe209, Asn257, Leu428, and Lys699 for GCPII affinity toward small-molecule compounds featuring hydrophobic moieties in the P1′ position. Although ionic interactions between the Arg210 guanidinum group and the α-carboxylate group of the C-terminal (P1′ position) residue are common to all dipeptidic substrates tested in this study, these are obviously not sufficient with respect to efficient substrate positioning and subsequent hydrolysis, as the dipeptide with glycine in the P1′ position is not cleaved. Additionally, the dipeptide with a C-terminal alanine, the amino acid with the shortest side chain, in the P1′ position is the least efficient GCPII substrate (see Table 1).

In summary, the new findings presented here expand the chemical space that can be explored during the rational design of GCPII inhibitors with increased lipophilicity. By linking a lipophilic "non-glutamate" C-terminal moiety to a nonpolar P1 functionality, one can design inhibitors with increased lipophilicity that are more likely to penetrate the blood—brain barrier. However, lipophilicity is only one of physicochemical parameters related to the druglike molecular properties (others being molecular weight, polar surface area, number of hydrogen bond donors/acceptors, number of rotatable bonds). In this regard, compounds presented here can be viewed as a precedent for the development of GCPII-specific inhibitor analogues, with the ultimate goal of designing the truly BBB-permeable compounds.

■ CONCLUSIONS

In this study we (i) report the design and characterization of a novel set of dipeptidic GCPII substrates, (ii) provide structural and computational evidence for recognition of such dipeptidic substrates by GCPII, and (iii) report the design and evaluation of novel substrate-based GCPII inhibitors with nanomolar affinity and increased lipophilicity. Besides contributing to the understanding of GCPII function, these data also serve as a starting point for the design of "non-glutamate" small molecule GCPII ligands with the increased lipophilicity that may represent a novel and important class of inhibitors of GCPII.

■ EXPERIMENTAL SECTION

Wild-Type rhGCPII Expression and Purification. The cloning, expression, and purification of recombinant human GCPII (rhGCPII) have been described previously.[21] Briefly, the extracellular part of human glutamate carboxypeptidase II, which spans amino acid residues 44—750, was cloned into the pMT/BiP/V5-His A plasmid (Invitrogen, Carlsbad, U.S.), and the recombinant protein (designated rhGCPII) was expressed in *Drosophila* Schneider's S2 cells and purified to homogeneity.

Expression and Purification of rhGCPII(E424A) and rhGCPII(K699S) Mutants. Cloning, expression, and purification of the rhGCPII(E424A) and rhGCPII(K699S) mutants have been described elsewhere.[22,23] In short, desired mutations were introduced into a GCPII coding sequence using QuikChange site-directed mutagenesis kit (Stratagene, La Jolla, CA, U.S.) and the mutated protein expressed in S2 cells. Purification protocols included ion-exchange chromatography steps (QAE-Sephadex A50, source S15) followed by affinity chromatography on lentil lectin and size-exclusion chromatography on a Superdex 200 column. The final protein preparations were >95% pure as determined by silver-stained SDS—PAGE (data not shown). For crystallization experiments, purified rhGCPII(E424A) was dialyzed against 20 mM MOPS, 20 mM NaCl, pH 7.4, and concentrated to 8.7 mg/mL.

Crystallization and Data Collection. The rhGCPII(E424A) stock solution was mixed with $^1/_{10}$ volume of 100 mM aqueous solutions of NAAM, **7S**, and **8S**. For the GCPII/**9I** complex, rhGCPII stock solution (8 mg/mL) was mixed with $^1/_{10}$ volume of **9I** (3 mM final concentration). The protein/dipeptide or protein/inhibitor mixtures were combined with an equal volume of the reservoir solution containing 33% (v/v) pentaerythritol propoxylate PO/OH 5/4 (Hampton Research), 0.5% (w/v) PEG 3350, and 100 mM Tris-HCl, pH 8.0. Crystals were grown from 2 μL droplets by the hanging-drop vapor-diffusion method at 293 K. For each complex, the diffraction intensities were collected from a single crystal at 100 K using synchrotron radiation ($\lambda = 1.00$ Å) at the SER-CAT beamline 22-ID at the Advanced Photon Source (Argonne, IL, U.S.) equipped with a MAR225 CCD detector. The data sets were indexed, integrated, and scaled using the HKL software package (Table S1).[38]

Structure Determination and Refinement. Structure determination of GCPII complexes presented here were carried out using difference Fourier methods with the ligand-free rhGCPII (PDB code 2OOT)[39] as a starting model. Calculations were performed with the program Refmac 5.5,[40] and the refinement protocol was interspersed with manual corrections to the model employing the program Coot.[41] The restrains library and the coordinate files for individual inhibitors were prepared using the PRODRG server,[42] and the inhibitors/substrates were fitted into the positive electron density map in the final stages of the refinement. Approximately 1% of the randomly selected reflections were kept aside for cross-validation (R_{free}) during the refinement process. The quality of the final models was evaluated using MolProbity.[43] The data collection and refinement statistics are summarized in Table S1. Atomic coordinates of the present structures together with the experimental structure factor amplitudes were deposited at the RCSB Protein Data Bank under accession numbers 3SJX [GCPII-(E424A)/NAAM], 3SJG [GCPII(E424A)/**7S**], 3SJE [GCPII(E424A)/**8S**], and 3SJF (GCPII/**9I**).

Substrate Synthesis. Glycine, (*S*)-alanine, (*S*)-norleucine, (*S*)-methionine, (*S*)-aminobutyric acid, (*S*)-glutamic acid, and (*S*)-norvaline were purchased from Sigma. (*S,R*)-forms of 2-aminoheptanoic, octanoic, and nonanoic acids were purchased from Fluka. N-Acetylated dipeptides were synthesized using standard Fmoc-based approach on a Wang hydroxymethylphenyl-functionalized resin.[44] The identity and purity of the peptides were checked by mass spectrometry, reversed-phase HPLC, and amino acid analysis, and the purity was determined to be >95% (data not shown).

Determination of Kinetic Constants. Kinetic constants of N-terminally acetylated dipeptidic substrates were determined by high-performance liquid chromatography with fluorimetric detection (excitation 250 nm, emission 395 nm) of precolumn derivatized amino acids. Typically, 1—2 μg/mL rhGCPII in 20 mM MOPS, 20 mM NaCl, pH 7.4, was reacted with 5—300 μM relevant substrate for 30 min at 37 °C in a final volume of 120 μL. The reaction was stopped by the addition of 20 μL of 100 mM EDTA, pH 9.2, and the pH of the reaction mixture was adjusted by the addition of 40 μL of 100 mM borate buffer, pH 9.0. The released amino acids were derivatized using 20 μL of 2.5 mM AccQ-Fluor reagent (Waters, Milford, MA, U.S.) dissolved in acetonitrile. Then 30 μL of the resulting mixture was applied to a Luna C18(2) column (250 mm × 4.6 mm, 5 μm particle size, Phenomenex) mounted to a Waters Alliance 2795 system equipped with a Waters 2475 fluorescence detector.

Synthesis of GCPII Inhibitors. Some of the tested inhibitors (**1I**, **4I**, **DCIBzL**, and **9I**) were already reported previously by our laboratory.[32] The other GCPII inhibitors (**2I**, **3I**, **5I**—**8I**) were prepared by a general procedure as follows.

To N^ε-Boc-L-lysine *tert*-butyl ester hydrochloric acid (339 mg, 1 mmol) in 20 mL of CH_2Cl_2 at −78 °C was added triphosgene (98 mg, 0.33 mmol) followed by triethylamine (1 mL). The reaction mixture was

47

stirred at $-78\ °C$ for 1 h, and the dry ice/acetone bath was removed. The stirring was continued for another 30 min at room temperature and the reaction mixture cooled back to $-78\ °C$. To the reaction mixture were added the individual amino acid (1 mmol) in anhydrous DMF (10 mL) and triethylamine (1 mL). After the mixture was stirred overnight, the excess solvent was removed under reduced pressure and the residue was purified by reverse phase HPLC to give urea compounds (20−50% yield). The urea compounds (0.1 mmol) were dissolved in 1 mL of TFA and stirred at room temperature for 60 min. The completion of the deprotection reaction was monitored by ESI-MS. Excess TFA was removed by reduced pressure. The residue was dissolved in DMF (5 mL) and triethylamime (0.5 mL), followed by the addition of 4-iodosuccinimide benzoate (0.12 mmol). The reaction mixture was stirred at room temperature for 3 h. The excess solvent was removed and the residue was purified by reverse phase HPLC to give the target compounds (40−60% yield). The final purity of inhibitors was >95% as determined by analytical HPLC.

(S)-2-(3-((S)-1-Carboxyethyl)ureido)-6-(4-iodobenzamido)hexanoic Acid (2I). HPLC conditions: H_2O/CH_3CN (0 min, 90/10 → 30 min, 50/50, 0.1% TFA), flow rate 3 mL/min, retention time 23 min. ^1H NMR (400 MHz, H_2O-d_2) δ: 8.17 (d, $J = 8.0$ Hz, 2H), 7.80 (d, $J = 7.2$ Hz, 2H), 4.40−4.44 (m, 2H), 3.41−3.44 (m, 2H), 1.95−2.05 (m, 2H), 1.86−1.89 (m, 2H), 1.67−1.72 (m, 2H). [M + H] calculated for $C_{17}H_{22}IN_3O_6$ 492.1, found 491.9. Yield: 21%.

(S)-2-(3-((S)-1-Carboxypropyl)ureido)-6-(4-iodobenzamido)hexanoic Acid (3I). HPLC conditions: H_2O/CH_3CN (0 min, 75/25 → 30 min, 40/60, 0.1% TFA), flow rate 3 mL/min, retention time 13 min. ^1H NMR (400 MHz, CD_3CN) δ: 7.81 (d, $J = 6.8$ Hz, 2H), 7.46 (d, $J = 6.8$ Hz, 2H) 4.08 (m, 1H), 4.01 (m, 1H), 3.26 (d, $J = 6.8$ Hz, 2H), 1.70−1.75 (m, 2H), 1.63−1.68 (m, 2H), 1.60−1.64 (m, 2H), 1.32−1.38 (m, 2H), 0.84 (t, $J = 7.2$ Hz, 3H). [M + H] calculated for $C_{18}H_{24}IN_3O_6$ 506.1, found 505.8. Yield: 19%.

(S)-2-(3-((S)-1-Carboxypentyl)ureido)-6-(4-iodobenzamido)hexanoic Acid (5I). HPLC conditions: H_2O/CH_3CN (0 min, 75/25 → 30 min, 40/60, 0.1% TFA), flow rate 3 mL/min, retention time 15 min. ^1H NMR (400 MHz, MeOH-d_4) δ: 7.82 (d, $J = 7.2$ Hz, 2H), 7.56 (d, $J = 7.2$ Hz, 2H), 4.25 (m, 1H), 4.22 (m, 1H), 3.31−3.39 (m, 2H), 1.83−1.89 (m, 2H), 1.62−1.67 (m, 4H), 1.45−1.49 (m, 2H), 1.32−1.39 (m, 4H), 0.89 (t, 3H). [M + H] calculated for $C_{20}H_{28}IN_3O_6$ 534.1, found 533.8. Yield: 17%.

(S)-2-(3-((S)-1-Carboxyhexyl)ureido)-6-(4-iodobenzamido)hexanoic Acid (6I). HPLC conditions: H_2O/CH_3CN (58/42, 0.1% TFA), flow rate 3 mL/min, retention time 13.5 min. ^1H NMR (400 MHz, CD_3CN) δ: 7.80 (d, $J = 7.2$ Hz, 2H), 7.49 (d, $J = 7.2$ Hz, 2H), 4.13−4.18 (m, 1H), 4.08−4.12 (m, 1H), 3.27 (t, $J = 6.8$ Hz, 2H), 1.86−1.89 (m, 1H), 1.74−1.78 (m, 2H), 1.62−1.66 (m, 2H), 1.52−1.55 (m, 2H), 1.29−1.37 (m, 6H), 0.87 (t, $J = 6.2$ Hz, 3H). [M + H] calculated for $C_{21}H_{30}IN_3O_6$ 548.2, found 547.8. Yield: 18%.

(S)-2-(3-((S)-1-Carboxyheptyl)ureido)-6-(4-iodobenzamido)hexanoic Acid (7I). HPLC conditions: H_2O/CH_3CN (58/42, 0.1% TFA), flow rate 3 mL/min, retention time 16.5 min. ^1H NMR (400 MHz, CD_3CN) δ: 7.82 (d, $J = 7.2$ Hz, 2H), 7.50 (d, $J = 7.2$ Hz, 2H), 4.15−4.18 (m, 1H), 4.09−4.12 (m, 1H), 3.30 (t, $J = 6.8$ Hz, 2H), 1.83−1.89 (m, 1H), 1.62−1.67 (m, 3H), 1.45−1.49 (m, 2H), 1.26−1.38 (m, 10H), 0.89 (t, $J = 6.2$ Hz, 3H). [M + H] calculated for $C_{22}H_{32}IN_3O_6$ 562.1, found 561.9. Yield: 16%.

(S)-2-(3-((S)-1-Carboxyoctyl)ureido)-6-(4-iodobenzamido)hexanoic Acid (8I). HPLC conditions: H_2O/CH_3CN (58/42, 0.1% TFA), flow rate 3 mL/min, retention time 19.5 min. ^1H NMR (400 MHz, CD_3CN) δ: 7.79 (d, $J = 8.0$ Hz, 2H), 7.48 (d, $J = 8.0$ Hz, 2H), 4.11−4.16 (m, 1H), 4.04−4.08 (m, 1H), 3.26 (t, $J = 6.8$ Hz, 2H), 1.73−1.81 (m, 1H), 1.52−1.63 (m, 3H), 1.32−1.38 (m, 2H), 1.17−1.30 (m, 12H), 0.88 (t, $J = 6.2$ Hz, 3H). [M + H] calculated for $C_{23}H_{34}IN_3O_6$ 576.1, found 575.8. Yield: 14%.

In Vitro GCPII Inhibitory Constants. Inhibition constants were determined using a fluorescence-based assay according to a previously reported procedure.[45] Briefly, lysates of LNCaP cell extracts (25 μL) were incubated with the inhibitor (12.5 μL) in the presence of 4 μM NAAG (12.5 μL) for 120 min. The amount of the released glutamate was determined by incubating with a working solution (50 μL) of the Amplex Red glutamic acid kit (Invitrogen Corp., CA, U.S.) for 60 min. The fluorescence was measured using a VICTOR^{3}V multilabel plate reader (Perkin-Elmer Inc., Waltham, MA, U.S.) with excitation at 490 nm and emission at 640 nm. Inhibition curves were determined using semilog plots, and IC_{50} values were calculated. Assays were performed in triplicate. Enzyme inhibitory constants (K_i) were generated using the Cheng−Prusoff conversion. Data analysis was performed using GraphPad Prism, version 4.00, for Windows (GraphPad Software, San Diego, CA).

Quantum Chemical Calculations and QM/MM Modeling. All QM/MM calculations were carried out with the COMQUM program.[46] In the current version, the program uses Turbomole 5.7[47] for the QM part and AMBER 8 (University of California, San Francisco, U.S.) with the Cornell force field[48] for the MM part. The details of the QM/MM procedure that are essentially identical to the ones described in ref 23 can be found in the Supporting Information.

Protein (GCPII) Setup. All structural models used in QM/MM calculations were based on the reported crystal structures and on our previous work[23] where we carefully described the strategy to include missing loops, addition of hydrogens, protonation states of His residues, and construction of solvation sphere, including initial simulated annealing protocol leading to the optimization of positions of all the atoms missing in the crystal structures. All these structural details can be found in the PDB files deposited. Therefore, starting from the QM/MM optimized structure of the NAAG (GCPII substrate) complexed with the enzyme,[23] we have replaced NAAG with the studied substrates/inhibitors (NAAM, **7S**, **8S**, **S8**, **8I**, **10I**) using their experimental crystal structures as templates. In case of **8I**, for which the crystal structure has not been yet determined, we used GCPII/DCIBzL and GCPII-(E424A)/**7S** structures as templates for positioning their P1 and P1′ parts, respectively. Because of the high similarity of the structures, we considered this approach as physically more sound, since the (highly optimized) QM/MM structure already contained all hydrogen atoms and missing parts of the protein. This approach is also justified a posteriori by an excellent agreement of the equilibrium QM/MM and crystal structures for a given enzyme/inhibitor complex. The only significant structural change involved the Lys699 residue which swings by ∼3.5 Å upon binding of the inhibitors with longer alkyl chains as described above. Also, we have tried to carefully adapt the positions of two to three water molecules in the vicinity of the active site to match their positions in the crystal structures. The quantum region in the calculations consisted of the following residues: two Zn^{2+} ions, bringing hydroxide moiety, inhibitor, side chains of Phe209, Arg210, Asn257, His377, Asp387, Glu424, Glu425, Asp453, Arg463, Asp465, Arg534, Arg536, Tyr552, His553, Lys699, Tyr700, the Gly427-Leu428 chain (capped by CHO moiety of the Phe426 at the N-terminus and NH−CH₃ moiety of the Leu429 residue at the C-terminus), the Ser517-Asp520 chain (capped by CHO moiety of the Gly516 at the N-terminus and NH−CH₃ moiety of the Phe521), and six to eight water molecules in the vicinity of the active site. It resulted in fairly large QM system of ∼350 atoms.

Quantum Chemical Calculations. All quantum chemical calculations were performed at the density functional theory (DFT) level. Geometry optimizations were carried out at the Perdew−Burke−Ernzerhof (PBE) level.[49] The DFT/PBE calculations were expedited by expanding the Coulomb integrals in an auxiliary basis set, the resolution-of-identity (RI-J) approximation.[50] In QM/MM optimizations, the def2-SVP basis set was employed for all atoms.[51] The calculations of the interaction energy of the nonpolar side chains of the inhibitors with the S1′ residues and its decomposition into the pair

contributions were carried out using the recent DFT-D3 computational protocol (DFT with the empirical dispersion) of Grimme[52] that was shown to yield, in combination with the B-LYP functional[53] and TZVPP basis set,[51] excellent values of the interaction energies for noncovalently bound complexes.

■ ASSOCIATED CONTENT

ⓢ Supporting Information. Details of data collection and refinement statistics, spectroscopic data for inhibitors, and QM/MM calculations together with resulting PDB structures. This material is available free of charge via the Internet at http://pubs.acs.org.

Accession Codes

[†]Atomic coordinates of the present structures together with the experimental structure factor amplitudes were deposited at the RCSB Protein Data Bank under accession numbers 3SJX [GCPII-(E424A)/NAAM], 3SJG [GCPII(E424A)/7S], 3SJE [GCPII-(E424A)/8S], and 3SJF (GCPII/9I).

■ AUTHOR INFORMATION

Corresponding Author
*Phone: +420-296-443-615. Fax: +420-296-443-610. E-mail: cyril.barinka@img.cas.cz.

Author Contributions
●These author contributed equally.

■ ACKNOWLEDGMENT

■ ABBREVIATIONS USED

rhGCPII, recombinant human glutamate carboxypeptidase II; QM/MM, quantum mechanics/molecular mechanics; NAAM, N-acetyl-aspartyl-methionine; NAAG, N-acetyl-aspartyl-glutamate; ANO, 2-aminononanoic acid; AOC, 2-aminooctanoic acid; SAR, structure−activity relationship; ESI-MS, electrospray ionization mass spectrometry; PET, positron emission tomography; Ac, acetyl group; GCPII, glutamate carboxypeptidase II; SPECT-CT, single photon emission computed tomography; HPLC, high performance liquid chromatography; DFT, density functional theory; PBE, Perdew−Burke−Ernzerhof; PCa, prostate cancer

■ REFERENCES

(1) Robinson, M. B.; Blakely, R. D.; Couto, R.; Coyle, J. T. Hydrolysis of the brain dipeptide N-acetyl-L-aspartyl-L-glutamate. Identification and characterization of a novel N-acetylated alpha-linked acidic dipeptidase activity from rat brain. *J. Biol. Chem.* **1987**, 262, 14498−14506.

(2) Sacha, P.; Zamecnik, J.; Barinka, C.; Hlouchova, K.; Vicha, A.; Mlcochova, P.; Hilgert, I.; Eckschlager, T.; Konvalinka, J. Expression of glutamate carboxypeptidase II in human brain. *Neuroscience* **2007**, 144, 1361−1372.

(3) Sokoloff, R. L.; Norton, K. C.; Gasior, C. L.; Marker, K. M.; Grauer, L. S. A dual-monoclonal sandwich assay for prostate-specific membrane antigen: levels in tissues, seminal fluid and urine. *Prostate* **2000**, 43, 150−157.

(4) Banerjee, S. R.; Pullambhatla, M.; Byun, Y.; Nimmagadda, S.; Green, G.; Fox, J. J.; Horti, A.; Mease, R. C.; Pomper, M. G. ^{68}Ga-labeled inhibitors of prostate-specific membrane antigen (PSMA) for imaging prostate cancer. *J. Med. Chem.* **2010**, 53, 5333−5341.

(5) Chen, Y.; Dhara, S.; Banerjee, S. R.; Byun, Y.; Pullambhatla, M.; Mease, R. C.; Pomper, M. G. A low molecular weight PSMA-based fluorescent imaging agent for cancer. *Biochem. Biophys. Res. Commun.* **2009**, 390, 624−629.

(6) Rosenthal, S. A.; Haseman, M. K.; Polascik, T. J. Utility of capromab pendetide (ProstaScint) imaging in the management of prostate cancer. *Tech. Urol.* **2001**, 7, 27−37.

(7) Zhang, A. X.; Murelli, R. P.; Barinka, C.; Michel, J.; Cocleaza, A.; Jorgensen, W. L.; Lubkowski, J.; Spiegel, D. A. A remote arene-binding site on prostate specific membrane antigen revealed by antibody-recruiting small molecules. *J. Am. Chem. Soc.* **2010**, 132, 12711−12716.

(8) Zhou, J.; Neale, J. H.; Pomper, M. G.; Kozikowski, A. P. NAAG peptidase inhibitors and their potential for diagnosis and therapy. *Nat. Rev. Drug Discovery* **2005**, 4, 1015−1026.

(9) Neale, J. H.; Olszewski, R. T.; Gehl, L. M.; Wroblewska, B.; Bzdega, T. The neurotransmitter N-acetylaspartylglutamate in models of pain, ALS, diabetic neuropathy, CNS injury and schizophrenia. *Trends Pharmacol. Sci.* **2005**, 26, 477−484.

(10) Slusher, B. S.; Vornov, J. J.; Thomas, A. G.; Hurn, P. D.; Harukuni, I.; Bhardwaj, A.; Traystman, R. J.; Robinson, M. B.; Britton, P.; Lu, X. C.; Tortella, F. C.; Wozniak, K. M.; Yudkoff, M.; Potter, B. M.; Jackson, P. F. Selective inhibition of NAALADase, which converts NAAG to glutamate, reduces ischemic brain injury. *Nat. Med.* **1999**, 5, 1396−1402.

(11) Zhang, W.; Slusher, B.; Murakawa, Y.; Wozniak, K. M.; Tsukamoto, T.; Jackson, P. F.; Sima, A. A. GCPII (NAALADase) inhibition prevents long-term diabetic neuropathy in type 1 diabetic BB/Wor rats. *J. Neurol. Sci.* **2002**, 194, 21−28.

(12) Ghadge, G. D.; Slusher, B. S.; Bodner, A.; Canto, M. D.; Wozniak, K.; Thomas, A. G.; Rojas, C.; Tsukamoto, T.; Majer, P.; Miller, R. J.; Monti, A. L.; Roos, R. P. Glutamate carboxypeptidase II inhibition protects motor neurons from death in familial amyotrophic lateral sclerosis models. *Proc. Natl. Acad. Sci. U.S.A.* **2003**, 100, 9554−9559.

(13) Carpenter, K. J.; Sen, S.; Matthews, E. A.; Flatters, S. L.; Wozniak, K. M.; Slusher, B. S.; Dickenson, A. H. Effects of GCP-II inhibition on responses of dorsal horn neurones after inflammation and neuropathy: an electrophysiological study in the rat. *Neuropeptides* **2003**, 37, 298−306.

(14) Chen, S. R.; Wozniak, K. M.; Slusher, B. S.; Pan, H. L. Effect of 2-(phosphono-methyl)-pentanedioic acid on allodynia and afferent ectopic discharges in a rat model of neuropathic pain. *J. Pharmacol. Exp. Ther.* **2002**, 300, 662−667.

(15) Yamamoto, T.; Nozaki-Taguchi, N.; Sakashita, Y.; Inagaki, T. Inhibition of spinal N-acetylated-alpha-linked acidic dipeptidase produces an antinociceptive effect in the rat formalin test. *Neuroscience* **2001**, 102, 473−479.

(16) Olszewski, R. T.; Bukhari, N.; Zhou, J.; Kozikowski, A. P.; Wroblewski, J. T.; Shamimi-Noori, S.; Wroblewska, B.; Bzdega, T.; Vicini, S.; Barton, F. B.; Neale, J. H. NAAG peptidase inhibition reduces locomotor activity and some stereotypes in the PCP model of schizophrenia via group II mGluR. *J. Neurochem.* **2004**, 89, 876−885.

(17) Kozela, E.; Wrobel, M.; Kos, T.; Wojcikowski, J.; Daniel, W. A.; Wozniak, K. M.; Slusher, B. S.; Popik, P. 2-MPPA, a selective glutamate carboxypeptidase II inhibitor, attenuates morphine tolerance but not dependence in C57/Bl mice. *Psychopharmacology (Berlin, Ger.)* **2005**, 183, 275−284.

(18) Popik, P.; Kozela, E.; Wrobel, M.; Wozniak, K. M.; Slusher, B. S. Morphine tolerance and reward but not expression of morphine dependence are inhibited by the selective glutamate carboxypeptidase II (GCP II, NAALADase) inhibitor, 2-PMPA. *Neuropsychopharmacology* **2003**, *28*, 457–467.

(19) Guilarte, T. R.; Hammoud, D. A.; McGlothan, J. L.; Caffo, B. S.; Foss, C. A.; Kozikowski, A. P.; Pomper, M. G. Dysregulation of glutamate carboxypeptidase II in psychiatric disease. *Schizophr. Res.* **2008**, *99*, 324–332.

(20) Guilarte, T. R.; McGlothan, J. L.; Foss, C. A.; Zhou, J.; Heston, W. D.; Kozikowski, A. P.; Pomper, M. G. Glutamate carboxypeptidase II levels in rodent brain using [^{125}I]DCIT quantitative autoradiography. *Neurosci. Lett.* **2005**, *387*, 141–144.

(21) Barinka, C.; Rinnova, M.; Sacha, P.; Rojas, C.; Majer, P.; Slusher, B. S.; Konvalinka, J. Substrate specificity, inhibition and enzymological analysis of recombinant human glutamate carboxypeptidase II. *J. Neurochem.* **2002**, *80*, 477–487.

(22) Mlcochova, P.; Plechanovova, A.; Barinka, C.; Mahadevan, D.; Saldanha, J. W.; Rulisek, L.; Konvalinka, J. Mapping of the active site of glutamate carboxypeptidase II by site-directed mutagenesis. *FEBS J.* **2007**, *274*, 4731–4741.

(23) Klusak, V.; Barinka, C.; Plechanovova, A.; Mlcochova, P.; Konvalinka, J.; Rulisek, L.; Lubkowski, J. Reaction mechanism of glutamate carboxypeptidase II revealed by mutagenesis, X-ray crystallography, and computational methods. *Biochemistry* **2009**, *48*, 4126–4138.

(24) Barinka, C.; Byun, Y.; Dusich, C. L.; Banerjee, S. R.; Chen, Y.; Castanares, M.; Kozikowski, A. P.; Mease, R. C.; Pomper, M. G.; Lubkowski, J. Interactions between human glutamate carboxypeptidase II and urea-based inhibitors: structural characterization. *J. Med. Chem.* **2008**, *51*, 7737–7743.

(25) Barinka, C.; Hlouchova, K.; Rovenska, M.; Majer, P.; Dauter, M.; Hin, N.; Ko, Y. S.; Tsukamoto, T.; Slusher, B. S.; Konvalinka, J.; Lubkowski, J. Structural basis of interactions between human glutamate carboxypeptidase II and its substrate analogs. *J. Mol. Biol.* **2008**, *376*, 1438–1450.

(26) Jackson, P. F.; Tays, K. L.; Maclin, K. M.; Ko, Y. S.; Li, W.; Vitharana, D.; Tsukamoto, T.; Stoermer, D.; Lu, X. C.; Wozniak, K.; Slusher, B. S. Design and pharmacological activity of phosphinic acid based NAALADase inhibitors. *J. Med. Chem.* **2001**, *44*, 4170–4175.

(27) Kozikowski, A. P.; Nan, F.; Conti, P.; Zhang, J.; Ramadan, E.; Bzdega, T.; Wroblewska, B.; Neale, J. H.; Pshenichkin, S.; Wroblewski, J. T. Design of remarkably simple, yet potent urea-based inhibitors of glutamate carboxypeptidase II (NAALADase). *J. Med. Chem.* **2001**, *44*, 298–301.

(28) Liu, T.; Toriyabe, Y.; Kazak, M.; Berkman, C. E. Pseudoirreversible inhibition of prostate-specific membrane antigen by phosphoramidate peptidomimetics. *Biochemistry* **2008**, *47*, 12658–12660.

(29) Hlouchova, K.; Barinka, C.; Klusak, V.; Sacha, P.; Mlcochova, P.; Majer, P.; Rulisek, L.; Konvalinka, J. Biochemical characterization of human glutamate carboxypeptidase III. *J. Neurochem.* **2007**, *101*, 682–696.

(30) Vitharana, D.; France, J. E.; Scarpetti, D.; Bonneville, G. W.; Majer, P.; Tsukamoto, T. Synthesis and biological evaluation of (*R*)- and (*S*)-2-(phosphonomethyl)pentanedioic acids as inhibitors of glutamate carboxypeptidase II. *Tetrahedron: Asymmetry* **2002**, *13*, 1609–1614.

(31) Barinka, C.; Rovenska, M.; Mlcochova, P.; Hlouchova, K.; Plechanovova, A.; Majer, P.; Tsukamoto, T.; Slusher, B. S.; Konvalinka, J.; Lubkowski, J. Structural insight into the pharmacophore pocket of human glutamate carboxypeptidase II. *J. Med. Chem.* **2007**, *50*, 3267–3273.

(32) Wang, H.; Byun, Y.; Barinka, C.; Pullambhatla, M.; Bhang, H. E.; Fox, J. J.; Lubkowski, J.; Mease, R. C.; Pomper, M. G. Bioisosterism of urea-based GCPII inhibitors: synthesis and structure–activity relationship studies. *Bioorg. Med. Chem. Lett.* **2010**, *20*, 392–397.

(33) Majer, P.; Hin, B.; Stoermer, D.; Adams, J.; Xu, W.; Duvall, B. R.; Delahanty, G.; Liu, Q.; Stathis, M. J.; Wozniak, K. M.; Slusher, B. S.; Tsukamoto, T. Structural optimization of thiol-based inhibitors of glutamate carboxypeptidase II by modification of the P1′ side chain. *J. Med. Chem.* **2006**, *49*, 2876–2885.

(34) Kozikowski, A. P.; Zhang, J.; Nan, F.; Petukhov, P. A.; Grajkowska, E.; Wroblewski, J. T.; Yamamoto, T.; Bzdega, T.; Wroblewska, B.; Neale, J. H. Synthesis of urea-based inhibitors as active site probes of glutamate carboxypeptidase II: efficacy as analgesic agents. *J. Med. Chem.* **2004**, *47*, 1729–1738.

(35) Mease, R. C.; Dusich, C. L.; Foss, C. A.; Ravert, H. T.; Dannals, R. F.; Seidel, J.; Prideaux, A.; Fox, J. J.; Sgouros, G.; Kozikowski, A. P.; Pomper, M. G. *N*-[*N*-[(*S*)-1,3-Dicarboxypropyl]carbamoyl]-4-[^{18}F]fluorobenzyl-L-cysteine, [^{18}F]DCFBC: a new imaging probe for prostate cancer. *Clin. Cancer Res.* **2008**, *14*, 3036–3043.

(36) Gingras, R.; Richard, C.; El-Alfy, M.; Morales, C. R.; Potier, M.; Pshezhetsky, A. V. Purification, cDNA cloning, and expression of a new human blood plasma glutamate carboxypeptidase homologous to *N*-acetyl-aspartyl-alpha-glutamate carboxypeptidase/prostate-specific membrane antigen. *J. Biol. Chem.* **1999**, *274*, 11742–11750.

(37) Zajc, T.; Suban, D.; Rajkovic, J.; Dolenc, I. Baculoviral expression and characterization of human recombinant PGCP in the form of an active mature dimer and an inactive precursor protein. *Protein Expression Purif.* **2011**, *75*, 119–126.

(38) Otwinowski, Z.; Minor, W. Processing of X-ray Diffraction Data Collected in Oscillation Mode. In *Methods in Enzymology*; Carter, C. W., Jr., Sweet, R. M., Eds.; Academic Press: New York, 1997; pp 307–326; Vol. 276.

(39) Barinka, C.; Starkova, J.; Konvalinka, J.; Lubkowski, J. A high-resolution structure of ligand-free human glutamate carboxypeptidase II. *Acta Crystallogr., Sect. F: Struct. Biol. Cryst. Commun.* **2007**, *63*, 150–153.

(40) Murshudov, G. N.; Vagin, A. A.; Lebedev, A.; Wilson, K. S.; Dodson, E. J. Efficient anisotropic refinement of macromolecular structures using FFT. *Acta Crystallogr., Sect. D: Biol. Crystallogr.* **1999**, *55*, 247–255.

(41) Emsley, P.; Cowtan, K. Coot: model-building tools for molecular graphics. *Acta Crystallogr., Sect. D: Biol. Crystallogr.* **2004**, *60*, 2126–2132.

(42) Schuttelkopf, A. W.; van Aalten, D. M. PRODRG: a tool for high-throughput crystallography of protein–ligand complexes. *Acta Crystallogr., Sect. D: Biol. Crystallogr.* **2004**, *60*, 1355–1363.

(43) Davis, I. W.; Leaver-Fay, A.; Chen, V. B.; Block, J. N.; Kapral, G. J.; Wang, X.; Murray, L. W.; Arendall, W. B., III; Snoeyink, J.; Richardson, J. S.; Richardson, D. C. MolProbity: all-atom contacts and structure validation for proteins and nucleic acids. *Nucleic Acids Res.* **2007**, *35*, W375–W383.

(44) Wang, S. S. *p*-Alkoxybenzyl alcohol resin and *p*-alkoxybenzyloxycarbonylhydrazide resin for solid phase synthesis of protected peptide fragments. *J. Am. Chem. Soc.* **1973**, *95*, 1328–1333.

(45) Chen, Y.; Foss, C. A.; Byun, Y.; Nimmagadda, S.; Pullambhatla, M.; Fox, J. J.; Castanares, M.; Lupold, S. E.; Babich, J. W.; Mease, R. C.; Pomper, M. G. Radiohalogenated prostate-specific membrane antigen (PSMA)-based ureas as imaging agents for prostate cancer. *J. Med. Chem.* **2008**, *51*, 7933–7943.

(46) Ryde, U. The coordination of the catalytic zinc ion in alcohol dehydrogenase studied by combined quantum-chemical and molecular mechanics calculations. *J. Comput.-Aided Mol. Des.* **1996**, *10*, 153–164.

(47) Treutler, O.; Ahlrichs, R. Efficient molecular numerical-integration schemes. *J. Chem. Phys.* **1995**, *102*, 346–354.

(48) Cornell, W. D.; Cieplak, P.; Bayly, C. I.; Gould, I. R.; Merz, K. M.; Ferguson, D. M.; Spellmeyer, D. C.; Fox, T.; Caldwell, J. W.; Kolman, P. A. A 2nd generation force-field for the simulation of proteins, nucleic-acids, and organic molecules. *J. Am. Chem. Soc.* **1995**, *117*, 5179–5197.

(49) Perdew, J. P.; Burke, K.; Erzerhof, M. Generalized gradient approximation made simple. *Phys. Rev. Lett.* **1996**, *77*, 3865–3868.

(50) Eichkorn, K.; Weigend, F.; Treutler, O.; Ahlrichs, R. Auxiliary basis sets for main row atoms and transition metals and their use to approximate Coulomb potentials. *Theor. Chim. Acta* **1997**, *97*, 119–124.

(51) Weigend, F.; Ahlrichs, R. Balanced basis sets of split valence, triple zeta valence and quadruple zeta valence quality for H to Rn: design and assessment of accuracy. *Phys. Chem. Chem. Phys.* **2005**, *7*, 3297–3305.

50

(52) Grimme, S.; Antony, J.; Ehrlich, S.; Krieg, H. A consistent and accurate ab initio parametrization of density functional dispersion correction (DFT-D) for the 94 elements H−Pu. *J. Chem. Phys.* **2010**, *132*, 154104.

(53) Becke, A. D. Density-functional exchange-energy approximation with correct asymptotic behavior. *Phys. Rev. A* **1988**, *38*, 3098−3100.

51

Novel substrate-based inhibitors of human glutamate carboxypeptidase II with enhanced lipophilicity

Anna Plechanovová,[1,2] Youngjoo Byun,[3,4] Glenda Alquicer,[5] Ľubica Škultétyová,[5] Petra Mlčochová,[1,2] Adriana Němcová,[1] Hyung-Joon Kim,[3] Michal Navrátil,[1,2] Ronnie Mease,[3] Jacek Lubkowski,[6] Martin Pomper,[3] Jan Konvalinka,[1,2] Lubomír Rulíšek,[1] and Cyril Bařinka[5,]*

[1] Institute of Organic Chemistry and Biochemistry, Gilead Sciences Research Center at IOCB, Academy of Sciences of the Czech Republic, Flemingovo náměstí 2, 166 10 Praha 6, Czech Republic

[2] Dept. of Biochemistry, Faculty of Natural Science, Charles University in Prague, Hlavova 2030, Prague, Czech Republic

[3] Russell H. Morgan Department of Radiology and Radiological Sciences, Johns Hopkins Medical Institutions, 1550 Orleans Street, Baltimore, Maryland 21231

[4] College of Pharmacy, Korea University, Sejong-ro, Jochiwon-eup, Yeongi-gun, Chungnam 339-700, South Korea

[5] Institute of Biotechnology, Academy of Sciences of the Czech Republic, Videnska 1083, 14200 Praha 4, Czech Republic

[6] National Cancer Institute at Frederick, Center for Cancer Research, Frederick, MD 21702, USA

Contents:

1

Table S1: Data collection and refinement statistics

Inhibitor/Substrate	9I	NAAM	7S	8S
PDB code	3SJF	3SJX	3SJG	3SJE
Wavelength (Å)	1.00			
Space group	I222			
Unit-cell parameters a, b, c (Å)	101.7, 130.8, 159.3	101.6, 130.0, 159.0	102.3, 130.0, 159.1	101.7, 130.2, 159.1
Resolution limits (Å)	30.0 – 1.65 (1.71 – 1.65)	30.0 – 1.66 (1.72 – 1.66)	30.0 – 1.65 (1.71 – 1.65)	30.0 – 1.70 (1.76 – 1.70)
Number of unique reflections	125,829 (12,257)	122,079 (10,816)	126,870 (12,577)	111,992 (8,520)
Redundancy	7.3 (5.6)	8.2 (5.9)	6.7 (4.8)	8.8 (5.8)
Completeness (%)	99.7 (97.9)	98.6 (88.3)	99.9 (99.8)	96.8 (74.3)
I/σI	20.9 (2.8)	27.6 (2.7)	19.9 (2.8)	20.8 (2.4)
Rmerge	0.076 (0.514)	0.062 (0.404)	0.110 (0.434)	0.080 (0.505)
Refinement statistics				
Resolution limits (Å)	29.52 – 1.65 (1.69 – 1.65)	28.21 – 1.66 (1.70 – 1.66)	28.05 – 1.65 (1.69 – 1.65)	29.57 – 1.70 (1.74 – 1.70)
Total number of	124,196	120,007	120,461	110,293

2

reflections	(8,916)	(7,665)	(8,584)	(5,927)
Number of reflection in working set	122,938 (8,831)	118,192 (7,544)	114,081 (8,131)	108,624 (5,866)
Number of reflection in test set	1,258 (85)	1,815 (121)	6,380 (453)	1,669 (61)
R / R_{free} (%)	15.9/17.8 (24.4/27.2)	18.0/20.4 (29.3/34.7)	16.7/18.3 (22.5/24.6)	17.3/18.8 (27.3/31.0)
Total number of non-H atoms	6,740	6,633	6,546	6,457
Number of non-H non-protein atoms	616	478	543	424
Number of water molecules	586	457	521	401
Average B-factor (Å²)				
Protein atoms	18.6	19.9	21.1	22.1
Waters	28.9	26.8	29.9	29.0
Inhibitor	29.2	27.5	31.5	37.5
R.m.s deviations:				
Bond lengths (Å)	0.016	0.018	0.017	0.020

3

Bond angles (°)	1.60	1.69	1.69	1.74
Ramachandran Plot (%)[&]				
Favored	97.6	96.2	98.2	97.6
Allowed	99.9	99.6	99.7	100
Disallowed	G335	E153;A222; K223	W541	
Missing residues	44-54, 654-655	44-54, 654-655	44-54, 654-655	44-54, 654-655

Values in parentheses correspond to the highest resolution shells.

[&] Structures were analyzed using the MolProbity package [43].

4

QM/MM Calculations – Computational Details

In the use QM/MM approach (ComQum program),[1] the protein and solvent are split into three subsystems: the QM region (system 1) contains most of the atoms relevant for the chemical process under consideration (i.e. the active site and its nearest vicinity) and is relaxed by QM/MM forces. System 2 consists of all residues within 5 Å of any atom in system 1 and is relaxed by a full MM minimization in each step of the QM/MM geometry optimization. Finally, system 3 contains the remaining part of the protein and surrounding solvent molecules and is kept fixed at the original (crystallographic) coordinates. In the quantum chemical calculations, the QM system is represented by a wave function, whereas all the other atoms are represented by an array of partial point charges, one per atom, taken from Amber libraries. Thereby, the polarization of the quantum chemical system by the surroundings is included in a self-consistent manner. In the MM calculations for the QM/MM forces and energies, all atoms are represented by the Amber force field. When there is a bond spanning the boundary of systems 1 and 2 (a junction), the quantum region is reduced to hydrogen atoms, the positions of which are linearly related to the corresponding carbon atoms in the full system (the hydrogen link approach).[1] In order to avoid overpolarization of the quantum system, point charges on the atoms in the MM region bound to the junction atoms are omitted, and the remaining charges on the truncated amino acid are adjusted to keep the fragment neutral. The actual charges used for all atoms can be found in the sample PDB file in the Supporting Information (last column). The total energy is calculated as:

$$E_{tot} = E_{QM} + E_{MM123} - E_{MM1} \qquad (1)$$

E_{QM} is the QM energy of the quantum system truncated by hydrogen atoms in the field of the surrounding point charges, but excluding the self-energy of the atoms associated with point charges. E_{MM1} is the MM energy of the quantum system, still truncated by hydrogen atoms but without any electrostatic interactions. Finally, E_{MM123} is the classical energy of all atoms in the system with original atoms at the junctions and with the charges of the quantum system set to zero (to avoid double-counting of the electrostatic interactions).
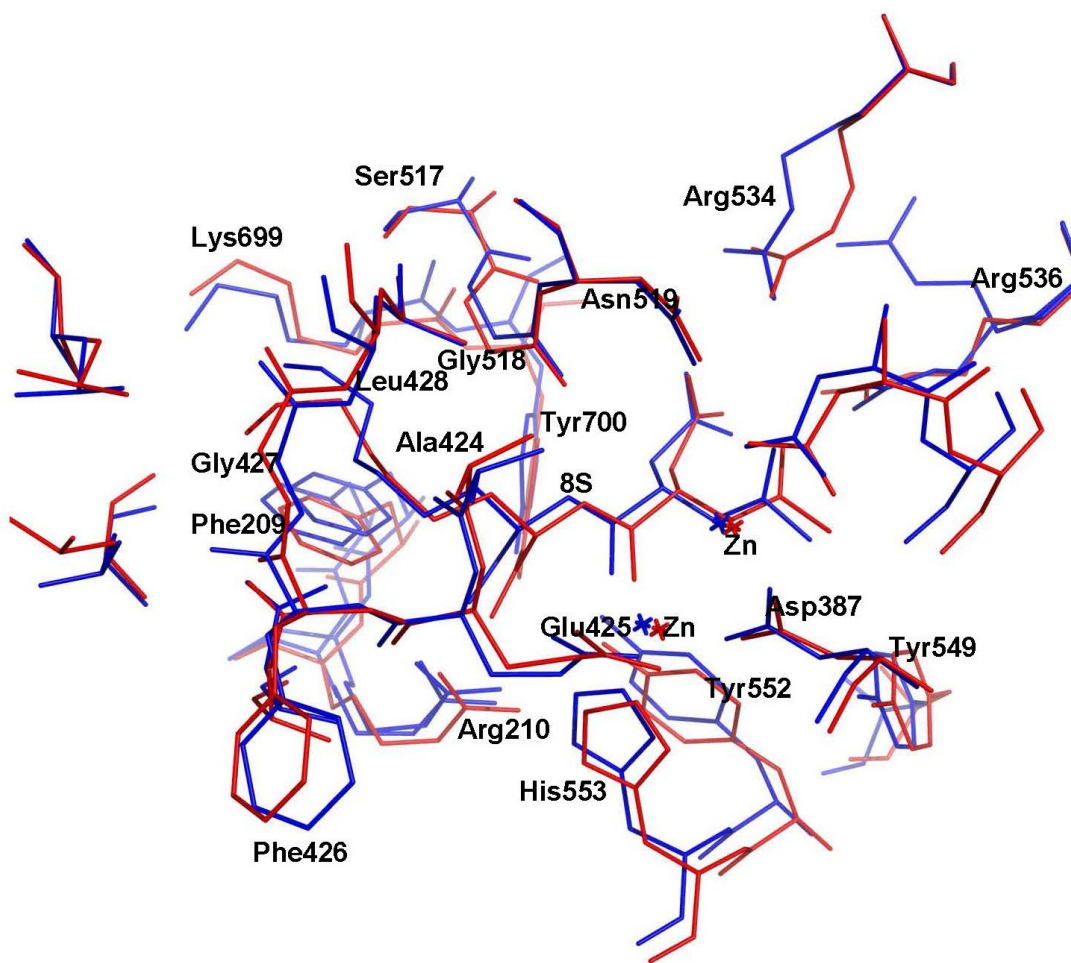
Reference List

5

1. Ryde, U. The coordination of the catalytic zinc ion in alcohol dehydrogenase studied by combined quantum-chemical and molecular mechanics calculations. *Journal of Computer-Aided Molecular Design* **1996,** *10,* 153-164.
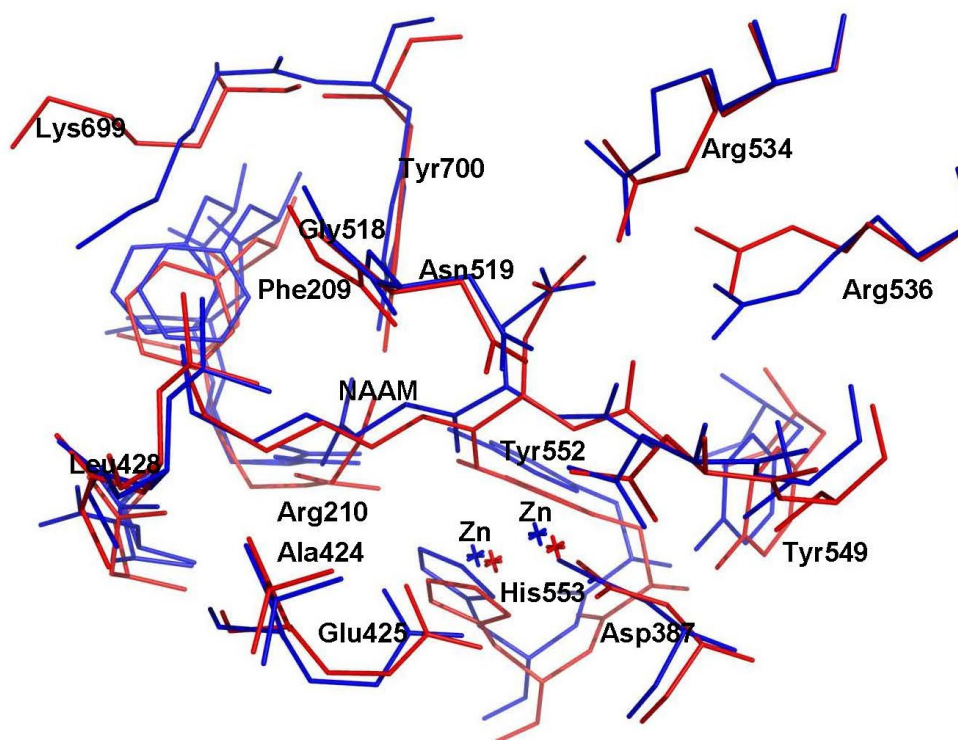
6
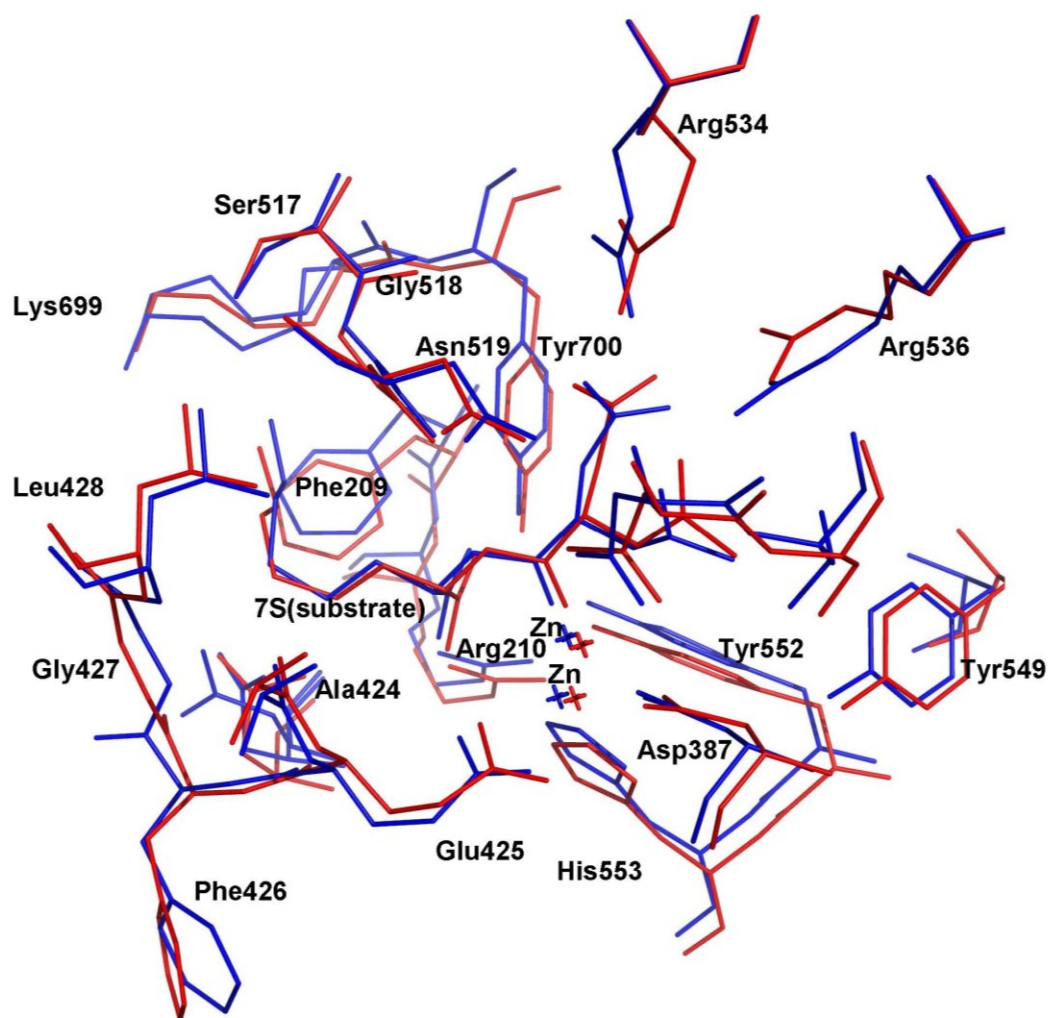
a
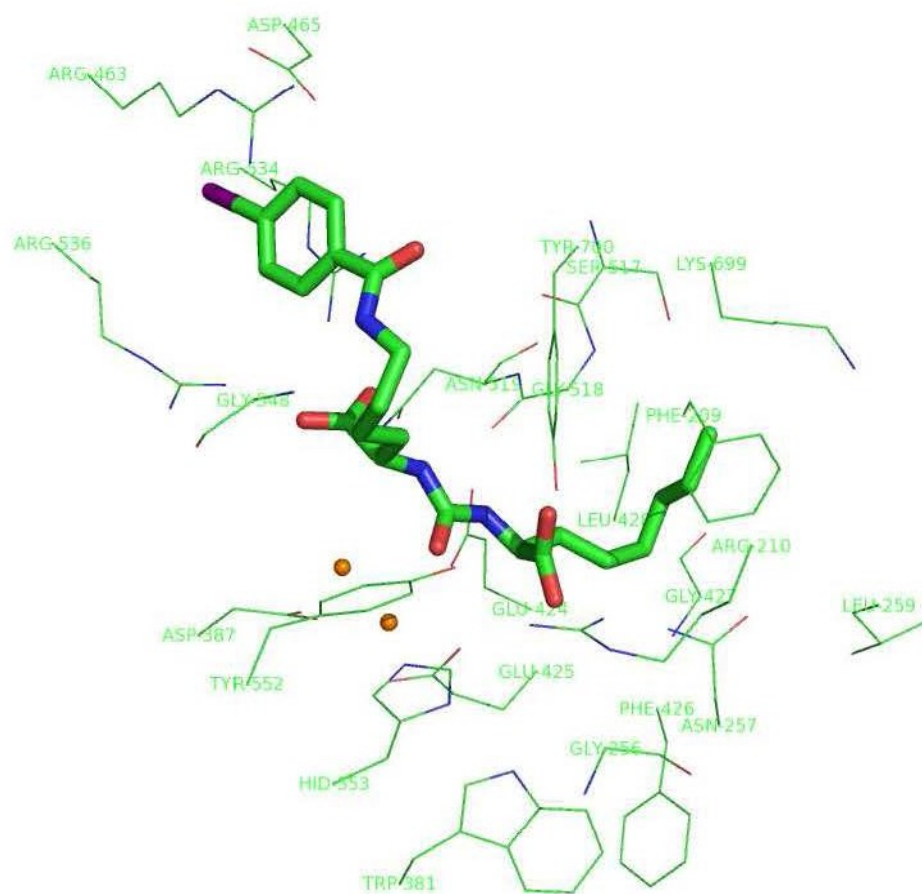
b

c

Figure S1: The superposition of the QM/MM optimized (red) and experimental (blue) crystal structures: (a) GCPII/**7S**, (b) GCPII/**8S**, (c) GCPII/**NAAM** complexes. For the GCPII/**8S** complex, two conformers of Arg536 are depicted in the experimental structure, whereas the QM/MM optimized corresponds to only one orientation.

9

Figure S2: The QM/MM optimized structure of the GCPII/**I7** complex. The **I7** inhibitor is shown in stick representation and GCPII residues within 4Å as lines. Zinc atoms are shown as orange spheres and individual atoms colored green (carbon), blue (nitrogen), red (oxygen), and purple (iodine). Hydrogen atoms and water molecules were omitted for clarity.

10
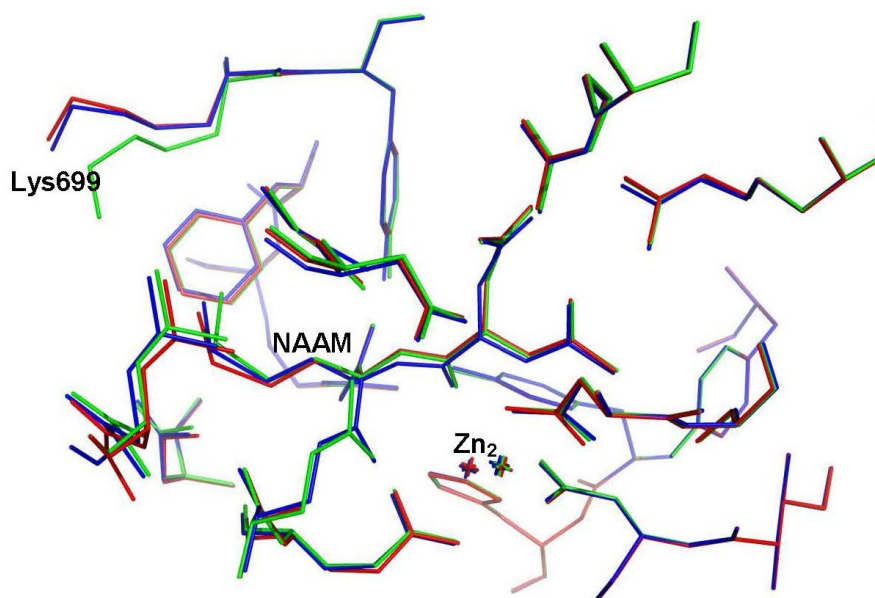
Figure S3: The superposition of the QM/MM optimized structures of the GCPII/**NAAM** complex for the wild-type GCPII with Glu424 deprotonated (blue), the E424A mutant, also with Glu424 deprotonated (red) and wild-type GCPII with the Glu424 protonated (green). The movement of the Lys699 side chain (1.9 Å) upon very small perturbation of the active site (protonation of Glu424) clearly demonstrates its high flexibility.

11
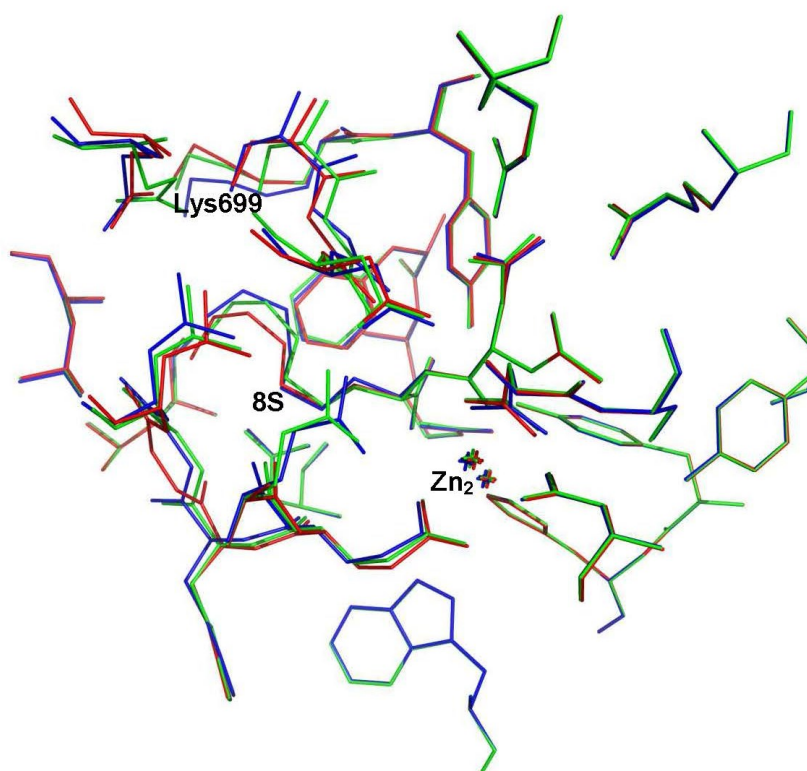
Figure S4: The superposition of the QM/MM optimized structures of the GCPII/**8S** complex for the wild-type GCPII with Glu424 deprotonated (blue), the E424A mutant, also with Glu424 deprotonated (red) and wild-type GCPII with the Glu424 protonated (green).

12
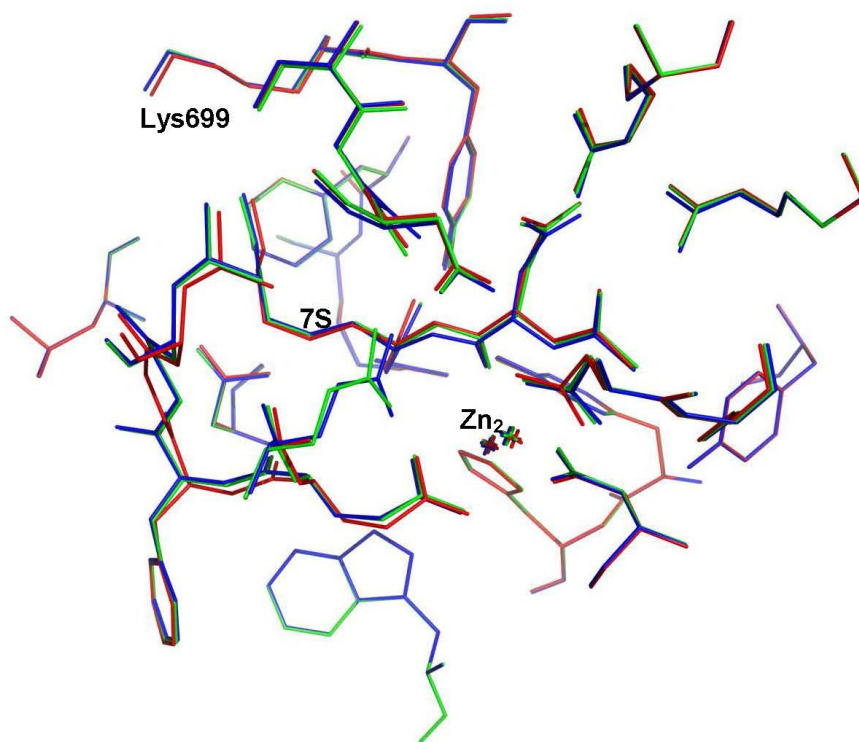
Figure S5: The superposition of the QM/MM optimized structures of the GCPII/**7S** complex for the wild-type GCPII with Glu424 deprotonated (blue), the E424A mutant, also with Glu424 deprotonated (red) and wild-type GCPII with the Glu424 protonated (green).

13

Publication II: Structural characterization of P1'-diversified urea-based inhibitors of glutamate carboxypeptidase II.

BACKGROUND:

Targeting GCPII to treat neuropathologies has been hindered by a lack of drugs capable of crossing the blood brain barrier. DCIBzL is to date the most potent urea based GCPII inhibitor [54]. However, it is too hydrophilic to be used as a CNS drug. Wang *et al*., 2010, [207] synthesized and tested 20 DCIBzL derivatives. They preserved the 4-iodobenzoyl-ε-lysine moiety of the parental DCIBzL as its interactions with the hydrophobic patch accessory to the S1 binding site contribute substantially to DCIBzL inhibitory potency. To increase lipophilicity of the parent molecule, they replaced the P1' glutamate with bioisosteric functions. While new compounds were somewhat less potent inhibitors than DCIBzL, several of them still retained *Ki* in the low nanomolar range. Moreover, the new inhibitors were more lipophilic, indicating the modifications were a step in the right direction. Our follow-up publication consists of structure–activity relationship study of 6 of these compounds in complex with GCPII. Our goal is to analyze the interactions of bioisosteric moieties at the P1' position in the S1' pocket of GCPII.

METHODS:

Extracellular portion of hGCPII (amino acids 44-750) was expressed in S2 cells. The protein was purified to homogeneity by a combination of affinity and size exclusion chromatography. Hanging drop method was used to co-crystallize GCPII with the tested inhibitors. X-ray diffraction data were collected at a synchrotron beamline and processed using the HKL2000 software. The crystal structures of GCPII with the inhibitors studied were determined by difference Fourier methods using the ligand free GCPII structure (PDB code 2OOT) as a starting model. All of the structures were refined in REFMAC5.5 with manual changes performed in Coot 0.6. The restrains library and the coordinate files for the inhibitors were generated by the PRODRUG server. Finally, quantum mechanics calculations were performed to determine contribution of the individual parts of the inhibitors to GCPII binding.

RESULTS:

We characterized in detail interaction patterns of glutamate bioisosteres with the residues forming the S1' pocket of GCPII and described for the first time the structural plasticity of the S1'. Flexibility and repositioning of several structural elements within the S1' pocket, including the Lys699 of the glutarate sensor, the Leu259 – Gly263 loop (forming the bottom of the pocket) and the side chain of Asn256 enable the enzyme to accommodate bioisosteres with diverse physicochemical properties that can be used in the design of the future generation of GCPII inhibitors.

CONCLUSION:

Our analysis of the interactions of GCPII and inhibitors with the P1' glutamate replaced by bioisosteric moieties revealed unexplored plasticity of the S1' pocket. This information is potentially valuable for rational design of new hydrophobic GCPII inhibitors in which the glutamate moiety at the P1' position would be replaced.

MY CONTRIBUTION:

I determined, refined and analyzed the structure of two of the six compounds tested in complex with the GCPII. GCPII/CCIBzL was submitted in the RCSB database as PDB 4OC0 and GCPII/CPIBzL as 4OC4.

Structural characterization of P1′-diversified urea-based inhibitors of glutamate carboxypeptidase II

CrossMark

Jiri Pavlicek [a], Jakub Ptacek [a], Jiri Cerny [a], Youngjoo Byun [b,c], Lubica Skultetyova [a], Martin G. Pomper [b], Jacek Lubkowski [d], Cyril Barinka [a,*]

[a] Institute of Biotechnology, Academy of Sciences of the Czech Republic, v.v.i., Laboratory of Structural Biology, Vídeňská 1083, 14220 Prague 4, Czech Republic
[b] Russell H. Morgan Department of Radiology and Radiological Science, Johns Hopkins Medical Institutions, 1550 Orleans Street, Baltimore, MD 21231, USA
[c] College of Pharmacy, Korea University, 2511 Sejong-ro, Sejong 339-700, South Korea
[d] Center for Cancer Research, Frederick National Laboratory for Cancer Research, Macromolecular Crystallography Laboratory, Frederick, MD 21702, USA

ABSTRACT

Urea-based inhibitors of human glutamate carboxypeptidase II (GCPII) have advanced into clinical trials for imaging metastatic prostate cancer. In parallel efforts, agents with increased lipophilicity have been designed and evaluated for targeting GCPII residing within the neuraxis. Here we report the structural and computational characterization of six complexes between GCPII and P1′-diversified urea-based inhibitors that have the C-terminal glutamate replaced by more hydrophobic moieties. The X-ray structures are complemented by quantum mechanics calculations that provide a quantitative insight into the GCPII/inhibitor interactions. These data can be used for the rational design of novel glutamate-free GCPII inhibitors with tailored physicochemical properties.

© 2014 Elsevier Ltd. All rights reserved.

Urea-based small-molecule inhibitors targeting human glutamate carboxypeptidase II (GCPII) were originally developed for application within the central nervous system (CNS), however, they were first used in vivo to image a peripheral version of GCPII known as the prostate-specific membrane antigen (PSMA) and prostate cancer (PCa).[1–3] GCPII/PSMA (referred to throughout as GCPII) is now a well-established biomarker for imaging PCa, as this membrane-tethered metallopeptidase is over-expressed on the surface of castrate-resistant prostate tumors with its active site facing the extracellular milieu. Additionally, GCPII expression in the neovasculature of most solid tumors, but not normal vasculature, expands the utility of the enzyme for imaging/therapy of tumors other than prostate.[4] In the nervous system, GCPII cleaves *N*-acetylaspartylglutamate (NAAG), releasing *N*-acetylaspartate and glutamate. Excessive glutamate production and release may overstimulate several glutamate receptor subtypes and lead to

glutamate-associated neurotoxicity. Furthermore, a glutamate imbalance is linked to the pathophysiology of certain neurological diseases including schizophrenia, amyotrophic lateral sclerosis, neuropathic/diabetic pain and ischemia. Given the involvement of GCPII in a glutamate metabolism, inhibition of GCPII can be used as a therapeutic option for the prevention and treatment of neurological disorders as documented in several animal models of aforementioned diseases.[5]

Imaging agents targeting GCPII can be divided into three categories that include antibodies, aptamers and small-molecule ligands. Currently, only ProstaScint®, an ^{111}In-labeled monoclonal antibody, has been approved by the FDA and is used clinically for imaging PCa, although with variable degrees of success.[6] Because of the long biological half-life of antibodies, leading to excessive non-specific binding, several small-molecule ligands have recently entered clinical trials as viable alternatives for imaging PCa.[7,8] Typically, GCPII inhibitors for imaging applications are derivatives of NAAG with the principal C-terminal (P1′) docking glutamate moiety and the distal (P1) moiety that fine-tunes inhibitor affinity towards GCPII and harbors a radioactive or fluorescent tracer. The P1 and P1′ functionalities are connected via a zinc-binding group (ZBG), resistant to hydrolysis. The most common ZBGs are

---

phosphonates, phosphinates, phosporamidates, and ureas, with the latter being closest to become human medicines.[9–13]

Inhibitors of GCPII that target the CNS or peripheral nervous system, show promise in various animal models of neurological disorders.[14,15] For example, 2-phosphonomethylpropanedioic acid (2-PMPA), a phosphonate-based picomolar GCPII inhibitor, was used successfully to provide neuroprotection following middle cerebral artery occlusion, attenuate cocaine/ethanol-induced drug-seeking behavior, and alleviate hyperalgesia/allodynia in rat pain models.[16–18] The urea-based GCPII inhibitor, ZJ-43, was effective in several pain as well as brain and spinal cord injury models.[18,19] The main pitfall associated with a use of NAAG-based or glutamate-based inhibitors is their high polarity, which stems from the presence of the C-terminal glutamate moiety. In consequence, such inhibitors poorly penetrate the blood–brain barrier (BBB) and their efficacy is limited. Several strategies are being developed to address that problem, including a use of lipophilic prodrugs and the substitution of the P1′ glutamate with a less polar functionality.[20–22]

Recently, we have published a comprehensive study of structure–activity relationship (SAR), in which we described modifications of the urea-based inhibitor, DCIBzL [compound (**7**)], at the P1′ glutamate.[23] The aim of that study was to map the specificity of the S1′ pocket in GCPII towards non-glutamate moieties. We have showed that a variety of isosteres in the P1′ position is tolerated by the enzyme, however, substitution of the C-terminal glutamate inevitably leads to a decrease in inhibitor affinity by several orders of magnitude. Despite that drop in potency, the most potent isosteres still displayed low-nanomolar inhibition constants and were suitable for imaging GCPII-positive peripheral tumors in mice. Retention of high affinity combined with a significant increase in lipophilicity of the new isosteres suggest that further optimization of a functionality placed at the P1′ position might provide BBB-penetrable compounds.

Here, we present the follow-up report, detailing interactions between GCPII and a series of six selected isosteres of (**7**) in the P1′ position. By the combination of X-ray crystallography and quantum mechanics (QM) calculations, we aim to increase an understanding of interactions between non-glutamate moieties in the P1′ position of an inhibitor and the S1′ pocket of the enzyme. We selected six compounds to encompass a diversity of isosteres that span affinities for GCPII across two orders of magnitude (Fig. 1). Included are the most potent isosteres (**6**), K_i = 5.3 nM, and (**1**), K_i = 5.3 nM, representing an unsaturated linear chain and a five-membered heteroaromatic ring, respectively, less active (**4**), K_i = 105 nM, and (**2**), K_i = 85 nM, featuring six-membered aromatic rings, and finally, high nanomolar (**3**), K_i = 318 nM, and (**5**), K_i = 254 nM, three-membered ring compounds. Additionally, we included the parent molecule (**7**), featuring a glutarate moiety at P1′ with K_i = 10 pM. Based on previous SAR and structural reports, all compounds have a P1′ configuration corresponding to L-glutamate, with the exception of (**3**), which has no stereogenic center at the P1′ position. The L-stereoisomers typically bind to GCPII with affinities that are several orders of magnitude higher than their D-counterparts, which are unlikely to generate lead compounds. Additionally, excluded were inhibitors lacking the P1′ side chain altogether (i.e., glycine in the P1′) or missing the α-carboxylate functionality of the P1′ moiety. Interactions between the latter and the guanidinium group of Arg210 from GCPII were shown to be crucial to retain affinity to GCPII in both SAR and mutagenesis studies.[23,24]

Crystallization experiments were carried out using an extracellular part of human GCPII (amino acids 44–750) that was heterologously expressed in *Drosophila* S2 cells and purified to homogeneity according to established protocols.[25] Following the final size-exclusion purification step, the protein was concentrated

to 10 mg/mL (in 20 mM Tris–HCl, 150 mM NaCl, pH 8.0), flash-frozen in liquid nitrogen and kept at −80 °C until further use.

Diffracting crystals of GCPII/inhibitor complexes were obtained by first preparing a mixture of GCPII and a given inhibitor [mixing stock solution of GCPII (10 mg/mL) and inhibitor (20 mM) at 9:1 (v/v) ratio] and then mixing the GCPII/inhibitor solution with the same volume of the reservoir solution [33% pentaerythritol propoxylate (Sigma), 1.5% polyethylene glycol 3350 (Sigma), and 100 mM Tris–HCl, pH 8.0]. Crystals were grown using the hanging-drop vapor-diffusion setup at 293 K and diffraction intensities for each complex were collected from a single crystal at 100 K using synchrotron radiation at the SER-CAT beamlines 22-ID and 22-BM at the Advanced Photon Source (Argonne, USA). For each complex, a complete dataset was collected from a single crystal and data were processed using the HKL2000 software package.[26] Difference Fourier methods were used to determine structures of GCPII/inhibitor complexes with the ligand-free GCPII structure (PDB code 2OOT)[27] used as a starting model. Calculations were performed using the program Refmac 5.5.[28] and the structural refinement was interspersed by manual corrections to the model with aid of the program Coot 0.6.[29] The PRODRG server was used to generate the restrains library and the coordinate files for individual inhibitors.[30] Detailed procedures, the data collection and refinement statistics are summarized in Supplementary Table S1. Atomic coordinates of the present structures together with the experimental structure factor amplitudes were deposited at the RCSB Protein Data Bank under accession numbers shown in Figure 1.

Structures of GCPII/inhibitor complexes were refined at the resolution range between 1.65 and 1.85 Å, with suitable crystallographic parameters (Table S1). The overall fold of the protein component is nearly invariant as reflected by the maximum root mean square deviation of 0.16 Å for the 683 equiv Cα pairs between GCPII/(**1**) and GCPII/(**2**) complexes. During the final stages of refinement, inhibitors were modeled into the well-defined Fo–Fc positive density peaks with high confidence for all six inhibitors (Fig. 1).

The 4-iodobenzoyl-ε-lysine, which is derived from the parent DCIBzL (**7**) molecule, is a structural motif common to all inhibitors presented here. This motif was included in the inhibitor design as its addition increases the affinity of a given compound nearly tenfold compared to urea-based scaffolds lacking this functionality.[31] That effect results primarily from the engagement of the terminal 4-iodobenzoyl group with an S1 hydrophobic 'accessory pocket' of GCPII shaped by the side chains of Glu457, Arg463, Asp465, Arg534, and Arg536. As expected, all structures feature the 4-iodobenzoyl group inserted into the pocket. The benzene ring of the inhibitor is parallel to guanidinium groups of Arg463 and Arg534, highlighting the importance of π-cation interaction for the inhibitor binding.

The lysine linker connecting the distal 4-iodobenzoyl functionality to the urea isostere is somewhat flexible, yet its conformation is constrained by the invariant positioning of the 4-iodobenzoyl group at one end and the urea at the other. Moreover, the P1 carboxylate group forms hydrogen bonds with side-chains of Asn519 (2.9 Å; in GCPII/(**6**) complex), Arg534 (2.9 Å), and Arg536 (2.9 Å and 3.0 Å), adding additional constraints. The P1 carboxylate has been reported to be an important signature of the NAAG-based inhibitors as its absence or substitution results in a weaker binding to GCPII.[23,32]

Similar to structures of urea-based inhibitors described previously,[31,33] the ureido group of the six inhibitors studied here mimics a planar peptide bond of a GCPII substrate and interacts with several residues in the active site. The ureido carbonyl oxygen is polarized by the catalytic Zn ion (2.7 Å) and also interacts with side chains of Tyr552 (OH, 2.6 Å) and His553 (Nε2, 3.2 Å), and with the hydroxide anion (2.9 Å). The N1 and N2 ureido nitrogen atoms
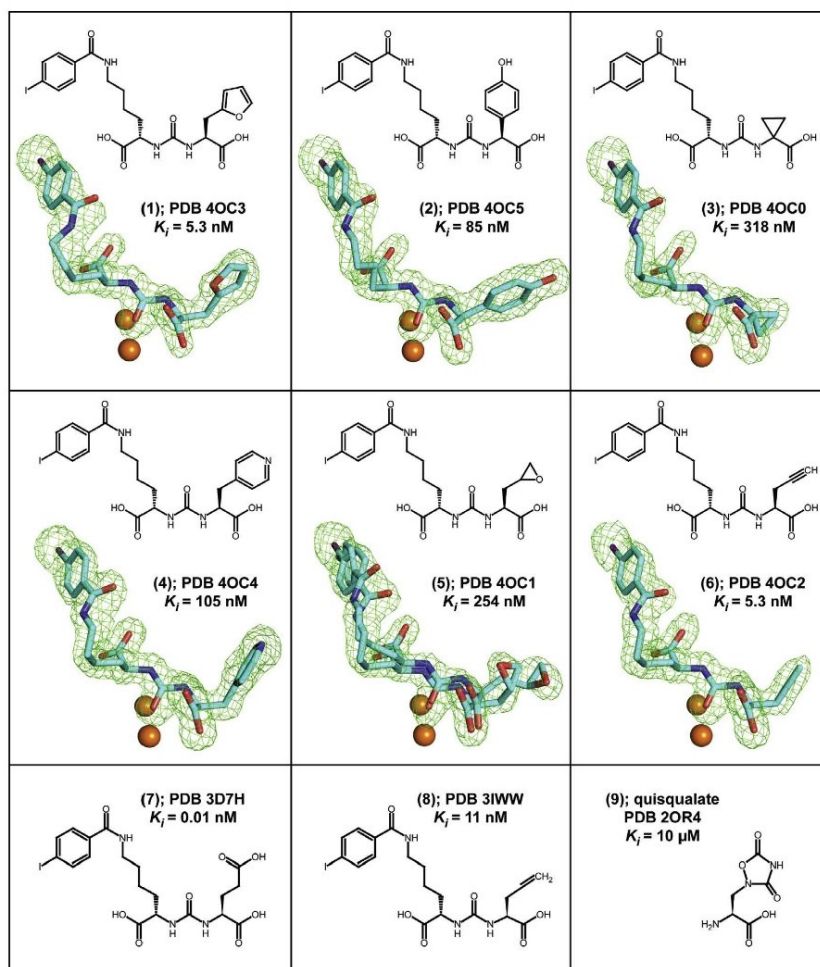
Figure 1. Chemical formulas, PDB codes, and inhibition constants of inhibitors used in this study. Fo–Fc maps (green) for individual inhibitors are contoured at 3.0 σ and modeled inhibitors are shown in stick representation with atoms colored cyan (carbon), red (oxygen), blue (nitrogen), and violet (iodine). The active-site zinc ions are shown as orange spheres.

form pairs of hydrogen bonds with the Gly518 main-chain carbonyl (3.0 Å) and the Glu424 γ-carboxylate (Oɛ2, 3.1 Å), and with the Gly518 carbonyl oxygen (2.9 Å) and the hydroxide anion (3.2 Å), respectively.

Glutarate functionality at the P1′ (C-terminal) position is a hallmark of virtually all GCPII inhibitors.[10] As the S1′ pocket of the enzyme is fine-tuned for glutamate binding, the presence of P1′ glutamate ensures high affinity of the inhibitor and its specificity towards GCPII (and orthologous GCP3[34]). Yet, isostere replacements of the P1′ glutamate are possible, primarily to increase the lipophilicity of an inhibitor with the aim to facilitate passive diffusion across biological membranes, including the BBB.[22,23]

Both structure–activity relationships (SAR) and site-directed mutagenesis studies indicate the P1′ α-carboxylate function of an inhibitor as an element prominently contributing to affinity towards GCPII. That contribution is realized via interactions with Arg210 of the enzyme. A role of that interaction is well-illustrated by a decrease of approximately five orders of magnitude in IC_{50} of 2-PMPA in the case of an Arg210Ala mutant as compared to the wild-type enzyme,[24,35] as well as in a setup pairing the wild-type GCPII with an inhibitor missing the α-carboxylate.[23] Consequently, all inhibitors in this study feature the α-carboxylate function that predictably engages the guanidinium group of Arg210 and forms additional hydrogen bonds with an invariant water molecule (2.5 Å) and the hydroxyl groups of Tyr552 (3.4 Å) and Tyr700 (2.6 Å).

Although the S1′ pocket of GCPII is evolutionarily optimized for the binding of the glutamate moiety and structurally can be viewed as more rigid compared to the S1 pocket, we have recently observed limited plasticity of the S1′ pocket that allows for non-glutamate functionalities. Those limited variations in the shape of the S1′ pocket are permitted by the flexibility of the Asn257 side

69

chain,[35] the swinging motion of Lys699,[22] and repositioning of the Leu259-Gly263 amino acid stretch closing the bottom of the S1′ pocket.[23] Concurrently, fixed conformations of side chains in Phe209 and Leu428 define the width of the S1′ pocket, represented by an approximate distance of 8.2 Å between the Leu428 Cβ and Phe209 Cζ atoms. The rigidity of the S1′ pocket limits the orientation and size of side chains that can be placed on the P1′ portion of the inhibitor (but see below).

In structures presented here the major re-arrangement of the S1′ pocket is observed in the GCPII/(6) complex. In that complex, the Leu259-Gly263 amino acid stretch is repositioned from the 'canonical' conformation by 3.1 Å (as measured for the Cα of Leu261), resulting in a smaller S1′ pocket (Fig. 2B). That change is accompanied by the relocation of the Lys699 side chain, represented by the 7.3 Å shift of the Nζ atom, to avoid clash with the Leu261 side chain. It is noteworthy that a similar re-arrangement was observed by us previously for GCPII/(8).[23] Therefore, those conformational adjustments reflect the inherent plasticity of the S1′ pocket of GCPII, not a crystallization artifact. On the other hand, small molecules featuring longer aliphatic side-chains of the terminal moiety, as opposed to the short alkenes/alkynes reported here, can be accommodated by the S1′ pocket with conformational changes limited only to the side chain of Lys699.[22] Furthermore, flexibility of the Leu259-Gly263 segment is observed in nearly all

structures of GCPII and is reflected by elevated B-factors and inferior electron density as compared to other regions of the enzyme.

Several GCPII inhibitors harbor five- or six-membered rings at the P1′ position. Those include (1), (2) and (4), reported here as well as quisqualate (9) a natural glutamate isostere, reported previously (PDB code 2OR4).[35] Unexpectedly and somewhat counter-intuitively, the planar rings of the different inhibitors assume orientations that differ by up to 70° from each other (Fig. 2C). Apparently, the positioning of the ring planes is determined by (i) chemical composition of the ring, (ii) interactions of the ring with the reminder of the inhibitor molecule, and (iii) interactions of the ring and its substituents with the enzyme. The plane of the quisqualate oxadiazolidine ring is placed parallel to side-walls of the S1′ pocket, the latter defined by the side chains of Phe209 and Leu428. Previously, we proposed that more extensive van der Waals interactions between quisqualate and side chains of Phe209 and Leu428, as compared to the glutamate isostere, may be associated with higher affinity of the former towards GCPII.[35] Interestingly, the plane of the pyridine ring in (4) is oriented at a 70° angle compared to the oxadiazolidine ring, positioning it nearly perpendicular to the 'side walls' of the S1′ pocket. Such an orientation of the pyridine ring leads to an expansion of the S1′ pocket, realized by the increase of the distance between side chains of Phe209 and Leu428 by approximately 1.0 Å. The ring orientations
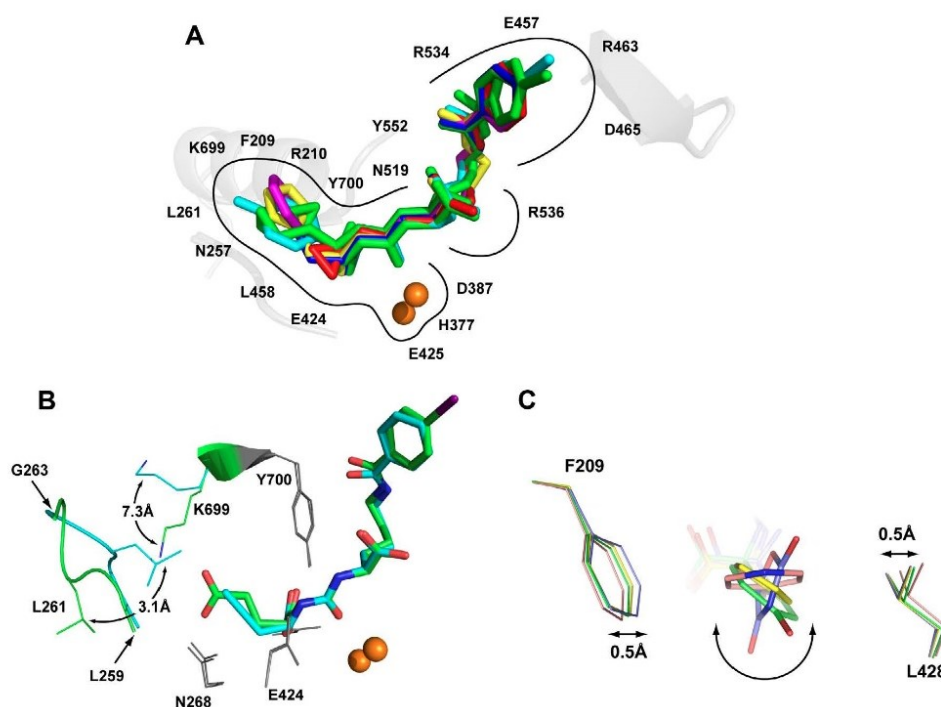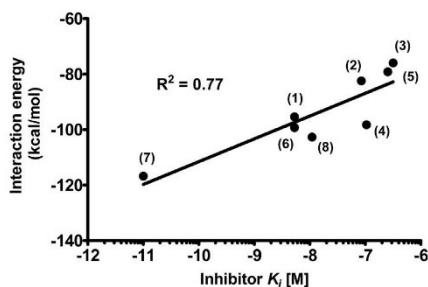

Figure 2. Panel A: The superposition of the active-site bound inhibitors. Complexes of GCPII/inhibitor were superimposed on corresponding Cα atoms of the enzyme. Individual inhibitors are colored yellow, cyan, red, magenta, green, and blue for (1), (2), (3), (4), (5), and (6), respectively. The zinc ions are shown as orange spheres. Panel B: Re-arrangement within the S1 pocket of GCPII induced by the inhibitor binding. Structures of GCPII/(6) (cyan) and GCPII/(7) (PDB code 3D7H; green) were superimposed on corresponding Cα atoms of the enzyme. The active site-bound inhibitors are shown in stick representation, while selected residues forming the S1′ site of the enzyme are shown as lines, the active-site zinc ions as spheres, and the Leu259-Gly263 loop in the cartoon representation. Notice the repositioning of the Leu261 side chain (3.1 Å for Cα's) accompanied by the swing motion of the Lys699 (7.3 Å for the Nζ). Positions of remaining residues forming the S1′ pocket are unchanged (grey). Panel C: Conformations of ring functionalities of inhibitors in the S1′ pocket. Complexes of GCPII/(2) (green), GCPII/(4) (pink), GCPII/(1) (yellow), and GCPII/(9) (blue) were superimposed on corresponding Cα atoms of the enzyme. The active site-bound inhibitors are shown in stick representation, while Phe209 and Leu428, the two residues defining the side-walls of the S1′ pocket, are shown as lines. The quisqualate oxadiazolidine ring is placed virtually parallel to the walls of the S1 pocket, while the plane of the (4) pyridine ring is rotated by 70°. This orientation brings about the increase in the Phe209-Leu428 side chain spacing by approximately 1.0 Å.

in the two remaining complexes, (**1**) and (**2**), are between the two extremes, and side chains of Phe209 and Leu428 have conformations as in the GCPII/(**9**) (quisqualate) complex, that is, corresponding to a compact S1′ pocket.

To gain a quantitative description of contributions by individual parts of inhibitors to GCPII binding and to elucidate the role of (de)solvation in complex formation, we performed detailed QM calculations for individual structures and compared results with those obtained for the parent (**7**) (DClBzL) complex. Initial geometries of the GCPII/ligand complexes were taken from individual crystal structures. The protein residues, water molecules, and ions located within 10 Å from the ligand atoms were selected using the VMD program.[36] The radius of 10 Å was necessary to obtain a satisfactory correlation between experimental inhibition values and calculated interaction energies (Fig. 3). In the initial calculations, we included only the elements of the enzyme located within a distance of 4 Å from the ligand, which allowed for the description of the system at a higher level of theory. However, for the 4 Å radius, energies calculated by PM7 and DFT-D,[37] equivalent to TPSS[38]/TZVP[39] with corrections for the dispersion and higher order correlation effects, did not correlate well with the experimental data.

Hydrogen atoms were added to experimental structures and their positions were optimized using the semi-empirical method PM7[40] as implemented in the MOPAC2012 package.[41] The geometry of the entire model was partially relaxed using the same method combined with the 'geo_ref' keyword and the proportionality constant equal to 10. Water molecules, with the exception of the hydroxide anion shared by the two active-site zinc ions, were removed and the PM7 interaction energy was calculated using implicit solvation in MOPAC2012. The implicit solvation is preferable as different resolutions of individual structures resulted in different numbers of experimental water molecules, from 29 (GCPII/(**8**)complex) to 56 (GCPII/(**7**)), found inside the region defined by the 10-Å selection radius.

Finally, the calculated interaction energies were correlated with $\log(K_i)$ and the result is shown in Figure 3. Calculated and experimental energies correlated reasonably well with the R^2 value for least square linear fit equal to 0.77. In an attempt to improve further the correlation coefficient, we included the effects of the solvation free energy of ligands using COSMO calculations. We also accounted for the deformation energy, resulting from the geometry change induced by the binding of ligands to the binding pocket of GCPII. However, the inclusion of any of those contributions did not lead to an improvement in correlation. Although we succeeded in correlating the overall interaction energy with the experimental data, attempts to partition the energy and identify (de)stabilizing contributions of groups of residues showed poor additivity of energy, making interpretation unreliable, especially at the level of individual amino acid residues. Only a weak correlation ($R^2 = 0.54$) was found for the interaction of the ligands with the active site zinc alone ($2 \times Zn^{2+} + OH^-$). Our findings reflect the generally accepted notion that QM calculations for zinc-containing systems are very challenging, even when extensive experimental information is available.[42]

In conclusion, here we extend a structural insight into the S1′ pocket of GCPII. Our data reveal previously unreported plasticity of the S1′ site, a property required to accommodate bulkier functionalities at the P1′ position of an inhibitor. These findings will be valuable for the rational design of novel GCPII inhibitors with non-glutamate moieties at the P1′ position, eventually enabling compounds that cross the BBB.

PDB ID codes: Atomic coordinates of the present structures together with the experimental structure factor amplitudes were deposited at the RCSB Protein Data Bank under accession numbers 4OC3 (complex with (**1**)), 4OC5 (complex with (**2**)), 4OC0 (complex with (**3**)), 4OC4 (complex with (**4**)), 4OC1 (complex with (**5**)), and 4OC2 (complex with (**6**)).

Acknowledgments

Supplementary data

Supplementary data associated with this article can be found, in the online version, at http://dx.doi.org/10.1016/j.bmcl.2014.03.066.

References and notes

1. Foss, C. A.; Mease, R. C.; Fan, H.; Wang, Y.; Ravert, H. T.; Dannals, R. F.; Olszewski, R. T.; Heston, W. D.; Kozikowski, A. P.; Pomper, M. G. *Clin. Cancer Res.* **2005**, *11*, 4022.
2. Nan, F.; Bzdega, T.; Pshenichkin, S.; Wroblewski, J. T.; Wroblewska, B.; Neale, J. H.; Kozikowski, A. P. *J. Med. Chem.* **2000**, *43*, 772.
3. Pomper, M. G.; Musachio, J. L.; Zhang, J.; Scheffel, U.; Zhou, Y.; Hilton, J.; Maini, A.; Dannals, R. F.; Wong, D. F.; Kozikowski, A. P. *Mol. Imaging* **2002**, *1*, 96.
4. Chang, S. S.; Reuter, V. E.; Heston, W. D.; Bander, N. H.; Grauer, L. S.; Gaudin, P. B. *Cancer Res.* **1999**, *59*, 3192.
5. Barinka, C.; Rojas, C.; Slusher, B.; Pomper, M. *Curr. Med. Chem.* **2012**, *19*, 856.
6. Taneja, S. S. *Rev. Urol.* **2004**, *6*, S19.
7. Mease, R. C.; Foss, C. A.; Pomper, M. G. *Curr. Top. Med. Chem.* **2013**, *13*, 951.
8. Afshar-Oromieh, A.; Malcher, A.; Eder, M.; Eisenhut, M.; Linhart, H. G.; Hadaschik, B. A.; Holland-Letz, T.; Giesel, F. L.; Kratochwil, C.; Haufe, S.; Haberkorn, U.; Zechmann, C. M. *Eur. J. Nucl. Med. Mol. Imaging* **2013**, *40*, 486.
9. Banerjee, S. R.; Pullambhatla, M.; Byun, Y.; Nimmagadda, S.; Green, G.; Fox, J. J.; Horti, A.; Mease, R. C.; Pomper, M. G. *J. Med. Chem.* **2010**, *53*, 5333.
10. Ferraris, D. V.; Shukla, K.; Tsukamoto, T. *Curr. Med. Chem.* **2012**, *19*, 1282.
11. Kozikowski, A. P.; Nan, F.; Conti, P.; Zhang, J.; Ramadan, E.; Bzdega, T.; Wroblewska, B.; Neale, J. H.; Pshenichkin, S.; Wroblewski, J. T. *J. Med. Chem.* **2001**, *44*, 298.

Figure 3. The correlation between the calculated interaction energies and experimental inhibition constants. The PM7 interaction energy was calculated using implicit solvation in MOPAC2012 with the initial geometries of GCPII/ligand complexes taken from individual crystal structures. Calculated interaction energy and experimental inhibition constants correlate with the R^2 value for the least square linear fit equal to 0.77. Corresponding compound descriptors are attached to each individual experimental data point.

Table S1: Data Collection and Refinement Statistics.

Data collection statistics						
Inhibitor	**CHIBzL**	**CFIBzL**	**CCIBzL**	**CPIBzL**	**COIBzL**	**CEIBzL**
Wavelength (Å)	0.979	1.000	0.979	1.000	1.000	1.000
Space group	I222	I222	I222	I222	I222	I222
Unit-cell parameters a, b, c (Å)	a=101.5 b=130.4 c=159.1	a=101.6 b=130.4 c=159.0	a=101.4 b=130.0 c=158.6	a=101.4 b=130.5 c=159.1	a=101.4 b=130.4 c=159.0	a=101.3 b=130.2 c=159.1
Resolution limits (Å)	30.0 – 1.70 (1.73 – 1.70)*	30.0 – 1.79 (1.85 – 1.79)	30.0 – 1.85 (1.92 – 1.85)	30.0 – 1.66 (1.72 – 1.66)	30.0 – 1.75 (1.81 – 1.75)	30.0 – 1.65 (1.71 – 1.65)
Number of unique reflections	113311 (4741)	96266 (8274)	89273 (8813)	123183 (11501)	105692 (10417)	124655 (11512)
Redundancy	6.9 (3.4)	4.6 (3.1)	5.6 (5.0)	7.1 (5.6)	7.4 (6.1)	7.1 (4.6)
Completeness (%)	97.9 (82.5)	97.6 (84.8)	99.9 (99.6)	99.3 (93.6)	99.8 (99.0)	99.0 (92.1)
$I/\sigma(I)$	42.4 (2.5)	14.8 (3.8)	20.3 (3.5)	23.8 (2.6)	18.0 (3.3)	16.0 (2.4)
R_{merge}	0.085 (0.513)	0.058 (0.260)	0.065 (0.453)	0.067 (0.480)	0.090 (0.526)	0.085 (0.516)
Refinement statistics						
Resolution limits (Å)	20.0-1.70 (1.74-1.70)	29.5-1.79 (1.84-1.79)	28.5-1.85 (1.90-1.85)	20.0-1.66 (1.70-1.66)	29.5-1.75 (1.80-1.75)	29.5-1.65 (1.69-1.65)
Total number of reflections	111876 (7038)	94638 (7227)	87605 (6248)	121241 (8226)	104328 (7625)	121587 (8055)
Number of reflections in working set	110737 (6962)	93209 (5798)	86286 (6155)	119651 (8125)	103275 (7556)	119093 (7881)
Number of reflections in test set	1139 (76)	1429 (91)	1319 (93)	1590 (101)	1053 (69)	2494 (174)
R	0.170 (0.242)	0.161 (0.214)	0.161 (0.215)	0.159 (0.215)	0.168 (0.240)	0.166 (0.257)
R_{free}	0.204 (0.270)	0.181 (0.259)	0.182 (0.197)	0.191 (0.252)	0.193 (0.266)	0.188 (0.283)

Total number of non-H atoms	6466	6495	6490	6364	6447	6674
Number of non-H protein atoms	5934	6100	6012	5964	5858	6111
Number Inhibitor molecules	1	1	1	1	1	1
Number of water molecules	499	363	450	367	529	534
[#]Average B-factor ($Å^2$)	31.9	29.2	36.4	31.2	28.7	32.0
Protein atoms	31.2	28.8	35.8	30.9	28.0	31.2
Waters	40.6	34.9	44.2	36.6	37.4	40.9
Inhibitor	30.9	32.8	45.0	27.9	23.2	33.3
[&]Ramachandran Plot (%)						
Most favored	97.7	96.9	97.4	97.2	97.4	97.0
Additionally allowed	2.2	2.8	2.2	2.5	2.2	2.7
Disallowed	0.15; Val382	0.3; Val382	0.4; Val382, Trp541	0.3; Val382	0.4; Val382, Ser507	0.3; Glu152, Val382
R.m.s. deviations: bond lengths (Å)	0.019	0.020	0.019	0.016	0.019	0.018
bond angles (°)	1.7	1.7	1.7	1.6	1.7	1.7
planarity (Å)	0.01	0.01	0.01	0.01	0.01	0.01
chiral centers ($Å^3$)	0.13	0.13	0.20	0.11	0.13	0.13

* Values in parenthesis are for the highest resolution shells.

[#] Values obtained using the Baverage program.

[&] Structures were analyzed using the MolProbity package

12. Liu, T.; Wu, L. Y.; Choi, J. K.; Berkman, C. E. *Prostate* **2009**, *69*, 585.
13. Pavlicek, J.; Ptacek, J.; Barinka, C. *Curr. Med. Chem.* **2012**, *19*, 1300.
14. Rahn, K. A.; Slusher, B. S.; Kaplin, A. I. *Curr. Med. Chem.* **2012**, *19*, 1335.
15. Wozniak, K. M.; Rojas, C.; Wu, Y.; Slusher, B. S. *Curr. Med. Chem.* **2012**, *19*, 1323.
16. Slusher, B. S.; Thomas, A.; Paul, M.; Schad, C. A.; Ashby, C. R., Jr. *Synapse* **2001**, *41*, 22.
17. Slusher, B. S.; Vornov, J. J.; Thomas, A. G.; Hurn, P. D.; Harukuni, I.; Bhardwaj, A.; Traystman, R. J.; Robinson, M. B.; Britton, P.; Lu, X. C.; Tortella, F. C.; Wozniak, K. M.; Yudkoff, M.; Potter, B. M.; Jackson, P. F. *Nat. Med.* **1999**, *5*, 1396.
18. Yamamoto, T.; Saito, O.; Aoe, T.; Bartolozzi, A.; Sarva, J.; Zhou, J.; Kozikowski, A.; Wroblewska, B.; Bzdega, T.; Neale, J. H. *Eur. J. Neurosci.* **2007**, *25*, 147.
19. Zhong, C.; Zhao, X.; Sarva, J.; Kozikowski, A.; Neale, J. H.; Lyeth, B. G. *J. Neurotrauma* **2005**, *22*, 266.
20. Feng, J. F.; Gurkoff, G. G.; Van, K. C.; Song, M.; Lowe, D. A.; Zhou, J.; Lyeth, B. G. *Brain Res.* **2012**, *1469*, 144.
21. Feng, J. F.; Van, K. C.; Gurkoff, G. G.; Kopriva, C.; Olszewski, R. T.; Song, M.; Sun, S.; Xu, M.; Neale, J. H.; Yuen, P. W.; Lowe, D. A.; Zhou, J.; Lyeth, B. G. *Brain Res.* **2011**, *1395*, 62.
22. Plechanovova, A.; Byun, Y.; Alquicer, G.; Skultetyova, L.; Mlcochova, P.; Nemcova, A.; Kim, H. J.; Navratil, M.; Mease, R.; Lubkowski, J.; Pomper, M.; Konvalinka, J.; Rulisek, L.; Barinka, C. *J. Med. Chem.* **2011**, *54*, 7535.
23. Wang, H.; Byun, Y.; Barinka, C.; Pullambhatla, M.; Bhang, H. E.; Fox, J. J.; Lubkowski, J.; Mease, R. C.; Pomper, M. G. *Bioorg. Med. Chem. Lett.* **2010**, *20*, 392.
24. Mlcochova, P.; Plechanovova, A.; Barinka, C.; Mahadevan, D.; Saldanha, J. W.; Rulisek, L.; Konvalinka, J. *FEBS J.* **2007**, *274*, 4731.
25. Barinka, C.; Mlcochova, P.; Sacha, P.; Hilgert, I.; Majer, P.; Slusher, B. S.; Horejsi, V.; Konvalinka, J. *Eur. J. Biochem.* **2004**, *271*, 2782.
26. Minor, W.; Cymborowski, M.; Otwinowski, Z. *Acta Phys. Pol., A* **2002**, *101*, 613.
27. Barinka, C.; Starkova, J.; Konvalinka, J.; Lubkowski, J. *Acta Crystallogr., Sect. F: Struct. Biol. Cryst. Commun.* **2007**, *63*, 150.
28. Murshudov, G. N.; Skubak, P.; Lebedev, A. A.; Pannu, N. S.; Steiner, R. A.; Nicholls, R. A.; Winn, M. D.; Long, F.; Vagin, A. A. *Acta Crystallogr. D Biol. Crystallogr.* **2011**, *67*, 355.
29. Emsley, P.; Lohkamp, B.; Scott, W. G.; Cowtan, K. *Acta Crystallogr. D Biol. Crystallogr.* **2010**, *66*, 486.
30. Schuttelkopf, A. W.; van Aalten, D. M. *Acta Crystallogr. D Biol. Crystallogr.* **2004**, *60*, 1355.
31. Barinka, C.; Byun, Y.; Dusich, C. L.; Banerjee, S. R.; Chen, Y.; Castanares, M.; Kozikowski, A. P.; Mease, R. C.; Pomper, M. G.; Lubkowski, J. *J. Med. Chem.* **2008**, *51*, 7737.
32. Barinka, C.; Hlouchova, K.; Rovenska, M.; Majer, P.; Dauter, M.; Hin, N.; Ko, Y. S.; Tsukamoto, T.; Slusher, B. S.; Konvalinka, J.; Lubkowski, J. *J. Mol. Biol.* **2008**, *376*, 1438.
33. Klusak, V.; Barinka, C.; Plechanovova, A.; Mlcochova, P.; Konvalinka, J.; Rulisek, L.; Lubkowski, J. *Biochemistry* **2009**, *48*, 4126.
34. Hlouchova, K.; Barinka, C.; Klusak, V.; Sacha, P.; Mlcochova, P.; Majer, P.; Rulisek, L.; Konvalinka, J. *J. Neurochem.* **2007**, *101*, 682.
35. Barinka, C.; Rovenska, M.; Mlcochova, P.; Hlouchova, K.; Plechanovova, A.; Majer, P.; Tsukamoto, T.; Slusher, B. S.; Konvalinka, J.; Lubkowski, J. *J. Med. Chem.* **2007**, *50*, 3267.
36. Humphrey, W.; Dalke, A.; Schulten, K. *J. Mol. Graphics Modell.* **1996**, *14*, 33.
37. Jurecka, P.; Cerny, J.; Hobza, P.; Salahub, D. R. *J. Comp. Chem.* **2007**, *28*, 555.
38. Tao, J. M.; Perdew, J. P.; Staroverov, V. N.; Scuseria, G. E. *Phys. Rev. Lett.* **2003**, *91*, 146401.
39. Schafer, A.; Huber, C.; Ahlrichs, R. *J. Chem. Phys.* **1994**, *100*, 5829.
40. Stewart, J. J. P. *J. Mol. Model.* **2013**, *19*, 1.
41. Stewart, J. J. P. MOPAC2012, Stewart Computational Chemistry: Colorado Springs, CO, USA, 2012.
42. Raha, K.; Merz, K. M., Jr. *J. Am. Chem. Soc.* **2004**, *126*, 1020.

74

Publication III: Structure-Activity Relationship of (18)F-Labeled Phosphoramidate Peptidomimetic Prostate-Specific Membrane Antigen (PSMA)-Targeted Inhibitor Analogues for PET Imaging of Prostate Cancer.

BACKGROUND:

Imaging methods play an important role in diagnostics and establishment of treatment for cancer patients. GCPII is considered an ideal target for prostate cancer imaging because of its membrane localization, high level of expression, and restricted expression pattern in the prostate cancer tissue. The only antibody-based radiotracer targeting GCPII - ProstaScint - recognizes an epitope within the cytoplasmic part of GCPII which means that it can only serve to visualize necrotic tumor cells. Consequently, small-molecule imaging probes are being developed to target GCPII expressed at the surface of living cancer cells. Previously, we have synthesized a PET imaging agent CTT1057 (compound **5**) that features the aminohexanoate linker (AH) between the GCPII-targeting P1' module and the distal fluorobenzamido (FB) radiotracer. By X-ray crystallography we identified -stacking and π-cationic interactions of the distal FB ring with amino acids forming the arene-binding site (ABS) of the enzyme that can contribute substantially to the overall inhibitor affinity for GCPII. In this report, we modified CTT1057 by removing (**4**) or extending (**6**) the AH linker. Our goal was to study how the length/absence of the linker influences (i) the interaction of the distal FB ring with the ABS of GCPII; and (ii) *in vivo* imaging properties.

METHODS:

The compounds and their radioactive analogues (**4**, **5**, and **6**) were synthesized by coupling phosphoramidate precursors with 4-fluorobenzoate (SFB/[^{18}F]SFB). The extracellular portion of human GCPII (amino acids 44-750) was heterologously expressed in S2 cells and purified by the combination of affinity and size-exclusion chromatography. IC$_{50}$ values were determined using N-[4-(phenylazo)benzoyl]-glutamyl-γ-glutamic acid as a substrate in presence of the inhibitors and the reactions were quantified using HPLC. To determine the crystal structure of complexes of GCPII and the individual compounds, they were co-

crystalized and the X-ray structure solved by difference Fourier methods. Tumor growth in mice was induced by injection of CWR22Rv1 PSMA (+) cells and 4 weeks after implantation the $[^{18}F]$**4**, $[^{18}F]$**5**, and $[^{18}F]$**6** were administered and the PET imaging was performed. For the biodistribution and internalization studies the mice were euthanized, organs and blood harvested and counted using a γ counter.

RESULTS:

The crystal structures of the inhibitors in complex with GCPII reveal their distinct interaction patterns with GCPII, the most notably differences in interactions between the distal FB ring and the ABS site of GCPII. In the GCPII/**4** complex the fluorobenzoyl ring is parallel to the guanidinium group of Arg463 with ensuing weak π-cationic interaction in the ABS, but in compound **5** the FB ring is parallel to indole and guanidinium groups of Trp541 and Arg511 of the ABS, respectively. The density for the distal part of **6** is missing. We have determined the compounds tested to be irreversible inhibitors of GCPII with IC_{50} values of 1.3 nM (**4**), 0.4 nM (**5**), and 0.9 nM (**6**). While the inhibitory potency does not show a trend related to the AH linker, the tumor uptake and internalization studies indicate that these characteristics positively correlate with the AH linker length as the compound **6** (with the longest linker) has exceptionally high uptake with 4.23 % ID/g after 2 hrs.

CONCLUSION:

We have synthesized and characterized a radiotracer (compound **6**) exhibiting, similarly to the parental molecule **5** (CTT1057), exceptional binding, tumor uptake and retention, and blood- to-tumor ratios and characterized its binding to GCPII. We have also determined that the presence of the AH linker positively influences affinity towards GCPII and the tumor uptake in direct proportion to its length.

MY CONTRIBUTION:

I determined, refined and analyzed the structure of the extracellular portion of human GCPII in complex with phosphoramidate inhibitor CTT1056 (**4**) and submitted it to the RCSB database under PDB code 4LQG.

Structure−Activity Relationship of ^{18}F-Labeled Phosphoramidate Peptidomimetic Prostate-Specific Membrane Antigen (PSMA)-Targeted Inhibitor Analogues for PET Imaging of Prostate Cancer

Shorouk Dannoon,[†,⊥] Tanushree Ganguly,[‡,⊥] Hendry Cahaya,[†] Jonathan J. Geruntho,[‡] Matthew S. Galliher,[‡] Sophia K. Beyer,[‡] Cindy J. Choy,[‡] Mark R. Hopkins,[‡] Melanie Regan,[†] Joseph E. Blecha,[†] Lubica Skultetyova,[§] Christopher R. Drake,[†] Salma Jivan,[†] Cyril Barinka,[§] Ella F. Jones,[†,#] Clifford E. Berkman,*[,‡,‖,#] and Henry F. VanBrocklin*[,†,#]

[†]Department of Radiology and Biomedical Imaging, University of California—San Francisco, 185 Berry Street, San Francisco, California 94107, United States

[‡]Department of Chemistry, Washington State University, Pullman, Washington 99164-4630, United States

[§]Institute of Biotechnology, 252 50 Prague, Czech Republic

[‖]Cancer Targeted Technology, Woodinville, Washington 98072, United States

S Supporting Information

ABSTRACT: A series of phosphoramidate-based prostate specific membrane antigen (PSMA) inhibitors of increasing lipophilicity were synthesized (**4**, **5**, and **6**), and their fluorine-18 analogs were evaluated for use as positron emission tomography (PET) imaging agents for prostate cancer. To gain insight into their modes of binding, they were also cocrystallized with the extracellular domain of PSMA. All analogs exhibited irreversible binding to PSMA with IC_{50} values ranging from 0.4 to 1.3 nM. In vitro assays showed binding and rapid internalization (80−95%, 2 h) of the radiolabeled ligands in PSMA(+) cells. In vivo distribution demonstrated significant uptake in CWR22Rv1 (PSMA(+)) tumor, with tumor to blood ratios of 25.6:1, 63.6:1, and 69.6:1 for [18F]**4**, [18F]**5**, and [18F]**6**, respectively, at 2 h postinjection. Installation of aminohexanoic acid (AH) linkers in the phosphoramidate scaffold improved their PSMA binding and inhibition and was critical for achieving suitable in vivo imaging properties, positioning [18F]**5** and [18F]**6** as favorable candidates for future prostate cancer imaging clinical trials.
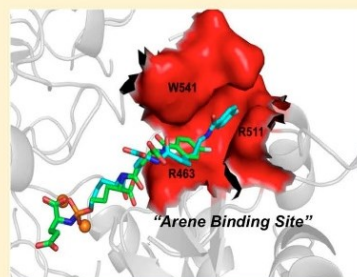
■ INTRODUCTION

Prostate specific membrane antigen (PSMA) is an ideal cell surface biomarker and has been extensively pursued as a target in the development of imaging and therapeutic agents for prostate cancer (PCa).[1−9] In the past several years, radiolabeled PSMA-targeted small molecules have successfully detected prostate tumor xenografts in mouse models and some have advanced to clinical studies.[10] These small molecular scaffolds exhibit high affinity and specificity for PSMA, some of which rapidly internalize into the PSMA(+) tumor cells, overcoming the in vivo pharmacokinetic drawbacks presented by antibodies.[1,11] Several urea-based inhibitors pioneered by Kozikowski and Pomper have been labeled with various isotopes such as ^{111}In, ^{99m}Tc, ^{123}I for SPECT[12,13] and ^{68}Ga, ^{18}F, [124]I for PET[11,14,15] imaging. Some of these urea-based inhibitors (e.g., [18F]DCFBC and [18F]DCFPyL) have been translated to human imaging in clinical trials.[16,17] While the pharmacokinetic profile and imaging with these urea-based agents appear superior to antibody-based diagnostics, the reversible mode of binding to PSMA may explain the observed tumor washout over several hours.[18]

In parallel, we developed a class of phosphoramidate compounds that exhibit irreversible or slow-reversible binding to PSMA, depending upon the structure, and that have shown similar promise for detection of PSMA(+) cells and tumors in mouse models.[19−22] On the basis of their mode of binding to PSMA, we envisioned that this would result in reduced tumor washout. In PSMA(+) cells, we found that the mode of binding exhibited a significant effect upon cell uptake and internalization.[23] Furthermore, when conjugated to either ^{18}F-labeled pendent groups[22] or chelators bearing ^{99m}Tc,[21] these compounds displayed consistent uptake and retention in PSMA(+) tumors in mice with minimal washout over several hours.

More recently, we reported a unique phosphoramidate-based PSMA inhibitor as a promising candidate for PET imaging of PCa (Figure 1).[24] The ^{18}F-labeled analogue [18F]**5** displayed rapid uptake (2.35% ID/g at 1 h) and retention (2.35% ID/g at 4 h) in PSMA(+) CW22Rv1 tumor xenografts in mice with an
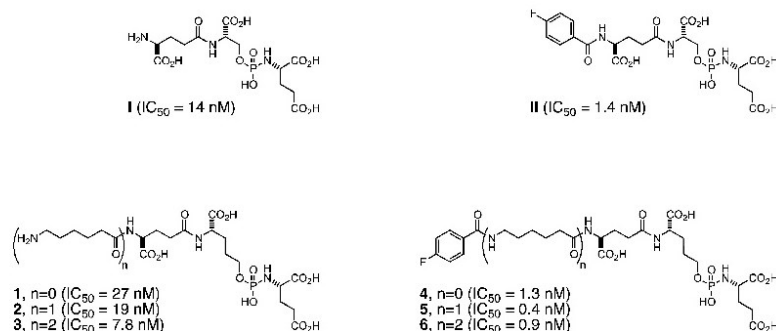
Figure 1. Phosphoramidate-based PSMA inhibitors and radiolabling precursors.

exceptional tumor-to-blood ratio of 265:1 at 4 h postinjection. An important feature of **5**, revealed by X-ray crystallography, was the π-stacking and π–cationic interaction of its fluorobenzamido (FB) ring with the Arg511/Try541 and Arg 463 residues, collectively known as the arene-binding site (ABS) located at the entrance PSMA's active site. This additional unique interaction was thought to be responsible for enhanced PSMA affinity and favorable in vivo characteristics of this radiotracer compared to our previous reported analogues.

In the current study, we modified the phosphoramidate scaffold of **5** by either omitting (**4**) or installing an extra (**6**) aminohexanoate (AH) linker to further understand the structure–activity relationship (SAR) of phosphoramidates with respect to the interactions with the PSMA arene-binding site and their corresponding in vivo pharmacokinetics and biodistribution (Figure 1). Herein, we report the synthesis, radiolabeling, and in vivo performance of phosphoramidates [^{18}F]**4** and [^{18}F]**6** in comparison to previously reported [^{18}F]**5**. The in vitro cell uptake and internalization in PSMA(+) CWR22Rv1 and PSMA(−) PC3 cells were determined at 1 and 2 h postincubation. Additionally, in vivo biodistribution data at 1 and 2 h time points as well as microPET/CT imaging at 2 h postinjection were obtained in mice implanted with PSMA(+) CWR22Rv1 and PSMA(−) PC3 tumors.

■ RESULTS

Synthesis of Cold Standards and Radiolabeling Precursors. The phosphoramidate-based PSMA inhibitors and synthetic intermediates were prepared using the same general methodology as previously reported.[24] Compound **1** was prepared in a final step by global deprotection of benzyl esters in precursor **7** (Scheme 1). Radiolabling precursor **1** represents a common structural core of the phosphoramidate analogues examined in the present study. The Boc-protected precursor **8** was N-deprotected and coupled to Cbz-AH-OH or Cbz-AH$_2$-OH to generate **9** and **10**, respectively. Subsequent global deprotection of **9** and **10** respectively yielded **2** and **3** (Scheme 2).

All the fluorobenzamide (FB and [^{18}F]) derivatives were synthesized in quantitative yields via coupling of the phosphoramidate radiolabeling precursors **1**, **2**, and **3** with succinamidyl 4-fluorobenzoate (SFB) and [^{18}F]SFB to generate **4** and [^{18}F]**4** (Scheme 1), **5** and[^{18}F]**5**, and **6** and [^{18}F]**6** (Scheme 2), respectively. The nonradioactive analogues served as cold standards to determine IC$_{50}$ values, mode of inhibition

Scheme 1. Synthetic Scheme for 4 and [^{18}F]4
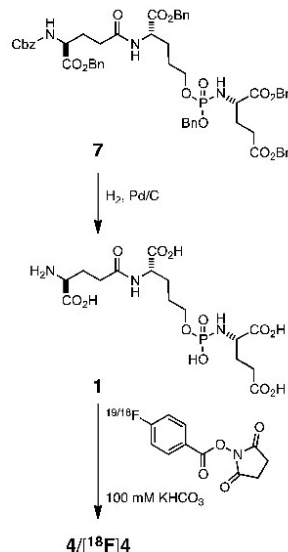
and as reference compounds to optimize the HPLC conditions for purification of their [^{18}F]-labeled analogues.

IC$_{50}$ and Mode of Inhibition. IC$_{50}$ values and mode of inhibition (reversible, slowly reversible, or irreversible) were determined as described previously.[25–28] As is common for small-molecule inhibitors of PSMA,[19,22] derivatization of the N-terminal amine of the parent compounds **1** (IC$_{50}$ = 27 nM), **2** (IC$_{50}$ = 19 nM), and **3** (IC$_{50}$ = 7.8 nM) with SFB led to enhanced inhibitory potency against PMSA (**4**, IC$_{50}$ = 1.3 nM; **5**, IC$_{50}$ = 0.4 nM; **6**, IC$_{50}$ = 0.9 nM) (Figure 1). As observed previously for a number of phosphoramidate-based PSMA inhibitors, compounds **4**, **5**, and **6** exhibited an irreversible mode of binding to PSMA.

Cocrystallization of Phosphoramidate-Based PSMA Inhibitors with Glutamate Carboxypeptidase II and Structural Determination. The extracellular domain of PSMA, also known as human glutamate carboxypeptidase II (hGCPII; amino acids 44–750), was expressed in an S2 cell and purified using described protocols.[29] To evaluate the effect

78

Scheme 2. Synthetic sScheme for 2, 3, 5, 6, [¹⁸F]5, and [¹⁸F] 6
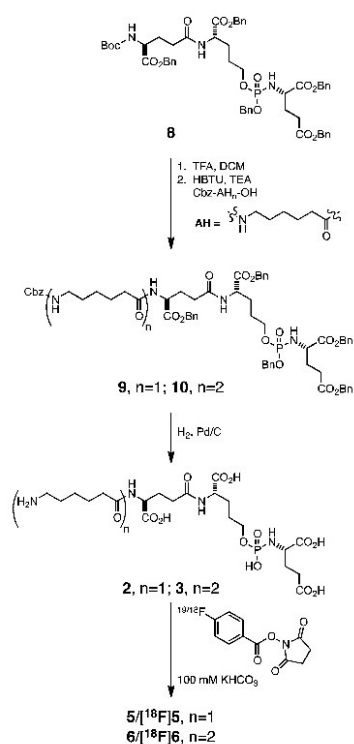
of the AH chain length on PSMA (or hGCPII) binding, the phosphoramidate PSMA inhibitors 4 and 6 (the crystal structure of hGCPII/5 was recently reported[24]) were cocrystallized with hGCPII and the crystal structures of complexes hGCPII/4 and hGCPII/6 were determined at a resolution of 1.77 and 1.71 Å, respectively. The structural characteristics of hGCPII/4 (PDB code 4LQG, reported as hGCPII/CTT1056) and hGCPII/6 were compared to the previously reported hGCPII/5[24] (PDB code 4JYW, reported as hGCPII/CTT1057).

Structures were determined using difference Fourier methods, and the final models had well-defined crystallographic parameters (section 3, Table S1 of Supporting Information). The overall fold of all three structures is nearly identical with a maximum root-mean-square deviation of 0.33 Å for the 681 equivalent $C\alpha$ pairs between hGCPII/5 and hGCPII/6 complex. The most pronounced difference in the loop arrangement is observed for the amino acids stretch spanning from Ser501 to Pro510.

Inhibitors were fitted into the $F_o - F_c$ positive density peaks in the final stages of the refinement. In the case of 4, there is the strong $F_o - F_c$ electron density for the inhibitor parts including the C-terminal glutamate, phosphoramidate group, and the linker up to the P1 carboxylate, and weaker, yet interpretable density for the remaining part of the molecule. As for 6, we built the model with the full confidence encompassing the C-terminal glutamate, phosphoramidate group, and the linker up

to the P1 carboxylate and the adjacent peptide bond. However, the distal part of the inhibitor including the P2 residue, the lipophilic linker, and the fluorobenzoyl group is not seen in the $F_o - F_c$ electron density; they are flexible and do not contribute to the interactions with GCPII (Figure 2A). In contrast to poorly defined distal parts of 4 and 6, positioning of 5 within the hGCPII binding pocket can be unambiguously assigned for the whole inhibitor (Figure 2B).

The core structural elements found to be common in all three inhibitors are the C-terminal glutamate, the phosphoramidate group, the P1 hydroxypropylglycine residue, and the P2 glutamate linker. There is an overlapping of the C-terminal glutamate and the phosphoramidate moieties between the three inhibitors. The C-terminal glutamate occupies the S1′ pocket of the enzyme in the same mode as previously reported. This includes direct interactions between α- and γ-carboxylates of inhibitors and the side chains Arg210, Asn257, Tyr552, Lys699, and Tyr700.[30,31] Free oxygen atoms from the phosphoramidate group chelate Zn^{2+} ions as well as interact with active-site residues including side chains of Tyr552, His553, Asp387, His377, Asp453, and Glu425. Additionally, the phosphoramidate amido group is involved in the hydrogen bonding with the Gly518 main-chain carbonyl and the Glu424 γ-carboxylate, whereas the oxygen atoms from the P–O bond and P1 hydroxypropylglycine form water-mediated contacts with the side chains of Asp453 and Arg536.

It is interesting to note that there are slight differences in the positioning between the AH linker and P1 carboxylate in 5 compared to that in 4 and 6. While the P1 carboxylate of 4 and 6 interact directly with both Arg534 and Arg536, this motif in 5 is shifted by approximately 1.1 Å (for the carbon atom of the P1 carboxylate), engaging NH1 of Arg536 only (3.1 Å).

The most important and prominent differences in the positioning of the inhibitor distal components are found in the lipophilic aminohexanoic linker and the fluorobenzoyl ring. For 4 (Figure 2C), the distance between the linker to the distal ring is approximately 13 Å. The distal fluorobenzoyl ring of 4 is positioned parallel to the guanidinium group of the Arg463 at a distance of approximately 4.0 Å with weak π–cation interactions in the arene-binding site. The terminal fluorobenzoyl functionality of 5 is wedged into the arene-binding cleft located at the "entrance lid" of the enzyme that is shaped by the side chains of Trp541 and Arg511 on sides and by the Arg463 side chain at the bottom. The plane of 5′s fluorobenzoyl ring is virtually parallel to both the indole and guanidinium groups of Trp541 and Arg511, respectively, and both these residues contribute to inhibitor binding (Figure 2D). In contrast to 4 and 5, the distal part of 6, possessing the longest linker (approximately 28 Å), is not observed in the electron density.

In Vitro Uptake and Internalization Study. Compounds [¹⁸F]4, [¹⁸F]5, and [¹⁸F]6 demonstrated specificity for PSMA showing uptake in PSMA(+) CWR22Rv1 cells but not in PSMA(−) PC3 cells. As early as 1 h postincubation, [¹⁸F]6 exhibited statistically significant higher uptake compared to that of [¹⁸F]4 and [¹⁸F]5 with P values of <0.0001 as determined by Student t-test; [¹⁸F]5 uptake was also statistically higher than [¹⁸F]4 with P value of 0.0012 (Table 1). The same trend was observed at 2 h. The activity measured within CWR22Rv1 cells, representing internalization for [¹⁸F]4, [¹⁸F]5, and [¹⁸F]6, at 1 h was 80.7%, 81.4%, and 84.9%, respectively, which increased to 94.2%, 84.2%, and 91.3%, respectively, at 2 h postincubation (Table 1).

79
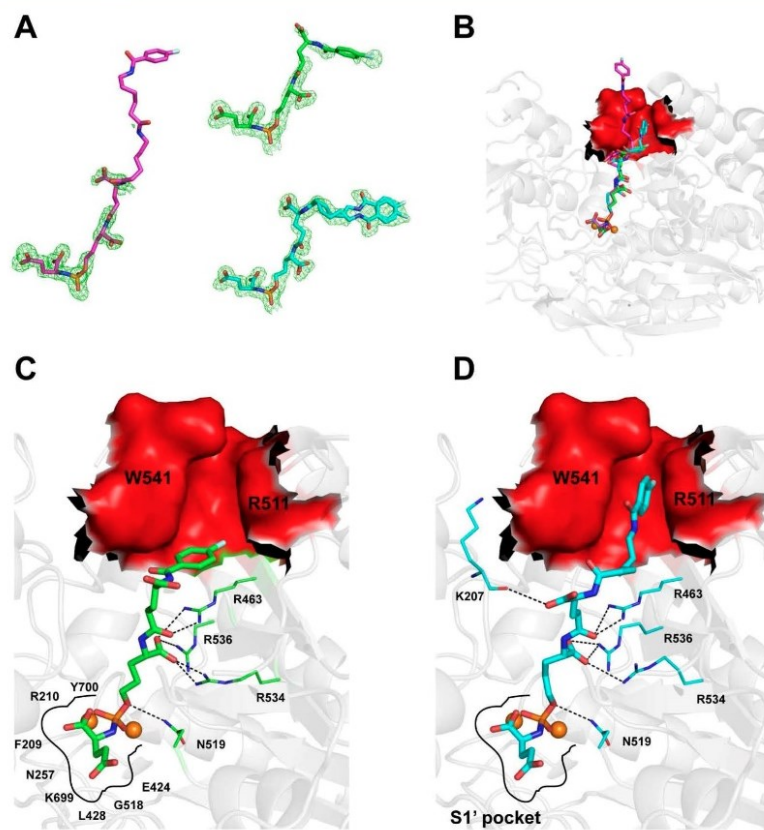
Figure 2. (A) Individual inhibitors shown in stick representation: **4** (green; PBD code 4LQG), **5** (double inhibitor conformation; cyan; PDB code 4JYW), **6** (magenta). Corresponding $F_o - F_c$ electron density map contoured at 3.0σ is shown in green. Note the completely missing electron density peaks for the distal part of **6**, while there is very well-defined electron density for **5** and weaker, yet interpretable density for **4**. (B) Comparison of binding modes of **4** (green), **5** (cyan, only a single conformation shown), and **6** (magenta). Zinc ions (orange spheres) and PSMA are shown in cartoon representation (gray). The arene-binding site (ABS) is highlighted in surface representation and colored red. (C, D) Details of interactions between **4** and **5**, respectively, with PSMA. For the clarity, only residues having direct hydrogen-bonding interactions (shown as black broken lines) with the nonprime atoms of a given inhibitor are shown as lines. Canonical interactions within the S1′ site are not shown.

Table 1. Cell Uptake Data in PSMA(+) CWR22Rv1 and PSMA(−) PC3 Cells and Internalization Data in the PSMA(+) CWR22Rv1 Cell Line for [¹⁸F]4, [¹⁸F]5, and [¹⁸F]6

	% uptake					
	[¹⁸F]4		[¹⁸F]5		[¹⁸F]6	
	1 h	2 h	1 h	2 h	1 h	2 h
CW22Rv1	0.39 ± 0.06	0.70 ± 0.45	0.56 ± 0.05	2.28 ± 0.12	2.28 ± 0.14	4.23 ± 0.64
PC3	0.18 ± 0.13	0.07 ± 0.02	0.04 ± 0.01	0.08 ± 0.02	0.14 ± 0.04	0.15 ± 0.01
	% internalization (CWR22Rv1)					
	[¹⁸F]4		[¹⁸F]5		[¹⁸F]6	
	1 h	2 h	1 h	2 h	1 h	2 h
internalized	80.68 ± 1.76	94.15 ± 2.05	81.4 ± 2.7	84.2 ± 2.3	84.87 ± 3.88	91.31 ± 0.94
bound	19.32 ± 1.76	5.85 ± 2.05	18.6 ± 2.7	15.8 ± 2.3	15.13 ± 3.88	8.69 ± 0.94

In Vivo Imaging and Biodistribution Studies. As seen in the microPET/CT images in Figure 3, uptake of the tracers [¹⁸F]4, [¹⁸F]5, and [¹⁸F]6 was clearly observed in the PSMA(+) CWR22Rv1 tumors at 2 h postinjection but not in the PSMA(−) PC3 tumors. While all compounds showed uptake in the kidneys and clearance through the bladder, minimal uptake was seen in all other organs, including bone (Figure 3).
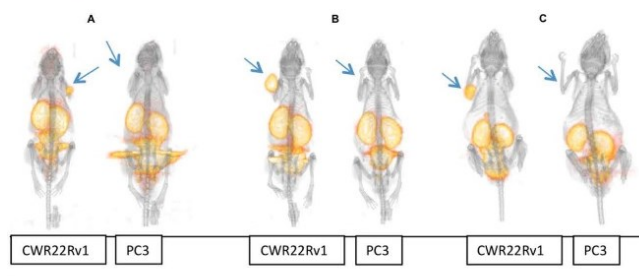
Figure 3. 3D MicroPET/CT images at 2 h postinjection of male nude mice bearing CWR22Rv1 and PC3 tumor xenografts respectively: (A) $[^{18}F]4$; (B) $[^{18}F]5$; (C) $[^{18}F]6$. Arrows indicate tumor placement.

Biodistribution data are provided for all three compounds in Table 2. Uptake of $[^{18}F]4$, $[^{18}F]5$, and $[^{18}F]6$ at 1 h postinjection in the PSMA(+) CWR22Rv1 tumor was 1.54 ± 0.40, 3.16 ± 0.39, and 2.92 ± 0.30% ID/g with a tumor-to-blood ratio of 10, 20, and 24, respectively. At 2 h postinjection, the tumor accumulations were 1.57 ± 0.50, 1.65 ± 0.32, and 1.86 ± 0.14% ID/g with rapid clearance from blood, providing a tumor-to-blood ratio of 26, 64, and 70, respectively. Kidneys showed the expected high uptake and retention of all compounds. At 1 h postinjection, kidney uptake of $[^{18}F]4$, $[^{18}F]5$, and $[^{18}F]6$ was 8.94 ± 2.93, 24.38 ± 3.72, and 5.87 ± 0.67% ID/g, respectively, and at 2 h was 9.97 ± 2.81, 21.54 ± 6.12, and 7.13 ± 1.45% ID/g, respectively. For the PSMA(−) PC3 xenografts, tumor uptake was similar to that in the background and nontarget organs while the uptake in kidneys for $[^{18}F]4$, $[^{18}F]5$, and $[^{18}F]6$ at 2 h postinjection was 5.64 ± 2.41, 18.98 ± 4.75, and 4.44 ± 1.03% ID/g, respectively.

DISCUSSION

A series of FB ring-containing compounds was designed with or without a linker to separate it from the common phosphoramidate core **1**. Compound **4**, in which the FB group was directly attached to the inhibitor **1** via its terminal amine, was expected to behave like our first generation analogue **II**. The other new compound in the series was compound **6** with the FB ring separated from the core inhibitor by two AH units. Compound **5**, where the inhibitor core was separated from the FB ring by one AH unit, has previously shown desirable PSMA targeting properties.[24] $[^{18}F]5$ retained high affinity for PSMA and showed consistent uptake and rapid internalization into CW22Rv1 (PSMA+) cells. The in vitro properties translated well to mouse models implanted with CW22Rv1 tumors xenografts. High uptake and retention of $[^{18}F]5$ over 4 h was observed with exceptional blood-to-tumor ratios of 265:1 at 4 h postinjection, suggesting rapid clearance of the radiotracer from blood and all nontarget organs. Cocrystallization of PSMA with **5** revealed the binding of the fluorobenzoyl (FB) ring in the arene-binding site (ABS), initially identified by Zhang et al.[32]

It was previously revealed that an optimal distance between the targeting core and the FB group is necessary to achieve efficient binding of the FB ring with the ABS. On the basis of the results obtained from modeling studies, and literature precedent, it was anticipated that the FB ring of the $[^{18}F]4$ would be too short to reach the ABS; the linker distance of >20 Å in $[^{18}F]6$ was expected to allow for ABS binding as a contribution to a bimodal binding interaction. In addition to the pharmacodynamic consequences of linker length, we sought to assess the effect of varying the AH linker units on the in vivo pharmacokinetics of the targeting agents.

The syntheses of compounds **1**, **2**, **5**, and $[^{18}F]5$ were reported previously,[22,24] while the syntheses of **4**/$[^{18}F]4$ and **6**/$[^{18}F]6$ are reported herein. Globally protected **3** was generated by acid deprotection of the Boc group of **8** followed by installation of Cbz-(AH)₂-OH linker. Global deprotection afforded **3** in quantitative yield. Fluorobenzoylation of the N-terminal amines of **1** and **3** yielded fluorobenzamide (FB) compounds **4** and **6**, respectively. As observed with **5** and other phosphoramidate analogues, these compounds maintained high affinity and irreversible modes of binding to PSMA upon derivatization of the N-terminal amine. Owing to the high affinity and the irreversible nature of the common scaffold, it was expected that compounds $[^{18}F]4$ and $[^{18}F]6$ would show uptake and retention in PSMA(+) tumors in vivo while rapidly clearing from all nontarget organs, as was observed in the case of $[^{18}F]5$.[24]

To gather insight into the molecular interactions of these analogues with PSMA and draw a comparison with the previous analogue **5**, compounds **4** and **6** were also cocrystallized with the extracellular domain of PSMA. While the P1′ carboxylate, the phosphoramidate binding group, and the P1 residue interact almost identically to PSMA, the distinct differences were the aminohexanoic acid linker(s) and the fluorobenzoyl ring. As anticipated, the linkage between the distal FB ring and the phosphoramidate core in **4** (approximately 13 Å) was insufficient to access the recently identified ABS.[32] Rather, the distal FB group was found parallel to the guanidinium group of the Arg463 at a distance of approximately 4.0 Å (Figure 2C). Clearly, π interactions play a prominent role in the stabilization of this inhibitor's positioning, although the strength of this interaction is likely much weaker compared to interactions in the ABS as observed for **5**. The terminal fluorobenzoyl moiety of **5** was found to be parallel to both indole and guanidinium groups of Trp541 and Arg511 in the ABS residues contributing to enhanced inhibitor binding (Figure 2D). In the case of **6**, possessing the longest linker (approximately 28 Å), the portion of the inhibitor distal to the active site was not observed in the electron density map, suggesting its positional flexibility and the absence of significant PSMA−inhibitor interactions (Figure 2A and Figure 2B).

The structural data are in a good agreement with the inhibitory properties toward PSMA contributed from the terminal FB group and the AH linker on the tested compounds. The coupling of the terminal FB group to the core structures **1**, **2**, and **3** led to an improvement of the IC₅₀ values for **4**, **5**, and

81

Table 2. Biodistribution of [18F]4, [18F]5, and [18F]6 As Determined by Radioactivity Assays in PSMA(+) CWR22Rv1 Tumor-Bearing Mice (n = 4 in Each Group)[a]

tissue	[18F]4			[18F]5			[18F]6		
	CWR22Rv1		PC3	CWR22Rv1		PC3	CWR22Rv1		PC3
	1 h	2 h	2 h	1 h	2 h	2 h	1 h	2 h	2 h
blood	0.15 ± 0.07	0.07 ± 0.02	0.08 ± 0.04	0.17 ± 0.05	0.04 ± 0.02	0.05 ± 0.02	0.12 ± 0.03	0.03 ± 0.01	0.02 ± 0.01
heart	0.75 ± 0.32	0.50 ± 0.05	0.36 ± 0.21	0.34 ± 0.11	0.17 ± 0.06	0.21 ± 0.07	0.23 ± 0.05	0.06 ± 0.01	0.07 ± 0.03
lung	0.65 ± 0.34	0.43 ± 0.11	0.29 ± 0.09	0.43 ± 0.09	0.21 ± 0.10	0.27 ± 0.08	0.25 ± 0.07	0.11 ± 0.04	0.09 ± 0.02
liver	0.83 ± 0.23	0.5 ± 0.11	0.44 ± 0.27	0.49 ± 0.11	0.29 ± 0.08	0.28 ± 0.05	0.49 ± 0.07	0.25 ± 0.04	0.25 ± 0.04
kidney	8.94 ± 2.93	9.97 ± 2.81	5.46 ± 2.41	24.38 ± 3.72	21.54 ± 6.12	18.98 ± 4.75	5.87 ± 0.67	7.13 ± 1.45	4.44 ± 1.03
spleen	1.18 ± 0.08	0.87 ± 0.16	0.76 ± 0.35	1.02 ± 0.04	0.84 ± 0.30	1.38 ± 1.05	0.32 ± 0.12	0.19 ± 0.03	0.14 ± 0.03
bone	0.46 ± 0.04	0.5 ± 0.42	0.24 ± 0.06	0.38 ± 0.09	0.23 ± 0.15	0.17 ± 0.04	0.45 ± 0.12	0.21 ± 0.11	0.14 ± 0.04
muscle	0.29 ± 0.09	0.19 ± 0.01	0.17 ± 0.04	0.12 ± 0.04	0.10 ± 0.06	0.06 ± 0.01	0.15 ± 0.04	0.08 ± 0.02	0.03 ± 0.01
tumor	1.54 ± 0.40	1.57 ± 0.45	0.40 ± 0.17	3.16 ± 0.39	1.65 ± 0.32	0.38 ± 0.03	2.92 ± 0.30	1.86 ± 0.14	0.27 ± 0.07
tumor/blood	9.88 ± 5.21	25.61 ± 14.99	5.42 ± 1.43	20.01 ± 9.06	63.60 ± 18.08	9.15 ± 3.76	24.21 ± 3.21	69.60 ± 15.72	11.19 ± 1.31

[a]Tissues were harvested at 1 and 2 h postinjection. Uptake values are expressed as % ID/g of tissue.

6 by approximately 20-, 50-, and 9-fold, respectively. A mechanistic explanation for the increase in inhibition potency may be the result of additional binding interactions between the distal motifs of the inhibitors and the protein in addition to entropic contributions. The most prominent effect (50-fold improvement) was observed for 5, for which the terminal FB group is fully engaged with the ABS. Considerably less (20-fold) enhancement of inhibition was observed for 4, where there were less pronounced interactions between the SFB and the ABS. Interactions with the ABS were absent for 6, which exhibited the least enhancement of inhibitory potency compared to its inhibitor core 3. However, it should be noted that more complex effects (including entropic factors and solvation effects) may also play a role in defining the absolute values of inhibition constants for individual molecules. The simple bimodal binding as in 5 or unimodal binding in 6 cannot be the sole determining factor for the inhibition potencies.

The PSMA(+) LNCaP cell lines have been used most widely in the PSMA research by various research groups, including us.[1,21,22] Although LNCaPs have a high PSMA concentration, their growth rate and proliferation as tumors in mice are unpredictable and often lead to tumor necrosis. In contrast, the CWR22Rv1 cells have a moderate PSMA expression (8-fold lower than LNCaPs) and a predictable growth pattern as tumor xenografts.[24,33] In addition, the cellular PSMA concentration in the CRW22Rv1 cells is more akin to the expression levels expected in human prostate cancer metastases. Therefore, for the in vitro and in vivo studies in the present research, CWR22Rv1 has been the PSMA(+) cell line of choice.

The in vitro studies indicated uptake of all the radiotracers in PSMA(+) CW22Rv1 cells, where an increase in uptake was observed as the lipophilic linker length in these compounds increased from [18F]4 to [18F]6. While the increased uptake of [18F]5 can be attributed to its unique bimodal interactions with PSMA, no such binding interaction was observed with 6. Therefore, the enhanced uptake in PSMA(+) cells in vitro cannot be explained solely on the basis of PSMA affinity. This trend has also been reported previously in the literature, where high uptake in PSMA(+) cells in vitro and tumors in vivo has often been correlated with increased lipophilicity.[12] As expected, all three compounds showed negligible uptake in PSMA(−) PC3 cell lines at all time points, due to lack of PSMA expression in this cell line. In addition, all compounds showed rapid internalization into PSMA(+) CW22Rv1 cells with more than 80% internalization at 1 h. We have previously reported that the mode of binding of PSMA inhibitors has a direct impact on the degree of internalization.[28,33,34] The irreversible nature of the scaffolds and findings from in vitro uptake and internalization suggest that the radiotracers will likely lead to both uptake and retention in the PSMA(+) tumors in vivo over time, allowing clearance from the nontarget organs.

Tumor uptake was observed for [18F]4, [18F]5, and [18F]6 at 1 and 2 h postinjection in mice bearing PSMA(+) CWR22Rv1 tumor cells. At 1 h, the uptake of [18F]5 (3.16%) and [18F]6 (2.92%) was about 2-fold higher than [18F]4 (1.54%) ($p <$ 0.05). However, there was no significant difference in tumor uptake between the three analogues at 2 h postinjection. At 2 h postinjection, all three tracers exhibited rapid clearance from blood and non-PSMA expressing organs, resulting in high tumor-to-blood ratios for [18F]5 and [18F]6, 64 and 70, respectively, that were significantly ($p < 0.05$) greater than [18F]4. The irreversible mode of binding of these compounds

possibly contributes to its tumor retention while rapidly clearing from other nontarget organs, in contrast to the washout that is reported over time for most urea-based agents.[35] As expected, kidney uptake was observed with all three analogues, due to the high expression of PSMA in mouse kidneys,[36] with the highest uptake shown in the case of [18F]5, which can be considered as a secondary positive indicator of PSMA specificity. The kidney uptake of [18F]5 was significantly higher ($p < 0.05$) at both time points and in both tumor bearing animal models. It is unknown why the kidney uptake of [18F]5 was 2- to 2.5-fold higher, as the magnitude of the difference does not correlate to a significant chemical or in vitro characteristic. For compounds [18F]4 and [18F]6 there was no significant difference in kidney uptake at either time point, nor was there any difference for all three tracers between the kidney uptake in the PC3 versus the CWR22Rv1 animal model at 2 h.

Given the structural similarities, it was expected that [18F]4 would exhibit similar in vivo properties to our first-generation PET agent. In our previous work, [18F]II was evaluated in PSMA(+) LNCaP tumor xenografts in mice with imaging and biodistribution data collected at 2 h postinjection. PSMA expression in LNCaP cells is approximately 5- to 10-fold greater than that in CW22Rv1 cells.[24] In comparison to the current work, [18F]4 had a modest uptake at 1.57% with a tumor-to-blood ratio of 64:1 in the lower PSMA expressing CW22Rv1 tumors vs 1.24% and tumor-to-blood ratio of 9:1 for [18F]II in LNCaP tumors. Though this may not be a head-to-head comparison because different tumor types were used, the in vivo uptake and clearance of [18F]4 suggest an overall trend toward higher affinity and more superior properties compared to [18F]II.

The most promising compounds of this study were [18F]5 and [18F]6, in which the installation of lipophilic AH linker units between the phosphoramidate targeting core and the FB ring improved the in vivo tumor uptake and clearance compared to that of [18F]4. While the excellent in vivo properties of [18F]5 can be attributed to its unique interactions with the ABS which resulted in higher PSMA affinity, the added lipophilicity from the additional AH spacer in [18F]6 may have contributed to reduced renal clearance and consequent tumor uptake. Although we observed no direct crystallographic evidence for the FB group of [18F]6 interacting with the ABS, the high degree of rotational freedom afforded by the two AH units may allow for the secondary binding at the ABS in solution.

The PET/CT images confirmed the observations of the biodistribution studies. All three tracers demonstrated significant uptake in the PSMA(+) CWR22Rv1 tumors but not in PSMA(−) PC3 tumors, confirming their specificity for PSMA. All these analogues exhibited high tumor-to-background ratios at 2 h postinjection with rapid blood clearance and minimal uptake and retention in nontarget organs. No evidence of metabolic defluorination and subsequent bone accumulation by any of the analogues was observed.

The tumor uptake and biodistribution patterns are in good agreement with the other known F-18 PSMA urea agents that have been translated into the clinical setting, although it is hard to make a direct head-to-head comparison between these compounds due to the different models used between the different studies and the variable expression levels of PSMA in the PSMA(+) cell lines used. However, the observed pharmacokinetics are indicative of an overall trend of the uptake and clearance of these agents. [18F]DCFBC, the first generation urea compound to be tested in human clinical trials, showed an uptake of 4.7% in PSMA(+) PC3-PIP cells and a tumor/blood ratio of 13:1.[16] In comparison, compounds [18F]5 and [18F]6 show an uptake of 1.67% and 1.8%, with tumor/blood ratios of 64:1 and 69:1, respectively, at the 2 h time point. It has been shown that the concentration of PSMA in the PC3-PIP cells is significantly higher than that in CWR22Rv1 cells.[37] Although the tumor uptake values are comparatively higher in the second generation urea agent, [18F]DCFPyL (39.4% at 2 h in PC3-PIP cells), the renal and liver uptake for this compound is also significantly higher than our phosphoramidates.[17] The renal and liver uptake values for [18F]DCFPyL at 2 h are 15.7% and 2.14%, respectively, as compared to 7.13% and 0.25% for [18F]6.

As both these reported urea compounds have been able to successfully detect primary and metastatic lesions in clinical trials,[15,18] the comparable trends in tumor uptake and pharmacokinetics, and excellent clearance from nontarget organs, observed for [18F]5 and [18F]6 are positive indicators of their success in future clinical trials. In fact, after successful completion of preclinical, dosage, and toxicology studies, the first-in-human clinical trials for compound [18F]5 is currently underway.

CONCLUSION

We have successfully synthesized and evaluated a bracketed series of PSMA-targeted phosphoramidate analogues, differing in the lipophilicity compared to compound 5, and evaluated them as PET imaging agents for prostate cancer. While capitalizing the unique bimodal interaction with the "arene-binding site" in PSMA can be a key element for future designs of inhibitors with improved affinity, a balance between hydrophilic and lipophilic properties in the core structure may also be critical for favorable in vivo properties of the radiotracer. With their exceptional binding, tumor uptake and retention, and remarkable tumor-to-blood ratios, [18F]5 and [18F]6 are well-positioned as favorable candidates for translation to future prostate cancer imaging studies in human.

EXPERIMENTAL SECTION

Cell Lines, Reagents, and General Methods. CWR22Rv1 and PC-3 cells were obtained from the American Type Culture Collection (Manassas, VA). NCr-nu/nu mice (strain code 088) were purchased from Charles River (Hollister, CA). Z-6-Aminohexanoic acid (Cbz-AH-OH) was purchased from Sigma-Aldrich (St. Louis, MO). All chemicals and cell-culture reagents were purchased from Fisher Scientific (Sommerville, NJ) or Sigma-Aldrich. All solvents used in chemical reactions were anhydrous and obtained as such from commercial sources or distilled prior to use. All other reagents were used as supplied unless otherwise stated. Liquid flash chomatography (silica or C18) was carried out using a Flash Plus chromatography system (Biotage, Charlotte, NC). High-resolution mass spectrometry was performed using an ABS 4800 MALDI TOF/TOF analyzer (Applied Biosystems, Framingham, MA). ^{1}H NMR chemical shifts were referenced to tetramethylsilane ($\delta = 0.00$ ppm), CDCl$_3$ ($\delta = 7.26$ ppm), or D$_2$O ($\delta = 4.87$ ppm). ^{13}C NMR chemical shifts were referenced to CDCl$_3$ ($\delta = 77.23$ ppm). ^{31}P NMR chemical shifts in CDCl$_3$ or D$_2$O were externally referenced to 85% H$_3$PO$_4$ ($\delta = 0.00$ ppm) in CDCl$_3$ or D$_2$O. Aqueous buffered solutions for in vitro experiments and HPLC chromatography were prepared with deionized distilled water (Milli-Q water system, Millipore, Billerica, MA).

The HPLC analysis and purification system for radioactive compounds were performed on a Waters model 600 multisolvent system pump equipped with a Shimudzu model SPD-10A UV detector

83

and an in-line radioactivity detector (model 105s, Carroll and Ramsey Associates, Berkeley, CA) that was coupled to a data collection system (PeakSimple model 304, SRI, Torrance, CA).

Purity of compounds **4**, **5**, and **6** was verified to be >95% via ^{31}P (formation of single product) and ^1H NMR.

1. Syntheses of Phosphoramidate Compounds and Their Respective ^{18}F Analogues.

The synthetic sequence of compounds **4** and [^{18}F]**4** is shown in Scheme 1. Syntheses and characterization of **7** and its precursors are provided as Supporting Information (section 1). The general synthetic scheme for compounds **2**, **3**, **5**, **6**, [^{18}F]**5**, and [^{18}F]**6** is shown in Scheme 2. Syntheses of compounds **2**, **5**, [^{18}F]**5**, and **8** have been reported previously.[24]

1.1. Synthesis of 6-(6-(((Benzyloxy)carbonyl)amino)-hexanamido)hexanoic Acid, Cbz-AH$_2$-OH. *Synthesis of CBZ-AH-OH.* 6-Aminocaproic acid (8 g, 61 mmol, 1 equiv) and sodium carbonate (61 mmol, 1 equiv) were dissolved in water (18 mL) in a round-bottom flask (100 mL) and placed in an ice bath. Benzoyl chloroformate (67.1 mmol, 1.1 equiv) was added to the flask dropwise. Sodium hydroxide (2 N, 15 mL) was added in 5 mL portions over a 15 min period. The reaction was monitored by TLC and stirred until completion. The crude product was washed with diethyl ether (2 × 20 mL), and the aqueous phase was acidified to pH = 2 and placed in 5 °C. The white precipitate was filtered and washed with 10% HCl. TLC (silica, 4:1 DCM/EtOAc, 1% AcOH) showed the presence of CBZ-AH-OH (R_f = 0.27). CBZ-AH-OH was isolated as a white solid by column chromatography (silica, 4:1 DCM/EtOAc, 1% AcOH), yield 25.5%. Mp = 57−59 °C. ^1H NMR (300 MHz, CDCl$_3$): δ 1.36 (m, 2H), 1.50 (m, 2H), 1.65 (m, 2H), 2.35 (t, 2H), 2.35 (t, 2H), 3.19 (m, 4H), 4.78 (s, 1H), 5.09 (s, 2H), 5.64 (s, 1H), 7.35 (m, 5H). ^{13}C NMR (100 MHz, CDCl$_3$): δ 24.23, 26.08, 29.57, 33.82, 40.79, 66.64, 128.08, 128.48, 136.53, 156.44, 179.11. HR mass spectrometry: calculated 288.1212; found 288.12106 (M + Na$^+$) for C$_{14}$H$_{19}$NO$_4$.

Synthesis of CBZ-AH$_2$-OH. CBZ-AH-OH (0.20 g, 0.754 mmol, 1 equiv) and HBTU (0.83 mmol, 1.0 equiv) were dissolved in distilled DCM (10 mL) and allowed to stir for 1 h under Ar$_{(g)}$ in a flame-dried flask (25 mL). A solution of NHS (0.83 mmol, 1.1 equiv) and TEA (0.75 mmol, 1 equiv) was prepared in distilled DCM (4 mL) and added to the reaction dropwise. This was allowed to stir overnight. The DCM was dried under vacuum. The crude product was extracted with ethyl acetate (25 mL) and washed with 10% HCl (3 × 25 mL), 10% NaHCO$_3$ (3 × 25 mL), and brine (3 × 25 mL) and dried with Na$_2$SO$_4$. The presence of CBZ-AH-NHS was determined by ^1H NMR (300 MHz, CDCl$_3$): δ 1.43 (m, 2H), 1.51 (m, 2H), 1.73 (m, 2H), 2.59 (t, 2H), 2.35 (t, 2H), 2.76 (s, 4H), 3.19 (m, 4H), 4.98 (s, 1H), 5.07 (s, 2H), 5.64 (s, 1H), 7.35 (m, 5H). CBZ-AH-NHS was used as a crude mixture without further purification.

6-Aminocaproic acid (0.12 g, 0.90 mmol, 1.2 equiv) and sodium bicarbonate (1.35 mmol, 1.8 equiv) were dissolved in water (8 mL). CBZ-AH-NHS (0.752 mmol, 1 equiv) was dissolved in acetone (5.2 mL) and was added dropwise to the round-bottom flask and stirred overnight. The reaction mixture was acidified to pH 2, and the white precipitate was filtered and washed with 10% HCl. The product was isolated as a white solid without any further purification (68% yield, 0.61 mmol). TLC (silica, 49:1 EtOAc/AcOH) showed the presence of CBZ-AH$_2$-OH (R_f = 0.17). Mp = 104−106 °C. ^1H NMR (300 MHz, CDCl$_3$): δ 1.36 (m, 4H), 1.50 (m, 4H), 1.61 (m, 4H), 2.16 (t, 2H), 2.35 (t, 2H), 3.16−3.34 (m, 4H), 4.94 (s, 1H), 5.09 (s, 2H), 5.69 (s, 1H), 7.34 (m, 5H). ^{13}C NMR (300 MHz, CDCl$_3$): δ 24.28, 25.28, 25.93, 26.06, 28.65, 29.15, 33.36, 35.57, 35.63, 38.73, 40.19, 65.85, 127.30, 127.48, 128.00, 137.05, 157.47, 174.60, 176.02. HR mass spectrometry: calculated 378.22, found 379.22906 (M + H$^+$) for C$_{20}$H$_{30}$N$_2$O$_5$.

1.2. 2-(((S)-((2R)-2-(4-Amino-4-carboxybutanamido)-2-carboxyethoxy)(hydroxy)phosphoryl)amino)pentanedioic Acid [1]. To a solution of a benzyl ester protected phosphoramidate (**7**) (0.100 g, 0.095 mmol) in THF (1 mL) were added 10% Pd/C (10 mg), K$_2$CO$_3$ (0.033 mg, 0.241 mmol), and H$_2$O (1 mL). The mixture was stirred vigorously, purged with Ar$_{(g)}$, and then charged with H$_{2(g)}$ under balloon pressure overnight at room temperature. The solution was filtered through a 0.2 mm PTFE micropore filtration disk

(Whatman). The solvent was removed in vacuo to yield a white solid, **1**, in 96% yield. ^1H NMR (300 MHz, D$_2$O): δ 1.44−1.54 (m, 3H), 1.62−1.67 (m, 3H), 1.86−1.93 (m, 2H), 2.02−2.05 (m, 2H), 2.21 (m, 1H), 2.25 (m, 1H), 3.31 (m, 1H), 3.47 (m, 1h), 3.56 (t, 2H), 3.92 (m, 1H). ^{31}P NMR (300 MHz, D$_2$O): δ 8.46. HR mass spectrometry: calculated 471.3, found 470.20 (M − H) for C$_{15}$H$_{26}$N$_3$O$_{12}$P$^+$.

1.3. 2-(((S)-((2R)-2-Carboxy-2-(4-carboxy-4-(4-fluorobenzamido)butanamido)ethoxy)(hydroxy)phosphoryl)-amino)pentanedioic Acid [4]. A solution of SFB (20.14 μmol, 1 equiv) in 400 μL of THF was added to a stirred solution of **1** (30.22 μmol, 1.5 equiv) in 600 μL of 0.1 M KHCO$_3$. The reaction mixture was stirred for 6 h in the dark at room temperature. The unreacted **1** was scavenged by stirring with 25 mg of Si isocyanate resin (SiliCycle, Inc., Quebec, Canada) overnight at room temperature. The solution was subsequently centrifuged (7800 rcf, 10 min), and the supernatant was lyophilized in a 2 mL microcentrifuge tube. The unreacted materials and/or hydrolyzed SFB was removed by successively triturating the lyophilized solid with 1 mL portions of DMSO and centrifuging the mixture (16 200 rcf, 1 min) after each wash; this process was repeated 10 times. The resulting solid was dried in vacuo providing the desired 4-fluorobenzamidophosphoramidate **4** in quantitative yield. ^1H NMR (300 MHz, D$_2$O): δ 1.44−1.54 (m, 2H), 1.56−1.68 (m, 2H), 1.86−2.14 (m, 4H), 2.27−2.35 (m, 2H), 3.27−3.34 (m, 1H), 3.50 (t, 2H), 3.73−3.87 (m, 2H), 4.05−4.08 (t, 1H, 3.9 Hz), 4.15−4.19 (dd, 1H, 4.4 Hz, 9.15 Hz), 7.04−7.10 (t, 2H), 7.66−7.70 (dd, 2H). ^{31}P NMR (300 MHz, D$_2$O): δ 8.42. HR mass spectrometry: calculated 720.03, found 719.96 (M + 4Na + K) for C$_{22}$H$_{29}$FN$_3$O$_{13}$P$^+$.

1.4. Synthesis of Dibenzyl 2-(((R)-(Benzyloxy)(((24R)-19,24-bis((benzyloxy)carbonyl)-3,10,17,22-tetraoxo-1-phenyl-2-oxa-4,11,18,23-tetraazaheptacosan-27-yl)oxy)phosphoryl)amino)-pentanedioate [10]. Cbz-AH2-acid (AH = aminohexanoic acid) (0.1 g, 0.264 mmol) was preactivated with HBTU (0.29 mmol, 1.1 equiv) and TEA (0.29 mmol, 1.1 equiv). **8** was treated with a mixture of dry TFA/DCM for deprotection of N-terminal Boc group and then added to the flask above with activated Cbz-AH2-acid. Purification was carried out using reversed phase C18 chromatography with 80% MeOH−water as the mobile phase. Pure **10** was isolated in 49% yield. ^1H NMR (300 MHz, CDCl$_3$): δ 1.28−1.30 (m, 4H), 1.41−1.46 (m, 4H), 1.56−1.61 (m, 6H), 1.86−1.89 (m, 2H), 2.09−2.27 (m, 10H), 2.37−2.39 (m, 2H), 3.12−3.18 (m, 4H), 3.74 (m, 1H), 3.89 (m, 2H), 4.51 (m, 2H), 4.91−4.96 (m, 2H), 5.05−5.11 (m, 10H), 5.95 (d, 1H, -NH), 6.98 (d, 1H, -NH), 7.03 (d, 1H, -NH), 7.27−7.31 (m, 27H). ^{31}P NMR (300 MHz, CDCl$_3$): δ 8.47. ESI mass spectrometry: calculated 1281.4, found 1282.4 (M + H), 1305.6 (M + Na) for C$_{70}$H$_{84}$N$_5$O$_{16}$P$^+$.

1.5. Synthesis of 2-(((S)-((4R)-4-(4-(6-(6-Aminohexanamido)-hexanamido)-4-carboxybutanamido)-4-carboxybutoxy)-(hydroxy)phosphoryl)amino)pentanedioic Acid [3]. To a solution of benzyl ester protected phosphoramidate (**10**) (0.160 g, 0.124 mmol) in THF (1 mL) were added 10% Pd/C (16 mg), K$_2$CO$_3$ (0.044 mg, 0.318 mmol), and H$_2$O (1 mL). The mixture was stirred vigorously, purged with Ar$_{(g)}$, and then charged with H$_{2(g)}$ under balloon pressure overnight at room temperature. The solution was filtered through a 0.2 mm PTFE micropore filtration disk (Whatman). The solvent was removed in vacuo to yield a white solid, **3**, in 94% yield. ^1H NMR (300 MHz, D$_2$O): δ 1.14−1.19 (m, 2H), 1.36 (m, 4H), 1.38−1.50 (m, 10H), 1.59−1.68 (m, 2H), 1.89 (m, 2H), 1.99−2.19 (m, 8H), 2.86 (t, 2H), 3.34 (m, 1H), 3.56 (dd, 1H), 3.94 (m, 3H). ^{31}P NMR (300 MHz, D$_2$O): δ 8.43. HR mass spectrometry: calculated 698.30, found 698.35 (M + H) for C$_{27}$H$_{49}$N$_5$O$_{14}$P$^+$.

1.6. Synthesis of 2-(((S)-((22R)-17,22-Dicarboxy-1-(4-fluoro-phenyl)-1,8,15,20-tetraoxo-2,9,16,21-tetraazapentacosan-25-yl)oxy)(hydroxy)phosphoryl)amino)pentanedioic Acid [6]. A solution of **3** (0.028g, 0.003 mmol, 1.5 equiv) was made in 500 μL of 100 mmol of KHCO$_3$, and SFB (0.005g, 1 equiv) in 400 μL of THF was added and stirred for 5 h. The unreacted **3** was scavenged by stirring with 5 mg of Si isocyanate resin (SiliCycle, Inc., Quebec, Canada) overnight at room temperature. The solution was subsequently centrifuged (7800 rcf, 10 min), and the supernatant was lyophilized in a 2 mL microcentrifuge tube. The unreacted

materials and/or hydrolyzed SFB was removed by successively triturating the lyophilized solid with 1 mL portions of DMSO and centrifuging the mixture (16 200 rcf, 1 min) after each wash; this process was repeated 10 times. The resulting solid was dried in vacuo providing the desired 4-fluorobenzamidophosphoramidate **6** in quantitative yield. ^{1}H NMR (300 MHz, D$_2$O): δ 1.09−1.19 (m, 2H), 1.16−1.24 (m, 6H), 1.30−1.35 (m, 2H), 1.41−1.45 (m, 5H), 1.61−1.68 (m, 5H),1.99−2.07 (m, 6H), 2.14−2.21 (m, 2H), 2.91−2.95 (m, 2H), 3.16−3.21(m, 2H), 3.25−3.33 (m, 2H), 3.54−3.56 (m, 2H), 3.87−3.96 (m, 2H), 7.02−7.08 (m, 2H), 7.56−7.61 (m, 2H). ^{31}P NMR (300 MHz, D$_2$O): δ 8.43. HR mass spectrometry: calculated 820.38, found 820.43 (M + H) and 858.40 (M + K) for C$_{34}$H$_{51}$N$_5$FO$_{15}$P$^+$.

1.7. Synthesis of [^{18}F]4, [^{18}F]5, or [^{18}F]6. Succinimidyl [^{18}F]fluorobenzoate ([^{18}F]SFB) was synthesized in a Neptis synthesizer (ORA—Optimized Radiochemical Applications, Belgium) equipped with commercially available kits and cassettes (ABX GmbH, Germany) that was then coupled to **1**, **2**, and **3** as was previously described with modifications.[22] The PSMA analogues (2 mg) were dissolved in 100 mL of H$_2$O, 20 mL of 0.1 M K$_2$CO$_3$, and an amount of 100 mL of [^{18}F]SFB in acetonitrile was added to a 1 dram vial charged with a stir bar (pH 9.5−10). The coupling reaction took place at 40 °C for 15 min. Prior to in vitro and in vivo studies, the radioconjugate was purified on a semipreparative RP-HPLC using a Phenomenex C18(2) 100 Å, 250 mm × 10 mm, 5 μm column, linear gradient (20−90% over 22 min) of solvent B in solvent A (A, 0.1% formic acid in water; B, 0.1% formic acid in acetonitrile) at a flow rate of 5 mL/min and UV detection at 254 nm. [^{18}F]4, [^{18}F]5, or [^{18}F]6 peak was collected and concentrated via QMA light SPE method using 0.5% NaCl for elution and diluted with 1× PBS for in vitro and in vivo studies. Radiochemical yields ranged between 50% and 60% decay-corrected from [^{18}F]SFB. Analytical RP-HPLC of the purified peak confirmed >95% purity of all three compounds via coinjection with the respective nonradioactive analogs.

2.1. General Method of Determining IC$_{50}$ Values. Inhibition studies were performed as previously described with minor modifications.[25,34] Description is provided in Supporting Information (section 2).

2.2. Mode of Inhibition Study. The mode of inhibition studies followed the procedure described in our previous work.[19] A description is provided in Supporting Information (section 2).

3.1. GCPII Expression, Purification, Crystallization, and Data Collection. The extracellular part of human GCPII (hGCPII; amino acids 44−750) was expressed in S2 cell and purified according to procedures described previously.[29] The final protein preparation in 20 mM Tris-HCl, 150 mM NaCl, pH 8.0, was concentrated to 9 mg/mL and stored at −80 °C until further use.

Complexes of hGCPII/4 and hGCPII/6 were prepared by mixing stock solutions of hGCPII (9 mg/mL) and a given inhibitor (20 mM in water, pH adjusted to 8.0 by the addition of NaOH) at the 9:1 ratio (v/v). Crystals were grown from 2 μL droplets made by mixing equal volumes of GCPII/inhibitor and reservoir solutions (33% pentaery-thritol propoxylate (Sigma), 1.5% polyethylene glycol 3350 (Sigma), and 100 mM Tris-HCl, pH 8.0) using the hanging-drop vapor diffusion setup at 293 K. Diffraction quality crystals were flash-frozen in liquid nitrogen directly from the crystallization droplet. The diffraction data for both complexes were collected at 100 K using synchrotron radiation at the MX 14.2 beamline (BESSYII, Helmholtz-Zentrum Berlin, Germany; 0.918 Å). The complete data set was collected from a single crystal, and data were processed with the XDSAPP package.[38]

3.2. Structure Determination and Refinement. Structures were determined by the difference Fourier methods using the structure of the hGCPII/NAAG complex (PDB entry 3BXM[39]) as the template model. Model building was accomplished using Coot,[40] and calculation steps were performed using Refmac 5.1.[41] The restrains library and the coordinate files for individual inhibitors were prepared using the PRODRG server,[42] and the inhibitors/substrates were fitted into the positive electron density map in the final stages of the refinement.

The stereochemical quality of final models was evaluated using MolProbity,[43] and the final model, together with experimental amplitudes, was deposited in the RCSB Protein Data Bank under the entry code 4LQG (hGCPII/4; deposited as hGCPII/CTT1056). Data collection and structure refinement statistics are provided in the Supporting Information, section 3, Table S1.

4. Cell Lines and Cell Culture. CWR22Rv1 and PC-3 cells were incubated in T-75 flasks with complete growth medium (RPMI 1640 containing 10% heat-inactivated fetal calf serum (FBS), 100 units of penicillin, and 100 μg/mL streptomycin) in a humidified incubator at 37 °C and 5% CO$_2$.

4.1. In Vitro Cell Uptake Studies. Confluent CWR22Rv1 and PC-3 cells were detached with 0.25% trypsin−0.53 mM EDTA solution. The cells were washed three times with 1% FBS 1X-RPMI 1640 phosphate-free medium. Cells were subdivided into micro-centrifuge tubes to contain approximately 500 000 cells each in 250 μL of 1% FBS 1X-RPMI 1640 phosphate-free medium and 6.25 μL of ethanol. A solution of [^{18}F]4, [^{18}F]5, or [^{18}F]6 (2 μCi in 3 μL) was added to microcentrifuge tubes containing one of the following: CWR22Rv1 cells (n = 5) in 1% FBS 1X-RPMI 1640 phosphate-free medium; PC-3 cells (n = 5) in 1% FBS 1X-RPMI 1640 phosphate-free medium; 1 mL of 1% FBS 1X-RPMI 1640 phosphate-free medium (n = 3) which served as reference for the total activity incubated with the cells. All samples above were incubated at 37 °C and 5% CO$_2$ for 1 and 2 h. At each time point, the cell pellets were repeatedly washed with PBS (1 mL), centrifuged (2 min at 14 700g) and the medium was removed. The radioactivity of the cell pellets was counted and compared to the total activity references.

4.2. Internalization Studies. Internalization studies followed the method describe for the in vitro cell uptake studies with a minor modification. Following the incubation periods (1 and 2 h) the cells were washed as described in the uptake studies with PBS cooled to 4 °C. The resulting cells were then treated with a solution of 50 mM glycine and 100 mM NaCl at pH 3 for 2 min at 37 °C and 5% CO$_2$. Cells were then centrifuged (2 min at 12 000g), and the supernatants were collected. This treatment was repeated two additional times, and the combined supernatants were counted for external binding, while the cell pellet was counted for internalization.[44,45]

5. In Vivo PET Imaging Studies. All animal experiments were conducted in accordance with the UCSF IACUC approved protocol. Approximately 10^6 CWR22Rv1 PSMA(+) or PC3 PSMA(−) cells in 50:50 mixture of complete medium and matrigel matrix were implanted in the right shoulder of athymic NCr-nu/nu male mice (approximately 8 weeks old) from Charles River (Hollister, CA). Approximately 4 weeks after implantation, animals with tumors reaching 150−300 mm^3 were anesthetized by isoflurane inhalation and were administered with [^{18}F]4, [^{18}F]5, or [^{18}F]6 at 200−250 μCi in 250 μL of saline through tail vein injection. The resulting animals were imaged with 10 min acquisition by a microPET/CT imaging system (Inveon, Siemens, Germany) at 2 h postinjection. PET imaging data were acquired in list mode and reconstructed with the iterative OSEM 2-D reconstruction algorithm provided by the manufacturer.

6. Biodistribution Studies. Four to five weeks after the implantation of CWR22Rv1 PSMA(+) cells or three to four weeks after the implantation of PC3 PSMA(−) cells, tumor bearing mice were anesthetized by isoflurane inhalation and administered with 50 μCi of [^{18}F]4, [^{18}F]5, or [^{18}F]6 in 150 μL of saline through tail vein injection. These mice (CWR22Rv1 at 1 and 2 h postinjection; PC3 at 2 h post injection; n = 4 for each time point) were euthanized for biodistribution analysis. Blood was collected by cardiac puncture. Major organs (heart, lung, liver, spleen, kidney, muscle, bone, and tumor xenografts) were harvested, weighed, and counted in an automated γ counter (Wizard 2, PerkinElmer, Waltham, MA). The percent injected dose per gram (% ID/g) of tissue was calculated by comparison with standards of known radioactivity. Statistical analysis was performed using two-tailed Student t-test (Microsoft Excel Prism software). A p value of <0.05 was considered statistically significant.

membrane antigen, in patients with metastatic prostate cancer. *J. Nucl. Med.* **2012**, *53*, 1883–1891.

(17) Szabo, Z.; Mena, E.; Rowe, S. P.; Plyku, D.; Nidal, R.; Eisenberger, M. A.; Antonarakis, E. S.; Fan, H.; Dannals, R. F.; Chen, Y.; Mease, R. C.; Vranesic, M.; Bhatnagar, A.; Sgouros, G.; Cho, S. Y.; Pomper, M. G. Initial Evaluation of [(18)F]DCFPyL for Prostate-Specific Membrane Antigen (PSMA)-Targeted PET Imaging of Prostate Cancer. *Mol. Imaging Biol.* **2015**, *17*, 565–574.

(18) Mease, R. C.; Dusich, C. L.; Foss, C. A.; Ravert, H. T.; Dannals, R. F.; Seidel, J.; Prideaux, A.; Fox, J. J.; Sgouros, G.; Kozikowski, A. P.; Pomper, M. G. N-[N-[(S)-1,3-Dicarboxypropyl]carbamoyl]-4-[18F]-fluorobenzyl-L-cysteine, [18F]DCFBC: a new imaging probe for prostate cancer. *Clin. Cancer Res.* **2008**, *14*, 3036–3043.

(19) Liu, T.; Toriyabe, Y.; Kazak, M.; Berkman, C. E. Pseudoirreversible inhibition of prostate-specific membrane antigen by phosphoramidate peptidomimetics. *Biochemistry* **2008**, *47*, 12658–12660.

(20) Liu, T.; Nedrow-Byers, J. R.; Hopkins, M. R.; Berkman, C. E. Spacer length effects on in vitro imaging and surface accessibility of fluorescent inhibitors of prostate specific membrane antigen. *Bioorg. Med. Chem. Lett.* **2011**, *21*, 7013–7016.

(21) Nedrow-Byers, J. R.; Jabbes, M.; Jewett, C.; Ganguly, T.; He, H.; Liu, T.; Benny, P.; Bryan, J. N.; Berkman, C. E. A phosphoramidate-based prostate-specific membrane antigen-targeted SPECT agent. *Prostate* **2012**, *72*, 904–912.

(22) Lapi, S. E.; Wahnishe, H.; Pham, D.; Wu, L. Y.; Nedrow-Byers, J. R.; Liu, T.; Vejdani, K.; VanBrocklin, H. F.; Berkman, C. E.; Jones, E. F. Assessment of an 18F-labeled phosphoramidate peptidomimetic as a new prostate-specific membrane antigen-targeted imaging agent for prostate cancer. *J. Nucl. Med.* **2009**, *50*, 2042–2048.

(23) Nedrow-Byers, J. R.; Moore, A. L.; Ganguly, T.; Hopkins, M. R.; Fulton, M. D.; Benny, P. D.; Berkman, C. E. PSMA-targeted SPECT agents: mode of binding effect on in vitro performance. *Prostate* **2013**, *73*, 355–362.

(24) Ganguly, T.; Dannoon, S.; Hopkins, M. R.; Murphy, S.; Cahaya, H.; Blecha, J. E.; Jivan, S.; Drake, C. R.; Barinka, C.; Jones, E. F.; VanBrocklin, H. F.; Berkman, C. E. A high-affinity [(18)F]-labeled phosphoramidate peptidomimetic PSMA-targeted inhibitor for PET imaging of prostate cancer. *Nucl. Med. Biol.* **2015**, *42*, 780–787.

(25) Wu, L. Y.; Anderson, M. O.; Toriyabe, Y.; Maung, J.; Campbell, T. Y.; Tajon, C.; Kazak, M.; Moser, J.; Berkman, C. E. The molecular pruning of a phosphoramidate peptidomimetic inhibitor of prostate-specific membrane antigen. *Bioorg. Med. Chem.* **2007**, *15*, 7434–7443.

(26) Maung, J.; Mallari, J. P.; Girtsman, T. A.; Wu, L. Y.; Rowley, J. A.; Santiago, N. M.; Brunelle, A. N.; Berkman, C. E. Probing for a hydrophobic a binding register in prostate-specific membrane antigen with phenylalkylphosphonamidates. *Bioorg. Med. Chem.* **2004**, *12*, 4969–4979.

(27) Anderson, M. O.; Wu, L. Y.; Santiago, N. M.; Moser, J. M.; Rowley, J. A.; Bolstad, E. S.; Berkman, C. E. Substrate specificity of prostate-specific membrane antigen. *Bioorg. Med. Chem.* **2007**, *15*, 6678–6686.

(28) Liu, T.; Toriyabe, Y.; Kazak, M.; Berkman, C. E. Pseudoirreversible inhibition of prostate-specific membrane antigen by phosphoramidate peptidomimetics. *Biochemistry* **2008**, *47*, 12658–12660.

(29) Barinka, C.; Mlcochova, P.; Sacha, P.; Hilgert, I.; Majer, P.; Slusher, B. S.; Horejsi, V.; Konvalinka, J. Amino acids at the N- and C-termini of human glutamate carboxypeptidase II are required for enzymatic activity and proper folding. *Eur. J. Biochem.* **2004**, *271*, 2782–2790.

(30) Barinka, C.; Rovenska, M.; Mlcochova, P.; Hlouchova, K.; Plechanovova, A.; Majer, P.; Tsukamoto, T.; Slusher, B. S.; Konvalinka, J.; Lubkowski, J. Structural insight into the pharmacophore pocket of human glutamate carboxypeptidase II. *J. Med. Chem.* **2007**, *50*, 3267–3273.

(31) Pavlicek, J.; Ptacek, J.; Barinka, C. Glutamate carboxypeptidase II: an overview of structural studies and their importance for structure-based drug design and deciphering the reaction mechanism of the enzyme. *Curr. Med. Chem.* **2012**, *19*, 1300–1309.

(32) Zhang, A. X.; Murelli, R. P.; Barinka, C.; Michel, J.; Cocleaza, A.; Jorgensen, W. L.; Lubkowski, J.; Spiegel, D. A. A remote arene-binding site on prostate specific membrane antigen revealed by antibody-recruiting small molecules. *J. Am. Chem. Soc.* **2010**, *132*, 12711–12716.

(33) Nedrow, J. R.; Latoche, J. D.; Day, K. E.; Modi, J.; Ganguly, T.; Zeng, D.; Kurland, B. F.; Berkman, C. E.; Anderson, C. J. Targeting PSMA with a Cu-64 labeled phosphoramidate inhibitor for PET/CT imaging of variant PSMA-expressing xenografts in mouse models of prostate cancer. *Mol. Imaging. Biol.* **2016**, *18*, 402–410.

(34) Liu, T.; Wu, L. Y.; Kazak, M.; Berkman, C. E. Cell-Surface labeling and internalization by a fluorescent inhibitor of prostate-specific membrane antigen. *Prostate* **2008**, *68*, 955–964.

(35) Hillier, S. M.; Maresca, K. P.; Femia, F. J.; Marquis, J. C.; Foss, C. A.; Nguyen, N.; Zimmerman, C. N.; Barrett, J. A.; Eckelman, W. C.; Pomper, M. G.; Joyal, J. L.; Babich, J. W. Preclinical evaluation of novel glutamate-urea-lysine analogues that target prostate-specific membrane antigen as molecular imaging pharmaceuticals for prostate cancer. *Cancer Res.* **2009**, *69*, 6932–6940.

(36) Bacich, D. J.; Pinto, J. T.; Tong, W. P.; Heston, W. D. Cloning, expression, genomic localization, and enzymatic activities of the mouse homolog of prostate-specific membrane antigen/NAALADase/folate hydrolase. *Mamm. Genome* **2001**, *12*, 117–123.

(37) Ghosh, A.; Wang, X.; Klein, E.; Heston, W. D. W. Novel role of prostate-specific membrane antigen in suppressing prostate cancer invasiveness. *Cancer Res.* **2005**, *65*, 727–731.

(38) Krug, M.; Weiss, M. S.; Heinemann, U.; Mueller, U. XDSAPP: a graphical user interface for the convenient processing of diffraction data using XDS. *J. Appl. Crystallogr.* **2012**, *45*, 568–572.

(39) Klusak, V.; Barinka, C.; Plechanovova, A.; Mlcochova, P.; Konvalinka, J.; Rulisek, L.; Lubkowski, J. Reaction mechanism of glutamate carboxypeptidase II revealed by mutagenesis, X-ray crystallography, and computational methods. *Biochemistry* **2009**, *48*, 4126–4138.

(40) Emsley, P.; Lohkamp, B.; Scott, W. G.; Cowtan, K. Features and development of Coot. *Acta Crystallogr., Sect. D: Biol. Crystallogr.* **2010**, *66*, 486–501.

(41) Murshudov, G. N.; Skubak, P.; Lebedev, A. A.; Pannu, N. S.; Steiner, R. A.; Nicholls, R. A.; Winn, M. D.; Long, F.; Vagin, A. A. REFMAC5 for the refinement of macromolecular crystal structures. *Acta Crystallogr., Sect. D: Biol. Crystallogr.* **2011**, *67*, 355–367.

(42) Schuttelkopf, A. W.; van Aalten, D. M. PRODRG: a tool for high-throughput crystallography of protein-ligand complexes. *Acta Crystallogr., Sect. D: Biol. Crystallogr.* **2004**, *60*, 1355–1363.

(43) Chen, V. B.; Arendall, W. B., 3rd; Headd, J. J.; Keedy, D. A.; Immormino, R. M.; Kapral, G. J.; Murray, L. W.; Richardson, J. S.; Richardson, D. C. MolProbity: all-atom structure validation for macromolecular crystallography. *Acta Crystallogr., Sect. D: Biol. Crystallogr.* **2010**, *66*, 12–21.

(44) Nedrow-Byers, J. R.; Jabbes, M.; Jewett, C.; Ganguly, T.; He, H.; Liu, T.; Benny, P.; Bryan, J. N.; Berkman, C. E. A phosphoramidate-based prostate-specific membrane antigen-targeted SPECT agent. *Prostate* **2012**, *72*, 904–912.

(45) Kuppuswamy, D.; Pike, L. J. Ligand-induced desensitization of 125I-epidermal growth factor internalization. *J. Biol. Chem.* **1989**, *264*, 3357–3363.

86

■ ASSOCIATED CONTENT

⑤ Supporting Information

The Supporting Information is available free of charge on the ACS Publications website at DOI: 10.1021/acs.jmedchem.5b01850.

> Synthesis and characterization of compound **7** and its precursors; complete experimental details of IC$_{50}$ and mode of inhibition studies; table of crystallographic data and refinement statistics of the compounds (PDF)
> Molecular formula strings (CSV)

Accession Codes

PDB codes are the following: 4LQG (hGCPII/**4**; deposited as hGCPII/CTT1056) and 4JYW (PSMA/**5**; deposited as hGCPII/CTT1057). Authors will release the atomic coordinates and experimental data upon manuscript publication.

■ AUTHOR INFORMATION

Corresponding Authors

*C.E.B.: phone, (509) 335-7613; fax, (509) 335-8389; e-mail, cberkman@wsu.edu.
*H.F.V.: phone, (415) 353-4569; fax, (415) 514-8242; e-mail, henry.vanbrocklin@ucsf.edu.

Notes

The authors declare no competing financial interest.
[⊥]S.D. and T.G. contributed equally.
[#]C.E.B. and H.F.V. contributed equally as senior authors.

■ ACKNOWLEDGMENTS

■ ABBREVIATIONS USED

PSMA, prostate-specific membrane antigen; PCa, prostate cancer; ABS, arene-binding site; AH, aminohexanoic acid; CT, computed tomography; SFB, succinamidyl 4-fluorobenzoate; FB, fluorobenzoate; hGCPII, human glutamate carboxypeptidase II; nM, nanomolar; ^{18}F, fluorine-18; ^{99m}Tc, technitium-99m; ID/g, injected dose/gram; [^{18}F]DCFBC, *N*-[*N*-[(*S*)-1,3-dicarboxypropyl]carbamoyl]-4-[^{18}F]fluorobenzyl-L-cysteine; [^{18}F]DCFPyL, 2-(3-(1-carboxy-5-[(6-[^{18}F]-fluoropyridine-3-carbonyl)amino]pentyl)ureido)pentanedioic acid

■ REFERENCES

(1) Foss, C. A.; Mease, R. C.; Fan, H.; Wang, Y.; Ravert, H. T.; Dannals, R. F.; Olszewski, R. T.; Heston, W. D.; Kozikowski, A. P.; Pomper, M. G. Radiolabeled small-molecule ligands for prostate-specific membrane antigen: in vivo imaging in experimental models of prostate cancer. *Clin. Cancer Res.* **2005**, *11*, 4022−4028.

(2) Gao, X.; Cui, Y.; Levenson, R. M.; Chung, L. W.; Nie, S. In vivo cancer targeting and imaging with semiconductor quantum dots. *Nat. Biotechnol.* **2004**, *22*, 969−976.

(3) Humblet, V.; Lapidus, R.; Williams, L. R.; Tsukamoto, T.; Rojas, C.; Majer, P.; Hin, B.; Ohnishi, S.; De Grand, A. M.; Zaheer, A.; Renze, J. T.; Nakayama, A.; Slusher, B. S.; Frangioni, J. V. High-affinity near-infrared fluorescent small-molecule contrast agents for in vivo imaging of prostate-specific membrane antigen. *Mol. Imaging* **2005**, *4*, 448−462.

(4) Pomper, M. G.; Musachio, J. L.; Zhang, J.; Scheffel, U.; Zhou, Y.; Hilton, J.; Maini, A.; Dannals, R. F.; Wong, D. F.; Kozikowski, A. P. 11C-MCG: synthesis, uptake selectivity, and primate PET of a probe for glutamate carboxypeptidase II (NAALADase). *Mol. Imaging* **2002**, *1*, 96−101.

(5) Smith-Jones, P. M.; Vallabhajosula, S.; Navarro, V.; Bastidas, D.; Goldsmith, S. J.; Bander, N. H. Radiolabeled monoclonal antibodies specific to the extracellular domain of prostate-specific membrane antigen: preclinical studies in nude mice bearing LNCaP human prostate tumor. *J. Nucl. Med.* **2003**, *44*, 610−617.

(6) Tasch, J.; Gong, M.; Sadelain, M.; Heston, W. D. A unique folate hydrolase, prostate-specific membrane antigen (PSMA): a target for immunotherapy? *Crit. Rev. Immunol.* **2001**, *21*, 249−261.

(7) Liu, T.; Wu, L. Y.; Choi, J. K.; Berkman, C. E. Targeted photodynamic therapy for prostate cancer: inducing apoptosis via activation of the caspase-8/-3 cascade pathway. *Int. J. Oncol.* **2010**, *36*, 777−784.

(8) Fracasso, G.; Bellisola, G.; Cingarlini, S.; Castelletti, D.; Prayer-Galetti, T.; Pagano, F.; Tridente, G.; Colombatti, M. Anti-tumor effects of toxins targeted to the prostate specific membrane antigen. *Prostate* **2002**, *53*, 9−23.

(9) Lu, J.; Celis, E. Recognition of prostate tumor cells by cytotoxic T lymphocytes specific for prostate-specific membrane antigen. *Cancer Res.* **2002**, *62*, 5807−5812.

(10) Mease, R. C.; Foss, C. A.; Pomper, M. G. PET imaging in prostate cancer: focus on prostate-specific membrane antigen. *Curr. Top. Med. Chem.* **2013**, *13*, 951−962.

(11) Chen, Y.; Foss, C. A.; Byun, Y.; Nimmagadda, S.; Pullambhatla, M.; Fox, J. J.; Castanares, M.; Lupold, S. E.; Babich, J. W.; Mease, R. C.; Pomper, M. G. Radiohalogenated prostate-specific membrane antigen (PSMA)-based ureas as imaging agents for prostate cancer. *J. Med. Chem.* **2008**, *51*, 7933−7943.

(12) Banerjee, S. R.; Foss, C. A.; Castanares, M.; Mease, R. C.; Byun, Y.; Fox, J. J.; Hilton, J.; Lupold, S. E.; Kozikowski, A. P.; Pomper, M. G. Synthesis and evaluation of technetium-99m- and rhenium-labeled inhibitors of the prostate-specific membrane antigen (PSMA). *J. Med. Chem.* **2008**, *51*, 4504−4517.

(13) Banerjee, S. R.; Pullambhatla, M.; Shallal, H.; Lisok, A.; Mease, R. C.; Pomper, M. G. A modular strategy to prepare multivalent inhibitors of prostate-specific membrane antigen (PSMA). *Oncotarget* **2011**, *2*, 1244−1253.

(14) Banerjee, S. R.; Pullambhatla, M.; Byun, Y.; Nimmagadda, S.; Green, G.; Fox, J. J.; Horti, A.; Mease, R. C.; Pomper, M. G. 68Ga-labeled inhibitors of prostate-specific membrane antigen (PSMA) for imaging prostate cancer. *J. Med. Chem.* **2010**, *53*, 5333−5341.

(15) Chen, Y.; Pullambhatla, M.; Foss, C. A.; Byun, Y.; Nimmagadda, S.; Senthamizhchelvan, S.; Sgouros, G.; Mease, R. C.; Pomper, M. G. 2-(3-{1-Carboxy-5-[(6-[18F]fluoro-pyridine-3-carbonyl)-amino]-pentyl}-ureido)-pen tanedioic acid, [18F]DCFPyL, a PSMA-based PET imaging agent for prostate cancer. *Clin. Cancer Res.* **2011**, *17*, 7645−7653.

(16) Cho, S. Y.; Gage, K. L.; Mease, R. C.; Senthamizhchelvan, S.; Holt, D. P.; Jeffrey-Kwanisai, A.; Endres, C. J.; Dannals, R. F.; Sgouros, G.; Lodge, M.; Eisenberger, M. A.; Rodriguez, R.; Carducci, M. A.; Rojas, C.; Slusher, B. S.; Kozikowski, A. P.; Pomper, M. G. Biodistribution, tumor detection, and radiation dosimetry of 18F-DCFBC, a low-molecular-weight inhibitor of prostate-specific

Supporting Information

Structure-Activity Relationship of ^{18}F-labeled phosphoramidate peptidomimetic Prostate-Specific Membrane Antigen (PSMA)-targeted inhibitor analogues for PET imaging of prostate cancer

Shorouk Dannoon [1#], Tanushree Ganguly [2#], Hendry Cahaya[1], Jonathan J. Geruntho[2], Matthew S. Galliher[2], Sophia K. Beyer[2], Cindy J. Choy[2], Mark R. Hopkins[2], Melanie Regan[1], Joseph E. Blecha[1], Lubica Skultetyova[3], Christopher R. Drake[1], Salma Jivan[1], Cyril Barinka[3], Ella F. Jones[1§], Clifford E. Berkman[2,4§*], Henry F. VanBrocklin[1§*]

[1]Department of Radiology and Biomedical Imaging, University of California San Francisco, USA; [2]Department of Chemistry, Washington State University, USA; [3]Institute of Biotechnology, CR, Prague; [4]Cancer Targeted Technology, USA

\# Contributed equally
§ Contributed equally as senior authors

*Correspondence to:
Prof. Henry F. VanBrocklin
Department of Radiology and Biomedical Imaging
University of California San Francisco
185 Berry Street, Suite 350
San Francisco, CA 94107
tel: (415) 353-4569
fax: (415) 514-8242
henry.vanbrocklin@ucsf.edu

* Prof. Clifford E. Berkman
Department of Chemistry
Washington State University
Pullman, WA 99164–4630.
tel: (509) 335-7613
fax: (509) 335-8389.
cberkman@wsu.edu

Table of contents:

Section 1	Synthesis of 7 and precursors
Section 2	IC_{50} and Mode of inhibition determinations
Section 3	Crystallographic studies - Structure determination and refinement

S2

89

Section 1: Synthesis of 7 and precursors.

1. iBuCOCl
2. —N⟨⟩O
3. NaBH₄, glyme

A
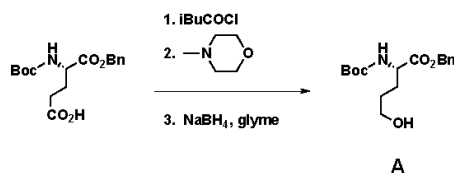
Benzyl 2-((tert-butoxycarbonyl)amino)-5-hydroxypentanoate, A. Boc-Glu(OBn) (1g, 1 equiv) and N-Methylmorpholine (3.55 mmol, 1.2 equiv) were dissolved in 3 mL glyme and stirred at -15C. iso-Butyloxychloride (2.96 mmol, 1 equiv) was then added and stirred for an additional 15 min. The resulting white precipitate was filtered off and NaBH₄ (4.44 mmol, 1.5 equiv) was added to the filterate along with 4 mL of water and stirred for 15 min. Th eraction mixture was dissolved in ethylacetate (EtoAc) and extracted with brine thrice . The organic layer was dried over Mg₂SO₄ and rotary-evaporated at 40°C. Pure product was obtained on drying (0.726 g, 76%). Characterization confirmed formation of the product.

BnOPCl₂

1. OH TEA
2. H₂O/acetonitrile, TEA

CCl₄, TEA

B
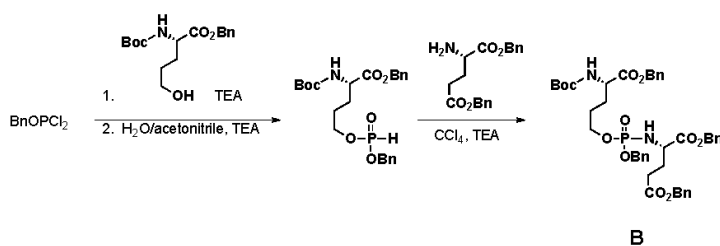
Dibenzyl 2-(((R)-(benzyloxy)(((R)-5-(benzyloxy)-4-((tert-butoxycarbonyl)amino)-5-oxopentyl)oxy)phosphoryl)amino)pentanedioate, B. In a flame dried 100 mL flask, 10 mL dry dichloromethane (DCM) was taken, argon flushed and cooled over dried ice. PCl₂OBn (2.31 mM, 1.5 equiv) and triethyamine (1.855 mM, 1.2 equiv) was added and stirred. A (1.56 mM, 1 equiv) was dissolved in 10 mL of DCM and added to the reaction mixture in parts. After complete addition, dry ice was replaced with ice bath and stirred for 5 h. 1:1 mixture of water:acetonitrile (ACN) was added and stirred for additional 1h. The reaction mixture was rotary-evaporated to remove the organic solvent, dissolved in EtOAc, and washed successively with 10% HCl, 10% NaHCO₃, and brine. Organic layer was dried, concentrated to remove solvent, and dried overnight. Crude phosphite was dissolved in 10 mL dry ACN, flushed with argon₍g₎, cooled on ice and 5 mL of CCl₄ was added. NH₂-Glu(OBn)₂ (1.546 mM, 1 equiv) and TEA (4.638 mM, 3.2 equiv) together were dissolved in 10 mL ACN and added to the phosphite in parts and stirred for 5 h. The reaction mixture was concentrated and purified by C-18 column chromatography using 80:20 MeOH:water as the mobile phase. Product **B** was obtained as pale yellow oil (36.7% yield). ^{1}HNMR (300 MHz, CDCl₃): δ 2.04 (s, 9H), 2.05–2.06 (m, 3H), 2.07 (m, 4h), 2.09 (m, 4h), 3.48–3.52 (m, 1H), 3.91 (t, 4h), 4.94 (m, 4h), 5.07 (m, 4h) , 7.30-7.31 (m, 20H). ^{13}C NMR (300 MHz, CDCl₃): δ 28.5, 28.9, 30.0, 53.8, 53.9, 66.6, 66.7, 67.2, 67.5, 76.9, 77.3, 77.7, 135.5, 154.8, 172.61, 172.65. ^{31}P NMR (300

MHz, CDCl$_3$): δ 8.41, 8.44. ESI mass spectroscopy (M+Na): Calculated 802.3, found 825.3 for C$_{43}$H$_{51}$N$_2$O$_{11}$P$^+$.
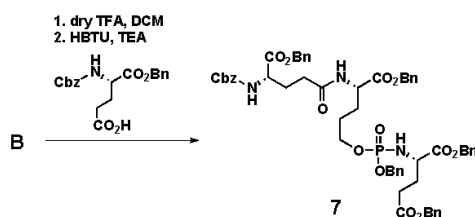
(2S)-dibenzyl 2-(((benzyloxy)(((S)-5-(benzyloxy)-4-((S)-5-(benzyloxy)-4-((tert-butoxycarbonyl)amino)-5-oxopentanamido)-5-oxopentyl)oxy)phosphoryl)amino) pentanedioate, 7. Cbz-Glu(OBn) (0.15g, 1equiv) was dissolved in 3mL of dry DMF in a flame dried flask and argon flushed. HBTU (0.44mmol, 1.1 equiv.) and triethylamine (0.44mmol, 1.1 equiv.) was added and stirred for 30 minutes for pre-activation of the carboxylic acid. In a separate flask, **B** was dissolved in 2mL dry DCM, argon flushed and cooled over ice bath. 1mL of dry TFA was added and stirred for 15 min. DCM was then evaporated off, reaction mixture dissolved in ethylacetate and washed with 10% NaHCO$_3$ (till pH neutralized), brine and organic layer dried on anhy. Na$_2$SO$_4$. It was then redissolved in 2mL dry DMF added to the flask with the pre-activated acid and stirred overnight under Argon$_{(g)}$. The reaction mixture was dissolved in ethyleacetate, and washed with 10% NaHCO$_3$ and brine. Organic layer dried over Na$_2$SO$_4$ and dried under vaccum. Purification was carried out using reversed phase C18 chromatography with 80% MeOH-water as the mobile phase. Pure **7** was isolated in 40% yield. ^{1}HNMR (300 MHz, CDCl$_3$): δ 1.45-1.6 (m, 3H), 1.80-1.98 (m, 2H), 2.04-2.18 (m, 2H), 2.20–2.34 (m, 3H), 2.38–2.48 (m, 2H), 3.45 (m, 1H), 3.82 (t, 2h), 4.37 (m, 1H), 4.56 (m, 1H), 4.81-5.00 (m, 2h), 5.04-5.2 (m, 10H) , 5.89 (d, 1H, -NH), 6.56 (d, 1H, -NH), 6.70 (d, 1H, -NH), 7.22-7.40 (m, 25H). ^{31}P NMR (300 MHz, CDCl$_3$): δ 8.46. ESI mass spectroscopy (M+Na): calculated 1055.40 (M), found 1078.5 for C$_{58}$H$_{62}$N$_3$O$_{14}$P$^+$.

Section 2: IC$_{50}$ and Mode of inhibition determinations.

General method of IC$_{50}$. Inhibition studies were performed as previously described with minor modifications.[1,2] Description is provided in Supplementary material (Section-2). Briefly, working solutions of the substrate N-[4-phenylazo)-benzoyl]-glutamyl-γ-glutamic acid, (PABGgG) and inhibitor were prepared in Tris buffer (50 mM, pH 7.4). Working solutions of purified PSMA were diluted in Tris buffer (50 mM, pH 7.4 containing 1% Triton X-100) to provide 15-20% conversion of substrate to product in the absence of inhibitor. A typical incubation mixture (final volume of 250 μL) was prepared by the addition of either 25 μL of an inhibitor solution or 25 μL TRIS buffer (50 mM, pH 7.4) to 175 μL TRIS buffer (50 mM, pH 7.4). PABGgG (25 μL, 10 μM) was added to the

above solution. The enzymatic reaction was initiated by the addition of 25 μL of the PSMA working solution. In all cases, the final concentration of PABGgG was 1 μM while the enzyme was incubated with five serially diluted inhibitor concentrations providing a range of inhibition from 10% to 90%. The reaction was allowed to proceed for 15 min with constant shaking at 37 °C and was terminated by the addition of 25 μL methanolic TFA (2% v/v trifluoroacetic acid in methanol) followed by vortex. The quenched incubation mixture was quickly buffered by the addition of 25 μL K_2HPO_4 (0.1 M), vortexed, and centrifuged (10 min at 7,000 g). An 85 μL aliquot of the resulting supernatant was subsequently quantified by HPLC as previously described.[3, 4] IC_{50} values were calculated using KaleidaGraph 3.6 (Synergy Software, Reading, PA).

Mode of inhibition Study. The mode of inhibition studies followed the procedure described in our previous work.[5] Description is provided in Supplementary material (Section-2). The concentration of PSMA (2.5μg/mL) was 100-fold greater than used in the typical ezyme activity assays. The enzyme was pre-incubated for 10 minutes with 0.1 μM of inhibitor (40 μL), at approximately 10-fold greater than the IC_{50} value. The solution was diluted with 1 mM of substrate in 50 mM tris + 1% triton buffer (100-fold, total volume 3960 μL). The formation of product was monitored every 5 minutes for 1 hour. A control sample was defined as incubation described here without inhibitor.

S5

92

Section 3: Crystallographic studies - Structure determination and refinement.

Table S1. Data collection and refinement statistics

Data collection statistics		
Inhibitor	**4**	**6**
PDB code	4LQG	---
Wavelength (Å)	0.918	0.918
Space group	I222	I222
Unit-cell parameters *a, b, c* (Å)	101.9, 130.3, 158.3	100.4, 130.5, 157.6
Resolution limits (Å)	50-1.77 (1.87-1.77)	50-1.71 (1.81-1.71)
Number of unique reflections	102,407 (15967)	111,302 (17797)
Redundancy	4.15 (4.14)	5.82 (5.80)
Completeness (%)	99.4% (97.4%)	99.7% (99.4%)
I/σI	13.47 (2.36)	23.42 (3.60)
R_{merge}	0.093 (0.693)	0.052 (0.551)
Refinement Statistics		
Resolution limits (Å)	19.51-1.77 (1.811-1.766)	29.25-1.71 (1.754-1.710)
Total number of reflections	97,284 (7,086)	105,653 (7,750)
Number of reflections in working set	92,164 (6,731)	100,093 (7,342)
Number of reflections in test set	5,120 (355)	5,560 (408)
R/R_{free} (%)	15.9/18.2	16.3/18.0
Total number of non-H atoms	6791	6438
Number of non-H protein atoms	5923	5791
Number Inhibitor molecules	1	1
Number of water molecules	591	409
Average B-factor (Å^2)	13.7	16.8
Protein atoms	12.2	15.6
Waters	20.8	22.2
Inhibitor	31.8	63.7
[&]Ramachandran Plot (%)		
Most favored	97.4	97.8
Additionally allowed	2.5	2.1
Disallowed	0.1	0.1
R.m.s. deviations: bond lengths (Å)	0.019	0.016
bond angles (°)	1.7	1.5
planarity (Å)	0.009	0.009
chiral centers (Å^3)	0.1	0.1
Missing residues	545-546, 654- 655	654-655

* Values in parenthesis are for the highest resolution shells.
[&] Structures were analyzed using the MolProbity package

S6

REFERENCES

1.   Liu, T.; Wu, L. Y.; Kazak, M.; Berkman, C. E. Cell-Surface labeling and internalization by a fluorescent inhibitor of prostate-specific membrane antigen. *Prostate* **2008,** *68,* 955-964.

2.   Wu, L. Y.; Anderson, M. O.; Toriyabe, Y.; Maung, J.; Campbell, T. Y.; Tajon, C.; Kazak, M.; Moser, J.; Berkman, C. E. The molecular pruning of a phosphoramidate peptidomimetic inhibitor of prostate-specific membrane antigen. *Bioorg Med Chem* **2007,** *15,* 7434-7443.

3.   Anderson, M. O.; Wu, L. Y.; Santiago, N. M.; Moser, J. M.; Rowley, J. A.; Bolstad, E. S.; Berkman, C. E. Substrate specificity of prostate-specific membrane antigen. *Bioorg Med Chem* **2007,** *15,* 6678-6686.

4.   Maung, J.; Mallari, J. P.; Girtsman, T. A.; Wu, L. Y.; Rowley, J. A.; Santiago, N. M.; Brunelle, A. N.; Berkman, C. E. Probing for a hydrophobic a binding register in prostate-specific membrane antigen with phenylalkylphosphonamidates. *Bioorg Med Chem* **2004,** *12,* 4969-4979.

5.   Liu, T.; Toriyabe, Y.; Kazak, M.; Berkman, C. E. Pseudoirreversible Inhibition of Prostate-Specific Membrane Antigen by Phosphoramidate Peptidomimetics. *Biochemistry* **2008,** *47,* 12658-12660.

Publication IV: Human histone deacetylase 6 shows strong preference for tubulin dimers over assembled microtubules.

BACKGROUND:

Acetylation of the side chain of α-tubulin Lys40 is a part the so-called tubulin code encompassing all tubulin PTMs. This code regulates polymerization/depolymerization of tubulin, binding of microtubule associated proteins, and as a consequence a myriad of cellular processes. The acetylation of the Lys40 itself seems to play role in sperm motility, fertility, cell signaling, cell cycle progression, intracellular transport, neurodegenerative diseases, and serves to protect long-lived microtubules against mechanical ageing. Relying on combination of microscopy and quantification of *in vitro* deacetylation assays using purified components (human full length HDAC6 and porcine tubulin) our publication provides the missing quantitative and qualitative data on HDAC6 preferences for different tubulin forms as well as direct visualization of HDAC6/tubulin interaction.

METHODS:

Human HDAC6 (amino acids 2-1215) was heterologously expressed in HEK-293-T17 cells and purified to homogeneity by a combination of affinity and size exclusion chromatography. LC-MS/MS was used to determine possible PTMs of HDAC6 and acetylation levels of tubulin isolated from porcine brains. Activity and sensitivity to inhibitors was assessed using fluorometric *in vitro* deacetylation assays with AMC labeled peptide substrates. Deacetylation rates of free tubulin dimers and tubulin polymers were determined by Western blot quantification. Tubulin polymers were prepared by incubation of tubulin with GMP/GMPCPP (MT), Zn^{2+} (zinc sheets), or Dolastatin-10 (dolastatin rings) and stabilized by taxol. Deacetylation rates of fluorophore tubulin peptides derived from αAcK40 loop were determined by HPLC-based quantification of *in vitro* deacetylation assays. Visualization of HDAC6 binding and deacetylation of MTs was done by TIRF and indirect immunofluorescence microscopy using fluorescently labeled HDAC6 and MTs.

RESULTS:

We have purified full length human HDAC6 without tags and PTMs. We have determined that the turnover rate for free tubulin dimers is 0.6 s^{-1} and that HDAC6 has strong (1500-fold) preference for the unpolymerized tubulin over the MTs. Deacetylation assays with other tubulin polymers indicate that HDAC6 requires additional interactions outside the αAcK40 loop for efficient deacetylation of tubulin. Availability of particular surface regions of tubulin dimers is necessary for effective deacetylation. These regions are in polymers blocked by the lateral and longitudinal interactions. This is further supported by experiments in which we used a series of peptides derived from the α-tubulin sequence as HDAC6 substrate. These peptides are of varying length (3-19 amino acids) with acetylated Lys40 as the central amino acid. A lack of increase in affinity with the growing length of the peptide substrates was observed. This indicates a limited contribution of residues beyond the P_1 and P_{-1} positions to the substrate binding/recognition. Using a combination of TIRF microscopy and indirect immunofluorescence microscopy we have shown that the deacetylation is carried out uniformly along the MT length without preference for the MT tips.

CONCLUSION:

Our results represent quantitative proof of the hypothesis of opposing substrate preferences of the tubulin acetyl transferase and deacetylase originally formulated by Skoge *et al.*, 2014.

MY CONTRIBUTION:

I cloned human HDAC6 variants, performed pilot experiments identifying the optimal expression system, heterologously expressed and purified HDAC6 variants, and established experimental protocols for HDAC6 activity measurements on tubulin-derived substrates. I also contributed substantially to writing of the article.

SCIENTIFIC REPORTS

OPEN

Human histone deacetylase 6 shows strong preference for tubulin dimers over assembled microtubules

Lubica Skultetyova[1,2], Kseniya Ustinova[1], Zsofia Kutil[1], Zora Novakova[1], Jiri Pavlicek[1], Jana Mikesova[1], Dalibor Trapl[1], Petra Baranova[1], Barbora Havlinova[1], Martin Hubalek[3], Zdenek Lansky[1] & Cyril Barinka[1]

Human histone deacetylase 6 (HDAC6) is the major deacetylase responsible for removing the acetyl group from Lys40 of α-tubulin (αK40), which is located lumenally in polymerized microtubules. Here, we provide a detailed kinetic analysis of tubulin deacetylation and HDAC6/microtubule interactions using individual purified components. Our data unequivocally show that free tubulin dimers represent the preferred HDAC6 substrate, with a K_M value of 0.23 µM and a deacetylation rate over 1,500-fold higher than that of assembled microtubules. We attribute the lower deacetylation rate of microtubules to both longitudinal and lateral lattice interactions within tubulin polymers. Using TIRF microscopy, we directly visualized stochastic binding of HDAC6 to assembled microtubules without any detectable preferential binding to microtubule tips. Likewise, indirect immunofluorescence microscopy revealed that microtubule deacetylation by HDAC6 is carried out stochastically along the whole microtubule length, rather than from the open extremities. Our data thus complement prior studies on tubulin acetylation and further strengthen the rationale for the correlation between tubulin acetylation and microtubule age.

Tubulin post-translational modifications (PTMs) provide mechanisms enabling highly conserved α/β-tubulin dimers to form microtubules (MTs) endowed with different functional properties. The best studied PTMs, collectively called the "tubulin code", include detyrosination, glutamylation, glycylation, polyamination, phosphorylation, and acetylation[1–6]. Whereas the majority of PTMs are found within the unstructured C-terminal tubulin tails decorating the outer surface of microtubules, acetylation at the Lys40 side chain of the α-tubulin subunit (αK40) stands out due to its presumed localization within the microtubule lumen[7]. This αK40 acetylation is a hallmark of long-lived stable microtubules and can affect sperm motility, fertility, cell signaling, and cell cycle progression[8–10]. Additionally, microtubule acetylation may be a regulatory step for intracellular kinesin/dynein-mediated transport[11–13] and, consequently, has been implicated in the pathologies of a variety of human neurodegenerative diseases. At the same time, intraluminal positioning of the flexible loop harboring αK40 understandably brings about questions concerning the accessibility of this site for relevant modifying enzymes.

The acetylation status of αK40 is defined by the opposing activities of tubulin acetyl transferases, most notably the mammalian α-tubulin N-acetyltransferase 1 (αTAT1) and its ortholog MEC-17 from *C. elegans*[9,14], and lysine deacetylases, namely histone deacetylase 6 (HDAC6) and SIRT2[15–17]. Although HDAC6 and SIRT2 may interact and function together, several studies indicate that HDAC6, not SIRT2, is the major tubulin deacetylase[18,19]. A recent report[20] suggests that the two deacetylases might have both overlapping and distinct tubulin deacetylase activities depending on the specific structural contexts of αK40, as well as the physiological state of the cell. Of note, several additional acetylation sites in tubulin have been identified to date[21–23], but their functional role and the characterization of the enzymes responsible require further research in this direction.

[1]Institute of Biotechnology CAS, BIOCEV, Prumyslova 595, 252 50, Vestec, Czech Republic. [2]Department of Biochemistry, Faculty of Natural Science, Charles University, Albertov 6, Prague 2, Czech Republic. [3]Institute of Organic Chemistry and Biochemistry of the Academy of Sciences of the Czech Republic, Flemingovo n. 2, 166 10, Prague 6, Czech Republic. Correspondence and requests for materials should be addressed to C.B. (email: cyril.barinka@ibt.cas.cz)

HDAC6, a member of the class IIb zinc-dependent histone deacetylases, stands out as a structurally and functionally unique member of the HDAC family due to its complex domain organization and atypical predominantly cytosolic localization. HDAC6 harbors the tandem catalytic domains DD1 and DD2, a cytoplasm-anchoring serine/glutamate-rich repeat motifs, and the C-terminal ubiquitin binding domain, which is implicated in sequestering misfolded polyubiquitinated protein aggregates and transporting them to the aggresome[24]. Several post-translational modifications, including phosphorylation, acetylation, and S-nitrosylation, have been shown to regulate HDAC6 deacetylase activity, nucleus/cytoplasm shuttling, and interactions with physiological partners[25–28]. Given the broad repertoire of HDAC6 substrates and interaction partners (e.g., heat-shock protein 90, cortactin, peroxiredoxin, β-catenin, dynein)[29–33], it is not surprising that the enzyme is involved in many (patho) physiological processes, including cell motility and metastasis, cell signaling, protein folding and degradation, and inflammation. Consequently, targeting HDAC6 is a viable strategy for the treatment of various disorders, such as neurodegenerative diseases, multiple myelomas, and solid malignancies[34–37].

Despite the fact that HDAC6 was identified as the major tubulin deacetylase more than 10 years ago, there is a surprising nearly total absence of qualitative/quantitative data concerning HDAC6 preferences for different tubulin forms. Moreover, when available, these findings are relatively contentious and somewhat difficult to reconcile. Finally, the majority of studies have used either partially purified HDAC6 and/or tubulin preparations, or orthologs and truncated variants of human HDAC6, as these are more readily available in the amounts required for biochemical/structural studies. In their seminal paper, Hubbert *et al.*, described for the first time the way in which HDAC6 functions as a tubulin deacetylase. *In vitro* experiments using mouse HDAC6 revealed that the enzyme deacetylates assembled microtubules, but not free tubulin[15]. This notion was subsequently challenged by several reports showing that both free heterodimers and assembled MTs can serve as HDAC6 substrates, but no quantitative data to evaluate substrate preferences were presented[16, 17, 38]. In this report, we exploited a bottom-up biochemical approach using purified full-length human HDAC6 and tubulin to assess HDAC6 substrate preferences and shed light on the structural features that govern HDAC6/tubulin interactions. We also directly visualized HDAC6/tubulin interactions, suggesting that the enzyme binds preferentially to the external face of assembled microtubules.

Results

Expression and characterization of full-length human HDAC6.
The HEK293T-based mammalian system was selected for heterologous HDAC6 expression to secure the closest semblance to the native wild-type HDAC6 protein existing in human cells/tissues. Using a combination of affinity and size-exclusion chromatography, we were able to obtain homogenous preparation of untagged human HDAC6 (Fig. 1a) with yields of approximately 2 mgs per liter of original cell culture.

Previous reports have pointed out the influence of PTMs (namely acetylation and phosphorylation) on HDAC6 deacetylase activity[25, 26, 39–41]. To determine whether any such "activity-altering" PTMs existed in our HDAC6 preparation, the protein was analyzed using liquid chromatography-tandem mass spectrometry (LC-MS/MS). The deconvolution of the MS/MS spectra revealed the absence of any known (or unreported) PTM, thus excluding the possibility of our *in vitro* experiments being impacted by HDAC6 PTMs (data not shown).

To assess the deacetylase activity of untagged HDAC6, we determined its kinetic parameters in comparison to several commercially available substrates (Fig. 1b). K_M values were in the low micromolar range (3.7–11.3 μM) and turnover numbers (k_{cat}) ranged from 0.9–2.2 s^{-1}, in good agreement with data reported in the literature[42, 43]. Furthermore, using the same substrate set, we also verified that the attachment of N-terminal tags (either HALO- or GFP-tags) does not influence HDAC6 deacetylation activity (Supplementary Fig. S1). Finally, HDAC6 was profiled against suberoylanilide hydroxamic acid (SAHA), trichostatin (TSA), and nexturastat A (Nex A), with IC_{50} values of 3.8, 0.16, and 2.9 nM, respectively, also in the range reported in scientific literature[44–47] (Fig. 1c).

Overall, the above-mentioned characteristics confirm that our HDAC6 is a homogenous, properly folded, highly-active full-length enzyme well suited for the presented biochemical experiments.

HDAC6 prefers tubulin dimers to microtubules.
Several earlier studies assessed the deacetylation activity of HDAC6 on tubulin and polymerized microtubules[15–17, 38, 48]; however, these studies predominantly used orthologs of human HDAC (mouse, zebrafish), their truncated (or tagged and modified) variants, and/or unpurified (or partly purified) assay components. To the best of our knowledge, none of the prior studies attempted to quantify deacetylase preferences of the full-length human HDAC6 for free tubulin versus assembled MTs. For our biochemical experiments, we took advantage of the fact that tubulin isolated from porcine brain tissue is highly acetylated, with the αK40 acetylation levels comprising 36% of the total tubulin (Supplementary Fig. S2).

We directly compared the catalytic activity of human HDAC6 on free tubulin dimers against its activity on paclitaxel- and GMPCPP-stabilized MTs (Fig. 2). Using highly-purified components, we showed that free tubulin dimers are the preferred HDAC6 substrate. At a 1 μM substrate concentration, the deacetylation rate was 0.6 mol/mol*s and 0.0004 mol/mol*s for tubulin dimers and stabilized MTs, respectively; in other words, the deacetylation rate was approximately 1,500-fold higher for αβ-tubulin dimers. Importantly, deacetylation rates on both paclitaxel- and GMPCPP-stabilized MTs were virtually identical, suggesting that substantially slower deacetylation of assembled MTs does not result from the compound interference, but is rather linked to either tubulin lattice packing or the limited accessibility of the luminal αK40 loop.

Contacts within polymer lattices inhibit tubulin deacetylation by HDAC6.
Unlike other known microtubule PTMs, which are positioned at the external surface of MTs, αK40 is confined to the MT lumen. Consequently, the substantially lower MT deacetylation rates (as compared to tubulin dimers) could simply result from hindered accessibility of the αK40 loop by the enzyme. Additional factors, such as the transition from curved (free tubulin) to straight (microtubules) tubulin dimer conformations or the blockage of HDAC6/tubulin

98
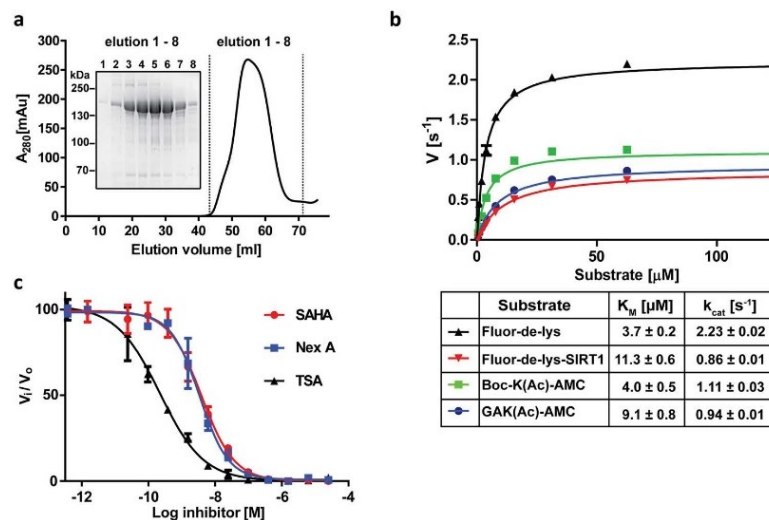
Figure 1. Purification and characterization of full length HDAC6. (**a**) Elution profile of human HDAC6 from a Superdex 16/600 HR200 size-exclusion column (SEC) and reducing SDS-PAGE analysis of HDAC6 fractions from the SEC, documenting monodispersity and >95% purity of the final enzyme preparation, respectively. (**b**) Steady-state kinetics of HDAC6 on commercial fluorogenic peptide substrates GAK(Ac)-AMC, Boc-K(Ac)-AMC, FLUOR-DE-LYS, and FLUOR-DE-LYS-SIRT1. Michaelis-Menten constants (K_M and k_{cat}) for individual peptides, calculated from non-linear regression fit using the GraphPad program, are shown in the embedded table. Data represent mean values ± s.d. (n = 3). (**c**) IC50 values for SAHA (3.8 nM), Nexturastat A (2.9 nM), and Trichostatin A (0.16 nM) were determined using a fluorometric assay with 10 μM (Ac)GAK(Ac)-AMC as a substrate. Data are plotted as mean values ± s.d. from three independent experiments (n = 3).

interaction interfaces by longitudinal/lateral contacts within the polymer lattice, may also play a role. To distinguish between the above-mentioned scenarios, we assessed HDAC6 deacetylation activity using microtubules, Zn-sheets, and Dolastatin-10 rings, three tubulin polymeric forms with distinctly different geometries (Fig. 2).

Dolastatin-10 induces single-walled tubulin rings by curving individual protofilaments such that their luminal surface becomes accessible on the exterior of the ring[49]. In Zn-sheets, protofilaments of alternating polarity are arrayed in parallel and the "luminal" surface, as would be defined in microtubules, is exposed to the solution[50]. All tubulin polymers were deacetylated substantially (100- to 1,500-fold) slower than were free dimers (Fig. 2). As the "luminal" surface harboring the αK40 loop is exposed in both Zn-sheets and Dolastatin-10 rings, lower deacetylation rates cannot be simply attributed to the inaccessibility of the αK40 within the lumen of assembled MTs. Instead, we argue that it is the presence of both lateral and longitudinal contacts within the tubulin polymer lattices that negatively influences deacetylation by HDAC6, as documented by 100- and 750-fold slower deacetylation rates observed for Dolastatin-10 rings and Zn-sheets, respectively.

Structural features outside the αK40 loop of αβ-tubulin are important for HDAC6 interactions.

We first turned our attention to HDAC6 recognition of the isolated αK40 loop to answer the following questions: (i) is the "isolated" sequence of the αK40 loop recognized by HDAC6; (ii) what is the minimum sequence length to be processed/recognized; and (iii) is there a difference in deacetylation rates between the αK40 loop in the form of a free peptide and within the context of an αβ-tubulin dimer?

To this end, we synthesized a series of peptides of different lengths derived from the human α-tubulin sequence that are centered at acetylated αK40 (T3–T19). Next, using a deacetylation assay followed by high-performance liquid chromatography (HPLC) analysis, we determined the kinetic parameters of HDAC6 against acetylated αK40-derived peptides (Fig. 3). The K_M values for the peptides were in the high micromolar range (88 μM to 328 μM for T9 and T15, respectively), revealing relatively low affinity of HDAC6 for the isolated αK40 sequences. At the same time, K_M values for all tubulin-derived peptides were very similar and there was no clear trend showing increasing affinity with the extension of the peptide sequence. Consequently, it is likely that within the isolated αK40 loop sequence, there is a limited contribution of residues beyond the P_1 and P_{-1} positions to substrate binding/recognition. We also noticed a negative correlation between the peptide length and deacetylation rates, with the shortest T3 tripeptide being deacetylated 20-fold more efficiently when compared to the T19 sequence (Fig. 3a).

We then used the same experimental setup to directly compare deacetylation rates of the αK40 loop in its "free" peptidic form and in the context of αβ-tubulin dimers at a 3 μM concentration. Interestingly, free peptides were deacetylated approximately 12- to 200-fold less efficiently than were tubulin dimers (Fig. 3c). Additionally,
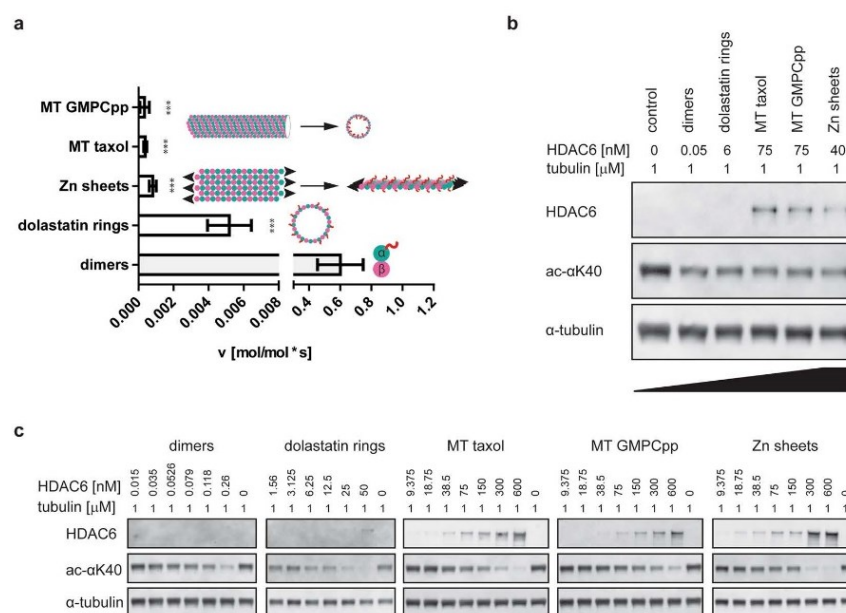
Figure 2. HDAC6 shows strong preference for tubulin dimers over polymeric forms. (**a**) Deacetylation activity of HDAC6 on tubulin polymers (zinc sheets, Dolastatin-10 rings, and taxol/GMPCPP-stabilized microtubules [MT]) and tubulin dimers was determined using Western blot quantification. Results clearly show that free dimers are deacetylated 100- to 1,500-fold more efficiently than are tubulin polymeric forms. Data represent mean values $\pm$ s.d. (n $>$ 3; ***p $<$ 0.001). Organization of tubulin in polymers is illustrated in schemes embedded in the graph, with α-tubulin and β-tubulin shown as blue and pink spheres, respectively, and the acetyl group as a red ribbon. (**b,c**) Representative Western blots illustrating distinct HDAC6 deacetylase activity on tubulin dimers and polymeric forms. Individual substrates (1 μM) were incubated with indicated concentrations of HDAC6 for 1 h at 37 °C. Protein samples were separated by SDS-PAGE, electrotransferred to a polyvinylidene difluoride (PVDF) membrane and acetylation levels quantified using an αK(Ac)40-specific fluorescence signal normalized to the amount of total tubulin detected by rabbit polyclonal anti-α tubulin antibody.

we determined the kinetic parameters of HDAC6 for free tubulin to be $K_M = 0.23 \pm 0.05\,\mu$M and $k_{cat} = 0.6\,\text{s}^{-1}$ (Fig. 3d), revealing that the dramatically higher ($>$6,000-fold) HDAC6 catalytic efficacy (K_M/k_{cat}) for the natively-folded tubulin, as compared to free peptides, stems mostly from the increase in binding affinity, rather than from the increase in reaction speed. These results suggest that sequences and/or structural features outside the αK40 loop contribute to HDAC6/tubulin interactions. Such additional interaction sites might include lateral/longitudinal interfaces buried within tubulin polymeric lattices, as revealed by experiments where different MT polymers were used as substrates (see above).

HDAC6 binds and deacetylates microtubules without a preference for microtubule tips.
Given the relatively slow, but clearly distinguishable deacetylation of MTs by HDAC6, we asked how the enzyme accesses the αK40 loop in the MT lumen. Non-exclusive options would involve entering the MT lumen via open tips, through bends and breaks in the MT lattice, or by deacetylation of the αK40 loop "protruding" from the external microtubule face.

To this end, we first investigated the localization and kinetics of HDAC6 interactions with assembled MTs using total internal reflection fluorescence (TIRF) microscopy. Rhodamine-labeled paclitaxel-stabilized MTs were immobilized on a cover slip, probed with either GFP-HDAC6, or FITC-HALO-HDAC6 fusions, and then directly visualized using a Nikon Ti-E microscope equipped with H-TIRF System (Fig. 4). The kinetics of HDAC6 binding to MTs were quite fast, with all MTs fully decorated in less than a minute. Based on signal distribution analysis during HDAC6 binding to the MTs, we did not detect any preferential binding to MT tips. Instead, we observed uniformly-distributed interactions along the MT length throughout the whole experiment, up until the time that the binding equilibrium was established. The rapid binding kinetics and even signal distribution suggest that HDAC6 does not enter the microtubule lumen from the open tips, but rather binds to and interacts with the external face of MTs.

Given the observed interactions of HDAC6 with the outer MT surface, we wondered whether HDAC6 binding to MTs is also translated into stochastic, rather than open-end favored, MT deacetylation. To answer this

100

Peptide	Sequence	V_{max} (s^{-1})	K_M (µM)
T3	Abz-D{K-Ac}T--NH2	2.03 ± 0.10	105 ± 13
T5	Abz-SD{K-Ac}TI--NH2	1.21 ± 0.03	93 ± 6
T7	Abz-PSD{K-Ac}TIG--NH2	0.44 ± 0.02	149 ± 12
T9	Abz-MPSD{K-Ac}TIGG--NH2	0.31 ± 0.04	88 ± 28
T11	Abz-QMPSD{K-Ac}TIGGG--NH2	0.25 ± 0.01	141 ± 19
T13	Abz-GQMPSD{K-Ac}TIGGGD--NH2	0.32 ± 0.03	223 ± 39
T15	Abz-DGQMPSD{K-Ac}TIGGGDD--NH2	0.12 ± 0.01	328 ± 64
T17	Abz-PDGQMPSD{K-Ac}TIGGGDDS--NH2	0.10 ± 0.01	153 ± 45
T19	Abz-QPDGQMPSD{K-Ac}TIGGGDDSF--NH2	0.10 ± 0.03	228 ± 139

Figure 3. Structural features outside the αK40 loop are required for efficient substrate deacetylation by HDAC6. (**a,b**) Michaelis-Menten kinetics for peptides derived from the Lys40 of α-tubulin (αK40) loop (3-mer to 19-mer; T3 through T19) were determined *in vitro* using an HPLC-based assay (**a**). Corresponding kinetic parameters derived from the non-linear regression fit of experimental data, together with peptide sequences, are shown in (**b**). High micromolar K_M values indicate low affinity of HDAC6 for tested peptides, with limited contribution of residues that do not directly neighbor the central acetyllysine for the overall HDAC6 affinity/specificity. (**c**) Comparison of HDAC6 deacetylation rates using various substrates (natively-folded αβ-tubulin dimers, denatured tubulin dimers, peptides T3 through T19) at identical 3 µM concentrations. Deacetylation rates were determined using an HPLC assay for peptides and Western blotting quantification for tubulin dimers. Natively folded tubulin dimers are deacetylated 50- to 800-fold more efficiently than are either denatured tubulin dimers or "isolated" αK40 loop-derived peptides, suggesting that interactions/structural features outside the αK40 loop are required for efficient HDAC6/tubulin interactions. Data are presented as mean values ± s.d. (n = 3). (**d**) Steady-state kinetics of tubulin dimer deacetylation by HDAC6. Michaelis-Menten constants (K_M and k_{cat}) were calculated from non-linear regression fit using the GraphPad program. Data represent mean values ± s.d. (n = 3).

question, taxol-stabilized MTs (1 µM) were deacetylated using 2 µM HDAC6 in the BRB80 buffer, and the time course of deacetylation was then evaluated side-by-side both via fluorescence microscopy and biochemically (Fig. 5). The fluorescence microscopy and the parallel quantitative Western blotting revealed that the αK40 acetylation decreased over time, with only 10–15% of the original acetylation levels remaining after 120 minutes. More importantly, we observed that the extent of the deacetylation by HDAC6 was uniform along the whole MT length, as evidenced by the constant ratio of the immunofluorescence signal between the αK40 and total tubulin at microtubule tips, and the distance of 10 µm towards the MT center (Fig. 5a). Surprisingly, the spatio-temporal pattern of MT deacetylation appears to differ from the opposite reaction carried out by tubulin acetyltransferase, which favors open MT tips as the site of action[51–53].

Discussion

Although it has been known for more than a decade that HDAC6 is the primary deacetylase responsible for the removal of the acetylation mark at the αK40 position of tubulin, there are surprisingly few quantitative data characterizing human HDAC6 as tubulin deacetylase. Our report thus fills this gap by offering a detailed biochemical analysis of tubulin deacetylation by full-length human HDAC6, which reveals a strong preference for tubulin dimers over assembled microtubules. Additionally, we show that although isolated peptides derived from the αK40 loop are deacetylated by the enzyme, the structural context of native tubulin outside the loop is critical for highly efficient deacetylation. Finally, we directly visualized HDAC6/tubulin interactions for the first time, suggesting predominant HDAC6 binding to the external surface of assembled MTs.

The present study employed a bottom-up approach, where individual, isolated components were first purified and then combined and examined in a panel of biochemical and biophysical experiments. To this end, we cloned, expressed, and purified to homogeneity several human HDAC6 constructs, together with the corresponding control proteins in HEK293T cells. When we compared the activity of our HDAC6 preparations to the activities of recombinant proteins produced in *E. coli* or baculovirus systems (commercially available and/or reported in literature) our HEK293T-expressed enzymes were typically more active on equivalent substrates[42, 43, 48]. As the

101
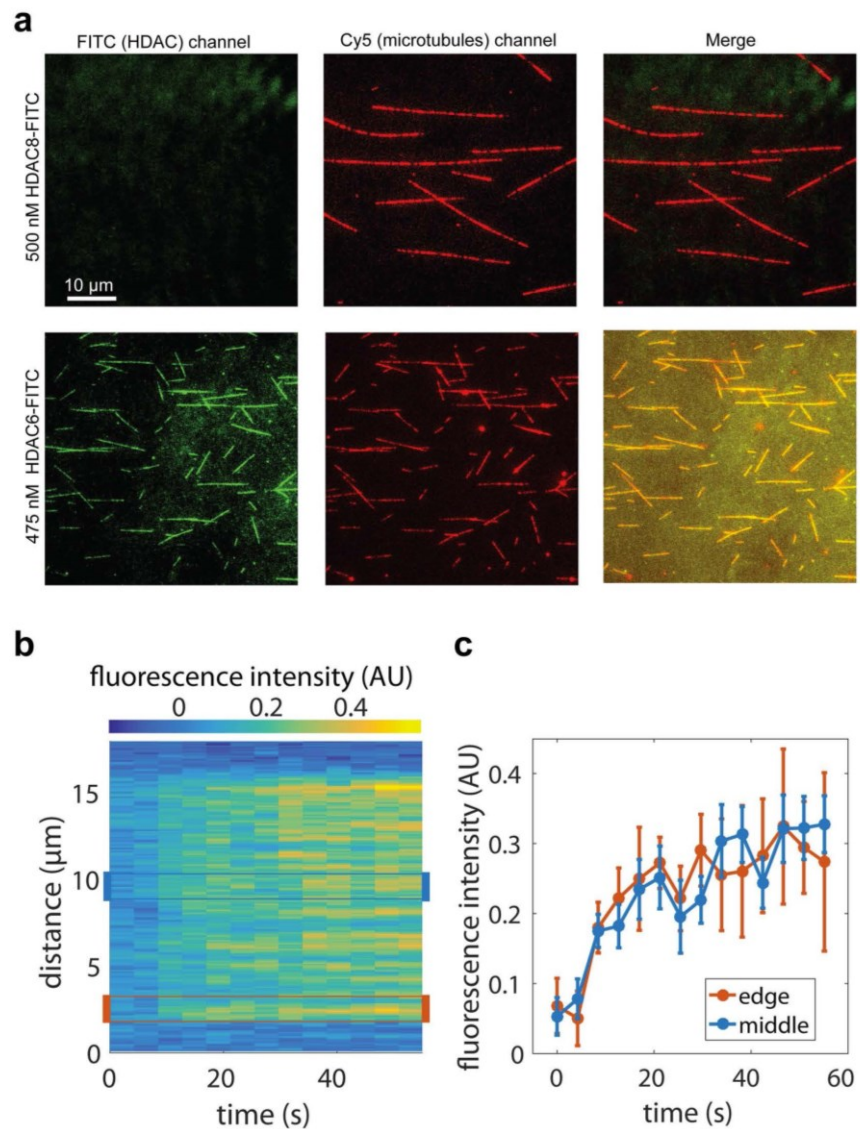
Figure 4. Interaction of HDAC6 with microtubules visualized by TIRF microscopy. (**a**) HDAC6 interacts directly with microtubules. Cy5-labeled microtubules were immobilized on a glass coverslip surface. Micrographs show microtubules (red) in the presence of 500 nM HDAC8-FITC (green; negative control, upper panel) or 475 nM FITC-labeled HDAC6 (green; lower panel). In the presence of FITC-labeled HDAC6, fluorescent signals of microtubules and HDAC6 co-localize along the whole length of microtubules (yellow). (**b,c**) HDAC6-GFP binds uniformly along the whole length of the microtubules. GFP-HDAC6 fusion was added to surface-immobilized microtubules and visualized in the 488 channel using TIRF microscopy. Uniform increase in GFP fluorescence intensity was observed along the whole length of microtubules. The kymograph in Panel B depicts averaged (background subtracted) GFP fluorescence intensity of 4 microtubules of the same length (approximately 12 µm) after the addition of HDAC6-GFP in the timespan from 0 to 60 seconds. The right panel shows the averaged GFP signal (±s.d.) over time at the edge of the microtubules (orange line) and in the middle (blue line). The regions (width of 1.5 µm) used for the averaging are indicated in the kymograph (**b**) by orange and blue rectangles.
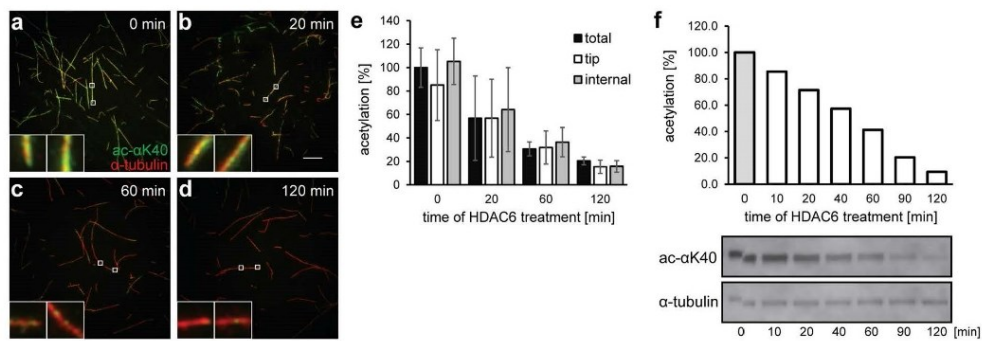
Figure 5. Stochastic, time-dependent deacetylation of assembled microtubules by HDAC6. *In vitro* assembled microtubules (1 μM) were treated with 2 μM human HDAC6 in BRB80 buffer. Deacetylation reactions were terminated at defined time points by the addition of 10 μM SAHA, and the acetylation of αK40 was quantified in parallel by indirect immunofluorescence microscopy (**a–e**) and Western blotting (**f**). (**a–e**) Indirect immunofluorescence microscopy was used to visualize the spatial distribution of αK40 acetylation signals along the length of microtubules at the given time points (upper right corner). Microtubules were immobilized on poly-L-lysine coverslips and probed with anti-αK(Ac)40 (green) and anti-α-tubulin (red) antibodies. The staining intensity of acetylated αK40 decreases over the time and the decrease parallels changes observed in the concomitant biochemical experiment. Additionally, the signal decrease is uniform over the whole length of the microtubules (see insets and panel e), suggesting that deacetylation of MTs by HDAC6 does not spread from the open tips, but is rather stochastic throughout the MT length. The left insets show microtubule tips and the right insets show the internal parts of microtubules positioned 10 μm from the tip. (**e**) Shows averaged intensity of the signal originating from a whole microtubule (total), the tip, and an area positioned 10 μm from the tip (internal). Bar = 10 μm. (**f**) Protein samples were electrotransferred to a PVDF membrane following SDS-PAGE separation, and then acetylation levels were quantified using an αK40-specific fluorescence signal normalized to the amount of total tubulin detected by rabbit polyclonal anti-α tubulin antibody. The decrease parallels changes observed in the concomitant immunofluorescence microscopy experiment.

increased activity cannot be linked to post-translation modifications, which are absent from our samples, a more likely explanation would be a higher percentage of enzymatically competent molecules in our HDAC6 preparations, which are thus more suitable for the present biochemical experiments.

Next, we evaluated the *in vitro* HDAC6 activity using a panel of different substrates. At the peptide level, HDAC6 deacetylates αK40-derived peptides with relatively low affinity (high micromolar K_M values) and k_{cat} values in the range of 0.1–2 s^{-1}. For comparison, SIRT2 deacetylates the T9 peptide somewhat less efficiently ($k_{cat} = 0.144 + 0.005$ s^{-1} and $k_{cat}/K_M = 894 + 100$ M^{-1}s^{-1})[17], whereas αTAT1 has no activity on the T19 peptide[54]. The HDAC6 deacetylation of the T3–T19 peptide series clearly shows that amino acids beyond positions P_{-1} and P_{+1} around the central lysine are not critical for the recognition of the target peptidic substrates by HDAC6. These results are consistent with our unpublished data, as well as with reports mapping substrate specificity of HDAC6, which show that the enzyme is rather promiscuous at the peptide level, with few positional amino acid preferences[55]. A mechanistic explanation of these biochemical observations was recently provided by the crystal structure of HDAC6 complexes with tubulin/histone-derived peptides, which revealed that HDAC6/peptide contacts are limited to the recognition of the scissile acetyllysine, namely direct and water-mediated contacts with the acetyllysine amide and carbonyl groups, respectively[56].

There is a clear difference between recognition and deacetylation of peptidic substrates and tubulin. Understandably, the recognition pattern of tubulin dimers by HDAC6 is considerably more complex than that of short peptides. This was supported in the current study by the substantially lower Michaelis constant ($K_M = 0.23$ μM) of the deacetylation reaction using tubulin dimers as a substrate (Fig. 3d). Additionally, overall catalytic efficacy (k_{cat}/K_M) was 2.6 μM^{-1}s^{-1} and 0.00044 μM^{-1}s^{-1} for tubulin dimers and the T19 peptide, respectively, revealing a striking 6,000-fold preference for native tubulin dimers as a substrate. Furthermore, in contrast to tubulin dimers isolated from porcine brains in a natively-folded state (confirmed by its ability to polymerize into MTs), when thermally-denatured tubulin was used as a substrate, its deacetylation rate by HDAC6 was much slower, more in the range of the deacetylation rates of free peptides (Fig. 3c), implying that the secondary/tertiary structural features, rather than simple linear amino acid motifs, outside the αK40 loop are critical for interactions with HDAC6. Our study points towards residues at the longitudinal/lateral interfaces of tubulin, which are buried in tubulin polymers, as being critical for free tubulin recognition/deacetylation. Although HDAC6/tubulin interactions are not fully understood, a study by Miyake *et al.*, provided some mechanistic explanation by showing that in addition to residues located at the rim of the HDAC6 tunnel leading to the catalytic site, a uniquely-positioned H25 α-helix and Trp459 and Asn460 residues in a flexible loop joining helices H20 and H21 are critical for tubulin deacetylation. At the same time, substitutions at these positions have a limited effect on the deacetylation of peptidic substrates, indicating that the capacity to use/bind tubulin as a substrate, rather than the catalytic potential of HDAC6, is impaired[48].

103

The quantitative data reported here demonstrate that free tubulin dimers are deacetylated by full-length human HDAC6 approximately 1,500-fold more efficiently than are assembled MTs. Similar preferences were also noticed by Miyake *et al.*, who showed that the truncated *Danio rerio* enzyme prefers free tubulin over MTs, although in that study, the difference in the deacetylation rate was only approximately 2.5-fold. This paper, which is to the best of our knowledge the only other report providing quantitative data on HDAC6 preferences for individual tubulin forms, suggests that there are substantial differences in tubulin deacetylation among individual HDAC6 orthologs and likely also between full-length proteins and constructs truncated beyond the tandem catalytic domains. Detailed studies concerning the impact of these and other variables (presence/absence of accessory proteins, post-translational modifications on HDAC6/tubulin) will be required to understand and reconcile intriguing discrepancies in HDAC6 substrate preferences (from an absolute preference for MTs to favoring free heterodimers) that have been reported in prior *in vivo/in vitro* studies[15–17, 38, 42, 48, 57].

Although HDAC6 is the major tubulin deacetylase, interactions between MTs and HDAC6 have not yet been visualized. Our study thus offers the first direct visualization of HDAC6 binding to the MT surface. The reported flush-in experiment, where the chamber with surface-immobilized MTs was injected with the GFP-HDAC6 fusion and binding kinetics quantified by TIRF microscopy, reveals that kinetics of HDAC6 binding to MTs are relatively fast. The initial increase in the fluorescence signal was observed within 10 seconds following the flush-in and the signal plateau was reached approximately 30 seconds later (Fig. 4). Such kinetics, together with the even distribution of the signal along the whole MT length within the monitored time period, strongly suggest that HDAC6 binds to the outer MT surface rather than diffusing into the MT lumen via open tips. This observation does not formally exclude the possibility of HDAC6 entering and binding/functioning within the lumenal cavity of MTs, but this would likely happen with considerably slower kinetics. It should also be noted that HDAC6 deacetylase activity is not required for HDAC6 binding to MTs, as the TIRF assay in the presence of the HDAC6 inhibitor Nexturastat A gave virtually indistinguishable binding curves (data not shown).

Biochemical or physiological implications of HDAC6 binding to the external surface of MTs are unclear at present. For example, such interactions can help with targeting and concentrating the enzyme at the site of its action, and binding can help HDAC6 to access the αK40 either via the open MT ends and/or through fluctuations/defects in the MT lattice observed in previous studies[58–60]. Alternatively, the binding of HDAC6 can influence the stability of MTs[61, 62] and/or the dynamic properties of MTs[16]. Further structural and biological studies are required to provide more insight into these outstanding issues.

It has been shown that αTAT1 enters MT lumen in order to acetylate αK40[2, 51, 63], and that acetylation starts at the open tips of MTs, followed by the acetylation mark progressively spreading by longitudinal diffusion of αTAT1 in the MT lumen. Alternatively, αTAT1 can enter MT lumen via structural defects in the MT lattice. Irrespective of the mode of αTAT1 entry into the MT lumen, assembled MTs are a preferred substrate for αTAT1[51–53]. In contrast, our study reveals stochastic deacetylation of MTs by HDAC6 without any tip preferences (Fig. 5), and a similar deacetylation pattern was reported for the tandem catalytic domain construct of *D. rerio* HDAC6[48]. The underlying cause for spatial differences in αK40 acetylation and deacetylation reactions by αTAT1 and HDAC6, respectively, remains unknown at present.

Overall, our study adds another piece of information to the complex puzzle of how tubulin acetylation status is controlled by the opposing activities of αTAT1 and HDAC6, as previously suggested by others[48, 64]. To this end, our data complement these findings concerning the αTAT1/tubulin interplay, and provide further rationale for the correlation between tubulin acetylation and microtubule age. As HDAC6 prefers free tubulin dimers with a velocity of >0.6 mol/mol*s, it is tempting to speculate that the pool of free tubulin dimers within cells should be mostly non-acetylated. Once MTs are formed, however, these become preferred substrates for αTAT1 and are therefore preferentially acetylated. At the same time, MTs are only inefficiently deacetylated by HDAC6. Consequently, given the inverse preferences of HDAC6 and αTAT1 for free tubulin and MTs, respectively, in the context of long-lived stable MTs, the equilibrium is clearly shifted towards acetylated αK40 (Fig. 6). Finally, ongoing investigations in our laboratory are focused on building up the complexity of our experimental system by evaluating certain variables encountered *in vivo*, such as post-translational modifications, HDAC6/tubulin interaction partners, and MT dynamics, with the aim of describing and dissecting their individual contributions and mutual interplay in relation to tubulin deacetylation by HDAC6.

Methods

Chemicals and peptides. If not stated otherwise, all chemicals were purchased from Sigma-Aldrich (St. Louis, MO, USA). Peptides were synthesized commercially by KareBay (Monmouth Junction, NJ, USA) at >90% purity and their identities were confirmed by analytical LC-MS (data not shown).

Expression plasmids. The sequence encoding human HDAC6 (NP_006035.2, UniProtKB - Q9UBN7) was used as a template for cloning all HDAC6 variants used in this report. In general, a nucleotide sequence encoding a given variant was PCR amplified with a set of desired primer pairs and inserted into the pDONR221 plasmid using the BP recombination reaction (Invitrogen, Carlsbad, CA, USA), according to the manufacturer's protocol. The identity of the resulting entry clone was confirmed by Sanger sequencing. Expression plasmids were generated via LR recombination reaction between the entry clone and a required destination vector, which typically introduced a TEV-cleavable tag at the N-terminus of the HDAC6 variant to simplify purification and/or visualization of the resulting fusion. Schematic representations of constructs used in this study are shown in Supplementary Fig. S1.

Large-scale expression of HDAC6 variants. All HDAC6 variants were expressed using HEK-293/T17 cells following transient transfection mediated by linear polyethylene imine (PEI) (Polysciences Inc., Warrington, PA, USA). To this end, the suspension culture of HEK-293/T17 cells was grown in 2 L Erlenmeyer flasks in Free

104
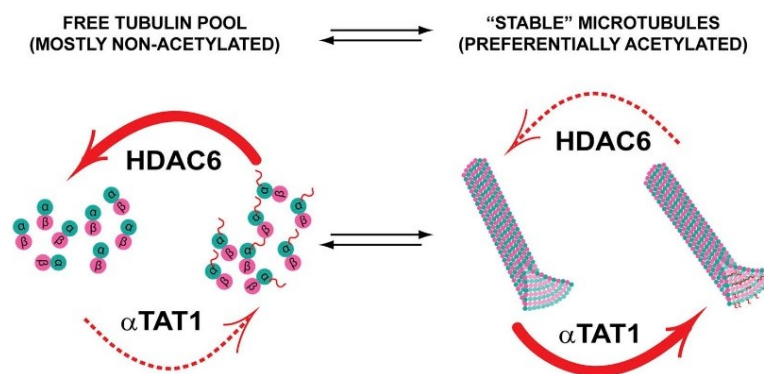
Figure 6. High acetylation levels of stable microtubules are linked to opposing substrate preferences of HDAC6 and αTAT1. HDAC6 prefers free tubulin as a substrate, whereas αTAT1 is 5-fold more active on assembled microtubules (preferences shown as thick red arrows). Consequently, it is likely that within the cell, the pool of free tubulin is mostly in the non-acetylated state. Once microtubules are assembled, however, they become preferentially acetylated by αTAT1. For dynamic microtubules, their lifetime may be too short to become extensively acetylated, whereas stable microtubules with long lifespans have a much higher probability of being fully acetylated by αTAT1. Both HDAC6 and αTAT1 thus serve as "timers" to set the clocks gauging microtubule age based on their acetylation status.

Style F17 medium (Thermo Fisher Scientific) supplemented by 0.1% Pluronic F-68 (Invitrogen) and 2 mM L-glutamine at 110 rpm under a humidified 5% CO_2 atmosphere at 37 °C. For large-scale expression, 0.7 mg of an expression plasmid was diluted in 17.5 ml of PBS, to which 2.1 ml of 1 mg/ml PEI was added. The mixture was vortexed briefly, incubated for 10 min at room temperature, and then added to 350 ml of cells at a concentration of 4×10^6 cell/ml. Four hours post-transfection, the cell suspension was diluted by an equal volume of ExCell serum-free medium. Cells were harvested 72 h post transfection by centrifugation at $500 \times g$ for 5 min, then the cell pellet was frozen in liquid nitrogen and stored at −80 °C until further use.

Purification of HDAC6 variants. The cell pellet was lysed by sonication (24 W/1 min) in ice-cold lysis buffer (100 mM Tris-HCl, 10 mM NaCl, 5 mM KCl, 2 mM $MgCl_2$, 10% glycerol; pH 8.0) supplemented with benzonase (1 U/ml; Merck, Darmstadt, Germany) and protease inhibitor coctail (Roche, Basel, Switzerland). To further assist cell lysis, Igepal-630 was added to the cell lysate to a final concentration of 0.2% (v/v) and the mixture was incubated for 20 min on ice. NaCl was added to a final concentration of 150 mM. The lysate was then cleared by centrifugation at $40,000 \times g$ for 30 min at 4 °C and the supernatant was loaded onto a Strep-Tactin column (IBA, Gottingen, Germany) equilibrated in the lysis buffer. Following the washing step with the lysis buffer, the fusion protein was eluted using 50 mM Tris-HCl, 150 mM NaCl, 10 mM KCl, 10% glycerol and 3 mM desthiobiotin (pH 8.0). The eluted fusion protein was concentrated to approximately 1 mg/ml and (if desired) the N-terminal tag was cleaved by the addition of the 1:20 (w/w) TEV protease overnight at 4 °C. The HDAC6 protein was then separated from tags and the TEV protease by size exclusion chromatography using the Superdex 16/600 HR200 column (GE Healthcare Bio-Sciences, Little Chalfont, UK) with 30 mM HEPES, 140 mM NaCl, 10 mM KCl, 3% glycerol, and 0.25 mM TCEP (AMRESCO, Solon, OH, USA), with a pH 7.4 adjusted with NaOH, as a mobile phase. The purified protein was concentrated to approximately 1 mg/ml and aliquots were flash frozen in liquid nitrogen and stored at −80 °C until further use.

Fluorometric assays. Deacetylation activity of HDAC6 variants was determined using acetyl-Gly-Ala-(acetyl-Lys)-AMC (GAK(Ac)-AMC; Bachem, Bubendorf, Switzerland), Boc-(acetyl-Lys)-AMC (Boc-K(Ac)-AMC; Bachem) and Fluor-de-Lys (Enzo Life Sciences, Plymouth Meeting, PA, USA) substrates. In general, a given HDAC6 variant was incubated with a substrate in a reaction buffer comprised of 50 mM HEPES, 140 mM NaCl, 10 mM KCl, 1 mg/ml bovine serum albumin (BSA), and 1 mM TCEP, at a pH 7.4 adjusted with NaOH (total volume 20 μl). This incubation occurred in 384-well plates for 30 min with vigorous shaking at 37 °C. The reaction was stopped by addition of 20 μl of trypsin solution (2 mg/ml trypsin, 20 mM Tris-HCl, 150 mM NaCl, 1 mM EDTA; pH 7.4 adjusted with NaOH). Following the 15-min incubation at 37 °C, a fluorescence signal of released aminomethylcoumarin was quantified using a CLARIOstar fluorimeter (BMG Labtech GmbH, Ortenberg, Germany) with excitation/emission wavelengths set at 365/440 nm, respectively. The data were fitted using the GraphPad Prism software (GraphPad Software, San Diego, CA, USA) and kinetic values were calculated by non-linear regression analysis.

HPLC-based assays. Individual fluorophore-labeled peptides were incubated with HDAC6 at 37 °C for 30 min in an assay buffer comprised of 50 mM HEPES, 140 mM NaCl, 10 mM KCl, 2 mg/ml BSA, and 1 mM TCEP, at a pH 7.4 adjusted with NaOH. The reaction was quenched by the addition of acetic acid to a final concentration

105

of 0.5%, and reaction products were quantified by means of RP-HPLC (Shimadzu, HPLC Prominence system) on the column Kinetex® 2.6 μm XB-C18 100 Å, 100 × 3 mm (Phenomenex, Torrance, CA, USA).

Determination of inhibition constant. The inhibition constants for SAHA (Selleckchem, Houston, TX, USA), Trichostatin A, and Nexturastat A (gift from A. Villagra and A. Kozikowski from George Washington University, USA, and University of Illinois at Chicago, USA, respectively) were determined using the slightly modified fluorogenic assay described above. Briefly, the tested compounds were preincubated with 0.3 nM human recombinant HDAC6 at 37 °C for 15 min, and then the deacetylation reaction was started by addition of 10 μM GAK(Ac)-AMC. After a 120-min incubation at 37 °C, the reaction was stopped by the addition of trypsin solution. Following the 15-min incubation at 37 °C, a fluorescence signal of released aminomethylcoumarin was quantified using a CLARIOstar fluorimeter with excitation/emission wavelengths set at 365/440 nm, respectively. The data were fitted using the GraphPad Prism software and IC_{50} values were calculated by non-linear regression analysis. The inhibitor and enzyme-free controls were defined as 100% and 0% HDAC6 activity, respectively.

Isolation of tubulin from porcine brains. Tubulin isolation from pig brain tissue was carried out according to an established protocol (details in the supplementary material)[65]. The concentration of the final tubulin preparation was determined based on the absorbance at 280 nm. Supernatant containing purified tubulin was flash frozen in aliquots using liquid nitrogen and stored at −80 °C.

Determination of αK40 acetylation levels. Five μg of porcine tubulin were diluted in 100 μl of 50 mM ammonium bicarbonate (pH 8.5) and then digested with GluC (V8) protease (Roche) for 10 hours at a ratio of 1:100. After complete evaporation on speedvac, the sample was dissolved in 15 μl of 0.1% formic acid, 10% dimethylsulfoxide in water. Acetylated and non-acetylated versions of the peptide HGIQPDGQMPSDKTIGGGDDSFNTFFSE with isotopically-labeled isoleucine (heavy peptides) was added into the mixture of the same concentration. Three μl of the sample were analyzed on the UltiMate 3000 RSLCnano system (Dionex, Sunnyvale, CA, USA) coupled to a TripleTOF 5600 mass spectrometer with a NanoSpray III source (AB Sciex, Framingham, MA, USA). The peptides were trapped and desalted with 2% acetonitrile in 0.1% formic acid at a flow rate of 5 μl/min on the Acclaim PepMap100 column (5 μm, 2 cm × 100 μm ID, Thermo Scientific). Eluted peptides were separated by the Acclaim PepMap100 analytical column (3 μm, 25 cm × 75 μm ID, Thermo Scientific) using a 70-min elution gradient at a constant flow of 300 nl/min, with mobile phase A being 0.1% formic acid and mobile phase B being 0.1% formic acid in acetonitrile. Extracted ion chromatogram of the αK40 containing identified peptides, either acetylated or nonacetylated, in light and heavy forms, were generated and the area of relevant peaks of charge state 3 was recorded. The area of light peptides was normalized to the heavy peptide area, and the percentage of acetylated versus non-acetylated peptides was calculated.

Labeling of HALO-HDAC6 fusions. The HALO-HDAC6 variants were labeled via covalent modification of the HALO fusion partner using the HaloTag-FITC ligand. The HALO-HDAC6 fusion (1 mg/ml) was incubated with a 5 molar excess of the ligand overnight at 4 °C. The unbound labels were removed by size exclusion chromatography using the Superdex 10/300 HR200 column with 30 mM HEPES, 140 mM NaCl, 10 mM KCl, 3% glycerol, and 0.25 mM TCEP, at pH 7.4 adjusted with NaOH, as a mobile phase, and labeled fusions were concentrated to approximately 1 mg/ml, aliquoted, and then snap-frozen in liquid nitrogen.

Preparation of tubulin polymers. To obtain taxol-stabilized microtubules, tubulin at a concentration of 4.4 mg/ml was polymerized for 30 min at 37 °C in BRB80 buffer supplemented with 4.8% DMSO, 4 mM $MgCl_2$, and 1 mM GTP, after which BRB80 with 20 μM paclitaxel was added. For GMPCPP-stabilized microtubules, tubulin at a concentration of 0.25 mg/ml was incubated for 2 h at 37 °C in BRB80 buffer supplemented with 1 mM $MgCl_2$ and 1 mM GMPCPP (Jena Bioscience, Jena, Germany). Dolastatin-10 rings resulted from the polymerization of 2.2 mg/ml tubulin for 40 min at room temperature with 40 μM dolastatin-10 in 80 mM PIPES (pH 6.9), 50 mM KCl, 1 mM EGTA, 1 mM $MgCl_2$, and 1 mM DTT. After the polymerization, all abovementioned polymers were pelleted at 30,000 × g for 40 min at 37 °C and the pellet was suspended in warm BRB80 with 20 μM taxol to the required concentration. Zn-sheets were prepared via 2 h incubation of 3 mg/ml tubulin at 37 °C in 80 mM MES, 200 mM NaCl, 3 mM GTP, 1.25 mM $MgSO_4$, 1.25 mM $ZnSO_4$, and 0.025 mg/ml pepstatin, adjusted to a pH of 5.5 with NaOH. Zn-sheets were then stabilized by the addition of paclitaxel to a final concentration of 31.5 μM. Zn-sheets were pelleted at 30,000 × g for 40 min at 37 °C and the pellet was suspended in a warm solution of 80 mM MES, 200 mM NaCl, 1.25 mM $MgSO_4$, and 20 μM taxol, adjusted to a of pH 5.5 with NaOH.

Microtubule binding assay. Microtubules and flow cells were prepared as described previously[66]. Briefly, taxol-stabilized microtubules were polymerized from tubulin purified from pig brains using a 1:30 ratio of Alexa-647-labeled to unlabeled tubulin, at a concentration of 2 μM and 1 mM GMPCPP in BRB80. Microscope chambers were constructed of silanized coverslips, with parafilm used to space them to form channels of 0.1-mm thickness, 3-mm width, and 18-mm length. Silanization was performed as described previously[67]. Microtubules were immobilized to the glass surface of a flow cell covered with anti-β-tubulin antibodies (Sigma-Aldrich, St. Louis, MO, USA, #T7816, 20 μg/ml in PBS), and then GFP-labeled HDAC6 was flushed into the flow cell at a final concentration of 300 nM. All experiments were carried out in a buffer consisting of BRB50, 1 mM TCEP, 0.5 mg/ml casein, 10 μM paclitaxel, 20 mM D-glucose, 110 μg/ml glucose oxidase, and 20 μg/ml catalase.

TIRF microscopy. Binding experiments were visualized using TIRF microscopy. Experiments were carried out using a Nikon Ti-E microscope equipped with H-TIRF System, 60x oil immersion 1.49 NA TIRF objective and Andor Ixon Ultra EMCCD camera (Andor Technology, Belfast, UK) controlled by NIS Elements software (Nikon). Alexa-647-labeled microtubules and GFP-labeled HDAC6 in microtubule binding assays were

visualized sequentially by switching between 640 nm and 488 nm excitation lasers. The image acquisition rate was 0.5 frames per second for sequential dual-color imaging, and image analysis was performed using Fiji[68] and MatLab (MathWorks).

Deacetylation of tubulin dimers and polymers. Using a fluorescence peptide-based assay, we first verified that small molecule components (e.g., taxol, GMPCPP, Dolastatin-10, Zn^{2+} ions) do not interfere with HDAC6 deacetylase activity at levels above the highest concentrations used in our assays (data not shown). Deacetylation reactions in a total volume of 20 µl were performed in BRB80 buffer (experiments with Zn sheets were performed in 80 mM MES, 200 mM NaCl, and 1.25 mM $MgSO_4$, adjusted to pH 5.5 with NaOH) supplemented with 1 mM TCEP and 0.5 mg/ml BSA, at 37 °C for 30 min in the case of dimers; for microtubules, the reaction was continuous and aliquots were usually harvested at 0.5, 1, 2, and 3 h. Prior to the reaction, HDAC6 was diluted to the required concentrations in the BRB80 buffer supplemented with TCEP and BSA, and the reaction was started by the addition of tubulin dimers/microtubules. Colchicine (40 µM) and paclitaxel (10 µM) were added to reaction mixtures of free tubulin dimers and microtubules, respectively. For assays with denatured tubulin dimers, the mixture of free tubulin dimers was incubated for 20 min at 95 °C, then cooled and deacetylated as native substrates. The deacetylation reaction was stopped by the addition of 20 µl of 2x Laemmli buffer and boiling samples at 95 °C for 5 min.

SDS-PAGE, Western blotting, and data analysis. Samples were loaded onto a 4–20% gradient PAGE gel (GenScript, Piscataway, NJ, USA) at 150 ng of tubulin per lane, and then run in MOPS-SDS running buffer at 160 V for 45 mins. Gels were electrotransferred onto a PVDF membrane that was subsequently blocked with 5% (w/v) BSA in TBS. The level of tubulin acetylation at αK40 was determined using a monoclonal anti-acetylated tubulin antibody[69] (Sigma, T7451, 0.3 µg/ml); a secondary goat anti-mouse antibody conjugated to Alexa Fluor 488 (Life Technologies, A11029, dilution 0.4 µg/ml) and normalized to the amount of total tubulin detected by rabbit polyclonal anti-α tubulin antibody (Abcam, Cambridge UK, ab18251, 1 µg/ml); and a secondary donkey anti-rabbit antibody conjugated to Alexa Fluor 568 (Life Technologies, USA, A10042, 0.4 µg/ml). HDAC6 was visualized using a custom-made anti-HDAC6 polyclonal rabbit sera at 1:5,000 dilution. Fluorescence intensity was measured by Typhoon FLA9500 imager (GE Healthcare Bio-Sciences) and quantified using Quantity One 1-D Analysis Software (Bio-Rad, Hercules, CA, USA). Data analysis of enzyme kinetics and statistical analysis using one-way ANOVA with Tukey's post hoc tests were performed using Graph Pad Prism software.

Indirect immunofluorescence microscopy. Deacetylation experiments were also visualized using indirect immunofluorescence microscopy. Deacetylation reactions were terminated by the addition of 10 µM SAHA, and the mixture of microtubules and HDAC6 was applied to a glass slide pretreated by poly-L-lysine. The following steps were carried out in PBS supplemented with 10 µM taxol at room temperature. Coverslips were washed with PBS and blocked with 0.5% BSA for 20 min. Coverslips were then incubated with anti-acetylated tubulin monoclonal antibody (10 µg/ml) and rabbit polyclonal anti-α tubulin antibody (2.5 µg/ml) for 20 min. Following the washing step, goat anti-mouse antibody conjugated to Alexa Fluor 488 and goat anti-rabbit antibody conjugated to Alexa Fluor 594 were applied for 20 min. After the final wash, coverslips were mounted in VectaShield medium (Vector Laboratories), and images were obtained using the Nikon Eclipse Ti fluorescence microscope equipped with a 100x immersion oil objective and additive 2.5x lens magnification (Nikon), as well as with the ORCA-flash 4.0 digital CMOS camera (Hamamatsu Photonics, Japan). Images were processed using Adobe Photoshop software and the signal intensity was quantified using Fiji.

Data availability. All data generated or analysed during this study are included in this published article (and its Supplementary Information files).

References

1. Gundersen, G. G. & Bulinski, J. C. Distribution of tyrosinated and nontyrosinated alpha-tubulin during mitosis. *J Cell Biol* **102**, 1118–1126 (1986).
2. Edde, B. *et al.* Posttranslational glutamylation of alpha-tubulin. *Science* **247**, 83–85 (1990).
3. Redeker, V. *et al.* Polyglycylation of tubulin: a posttranslational modification in axonemal microtubules. *Science* **266**, 1688–1691 (1994).
4. L'Hernault, S. W. & Rosenbaum, J. L. Chlamydomonas alpha-tubulin is posttranslationally modified by acetylation on the epsilon-amino group of a lysine. *Biochemistry* **24**, 473–478 (1985).
5. Song, Y. *et al.* Transglutaminase and polyamination of tubulin: posttranslational modification for stabilizing axonal microtubules. *Neuron* **78**, 109–123, doi:https://doi.org/10.1016/j.neuron.2013.01.036 (2013).
6. Eipper, B. A. Properties of rat brain tubulin. *J Biol Chem* **249**, 1407–1416 (1974).
7. Nogales, E., Wolf, S. G. & Downing, K. H. Structure of the alpha beta tubulin dimer by electron crystallography. *Nature* **391**, 199–203, doi:https://doi.org/10.1038/34465 (1998).
8. Tran, A. D. *et al.* HDAC6 deacetylation of tubulin modulates dynamics of cellular adhesions. *Journal of cell science* **120**, 1469–1479, doi:https://doi.org/10.1242/jcs.03431 (2007).
9. Kalebic, N. *et al.* alphaTAT1 is the major alpha-tubulin acetyltransferase in mice. *Nat Commun* **4**, 1962, doi:https://doi.org/10.1038/ncomms2962 (2013).
10. Jeong, S. G. & Cho, G. W. The tubulin deacetylase sirtuin-2 regulates neuronal differentiation through the ERK/CREB signaling pathway. *Biochem Biophys Res Commun* **482**, 182–187, doi:https://doi.org/10.1016/j.bbrc.2016.11.031 (2017).
11. Dompierre, J. P. *et al.* Histone deacetylase 6 inhibition compensates for the transport deficit in Huntington's disease by increasing tubulin acetylation. *The Journal of neuroscience: the official journal of the Society for Neuroscience* **27**, 3571–3583, doi:https://doi.org/10.1523/JNEUROSCI.0037-07.2007 (2007).
12. Reed, N. A. *et al.* Microtubule acetylation promotes kinesin-1 binding and transport. *Curr Biol* **16**, 2166–2172, doi:https://doi.org/10.1016/j.cub.2006.09.014 (2006).

107

13. Chen, S., Owens, G. C., Makarenkova, H. & Edelman, D. B. HDAC6 regulates mitochondrial transport in hippocampal neurons. *PloS one* **5**, e10848, doi:https://doi.org/10.1371/journal.pone.0010848 (2010).
14. Akella, J. S. *et al.* MEC-17 is an alpha-tubulin acetyltransferase. *Nature* **467**, 218–222, doi:https://doi.org/10.1038/nature09324 (2010).
15. Hubbert, C. *et al.* HDAC6 is a microtubule-associated deacetylase. *Nature* **417**, 455–458, doi:https://doi.org/10.1038/417455a (2002).
16. Matsuyama, A. *et al. In vivo* destabilization of dynamic microtubules by HDAC6-mediated deacetylation. *The EMBO journal* **21**, 6820–6831 (2002).
17. North, B. J, Marshall, B. L., Borra, M. T., Denu, J. M. & Verdin, E. The human Sir2 ortholog, SIRT2, is an NAD + -dependent tubulin deacetylase. *Molecular cell* **11**, 437–444 (2003).
18. Bobrowska, A., Donmez, G., Weiss, A., Guarente, L. & Bates, G. SIRT2 ablation has no effect on tubulin acetylation in brain, cholesterol biosynthesis or the progression of Huntington's disease phenotypes *in vivo*. *PloS one* **7**, e34805, doi:https://doi.org/10.1371/journal.pone.0034805 (2012).
19. Zhang, Y. *et al.* Mice lacking histone deacetylase 6 have hyperacetylated tubulin but are viable and develop normally. *Molecular and cellular biology* **28**, 1688–1701, doi:https://doi.org/10.1128/MCB.01154-06 (2008).
20. Skoge, R. H. & Ziegler, M. SIRT2 inactivation reveals a subset of hyperacetylated perinuclear microtubules inaccessible to HDAC6. *J Cell Sci* **129**, 2972–2982, doi:https://doi.org/10.1242/jcs.187518 (2016).
21. Choudhary, C. *et al.* Lysine acetylation targets protein complexes and co-regulates major cellular functions. *Science* **325**, 834–840, doi:https://doi.org/10.1126/science.1175371 (2009).
22. Chu, C. W. *et al.* A novel acetylation of beta-tubulin by San modulates microtubule polymerization via down-regulating tubulin incorporation. *Mol Biol Cell* **22**, 448–456, doi:https://doi.org/10.1091/mbc.E10-03-0203 (2011).
23. Huan, Y. *et al.* Epigenetic Modification Agents Improve Gene-Specific Methylation Reprogramming in Porcine Cloned Embryos. *PLoS One* **10**, e0129803, doi:https://doi.org/10.1371/journal.pone.0129803 (2015).
24. Ouyang, H. *et al.* Protein aggregates are recruited to aggresome by histone deacetylase 6 via unanchored ubiquitin C termini. *J Biol Chem* **287**, 2317–2327, doi:https://doi.org/10.1074/jbc.M111.273730 (2012).
25. Han, Y. *et al.* Acetylation of histone deacetylase 6 by p300 attenuates its deacetylase activity. *Biochem Biophys Res Commun* **383**, 88–92, doi:https://doi.org/10.1016/j.bbrc.2009.03.147 (2009).
26. Liu, Y., Peng, L., Seto, E., Huang, S. & Qiu, Y. Modulation of histone deacetylase 6 (HDAC6) nuclear import and tubulin deacetylase activity through acetylation. *J Biol Chem* **287**, 29168–29174, doi:https://doi.org/10.1074/jbc.M112.371120 (2012).
27. Okuda, K., Ito, A. & Uehara, T. Regulation of Histone Deacetylase 6 Activity via S-Nitrosylation. *Biol Pharm Bull* **38**, 1434–1437, doi:https://doi.org/10.1248/bpb.b15-00364 (2015).
28. Lafarga, V., Aymerich, I., Tapia, O., Mayor, F. Jr. & Penela, P. A novel GRK2/HDAC6 interaction modulates cell spreading and motility. *EMBO J* **31**, 856–869, doi:https://doi.org/10.1038/emboj.2011.466 (2012).
29. Kovacs, J. J. *et al.* HDAC6 regulates Hsp90 acetylation and chaperone-dependent activation of glucocorticoid receptor. *Mol Cell* **18**, 601–607, doi:https://doi.org/10.1016/j.molcel.2005.04.021 (2005).
30. Zhang, X. *et al.* HDAC6 modulates cell motility by altering the acetylation level of cortactin. *Mol Cell* **27**, 197–213, doi:https://doi.org/10.1016/j.molcel.2007.05.033 (2007).
31. Parmigiani, R. B. *et al.* HDAC6 is a specific deacetylase of peroxiredoxins and is involved in redox regulation. *Proc Natl Acad Sci USA* **105**, 9633–9638, doi:https://doi.org/10.1073/pnas.0803749105 (2008).
32. Li, Y., Zhang, X., Polakiewicz, R. D., Yao, T. P. & Comb, M. J. HDAC6 is required for epidermal growth factor-induced beta-catenin nuclear localization. *J Biol Chem* **283**, 12686–12690, doi:https://doi.org/10.1074/jbc.C700185200 (2008).
33. Kawaguchi, Y. *et al.* The deacetylase HDAC6 regulates aggresome formation and cell viability in response to misfolded protein stress. *Cell* **115**, 727–738 (2003).
34. Seidel, C., Schnekenburger, M., Dicato, M. & Diederich, M. Histone deacetylase 6 in health and disease. *Epigenomics* **7**, 103–118, doi:https://doi.org/10.2217/epi.14.69 (2015).
35. Li, G., Jiang, H., Chang, M., Xie, H. & Hu, L. HDAC6 alpha-tubulin deacetylase: a potential therapeutic target in neurodegenerative diseases. *J Neurol Sci* **304**, 1–8, doi:https://doi.org/10.1016/j.jns.2011.02.017 (2011).
36. Simoes-Pires, C. *et al.* HDAC6 as a target for neurodegenerative diseases: what makes it different from the other HDACs? *Mol Neurodegener* **8**, 7, doi:https://doi.org/10.1186/1750-1326-8-7 (2013).
37. Aldana-Masangkay, G. I. & Sakamoto, K. M. The role of HDAC6 in cancer. *J Biomed Biotechnol* **2011**, 875824, doi:https://doi.org/10.1155/2011/875824 (2011).
38. Zhao, Z., Xu, H. & Gong, W. Histone deacetylase 6 (HDAC6) is an independent deacetylase for alpha-tubulin. *Protein and peptide letters* **17**, 555–558 (2010).
39. Du, Y., Seibenhener, M. L., Yan, J., Jiang, J. & Wooten, M. C. aPKC phosphorylation of HDAC6 results in increased deacetylation activity. *PloS one* **10**, e0123191, doi:https://doi.org/10.1371/journal.pone.0123191 (2015).
40. Williams, K. A. *et al.* Extracellular signal-regulated kinase (ERK) phosphorylates histone deacetylase 6 (HDAC6) at serine 1035 to stimulate cell migration. *The Journal of biological chemistry* **288**, 33156–33170, doi:https://doi.org/10.1074/jbc.M113.472506 (2013).
41. Watabe, M. & Nakaki, T. Protein kinase CK2 regulates the formation and clearance of aggresomes in response to stress. *Journal of cell science* **124**, 1519–1532, doi:https://doi.org/10.1242/jcs.081778 (2011).
42. Zou, H., Wu, Y., Navre, M. & Sang, B. C. Characterization of the two catalytic domains in histone deacetylase 6. *Biochemical and biophysical research communications* **341**, 45–50, doi:https://doi.org/10.1016/j.bbrc.2005.12.144 (2006).
43. Schultz, B. E. *et al.* Kinetics and comparative reactivity of human class I and class IIb histone deacetylases. *Biochemistry* **43**, 11083–11091, doi:https://doi.org/10.1021/bi0494471 (2004).
44. Lai, M. J. *et al.* Synthesis and biological evaluation of 1-arylsulfonyl-5-(N-hydroxyacrylamide)indoles as potent histone deacetylase inhibitors with antitumor activity *in vivo*. *J Med Chem* **55**, 3777–3791, doi:https://doi.org/10.1021/jm300197a (2012).
45. Wagner, F. F. *et al.* Potent and selective inhibition of histone deacetylase 6 (HDAC6) does not require a surface-binding motif. *Journal of medicinal chemistry* **56**, 1772–1776, doi:https://doi.org/10.1021/jm301355j (2013).
46. Bergman, J. A. *et al.* Selective histone deacetylase 6 inhibitors bearing substituted urea linkers inhibit melanoma cell growth. *Journal of medicinal chemistry* **55**, 9891–9899, doi:https://doi.org/10.1021/jm301098e (2012).
47. Giannini, G. *et al.* N-Hydroxy-(4-oxime)-cinnamide: a versatile scaffold for the synthesis of novel histone deacetylase [correction of deacetilase] (HDAC) inhibitors. *Bioorganic & medicinal chemistry letters* **19**, 2346–2349, doi:https://doi.org/10.1016/j.bmcl.2009.02.029 (2009).
48. Miyake, Y. *et al.* Structural insights into HDAC6 tubulin deacetylation and its selective inhibition. *Nat Chem Biol* **12**, 748–754, doi:https://doi.org/10.1038/nchembio.2140 (2016).
49. Moores, C. A. & Milligan, R. A. Visualisation of a kinesin-13 motor on microtubule end mimics. *J Mol Biol* **377**, 647–654, doi:https://doi.org/10.1016/j.jmb.2008.01.079 (2008).
50. Wolf, S. G., Mosser, G. & Downing, K. H. Tubulin conformation in zinc-induced sheets and macrotubes. *J Struct Biol* **111**, 190–199, doi:https://doi.org/10.1006/jsbi.1993.1049 (1993).
51. Szyk, A. *et al.* Molecular basis for age-dependent microtubule acetylation by tubulin acetyltransferase. *Cell* **157**, 1405–1415, doi:https://doi.org/10.1016/j.cell.2014.03.061 (2014).

108

52. Friedmann, D. R., Aguilar, A., Fan, J., Nachury, M. V. & Marmorstein, R. Structure of the alpha-tubulin acetyltransferase, alphaTAT1, and implications for tubulin-specific acetylation. *Proc Natl Acad Sci USA* **109**, 19655–19660, doi:https://doi.org/10.1073/pnas.1209357109 (2012).
53. Taschner, M., Vetter, M. & Lorentzen, E. Atomic resolution structure of human alpha-tubulin acetyltransferase bound to acetyl-CoA. *Proc Natl Acad Sci USA* **109**, 19649–19654, doi:https://doi.org/10.1073/pnas.1209343109 (2012).
54. Li, W. *et al.* Molecular basis of the acetyltransferase activity of MEC-17 towards alpha-tubulin. *Cell Res* **22**, 1707–1711, doi:https://doi.org/10.1038/cr.2012.154 (2012).
55. Riester, D., Hildmann, C., Grunewald, S., Beckers, T. & Schwienhorst, A. Factors affecting the substrate specificity of histone deacetylases. *Biochem Biophys Res Commun* **357**, 439–445, doi:https://doi.org/10.1016/j.bbrc.2007.03.158 (2007).
56. Hai, Y. & Christianson, D. W. Histone deacetylase 6 structure and molecular basis of catalysis and inhibition. *Nat Chem Biol* **12**, 741–747, doi:https://doi.org/10.1038/nchembio.2134 (2016).
57. Zhang, Y. *et al.* HDAC-6 interacts with and deacetylates tubulin and microtubules *in vivo. The EMBO journal* **22**, 1168–1179, doi:https://doi.org/10.1093/emboj/cdg115 (2003).
58. Li, H., DeRosier, D. J., Nicholson, W. V., Nogales, E. & Downing, K. H. Microtubule structure at 8 A resolution. *Structure* **10**, 1317–1328 (2002).
59. Meurer-Grob, P., Kasparian, J. & Wade, R. H. Microtubule structure at improved resolution. *Biochemistry* **40**, 8000–8008 (2001).
60. Howes, S. C., Alushin, G. M., Shida, T., Nachury, M. V. & Nogales, E. Effects of tubulin acetylation and tubulin acetyltransferase binding on microtubule structure. *Molecular biology of the cell* **25**, 257–266, doi:https://doi.org/10.1091/mbc.E13-07-0387 (2014).
61. Asthana, J., Kapoor, S., Mohan, R. & Panda, D. Inhibition of HDAC6 deacetylase activity increases its binding with microtubules and suppresses microtubule dynamic instability in MCF-7 cells. *The Journal of biological chemistry* **288**, 22516–22526, doi:https://doi.org/10.1074/jbc.M113.489328 (2013).
62. Purev, E., Neff, L., Horne, W. C. & Baron, R. c-Cbl and Cbl-b act redundantly to protect osteoclasts from apoptosis and to displace HDAC6 from beta-tubulin, stabilizing microtubules and podosomes. *Molecular biology of the cell* **20**, 4021–4030, doi:https://doi.org/10.1091/mbc.E09-03-0248 (2009).
63. Ly, N. *et al.* alphaTAT1 controls longitudinal spreading of acetylation marks from open microtubules extremities. *Sci Rep* **6**, 35624, doi:https://doi.org/10.1038/srep35624 (2016).
64. Skoge, R. H., Dolle, C. & Ziegler, M. Regulation of SIRT2-dependent alpha-tubulin deacetylation by cellular NAD levels. *DNA Repair (Amst)* **23**, 33–38, doi:https://doi.org/10.1016/j.dnarep.2014.04.011 (2014).
65. Geuens, G. *et al.* Ultrastructural colocalization of tyrosinated and detyrosinated alpha-tubulin in interphase and mitotic cells. *J Cell Biol* **103**, 1883–1893 (1986).
66. Braun, M. *et al.* Adaptive braking by Ase1 prevents overlapping microtubules from sliding completely apart. *Nat Cell Biol* **13**, 1259–1264, doi:https://doi.org/10.1038/ncb2323 (2011).
67. Hyman, A. A. Preparation of marked microtubules for the assay of the polarity of microtubule-based motors by fluorescence. *J Cell Sci Suppl* **14**, 125–127 (1991).
68. Schindelin, J. *et al.* Fiji: an open-source platform for biological-image analysis. *Nat Methods* **9**, 676–682, doi:https://doi.org/10.1038/nmeth.2019 (2012).
69. Piperno, G. & Fuller, M. T. Monoclonal antibodies specific for an acetylated form of alpha-tubulin recognize the antigen in cilia and flagella from a variety of organisms. *J Cell Biol* **101**, 2085–2094 (1985).

Acknowledgements

Author Contributions

L.S. - design, acquisition, and interpretation of kinetic data, manuscript writing; K.U. and Z.L. - design, acquisition, and interpretation of TIRF data; Z.K., J.M., Z.N. - design, acquisition, and interpretation of kinetic experiments; J.P., D.T., P.B., B.H. - design, cloning and purification of HDAC6 constructs, M.H. - MS quantification; C.B. - conception and design of the project, manuscript writing. All authors reviewed the manuscript.

Additional Information

Supplementary information accompanies this paper at doi:10.1038/s41598-017-11739-3

Competing Interests: The authors declare that they have no competing interests.

Publisher's note: Springer Nature remains neutral with regard to jurisdictional claims in published maps and institutional affiliations.

Human histone deacetylase 6 shows strong preference for tubulin dimers over assembled microtubules

Lubica Skultetyova[1,2], Kseniya Ustinova[1], Zsofia Kutil[1], Zora Novakova[1], Jiri Pavlicek[1], Jana Mikesova[1], Dalibor Trapl[1], Petra Baranova[1], Barbora Havlinova[1], Martin Hubalek,[3] Zdenek Lansky[1] and Cyril Barinka[1]*

[1]Institute of Biotechnology CAS, BIOCEV, Prumyslova 595, 252 50 Vestec, Czech Republic
[2]Department of Biochemistry, Faculty of Natural Science, Charles University, Albertov 6, Prague 2, Czech Republic
[3]Gilead Sciences and IOCB Research Center, Institute of Organic Chemistry and Biochemistry of the Academy of Sciences of the Czech Republic, Flemingovo n. 2, 166 10 Prague 6, Czech Republic.

Supplementary M&M:

Isolation of tubulin from porcine brains
Ten fresh pig brains were homogenized in DB buffer (50 mM MES, 1 mM $CaCl_2$, pH 6.6 adjusted with NaOH) at 4°C using a blender (Waring Commercial, Stamford, CT, USA). Homogenate was centrifuged at 29,000xg for 1 hour at 4°C and supernatant mixed with HMP buffer (1 M PIPES, 10 mM $MgCl_2$, 20 mM EGTA, pH 6.9 adjusted with KOH) and glycerol in volume ratio 1:1:1 and supplemented with ATP (Jena Bioscience, Jena, Germany), and GTP (Jena Bioscience), to a final concentration 1.5 mM and 0.5 mM, respectively. The mixture was incubated for 1 hour at 37°C and then centrifuged at 151,000xg for 30 minutes at 37°C. The pellet was resuspended in 100 ml ice-cold DB buffer and homogenized by a teflon-glass manual homogenizer for 10 minutes on ice, incubated for 30 minutes on ice and then centrifuged at 70,000xg for 30 minutes at 4°C. Supernatant was mixed with HMP buffer and glycerol in volume ratio 1:1:1 and supplemented with ATP and GTP to a final concentration 1.5 mM and 0.5 mM, respectively. Mixture was incubated for 30 minutes at 37°C and centrifuged at 151,000xg for 30 minutes at 37°C. Pellet was suspended in 10 ml BRB80 buffer (80 mM PIPES, 1 mM $MgCl_2$, 1 mM EGTA, pH 6.8 adjusted with KOH), homogenized by teflon-glass manual homogenizer for 10 minutes on ice, incubated 10 minutes on ice, and centrifuged at 100,000xg for 30 minutes at 4°C. Supernatant containing purified tubulin was flash frozen in aliquots by liquid nitrogen and stored at -80°C.

Supplementary Figures

Fig. S1: Protein constructs used in this study. A; Schematic representation of full-length human HDAC6, its N-terminal fusions and the control GFP-HALO fusion. HDAC6 constructs and the GFP-HALO fusion were produced in suspension HEK293T cells, and purified to homogeneity *via* optimized protocols using the combination Streptactin affinity and size-exclusion chromatography. TEV – TEV-protease recognition site; Strep – Strep-tag; FLAG – FLAG tag. B; Coomassie-stained SDS-PAGE of purified HDAC6 variants. Purity of all protein versions was >98%. C; Steady-state kinetics of HDAC6, GFP-HDAC6 and HALO-HDAC6 on commercial fluorogenic peptide (Ac)GAK(Ac)-AMC. Michaelis-Menten constants (K_M and k_{cat}) for individual construct, calculated from non-linear regression fit using the GraphPad program, are shown in the embedded table.

Fig. S2: Determination of αK40 acetylation ratio

A; The extracted ion chromatogram of $[M+3H]^{3+}$ ions of light (m/z = 995.44) and heavy (m/z = 997.78) non-acetylated version of peptide HGIQPDGQMPSDKTIGGGDDSFNTFFSE. **B**; The extracted ion chromatogram of $[M+3H]^{3+}$ ions of light (m/z = 1009.44) and heavy (m/z = 1011.78) acetylated version of peptide HGIQPDGQMPSDK(Ac)TIGGGDDSFNTFFSE. **C**; Area of corresponding peaks with calculation of acetylation ratio.

Fig. S3: HDAC6 reveals significantly higher deacetylase activity on tubulin dimers than on polymeric tubulin forms.

Uncropped images of representative Western blots shown in Figure 2 of the main manuscript body.

Figure S1

A

GFP-HDAC6 Strep-FLAG | GFP | linker | TEV | HDAC6 (1–1215)

HALO-HDAC6 Strep-FLAG | HALO | linker | TEV | HDAC6

HDAC6 HDAC6

HALO-GFP Strep-FLAG | HALO | TEV | GFP

B

| | St | HDAC6 | GFP-HDAC6 | HALO-HDAC6 | HALO-GFP |

kDa
250
130
100
70
55
35

C

	Construct	K_M [µM]	k_{cat} [s^{-1}]
▲	HALO-HDAC6	5.3 ± 0.4	2.75 ± 0.05
▼	GFP-HDAC6	4.8 ± 0.5	2.15 ± 0.06
■	HDAC6	4.7 ± 0.3	1.89 ± 0.03

V [s^{-1}] vs (Ac)GAK(Ac)-AMC [µM]

112

Figure S2

A — HGIQPDGQMPSDKTIGGGDDSFNTFFSE

B — HGIQPDGQMPSDK(Ac)TIGGGDDSFNTFFSE

C

		Area	L/H ratio
αK40 NonAc	light	8.47E+06	2.13
	heavy	3.97E+06	
αK40 Ac	light	1.26E+06	0.76
	heavy	1.66E+06	

Ac/NonAc ratio = 0,36

Figure S3

5. Discussion

Inhibitors with enhanced lipophilicity

Ability to cross the blood brain barrier is the basic requirement for the drugs targeting the central nervous system (CNS). For drug delivery the cut-off for passage is: molecular weight <350 and lipophilicity with the partition coefficient ClogP < 4 [208]. Involvement of GCPII in several CNS disorders makes it an attractive target for synthesis of highly lipophilic inhibitors. Majority of the most potent inhibitors has either glutamate or its mimetic at the P1' position [21,51] as the S1' pharmacophore pocket is optimized for glutamate binding [25,45,209] and its use at the P1' position markedly increases inhibitory potency of a given compound. However, it is the presence of glutamate/glutarate at the P1' position that negatively affects lipophilicity of GCPII inhibitors.

In Plechanovova *et al*., 2011 [210] we presented a study of substrates where the canonical P1' glutamate moiety of NAAG was substituted by unbranched non-natural amino acids (aliphatic chains of 0-7 carbon atoms – see Figure 11). We observed that the catalytic efficiency increased in direct proportion to the increasing length of the aliphatic chain, starting from alanine. The observed inability of GCPII to recognize Ac-Asp-Gly as a substrate, indicated the necessity of a side chain at the P1' position. To study the binding of the substrates at the active site of enzyme, the rhGCPII E424A inactive mutant was complexed with substrates Ac-Asp-Met (NAAM), Ac-Asp-Aoc, and Ac-Asp-Ano. The use of the inactive mutant permitted us to observe unprocessed substrates. We concluded that the overall fold of the enzyme was unchanged (compared to structure of GCPII E424A with
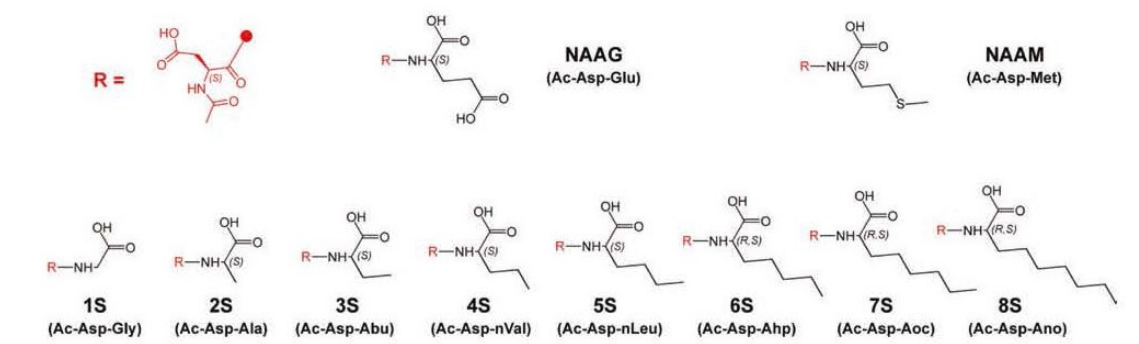
Figure 11 Compounds studied in Plechanovova *et al*., 2011 [210]

115

NAAG). There also was no difference in the polar enzyme-substrate interactions within the S1′ site, considered crucial for the selectivity of a GCPII inhibitor [19,211]. We observed, however, a loss of two hydrogen bonds, originally existing between the glutamate γ-carboxylate and the side chains of Asn257 and Lys699. The substrates with the non-polar side chains were stabilized within the active site by non-polar contacts with the side chains of Phe209, Asn257, Leu428, Lys699, and the main chains of Gly427 and Gly517. The use of substrates with the very long aliphatic chains (with 7 and 8 carbon atoms) forced the S1' site to display a previously unseen plasticity. The Nζ of Lys699 within the glutarate sensing hairpin was forced to shift by 3.9 Å in order to avoid clashing with the C-terminal side chain of the 8S inhibitor. This lead to a stretching of the S1' pocket. As a consequence, to fully occupy the S1' pocket, the bulky C-terminal side-chains was forced to adopt a bow-shaped conformation. Based on the biochemical/structural data on the substrates with aliphatic chains, new inhibitors were synthetized. Here, the Ac-Asp moiety and the peptide bond were replaced by (4-iodo-benzoylamino)hexanoyl group and a non-hydrolysable ureido linker, respectively, as this approach was successfully used in the most potent urea based inhibitor DCIBzL [54]. At the P1' position aliphatic unbranched side chains and methionine were used. Inhibitory constants decreased with the increasing chain length, yet the inhibitory potency of the best of the inhibitors (8I, K_i=29 nM and NAAM, K_i= 23 nM) was still three orders of magnitude lower than the DCIBzL molecule [21]. However, the experiment yielded the desired results, as the elongation of the aliphatic chain also lead to an increase in lipophilicity and the inhibitor with the longest chained had distribution coefficient ClogD = - 0.23. For comparison the ClogD of DCIBzL is -5.16. Analysis of crystallographic data shows that the substrates and inhibitors of the corresponding chain length bind into the pharmacophore pocket in the same manner. Our work also presents additional data supporting the hypothesis that GCPII prefers the *(S)*-enantiomers. In our experiments we used racemates of the substrates and inhibitors and we observed that the *(R)*-enantiomers were not processed by GCPII [20].

We have returned to the design of inhibitors with improved lipophilicity again in Pavlicek *et al.*, 2014, [212]. This article is a follow-up study to Wang *et al.*, [207] who have previously synthetized and tested a set of 20 urea based inhibitors derived from DCIBzL. This

compound, to date the most potent of all urea-based inhibitors, is unfortunately, too hydrophilic to reach CNS [54]. Wang *et al.*, used its scaffold and, adopting a structure-assisted drug design approach, prepared a series of new inhibitors with yet untested moieties replacing the canonical P1' glutamate. The resulting compounds were less potent inhibitors than DCIBzL, however, some of them still had *Ki* values in the low nanomolar range and could be used in imaging. Additionally, the new inhibitors were more lipophilic. Our goal was to understand how these inhibitors interact with GCPII and to identify what modification would allow to improve their properties. To achieve this, we solved the structure of several of these compounds in complex with GCPII. Out of the 20 isosteres of DCIBzL we ruled out 4 with the lowest affinity (*Ki* between 3.43 and 0.79 µM) and 1 due to hydrophilicity. Inhibitors without the P1' side chain or the P1' α-carboxylate were also excluded because

(1) CFIBzL
K_i = 5.3 nM
clogD = -2.4

(2) CHIBzL
K_i = 85.1 nM
clogD = -2.5

(3) CCIBzL
K_i = 318 nM
clogD = -3.9

(4) CPIBzL
K_i = 105 nM
clogD = -2.8

(5) COIBzL
K_i = 254 nM
clogD = -2.9

(6) CEIBzL
K_i = 5.3 nM
clogD = -2.8

DCIBzL
K_i = 0.01 nM clogD = -5.2

Quisqualate
K_i = 9.5 nM
clogD = -3.9
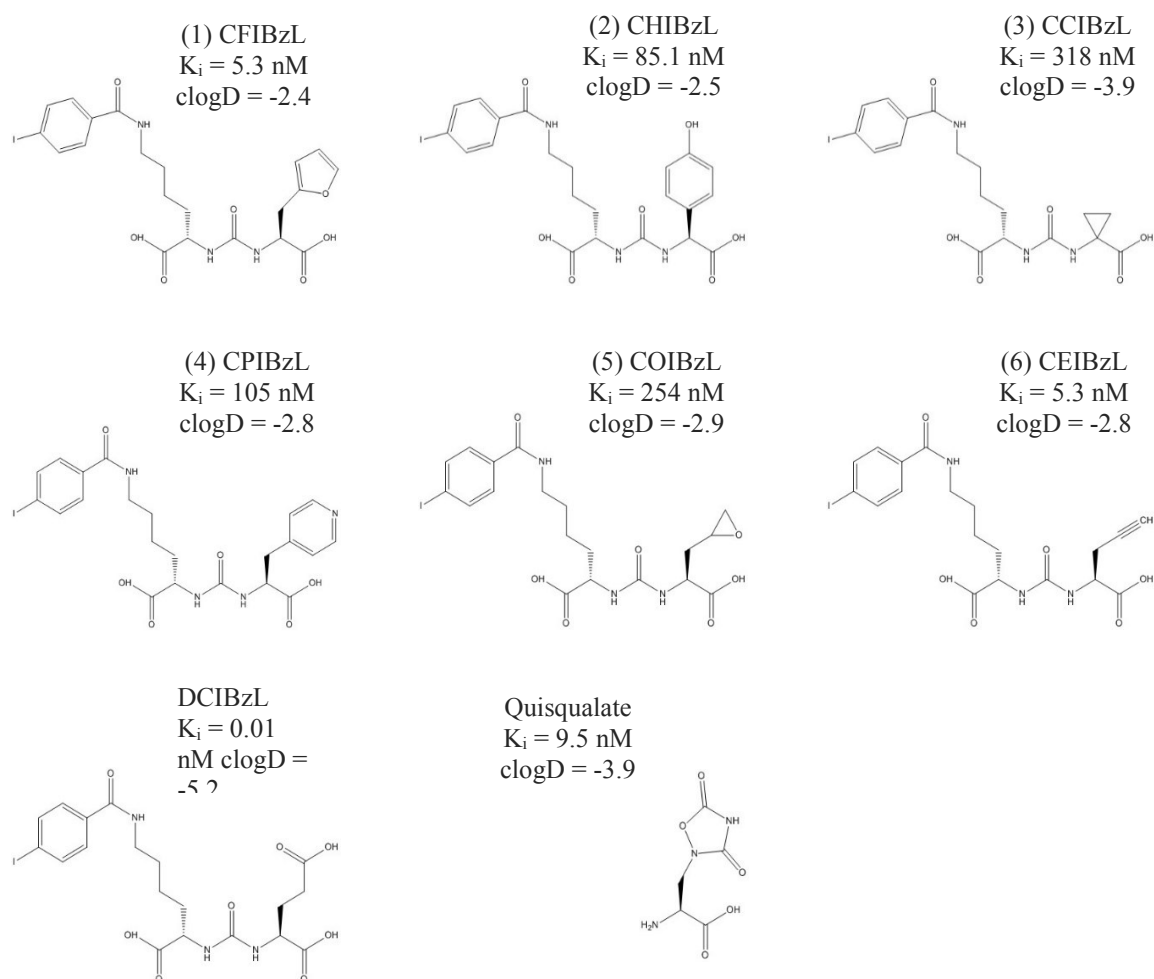
Figure 12: Compounds studied in Pavlicek *et al.*, 2014

these are critical for GCPII affinity [207,210,211]. From the remaining set we selected the six to represent different groups of isosteres. Among the chosen are the most potent inhibitors (**1**) and (**6**) with a five membered heteroaromatic ring and an unsaturated linear chain, then six-membered aromatic ring containing inhibitors (**2**) and (**4**) and finally we wanted to visualize how the three-membered ring isosteres (**3**) and (**5**) bind to GCPII. The parental DCIBzL and quisqualate were included for comparison. The compounds tested are: (**1**) N-2-([[(1S)-1-carboxy-2-(furan-2-yl)ethyl]carbamoyl)-N-6-(4-iodobenzoyl)-L-lysine (CFIBzL, in RCSB under accession number 4OC3), (**2**) N-2-([[(S)-carboxy(4-hydroxyphenyl)methyl]carbamoyl)-N~6-(4-iodobenzoyl)-L-lysine (CHIBzL, 4OC5), (**3**) N-2-[(1-carboxycyclopropyl)carbamoyl]-N~6-(4-iodobenzoyl)-L-lysine (CCIBzL, 4OC0), (**4**) N-2-([[(1S)-1-carboxy-2-(pyridin-4-yl)ethyl]carbamoyl)-N-6-(4-iodobenzoyl)-L-lysine(CPIBzL, 4OC4), (**5**) (2S)-2-[((((1S)-1-carboxy-2-[(2S)-oxiran-2-yl]ethyl)carbamoyl)amino]-6-[(4-iodobenzoyl)amino]hexanoic acid (COIBzL, 4OC1), and (**6**) N-2-([[(1S)-1-carboxybut-3-yn-1-yl]carbamoyl)-N-6-(4-iodobenzoyl)-L-lysine (CEIBzL, 4OC2). Structures of individual inhibitors can be found in Figure 12 on page 117. The general structure arrangement of the protein remained virtually identical. Also, the binding of the 4-iodobenzoyl-ε-lysine into the S1 hydrophobic accessory pocket and of the ureido group is nearly identical to the previously reported structures [207]. Briefly, the plane of the iodobenzoyl moiety is parallel to the guanidinium groups of Arg463 and the Arg534. These arginines interact via their guanidinium groups with the benzene π-electrons. The carbonyl oxygen of the ureido linkage interacts with the activated water, the catalytic Zn_1^{2+}, and with side chains of Tyr552 and His553. The ureido nitrogen atom N1 forms hydrogen bond with Gly518, the N2 with Glu424, Gly518 and the activated water molecule. In between the iodobenzoyl moiety and the urea linker, the lysine linker is as flexible as these two restraining moieties permit. However, there is an additional restrain. The P1 carboxylate forms hydrogen bonds with Arg534 and Arg536 of the hydrophobic accessory pocket. The importance of this interaction has been shown before, as the lack of the P1 carboxylate results in weaker binding of inhibitors to GCPII [17,21,207]. The inhibitors studied here all lack the glutamate moiety at the P1' position, yet they retain the P1' α-carboxylate. While glutamate replacement is possible, in order to increase lipophilicity, the α-carboxylate replacement leads to a drastic decrease in inhibitor potency [21].

The main difference from the previously characterized GCPII/urea based inhibitor complexes is the interaction pattern within the S1' pocket. The most profound changes are observed in the GCPII/(**6**) complex. Binding of the propargylic moiety within the S1' pocket elicits its compaction due to a 3.1 Å shift of the Leu259-Gly263 amino acid loop (the Cα of Leu261 as the reference point). Consequently, in order to not collide with the Leu261, the Lys699 is forced to shift by 7.3 Å (the Nζ atom), in a manner similar to the binding mode of the allylic isostere described by Wang *et al*., 2010 [207]. Taken together, these shifts indicate that the S1' pocket possesses a plasticity never described before.

Another new discovery was the variable orientation of the P1' isosteres consisting of five or six membered rings. The plane of the pyridine ring of inhibitor (**4**) was rotated 70° in regard to the oxadiazolidine ring of the quisqualate, that lays practically perpendicular to the sides of the S1' pocket defined by side chains of Phe209 and Leu428. This rotation results in a widening of the S1' pocket by shifting the Phe209 and the Leu428 by 1 Å. The rings of the other two inhibitors (**1**) and (**2**) are rotated to a lesser degree and their orientations have no effect on the S1' pocket that remains as compact as with bound quisqualate.

Of the six compounds studied in this report, two have identical inhibitory potency in low nanomolar range (**1**) and (**5**). These two inhibitors are weaker than the parental DCIBzL by two orders of magnitude, however, they are significantly more hydrophobic. Kozikowski *et al*., have synthetized and analyzed a series of 20 urea based inhibitors derived from 4,4'-phosphinicobis(butane-1,3-dicarboxylic acid. The best of these inhibitors was 6 times more potent than (**1**) and (**5**), but they were also hydrophilic. However, they obtained a low nanomolar hydrophobic inhibitor with analgesic effects in the inflammatory pain model [209].

This work has contributed new information into the growing body of knowledge about urea inhibitors. We looked at how the selected P1' glutamate isosteres bind into the active site. We have uncovered an ability of the S1' site to adjust its size to bind bigger moieties without affecting the affinity for the inhibitor. This permits more flexibility in future structure-assisted drug design.

The structural data gathered in our publications will help with identifying new ways to modify molecules to achieve higher lipophilicity for GCPII targeted CNS drugs, improved uptake rate, better retention, and high specificity for prostate imaging molecules.

119

Modification of the hydrophilic glutamate/glutarate moiety is not the only approach to address the BBB-permeability issue and deliver drugs inhibiting GCPII to CNS. An injection of ZJ43 and 2-PMPA directly into the cerebrospinal fluid in cerebral ventricles, thus bypassing the BBB, had an analgesic effect on an animal model of inflammatory pain [213]. Another approach is the use of prodrugs - inactive compounds that are metabolized into an active form. Peritoneal injection of PGI-02776, a di-ester prodrug of ZJ43, had been effective in attenuating the damage in a murine model of traumatic brain injury. Upon injection ZJ43 had been detected in brain [214]. Analgesic effects of para-acetoxy-benzyl ester prodrug of the hydroxamate based inhibitor of GPII 4-carboxy-α-[3-(hydroxyamino)-3-oxopropyl]-benzenepropanoic acid and δ-thiolactone prodrug of 2-MPPA exhibited analgesic effects in a rat model of neuropathic pain [215,216].

Phosphoramidate derivatives as PET biotracers

For the growing numbers of men diagnosed with prostate cancer an early diagnosis is a true life saver. Increased efforts are now invested into development of diagnostic and therapeutic methods. Effective diagnostics requires highly sensitive and highly specific tools. GCPII is an ideal target due to the restricted expression pattern in prostate cancer tissue and also its expression in cancer neovasculature in general. PET (positron emission tomography) is replacing the previously used imaging methods but GCPII targeted imaging is lagging behind. The need to replace ProstaScint has been mentioned in the introduction. Small molecules arise as promising probes compared to radio-labeled antibodies, because of their drug-like pharmacokinetics and reduced production costs. Previous research by Lapi *et al.*, 2009 [217] of phosphoramidate derivatives yielded a promising GCPII-specific radiotracer 4-^{18}F-fluorobenzamido-phosphoramidate with the *Ki* = 0.68 nM [218]. When radioactive conjugate was used in mice with PSMA$^+$ xenografts, the tumor accumulation was 1.24 ± 0.17 % ID/g 2 h post-injection, with a tumor-to-blood ratio of 9:1 [217]. Modification of the P1 serine/P1' glutamate phosphoramidate scaffold with 2-(3-hydroxypropyl)glycine, aminohexanoate, and fluorobenzoyl moieties yielded an irreversible inhibitor (**5**) (Figure 13C, page 121). It exhibited similar potency, but a more rapid uptake (2.35 ± 0.91 % ID/g at 1 h) and retention (2.33 ± 0.50 % ID/g at 4 h). Its tumor-to-blood ratio was 265:1 at 4 hours after injection.

The c13rystal structure of GCPII in complex with this inhibitor revealed that the P1 carboxylate interacts with the arginine patch via a salt bridge with the guanidinium group of Arg536 and water-mediated contacts with the side chains of Arg536 and Arg534. The atoms of the 20 Å linker reached into the arene binding site. The main-chain carbonyl accepted hydrogen bond from the guanidinium group of Arg463. The hydrogen bonding results in positioning of the fluorobenzoyl ring plane virtually parallel to both indole and guanidinium groups of Trp541 and Arg511 of the arene-binding cleft, respectively. To investigate this interaction in depth, Dannoon *et al.*, 2016 [219] modified the phosphoramidate scaffold by removing (**4,** CTT1056) or adding (**6**) an extra aminohexanoate (AH) linker to the previously
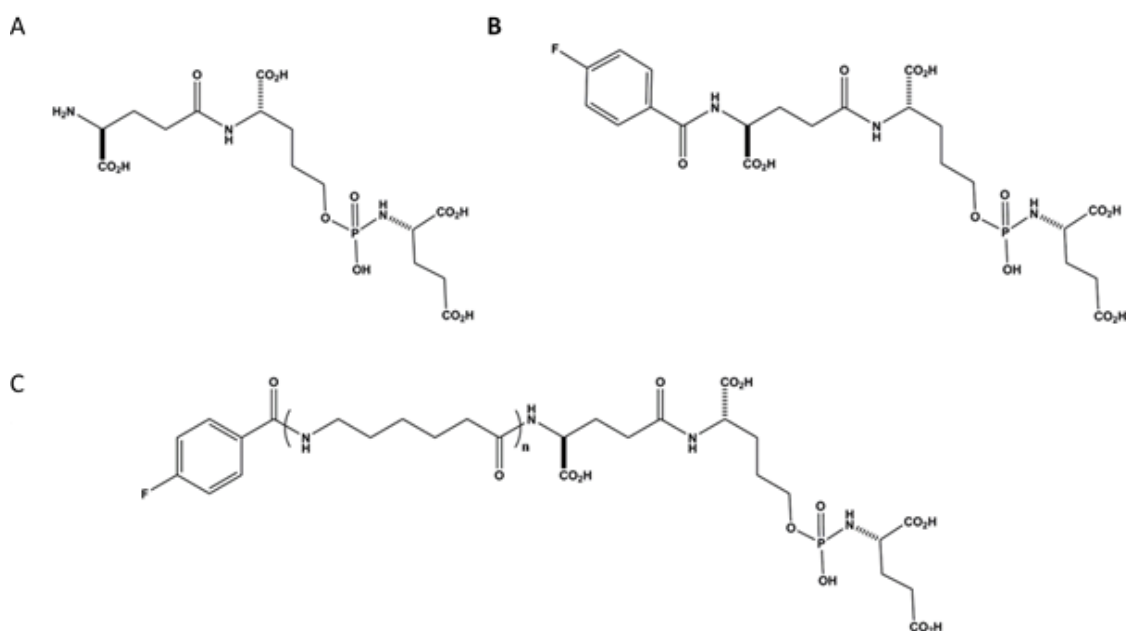
Figure 13: Phosphoramidate inhibitors
A) Phosphoramidate (IC_{50}=14 nM) B) 4-Fluorobenzamidophosphoramidate (IC_{50}=1.4 nM)
C) Compound (**4**) n=0 (IC_{50}=1.3 nM); Compound (**5**) n=1 (IC_{50}=0.4 nM), Compound (**6**) n=2 (IC_{50}=0.9 nM)

identified inhibitor (**5**, CTT1057) (Figure 13C) [219]. The inhibitory potencies of the new compounds were three (**4**, IC_{50} = 1.3 nM) and two fold (**6**, IC_{50} = 0.9 nM) lower than that of the parental molecule (**5**, IC_{50} = 0.4 nM). The use of the AH linker has been successfully used in various histone deacetylases inhibitors derived of hydroxamic acid. This alteration yielded inhibitors with low nanomolar potencies [220,221]. Recently, Tykvart *et al.*, have

121

evaluated the use of a PEG linker of varying length in small molecule inhibitors considered as potential bioimaging agents. The addition of the PEG linker lead to a 7-fold increase in inhibitory activity compared to the parental molecule [222]. All three molecules inhibit GCPII irreversibly which is favorable for imaging tracers. Co-crystallization with the extracellular domain of GCPII (amino acids 44-750) was performed to assess the effect of the AH chain length on binding. The overall fold was nearly invariant for all three complexes. The biggest divergence was detected for amino acids between Ser501 and Pro510. While the F_o-F_c density for the whole of (4) and (5) is visible, the distal part of (6) with the P2 residue, the lipophilic linker and the fluorobenzoyl group cannot be seen, indicating these portions of inhibitor are flexible and do not interact with GCPII. Unlike (4) and (6), where the P1 carboxylate interacts directly with the arginine patch Arg534 and Arg536, the P1 carboxylate of (5) is shifted by 1.1 Å and interacts with Arg536 (NH1, 3.1 Å) only. In all three cases the glutamate moiety occupies the S1' pocket in the canonical manner [19,223]. The difference in the length of the linkers (13, 20, and 28 Å for (4), (5), and (6) respectively) is the main cause for the difference in the positioning of the distal parts of the inhibitors. The fluorobenzoyl ring of (4) forms weak π-cation interactions with the arene binding site and is parallel to the guanidinium group of Arg463 (4 Å). The atoms of the 20 Å linker in (5) reach into the arene binding site with the main-chain carbonyl accepting the hydrogen bond from the guanidinium group of Arg463. The fluorobenzoyl ring plane is virtually parallel to both indole and guanidinium groups of Trp541 and Arg511 of the arene-binding cleft, respectively [223]. A very similar orientation towards Trp541 and Arg511 had previously been described for the pteridine ring of FolGlu$_2$ [23]. There is no detectable electron density for the distal part of (6). All three tracers are specific and are detectable in PSMA$^+$ cells only. A study in which the AH linker was inserted into another PET imaging agent (a DOTA-containing Affibody against HER2- a derivative of Z$_{HER2-342}$) indicates that the aliphatic linker addition might have a potential in improving the biodistribution pattern [224]. Our results are in good agreement with this study, as the tumor to blood ratios and *in vitro* uptake were significantly higher for [^{18}F](6) compared to those of [^{18}F](4) and [^{18}F](5). However, our results also indicate that elongation of the AH linker (as seen in [^{18}F](6)) results in an increase in lipophilicity leading to a decrease in renal clearance and tumor uptake compared to [^{18}F](5). This study has analyzed the difference in binding of this small

series of phosphoramidate derivatives with increasing lipophilicity, evaluated them as PET imaging agents and identified $[^{18}F](5)$ and $[^{18}F](6)$ as promising candidates.

The use of small molecules targeting GCPII as prostate cancer radiotracers in PET imaging circumvents the problem of insufficient pharmacokinetics of antibodies. ^{64}Cu-ABN-1 is another phosphoramidate based PET tracer, a derivative of the CTT-1297 inhibitor [225]. Urea based inhibitors have also been tested in PET imaging. ^{11}C-DCMC is the first urea-based radiotracer [226]. The urea-based $[^{18}F]DCFBC$ has successfully entered clinical studies and permits identification of primary prostate cancer, but is also suitable for identification of metastatic sites [227,228]. Recently, GCPII-binding aptamers (oligonucleotide or peptide molecules specifically binding GCPII) have been evaluated for PET imaging. The pioneering work of Lupold *et al.*, identified two aptamers A9 and A10 specifically binding to GCPII-positive cells [229]. The A10 aptamer has been labeled with ^{64}Cu and shown to bind GCPII-positive cells *in vitro*, yet no data from *in vivo* experiments have been published to date [230].

The ^{18}F labeling used here is not the only possibility for PET imaging. Use of ^{111}In is well documented thanks to its use in the ProstaScint [38]. However, this imaging agent was originally tested and even entered phase II clinical studies labelled with ^{90}Y. This label caused serious bone marrow toxicity and was abandoned for the current ^{111}In [231]. The use of ^{89}Zr and ^{64}Cu labeling had been reported for GCPII targeted antibodies and antibody fragments [232,233]. Labeling with ^{11}C, ^{68}Ga, and ^{64}Cu had been reported for low molecular weight inhibitors of GCPII [226,234–236].

Characterization of HDAC6 as tubulin deacetylase

Dysregulation of HDAC6 is associated with neurodegeneration and cancer. For this deacetylase to become a drug target, a deeper understanding of its many different roles is necessary. In our manuscript we studied deacetylase activity of HDAC6 on tubulin, the most abundant physiological substrate of HDAC6. The tubulin acetylation belongs to a complex system of posttranslational modifications collectively referred to as the tubulin code. The individual modifications and their combinations regulate tubulin polymerization and interactions with other proteins. This in turn affects many cellular processes. As the information on HDAC6 preference for different tubulin forms is unsatisfactory, we decided

to perform a detailed kinetic analysis of tubulin deacetylation and a study of HDAC6/microtubule interactions.

Our first step was cloning and purification of human HDAC6 in order to obtain sufficient amounts of the native protein. We cloned the full length HDAC6 construct into a Gateway donor plasmid. The advantage of the Gateway system is that once the donor plasmid is cloned and sequenced, recloning into the expression plasmids for any system available with as many tag combinations as needed takes less than a week. Since the gene is cloned into expression plasmids as a cassette by recombination, no further sequencing is required. Testing the expression in multiple expression systems warrants identification of the one with the highest yields, the availability of the PTMs required to achieve maximum activity, and the highest purity. We decided to avoid expression in *E. coli* as it is known to be suitable mainly for proteins up to 60 kDa [237]. At first we attempted to purify full length HDAC6 from *K. lactis* since this system provides acetylation, amidation and to some extent phosphorylation. However, these preparations contained massive contamination by alcohol dehydrogenase that could not be completely removed by any affinity purification approaches tested. Purification in insect cells gave yields so low that the expression in this system was not cost effective. Expression in mammalian cells is ideal for mammalian proteins that might require posttranslational modifications to achieve full activity, nonetheless usually at a cost of low yields of protein. In this case though, the transient transfection of HDAC6-containing plasmid yielded 2 mg of protein per liter of HEK293T cells grown in suspension. HDAC6 was then purified in 3 steps, producing mostly monomeric protein without tags with high purity.

As it has been reported that HDAC6 activity and localization is regulated by acetylation, phosphorylation, and S-Nitrosylation, we wanted to see if the protein we purified is modified. For this purpose, the protein was submitted to analysis by LC-MS/MS. Interestingly, this preparation of HDAC6 displays no posttranslational modifications. Since the protein lacks any of the up- or down- regulating modification the activity observed with this purification batch was considered as the basal level of activity. To further characterize our preparation of human HDAC6, we determined the enzymatic activity of our purified HDAC6 without tags and compared it to that described in literature. K_m values on previously described substrates were determined as 3.7 ± 0.2, 4 ± 0.5, 9.1 ± 0.8, and 11.3 ± 0.6 μM for

Fluor de Lys, Boc-K(Ac)-AMC, (Ac)GAK(Ac)-AMC, and Fluor de Lys SIR substrates, respectively. Zou et $al.$, and Miyake et $al.$, report K_m values for Fluor de Lys substrate measured with full length HDAC6 to be 3.3 and 6.45 ± 1.57 µM and k_{cat} 0.29 s-1 and 0.037± 0.002 respectively [65,68]. Schultz et $al.$, have determined K_m for (Ac)GAK(Ac) to be 18 µM and k_{cat} to be 0.7±0.2 s-1 [238]. The K_m values we have obtained are in good accord with the literature, however, the turnover numbers of our protein are 2.23 ± 0.02 and 0.94 ± 0.01 with Fluor de Lys and (Ac)GAK(Ac) substrates, respectively. This is one order of magnitude higher than previously described. We surmise that our HDAC6 preparation therefore contains more catalytically active molecules of enzyme per mol than those characterized elsewhere. Next we determined the inhibition constants for three known inhibitors SAHA, trichostatin A (TSA) and Nexturastat A. The IC_{50} values reported are 5 ± 0.4 nM, 1.2 ± 0.3, and 5.02 ± 0.06 nM, respectively. This again agrees with the values from our experiments which are 3.8 (SAHA), and 0.16 (TSA), and 2.9 nM (Nexturastat A) [200,239,240].

A lot of controversy exists concerning whether HDAC6 preferentially deacetylates free tubulin dimers or microtubules. Problem with the information available is that it is not quantitative and so far the enzyme used in the studies was either murine/zebrafish, tagged/truncated or with no information about its quality available. Given that acetylation is a reversible modification it would be logical that HDAC6 preferred the substrate disfavored by the major tubulin acetyltransferase αTAT1. The acetylase had been reported to preferentially deacetylate microtubules, albeit at a very slow rate. So far it has been shown that HDAC6 deacetylates only microtubules (Hubbert et $al.$, 2002), only dimers (Matsuyama et $al.$, 2002) or both (North et $al.$, 2003). In our manuscript we have shown that the enzyme we are using is mostly monomeric. We have characterized it and compared it to preparations used by other groups. With this full length wild type HDAC6 we see that the enzyme prefers dimers over microtubules. The rate of deacetylation is approximately 1500-fold higher with deacetylation rates 0.6 mol/mol*s and 0.0004 mol/mol*s for tubulin dimers and stabilized MTs, respectively. To exclude possible interference from the stabilization agent we tested both taxol and GMPCPP stabilized microtubules with the same result. Last year Miyake et $al.$, used the catalytic core of zebrafish HDAC6 to quantify the difference between deacetylation of microtubules and tubulin dimers. The difference they observed was

2.5-fold in favor of dimers. If this was true for the full length human HDAC6, the deacetylation rate for microtubules would be 0.24 s^{-1} and since the acetylation rate of αTAT1 has been determined to be 0.00044 s^{-1} this would mean that microtubules would exist in the deacetylated state only. The 1500-fold difference observed in our experiments for the full length protein compared to 2.5 fold observed by Miyake *et al*. for the catalytic core indicates that residues outside the DD1/DD2 core are required for recognition of dimers and microtubules as a substrate. For αTAT1, the binding of the dimeric and the polymeric (MT) substrates is not identical as demonstrated by an experiment where a mutation within the α2 helix affects acetylation rates of these two substrates to a different extent [186]. It is highly possible such a microtubule sensing domain exists within the major deacetylase as well. The pronounced difference in the turnover rate between dimeric tubulin and microtubules supports the hypothesis (formed by Skoge *et al*., 2014 and Miyake *et al*., 2016), that acetylation and deacetylation of tubulin are a result of opposing substrate preferences between HDAC6 and αTAT1 [65,241]. The result also suggests that the free tubulin in the cytoplasm exists solely in the deacetylated form. This conclusion is further backed up by a report in which treatment of mice with colchicine leads to significant decrease in acetylation [242].

Seeing that the deacetylation of microtubules is disfavored so strongly compared to dimers, we wanted to get a deeper understanding of substrate recognition mechanism by HDAC6. As the αAcK40 lies within the microtubule lumen, accessibility is a challenge for modifiers and readers. However, tubulin dimers integrated into microtubule also have a large portion of their surface inaccessible for interaction with MAPs. To see if the substrate preference stems from the limited accessibility of the αAcK40 loop or if it is a result of suboptimal binding to tubulin surface we looked at deacetylation rates of other polymers. Tubulin can polymerize into macromolecules with the αAcK40 loop exposed or hidden, with different tubulin curvature, and with different parts of surface exposed for binding. We have compared microtubules, zinc sheets, and dolastatin-10 rings to tubulin dimers. Zinc sheets form spontaneously in presence of at least 50 μM Zn^{2+}. Unlike in microtubules, where protofilaments bind parallel side by side, zinc sheets are formed of protofilaments in antiparallel orientation with twofold screw axis symmetry (Figure 10B, page 30) and the K40 loop protrudes into space. Dolastatin-10 induces curvature of a protofilament followed

by formation of mostly tetradecameric single-walled rings and mimics the depolymerization process. In the resulting rings the previously luminal side of protofilament becomes exposed to the exterior and is easily accessible. In this polymeric form, the longitudinal surfaces are already engaged by head to tail binding of tubulin to dimers leaving only lateral interactions free for interaction. The deacetylation rates of Dolastatin-10 rings and Zn-sheets are 100- and 750-fold slower than free tubulin. Taken together with the 1500-fold slower rate of microtubules deacetylation our findings indicate that accessibility is not the rate limiting factor. Rather, the longitudinal and lateral interactions are important for optimal turnover of the substrate by HDAC6. The substrate preference is thus complementary to that of αTAT1 for which dimers are the poorest substrates. The Zn^{2+} sheets and dolastatin-10 rings show statistically significant enhancement of acetylation, and microtubules are processed fastest [186].

The Lys40 residue is located in a rather flexible loop formed by 20 amino acids from Gln31 to Asn50, with residues 37 – 42 being highly conserved across tubulins from various species [186]. This raises the following questions: 1) is the sequence of the αK40 loop sufficient to be recognized as a substrate by HDAC6 2) If only 6 amino acids are conserved across the species how long a sequence is required for the optimal deacetylation by HDAC6 3) Is there a difference in the deacetylation rates between the αK40 loop in the form of a free peptide and within the context of αβ-tubulin dimer? We compared the deacetylation rates of α/β tubulin dimer and tri- to nonadecameric peptides derived of amino acids surrounding the central lysine of the αK40 loop. The deacetylation rates for peptides were determined using HPLC and for dimer by quantification from Western blots. Our results show that with the increasing length of the peptide the rate of conversion is decreasing. While the rate is 2.03 ± 0.1 s^{-1} for the T3 (Abz-D[AcK]T-NH2) tubulin peptide, it gradually decreases to 0.1 s^{-1} for peptides T17 (Abz-PDGQMPSD[AcK]TIGGGDDS-NH2) and T19 (Abz-QPDGQMPSD[AcK]TIGGGDDSF-NH2). Although this makes the tripeptide the substrate with the highest deacetylation rate, the α/β tubulin substrate is still deacetylated 12-fold faster. The difference in deacetylation rates indicates that interactions beyond the active site are necessary for optimal substrate turnover and recognition. This is further supported by K_m values for the peptides which are in the high micromolar range (88 µM to 328 µM for T9 and T15, respectively), and indicate relatively low affinity of HDAC6 for the

isolated αK40 sequences. We have determined K_m value for tubulin dimer to be 0.23 ± 0.03 μM and therefore the affinity towards free tubulin is nearly 400 x higher than for the best tubulin-derived peptide substrate. Recently published report by Miyake *et al.*, backs up these results as it shows that mutations of Trp459 and Asp460 in His20-His21 loop and Asn530, and Ser531 in His25 are crucial for α-tubulin recognition while deacetylation of the short peptidic Fluor-de-Lys substrate is unaffected by these mutations [65]. The decrease in deacetylation rate reversely proportional to the length of the peptides and is probably due to steric constrains. Nevertheless, for the optimal activity the substrate needs to interact with the substrate recognizing loop H20-H21 and the H25 helix. In case of tubulin, interaction with lateral and/or longitudinal interfaces seems to be required for maximum activity as indicated by these experiments and the deacetylation of tubulin polymers, where these surfaces are buried within the polymeric lattices. Interestingly, SIRT2 deacetylates α-tubulin peptide (amino acids 36–44, corresponds to T9 peptide) and the k_{cat} was determined to be 0.144 ± 0.005 s^{-1} [183]. We reported the HDAC6 deacetylation rate for the T9 peptide to be 0.31 ± 0.04 s^{-1}. This 2-fold difference might indicate that although both enzymes serve as tubulin deacetylases, their mode of binding the tubulin substrate are not identical and hint at a difference in the active site. However, in the absence of crystallographic data this notion remains only a hypothesis and might be just a result of slightly different experimental setups. One of the big questions of tubulin de/acetylation is how the deacetylases and acetyl transferase access the αK40 in microtubules, if it is buried in the lumen. This has been studied in depth for αTAT1, but data concerning HDAC6 are missing. The possibilities considered are: entering the lumen from the tips, accessing the loop through breaks existing within the microtubule lattice, or accessing it from the outside. Bending of microtubules causes mechanical stress that leads to torsion and consecutively to defects in the microtubule lattice. These are believed to increase accessibility of the microtubule lumen [243]. Also, tubulin monomers are globular proteins so the junctions between two neighboring protofilaments are not tight like between Lego cubes, but a gap forms between two adjacent dimers. The αK40 loop lies beneath this opening and can be modified, but data suggests that a massive reorganization would have to take place in the microtubule for modifying enzymes to be able to access αK40 [244]. Szyk *et al.*, have shown that *in vitro* acetylation of microtubules is evenly distributed without bias for ends or particular localizations that would

signal possible lattice defects. Their conclusion is that αTAT1 diffuses in the lumen and acetylates stochastically yet uniformly [186]. We have used TIRF microscopy with immobilized rhodamine labeled microtubules to study the kinetics of GFP or FITC-labeled HDAC6. This setup permits us to see that HDAC6 binds microtubules fast and without preference for ends. The analysis of the signal intensity at the tips and in the middle indicates synchronous increase at both microtubule tips and core. The dynamics of this interactions points towards HDAC6 binding the microtubule surface rather than entering from tips. In order to see if this binding pattern corresponds to deacetylation, fluorescent microscopy of HDAC6 mixed with microtubules at 2:1 molar ratio was performed. Our micrographs show uniform deacetylation of microtubules and subsequent analysis shows that the acetylation level of whole microtubule, the tips, and of the microtubule center decrease without showing preference for microtubule ends. The Western blots of these samples show this deacetylation that is linear in time. This result is in accord with recent findings about αTAT1 acetylation *in vivo* appearing at the extremities [245]. As the rates of acetylation and deacetylation of microtubules are rather similar if deacetylation had the same pattern this would be impossible to observe.

Our data adds to the understanding of the HDAC6 mediated tubulin acetylation. Hereby, we present sufficient argument and supporting quantitative data concerning HDAC6 to back up the existing hypothesis of the opposing substrate preference of αTAT1 and HDAC6 as the main tubulin acetylase and deacetylase. We also believe that the strong preference of HDAC6 for dimers leads to accumulation of acetylation on microtubules which consequently functions as a marker of microtubule age. Our results indicate that deacetylation of tubulin by HDAC6 requires complex interactions with the substrates surpassing the acetylated Lys40 of the substrate. This complexity might in future form basis for the rational design of inhibitors targeting tubulin deacetylation. Full understanding of interaction between HDAC6 and tubulin will permit discovery of highly selective inhibitors of HDAC6 as tubulin deacetylase.

6. CONCLUSION

We presented here an in-depth study-function study of two zinc-dependent hydrolases: GCPII and HDAC6. We have prepared new GCPII inhibitors and using X-ray crystallography studied their interaction with GCPII. The inhibitors exhibited properties better properties as clinically applicable agents than the parent molecules (lipophilicity and in some cases inhibitor potency too). Also the publications identified yet unknown properties of the enzyme's active site. We reported that GCPII tolerates the replacement of the canonical glutamate moiety within a substrate/inhibitor by aliphatic side chains of varying length at the C-terminal amino acid well. The enzyme even adapts to bind them more effectively. Correspondingly, unfamiliar plasticity was observed for urea-based inhibitor derived from the DCIBzL inhibitor by replacement of glutamate by propargylic moiety. The last strategy presented here consisted in a modification of the aminohexanoic acid linker between fluorobenzamido ring and the core inhibitor, an approach resulting in higher lipophilicity of the new inhibitor. Although we have not succeeded in identifying inhibitors able to cross the BBB barrier all three approaches yielded molecules with low nanomolar inhibition constants sufficient to test them as imaging agents. We have identified new scaffolds leading to improved lipophilicity which can be exploited in future.

As for HDAC6 we have successfully established expression in mammalian cells and purified the enzyme to near 100% purity. We have unequivocally identified tubulin dimers as its preferred substrate and quantified the preference. Using different tubulin polymers, we have shown that accessibility of the αAcK40 is not the rate determining factor. We have shown that efficiency of the tubulin deacetylation enzyme requires interactions additional to those with amino acids within the αAcK40. Lastly, using TIRF and indirect immunofluorescence microscopies, we have shown that HDAC6 does not exhibit preference for either binding or deacetylation of microtubule ends and deacetylates stochastically.

ABBREVIATIONS

αAcK40	Acetylated lysine 40 of α-tubulin
AH linker	Aminohexanoate linker
ARD1	Arrest-defective 1 protein
ATP	Adenosine triphosphate
Bax	Bcl-2-associated X protein
BBB	Blood–brain barrier
BDNF	Brain-derived neurotrophic factor
BIRC5	Baculoviral inhibitor of apoptosis repeat-containing 5
BUZ	Binding of ubiquitin zinc finger
CBP	CREB-binding protein
CDK9	Cyclin-dependent kinase 9
CK1/CK2	Casein kinase 1/Casein kinase 2
CNS	Central nervous system
CRM1	Chromosomal maintenance 1
DCIBzL	(S)-2-(3-((S)-1-Carboxy-(4-iodobenzamido)pentyl)ureido)pentanedioic acid
DD1/DD2	Deacetylase domains
DNA	Deoxyribonucleic acid
EGF	Epidermal growth factor
EGFR	Epidermal growth factor receptor
ELP	Elongator acetyltransferase
ERK1	Extracellular signal-regulated kinase 1
FITC	Fluorescein isothiocyanate
FOLH1	Folate hydrolase 1
GCN5	General control non-derepressible 5
GCPII	Glutamate carboxypeptidase II
GCPII KO mice	GCPII knock-out mice
GMPCPP	Guanosine-5'-[(α,β)-methyleno]triphosphate
GRK2	G protein-coupled receptor kinase 2

GSK3β	Glycogen synthase kinase 3β
GTP/GDP	Guanosine triphosphate/Guanosine diphosphate
HDA1	Histone deacetylase 1
HDAC6	Histone deacetylase 6
HIV1	Human immunodeficiency virus
HPLC	High-performance liquid chromatography
HSF1	Heat shock factor 1
HSP90	Heat shock protein 90)
IFN-γ	Interferon gamma
IgG	Immunoglobulin G
IL-1β	Interleukin 1 beta
IRT	Iron-regulated transporter
IUBMB	International Union of Biochemistry and Molecular Biology
JNK	c-Jun N-terminal kinase
kDa	Kilodalton
KDAC	Lysine deacetylase
MAPK	Mitogen-activated protein kinase
MAPs	Microtubule-associated proteins
MEC17	Mechanosensory abnormality family member 17
2-MPPA	2-(3-mercaptopropyl)pentanedioic acid
MSH2	MutS protein homologue 2
MT	Microtubule
MTOC	Microtubule-organizing center
MYH9	Myosin heavy chain 9
NAA	N-acetyl-L-aspartate
NAAG	N-acetylaspartylglutamate
NAALADase I	N-acetyl-L-aspartyl-L-glutamate peptidase I
NAAM	N-acetylaspartylmethionine
NAD$^+$	Oxidized form of nicotinamide adenine dinucleotide
NAT1	N-acetyltransferase 1
NES	Nuclear exclusion sequence

NLS	Nuclear localization sequence
PET	Positron emission tomography
pKa	Negative logarithm of the acid dissociation constant
PKCζ	Protein kinase C zeta type
2-PMPA	2-phosphonomethylpentanedioic acid
Prx1/PrxII	Peroxiredoxin I or II
PSMA	Prostate-specific membrane antigen
P-TEFb	Positive transcription elongation factor b
PTM	Posttranslational modification
RCSB PDB	Research Collaboratory for Structural Bioinformatics Protein Data Bank
ROS	Reactive oxygen species
RPD3	Reduced potassium dependency 3
SAHA	Suberoylanilide hydroxamic acid (vorinostat)
SE14	Serine-Glutamate containing tetradecapeptide
SIRT1	Silent mating type information regulation 2 homolog 1
αTAT1	Alpha-tubulin N-acetyltransferase
TDAC	Tubulin deacetylase
TIRF	Total internal reflection fluorescence
TNFα	Tumor necrosis factor alpha
TSA	Trichostatin A
US FDA	United States Food and Drug Administration
VCP	Valosin-containing protein
VEGFR1	Vascular endothelial growth factor receptor 1
VPA	Valproic acid
ZBG	Zinc-binding group
ZIP4	Zrt- and Irt-related protein
ZRT	Zinc transporter proteins

REFERENCES

1.   Andreini, C., Banci, L., Bertini, I., Rosato, A. (2006) Counting the zinc-proteins encoded in the human genome. *J Proteome Res* **5**, 196–201.

2.   Sehgal, V.N., Jain, S. (2000) Acrodermatitis enteropathica. *Clin Dermatol* **18**, 745–48.

3.   Hernick, M., Fierke, C.A. (2005) Zinc hydrolases: the mechanisms of zinc-dependent deacetylases. *Arch Biochem Biophys* **433**, 71–84.

4.   Auld, D.S. (2009) The ins and outs of biological zinc sites. *Biometals* **22**, 141–48.

5.   McCall, K.A., Huang, C., Fierke, C.A. (2000) Function and mechanism of zinc metalloenzymes. *J Nutr* **130**, 1437S–46S.

6.   Robinson, M.B., Blakely, R.D., Couto, R., Coyle, J.T. (1987) Hydrolysis of the brain dipeptide N-acetyl-L-aspartyl-L-glutamate. Identification and characterization of a novel N-acetylated alpha-linked acidic dipeptidase activity from rat brain. *J Biol Chem* **262**, 14498–506.

7.   Rawlings, N.D., Tolle, D.P., Barrett, A.J. (2004) MEROPS: the peptidase database. *Nucleic Acids Res* **32**, D160-4.

8.   O'Keefe, D.S., Su, S.L., Bacich, D.J., Horiguchi, Y., Luo, Y., Powell, C.T., Zandvliet, D., Russell, P.J., Molloy, P.L., Nowak, N.J., Shows, T.B., Mullins, C., Vonder Haar, R.A., Fair, W.R., Heston, W.D. (1998) Mapping, genomic organization and promoter analysis of the human prostate-specific membrane antigen gene. *Biochim Biophys Acta* **1443**, 113–27.

9.   Blakely, R.D., Robinson, M.B., Thompson, R.C., Coyle, J.T. (1988) Hydrolysis of the brain dipeptide N-acetyl-L-aspartyl-L-glutamate: subcellular and regional distribution, ontogeny, and the effect of lesions on N-acetylated-alpha-linked acidic dipeptidase activity. *J Neurochem* **50**, 1200–1209.

10.   Chang, S.S., O'Keefe, D.S., Bacich, D.J., Reuter, V.E., Heston, W.D., Gaudin, P.B. (1999) Prostate-specific membrane antigen is produced in tumor-associated neovasculature. *Clin Cancer Res* **5**, 2674–81.

11.   Silver, D.A., Pellicer, I., Fair, W.R., Heston, W.D., Cordon-Cardo, C. (1997) Prostate-specific membrane antigen expression in normal and malignant human tissues. *Clin Cancer Res* **3**, 81–85.

12.   Rawlings, N.D., Barrett, A.J. (1997) Structure of membrane glutamate carboxypeptidase. *Biochim Biophys Acta* **1339**, 247–52.

13.   Christiansen, J.J., Rajasekaran, S.A., Moy, P., Butch, A., Goodglick, L., Gu, Z., Reiter, R.E., Bander, N.H., Rajasekaran, A.K. (2003) Polarity of prostate specific membrane antigen, prostate stem cell antigen, and prostate specific antigen in prostate tissue and in a cultured epithelial cell line. *Prostate* **55**, 9–19.

14.   Anilkumar, G., Barwe, S.P., Christiansen, J.J., Rajasekaran, S.A., Kohn, D.B., Rajasekaran, A.K. (2006) Association of prostate-specific membrane antigen with caveolin-1 and its caveolae-dependent internalization in microvascular endothelial cells: implications for targeting to tumor vasculature. *Microvasc Res* **72**, 54–61.

15.   Liu, H., Rajasekaran, A.K., Moy, P., Xia, Y., Kim, S., Navarro, V., Rahmati, R., Bander, N.H. (1998) Constitutive and antibody-induced internalization of prostate-specific membrane antigen. *Cancer Res* **58**, 4055–60.

16.   Mesters, J.R., Barinka, C., Li, W., Tsukamoto, T., Majer, P., Slusher, B.S., Konvalinka, J., Hilgenfeld, R. (2006) Structure of glutamate carboxypeptidase II, a drug target in neuronal damage and prostate cancer. *EMBO J* **25**, 1375–84.

17.   Barinka, C., Hlouchova, K., Rovenska, M., Majer, P., Dauter, M., Hin, N., Ko, Y.S., Tsukamoto, T., Slusher, B.S., Konvalinka, J., Lubkowski, J. (2008) Structural basis of interactions between human glutamate carboxypeptidase II and its substrate analogs. *J Mol Biol* **376**, 1438–50.

18.   Davis, M.I., Bennett, M.J., Thomas, L.M., Bjorkman, P.J. (2005) Crystal structure of prostate-specific membrane antigen, a tumor marker and peptidase. *Proc Natl Acad Sci U A* **102**, 5981–86.

19.   Barinka, C., Rovenska, M., Mlcochova, P., Hlouchova, K., Plechanovova, A., Majer, P., Tsukamoto, T., Slusher, B.S., Konvalinka, J., Lubkowski, J. (2007) Structural insight into the pharmacophore pocket of human glutamate carboxypeptidase II. *J Med Chem* **50**, 3267–73.

20.   Vitharana, D., France, J.E., Scarpetti, D., Bonneville, G.W., Majer, P., Tsukamoto, T. (2002) Synthesis and biological evaluation of (R)- and (S)-2-(phosphonomethyl)pentanedioic acids as inhibitors of glutamate carboxypeptidase II. *Tetrahedron Asymmetry* **13**, 1609–14.

21.   Barinka, C., Byun, Y., Dusich, C.L., Banerjee, S.R., Chen, Y., Castanares, M., Kozikowski, A.P., Mease, R.C., Pomper, M.G., Lubkowski, J. (2008) Interactions between human glutamate carboxypeptidase II and urea-based inhibitors: structural characterization. *J Med Chem* **51**, 7737–43.

22.   Zhang, A.X., Murelli, R.P., Barinka, C., Michel, J., Cocleaza, A., Jorgensen, W.L., Lubkowski, J., Spiegel, D.A. (2010) A remote arene-binding site on prostate specific membrane antigen revealed by antibody-recruiting small molecules. *J Am Chem Soc* **132**, 12711–16.

23.   Navratil, M., Ptacek, J., Sacha, P., Starkova, J., Lubkowski, J., Barinka, C., Konvalinka, J. (2014) Structural and biochemical characterization of the folyl-poly-gamma-l-glutamate hydrolyzing activity of human glutamate carboxypeptidase II. *FEBS J* **281**, 3228–42.

24.   Barinka, C., Sacha, P., Sklenar, J., Man, P., Bezouska, K., Slusher, B.S., Konvalinka, J. (2004) Identification of the N-glycosylation sites on glutamate carboxypeptidase II necessary for proteolytic activity. *Protein Sci* **13**, 1627–35.

25.   Barinka, C., Rinnova, M., Sacha, P., Rojas, C., Majer, P., Slusher, B.S., Konvalinka, J. (2002) Substrate specificity, inhibition and enzymological analysis of recombinant human glutamate carboxypeptidase II. *J Neurochem* **80**, 477–87.

26.   Choi, J.Y., Kim, J.H., Jo, S.A. (2014) Acetylation regulates the stability of glutamate carboxypeptidase II protein in human astrocytes. *Biochem Biophys Res Commun* **450**, 372–77.

27.   Klusak, V., Barinka, C., Plechanovova, A., Mlcochova, P., Konvalinka, J., Rulisek, L., Lubkowski, J. (2009) Reaction mechanism of glutamate carboxypeptidase II revealed by mutagenesis, X-ray crystallography, and computational methods. *Biochemistry (Mosc.)* **48**, 4126–38.

28.   Bacich, D.J., Ramadan, E., O'Keefe, D.S., Bukhari, N., Wegorzewska, I., Ojeifo, O., Olszewski, R., Wrenn, C.C., Bzdega, T., Wroblewska, B., Heston, W.D., Neale, J.H.

(2002) Deletion of the glutamate carboxypeptidase II gene in mice reveals a second enzyme activity that hydrolyzes N-acetylaspartylglutamate. *J Neurochem* **83**, 20–29.

29.	Tsai, G., Dunham, K.S., Drager, U., Grier, A., Anderson, C., Collura, J., Coyle, J.T. (2003) Early embryonic death of glutamate carboxypeptidase II (NAALADase) homozygous mutants. *Synapse* **50**, 285–92.

30.	Han, L., Picker, J.D., Schaevitz, L.R., Tsai, G., Feng, J., Jiang, Z., Chu, H.C., Basu, A.C., Berger-Sweeney, J., Coyle, J.T. (2009) Phenotypic characterization of mice heterozygous for a null mutation of glutamate carboxypeptidase II. *Synapse* **63**, 625–35.

31.	Gao, Y., Xu, S., Cui, Z., Zhang, M., Lin, Y., Cai, L., Wang, Z., Luo, X., Zheng, Y., Wang, Y., Luo, Q., Jiang, J., Neale, J.H., Zhong, C. (2015) Mice lacking glutamate carboxypeptidase II develop normally, but are less susceptible to traumatic brain injury. *J Neurochem* **134**, 340–53.

32.	Mlcochova, P., Barinka, C., Tykvart, J., Sacha, P., Konvalinka, J. (2009) Prostate-specific membrane antigen and its truncated form PSM'. *Prostate* **69**, 471–79.

33.	Berger, U.V., Carter, R.E., Coyle, J.T. (1995) The immunocytochemical localization of N-acetylaspartyl glutamate, its hydrolysing enzyme NAALADase, and the NMDAR-1 receptor at a vertebrate neuromuscular junction. *Neuroscience* **64**, 847–50.

34.	Sacha, P., Zamecnik, J., Barinka, C., Hlouchova, K., Vicha, A., Mlcochova, P., Hilgert, I., Eckschlager, T., Konvalinka, J. (2007) Expression of glutamate carboxypeptidase II in human brain. *Neuroscience* **144**, 1361–72.

35.	Pinto, J.T., Suffoletto, B.P., Berzin, T.M., Qiao, C.H., Lin, S., Tong, W.P., May, F., Mukherjee, B., Heston, W.D. (1996) Prostate-specific membrane antigen: a novel folate hydrolase in human prostatic carcinoma cells. *Clin Cancer Res* **2**, 1445–51.

36.	Conway, R.E., Petrovic, N., Li, Z., Heston, W., Wu, D., Shapiro, L.H. (2006) Prostate-specific membrane antigen regulates angiogenesis by modulating integrin signal transduction. *Mol Cell Biol* **26**, 5310–24.

37.	Israeli, R.S., Powell, C.T., Fair, W.R., Heston, W.D. (1993) Molecular cloning of a complementary DNA encoding a prostate-specific membrane antigen. *Cancer Res* **53**, 227–30.

38.	Manyak, M.J. (2008) Indium-111 capromab pendetide in the management of recurrent prostate cancer. *Expert Rev Anticancer Ther* **8**, 175–81.

39.	Chang, S.S., Reuter, V.E., Heston, W.D., Bander, N.H., Grauer, L.S., Gaudin, P.B. (1999) Five different anti-prostate-specific membrane antigen (PSMA) antibodies confirm PSMA expression in tumor-associated neovasculature. *Cancer Res* **59**, 3192–98.

40.	Kass, I.S., Lipton, P. (1982) Mechanisms involved in irreversible anoxic damage to the in vitro rat hippocampal slice. *J Physiol* **332**, 459–72.

41.	Shaw, P.J., Ince, P.G. (1997) Glutamate, excitotoxicity and amyotrophic lateral sclerosis. *J Neurol* **244 Suppl 2**, S3-14.

42.	Chamoun, R., Suki, D., Gopinath, S.P., Goodman, J.C., Robertson, C. (2010) Role of extracellular glutamate measured by cerebral microdialysis in severe traumatic brain injury. *J Neurosurg* **113**, 564–70.

43.	Olszewski, R.T., Janczura, K.J., Bzdega, T., Der, E.K., Venzor, F., O'Rourke, B., Hark, T.J., Craddock, K.E., Balasubramanian, S., Moussa, C., Neale, J.H. (2017) NAAG Peptidase Inhibitors Act via mGluR3: Animal Models of Memory, Alzheimer's, and Ethanol Intoxication. *Neurochem Res* .

44.   Takatsu, Y., Fujita, Y., Tsukamoto, T., Slusher, B.S., Hashimoto, K. (2011) Orally active glutamate carboxypeptidase II inhibitor 2-MPPA attenuates dizocilpine-induced prepulse inhibition deficits in mice. *Brain Res* **1371**, 82–86.

45.   Jackson, P.F., Tays, K.L., Maclin, K.M., Ko, Y.S., Li, W., Vitharana, D., Tsukamoto, T., Stoermer, D., Lu, X.C., Wozniak, K., Slusher, B.S. (2001) Design and pharmacological activity of phosphinic acid based NAALADase inhibitors. *J Med Chem* **44**, 4170–75.

46.   Majer, P., Jackson, P.F., Delahanty, G., Grella, B.S., Ko, Y.S., Li, W., Liu, Q., Maclin, K.M., Polakova, J., Shaffer, K.A., Stoermer, D., Vitharana, D., Wang, E.Y., Zakrzewski, A., Rojas, C., Slusher, B.S., Wozniak, K.M., Burak, E., Limsakun, T., Tsukamoto, T. (2003) Synthesis and biological evaluation of thiol-based inhibitors of glutamate carboxypeptidase II: discovery of an orally active GCP II inhibitor. *J Med Chem* **46**, 1989–96.

47.   Zhang, W., Murakawa, Y., Wozniak, K.M., Slusher, B., Sima, A.A. (2006) The preventive and therapeutic effects of GCPII (NAALADase) inhibition on painful and sensory diabetic neuropathy. *J Neurol Sci* **247**, 217–23.

48.   Majer, P., Hin, B., Stoermer, D., Adams, J., Xu, W., Duvall, B.R., Delahanty, G., Liu, Q., Stathis, M.J., Wozniak, K.M., Slusher, B.S., Tsukamoto, T. (2006) Structural optimization of thiol-based inhibitors of glutamate carboxypeptidase II by modification of the P1' side chain. *J Med Chem* **49**, 2876–85.

49.   Slusher, B.S., Vornov, J.J., Thomas, A.G., Hurn, P.D., Harukuni, I., Bhardwaj, A., Traystman, R.J., Robinson, M.B., Britton, P., Lu, X.C., Tortella, F.C., Wozniak, K.M., Yudkoff, M., Potter, B.M., Jackson, P.F. (1999) Selective inhibition of NAALADase, which converts NAAG to glutamate, reduces ischemic brain injury. *Nat Med* **5**, 1396–1402.

50.   Barinka, C., Rojas, C., Slusher, B., Pomper, M. (2012) Glutamate carboxypeptidase II in diagnosis and treatment of neurologic disorders and prostate cancer. *Curr Med Chem* **19**, 856–70.

51.   Jackson, P.F., Cole, D.C., Slusher, B.S., Stetz, S.L., Ross, L.E., Donzanti, B.A., Trainor, D.A. (1996) Design, synthesis, and biological activity of a potent inhibitor of the neuropeptidase N-acetylated alpha-linked acidic dipeptidase. *J Med Chem* **39**, 619–22.

52.   Mesters, J.R., Henning, K., Hilgenfeld, R. (2007) Human glutamate carboxypeptidase II inhibition: structures of GCPII in complex with two potent inhibitors, quisqualate and 2-PMPA. *Acta Crystallogr Biol Crystallogr* **63**, 508–13.

53.   He, G.-X., Krise, J.P., Oliyai, R. (2007) Prodrugs of Phosphonates, Phosphinates, and Phosphates. **V**, 923–64.

54.   Chen, Y., Foss, C.A., Byun, Y., Nimmagadda, S., Pullambhatla, M., Fox, J.J., Castanares, M., Lupold, S.E., Babich, J.W., Mease, R.C., Pomper, M.G. (2008) Radiohalogenated prostate-specific membrane antigen (PSMA)-based ureas as imaging agents for prostate cancer. *J Med Chem* **51**, 7933–43.

55.   Novakova, Z., Wozniak, K., Jancarik, A., Rais, R., Wu, Y., Pavlicek, J., Ferraris, D., Havlinova, B., Ptacek, J., Vavra, J., Hin, N., Rojas, C., Majer, P., Slusher, B.S., Tsukamoto, T., Barinka, C. (2016) Unprecedented Binding Mode of Hydroxamate-Based Inhibitors of Glutamate Carboxypeptidase II: Structural Characterization and Biological Activity. *J Med Chem* **59**, 4539–50.

56.   Verdin, E., Dequiedt, F., Kasler, H.G. (2003) Class II histone deacetylases: versatile regulators. *Trends Genet* **19**, 286–93.

57.   Chen, H.P., Zhao, Y.T., Zhao, T.C. (2015) Histone deacetylases and mechanisms of regulation of gene expression. *Crit Rev Oncog* **20**, 35–47.

58.   Gao, L., Cueto, M.A., Asselbergs, F., Atadja, P. (2002) Cloning and functional characterization of HDAC11, a novel member of the human histone deacetylase family. *J Biol Chem* **277**, 25748–55.

59.   Mahlknecht, U., Schnittger, S., Landgraf, F., Schoch, C., Ottmann, O.G., Hiddemann, W., Hoelzer, D. (2001) Assignment of the human histone deacetylase 6 gene (HDAC6) to X chromosome p11.23 by in situ hybridization. *Cytogenet Cell Genet* **93**, 135–36.

60.   Voelter-Mahlknecht, S., Mahlknecht, U. (2003) Cloning and structural characterization of the human histone deacetylase 6 gene. *Int J Mol Med* **12**, 87–93.

61.   Riolo, M.T., Cooper, Z.A., Holloway, M.P., Cheng, Y., Bianchi, C., Yakirevich, E., Ma, L., Chin, Y.E., Altura, R.A. (2012) Histone deacetylase 6 (HDAC6) deacetylates survivin for its nuclear export in breast cancer. *J Biol Chem* **287**, 10885–93.

62.   Verdel, A., Curtet, S., Brocard, M.P., Rousseaux, S., Lemercier, C., Yoshida, M., Khochbin, S. (2000) Active maintenance of mHDA2/mHDAC6 histone-deacetylase in the cytoplasm. *Curr Biol* **10**, 747–49.

63.   Liu, Y., Peng, L., Seto, E., Huang, S., Qiu, Y. (2012) Modulation of histone deacetylase 6 (HDAC6) nuclear import and tubulin deacetylase activity through acetylation. *J Biol Chem* **287**, 29168–74.

64.   Han, Y., Jeong, H.M., Jin, Y.H., Kim, Y.J., Jeong, H.G., Yeo, C.Y., Lee, K.Y. (2009) Acetylation of histone deacetylase 6 by p300 attenuates its deacetylase activity. *Biochem Biophys Res Commun* **383**, 88–92.

65.   Miyake, Y., Keusch, J.J., Wang, L., Saito, M., Hess, D., Wang, X., Melancon, B.J., Helquist, P., Gut, H., Matthias, P. (2016) Structural insights into HDAC6 tubulin deacetylation and its selective inhibition. *Nat Chem Biol* **12**, 748–54.

66.   Lombardi, P.M., Cole, K.E., Dowling, D.P., Christianson, D.W. (2011) Structure, mechanism, and inhibition of histone deacetylases and related metalloenzymes. *Curr Opin Struct Biol* **21**, 735–43.

67.   Zhang, Y., Gilquin, B., Khochbin, S., Matthias, P. (2006) Two catalytic domains are required for protein deacetylation. *J Biol Chem* **281**, 2401–4.

68.   Zou, H., Wu, Y., Navre, M., Sang, B.C. (2006) Characterization of the two catalytic domains in histone deacetylase 6. *Biochem Biophys Res Commun* **341**, 45–50.

69.   Zhang, X., Yuan, Z., Zhang, Y., Yong, S., Salas-Burgos, A., Koomen, J., Olashaw, N., Parsons, J.T., Yang, X.J., Dent, S.R., Yao, T.P., Lane, W.S., Seto, E. (2007) HDAC6 modulates cell motility by altering the acetylation level of cortactin. *Mol Cell* **27**, 197–213.

70.   Hai, Y., Christianson, D.W. (2016) Histone deacetylase 6 structure and molecular basis of catalysis and inhibition. *Nat Chem Biol* **12**, 741–47.

71.   Bertos, N.R., Gilquin, B., Chan, G.K., Yen, T.J., Khochbin, S., Yang, X.J. (2004) Role of the tetradecapeptide repeat domain of human histone deacetylase 6 in cytoplasmic retention. *J Biol Chem* **279**, 48246–54.

72.   Kovacs, J.J., Murphy, P.J., Gaillard, S., Zhao, X., Wu, J.T., Nicchitta, C.V., Yoshida, M., Toft, D.O., Pratt, W.B., Yao, T.P. (2005) HDAC6 regulates Hsp90

acetylation and chaperone-dependent activation of glucocorticoid receptor. *Mol Cell* **18**, 601–7.

73.   Hook, S.S., Orian, A., Cowley, S.M., Eisenman, R.N. (2002) Histone deacetylase 6 binds polyubiquitin through its zinc finger (PAZ domain) and copurifies with deubiquitinating enzymes. *Proc Natl Acad Sci U A* **99**, 13425–30.

74.   Kawaguchi, Y., Kovacs, J.J., McLaurin, A., Vance, J.M., Ito, A., Yao, T.P. (2003) The deacetylase HDAC6 regulates aggresome formation and cell viability in response to misfolded protein stress. *Cell* **115**, 727–38.

75.   Borgas, D., Chambers, E., Newton, J., Ko, J., Rivera, S., Rounds, S., Lu, Q. (2016) Cigarette Smoke Disrupted Lung Endothelial Barrier Integrity and Increased Susceptibility to Acute Lung Injury via Histone Deacetylase 6. *Am J Respir Cell Mol Biol* **54**, 683–96.

76.   Watabe, M., Nakaki, T. (2011) Protein kinase CK2 regulates the formation and clearance of aggresomes in response to stress. *J Cell Sci* **124**, 1519–32.

77.   Deribe, Y.L., Wild, P., Chandrashaker, A., Curak, J., Schmidt, M.H., Kalaidzidis, Y., Milutinovic, N., Kratchmarova, I., Buerkle, L., Fetchko, M.J., Schmidt, P., Kittanakom, S., Brown, K.R., Jurisica, I., Blagoev, B., Zerial, M., Stagljar, I., Dikic, I. (2009) Regulation of epidermal growth factor receptor trafficking by lysine deacetylase HDAC6. *Sci Signal* **2**, ra84.

78.   Williams, K.A., Zhang, M., Xiang, S., Hu, C., Wu, J.Y., Zhang, S., Ryan, M., Cox, A.D., Der, C.J., Fang, B., Koomen, J., Haura, E., Bepler, G., Nicosia, S.V., Matthias, P., Wang, C., Bai, W., Zhang, X. (2013) Extracellular signal-regulated kinase (ERK) phosphorylates histone deacetylase 6 (HDAC6) at serine 1035 to stimulate cell migration. *J Biol Chem* **288**, 33156–70.

79.   Lafarga, V., Aymerich, I., Tapia, O., Mayor, F., Penela, P. (2012) A novel GRK2/HDAC6 interaction modulates cell spreading and motility. *EMBO J* **31**, 856–69.

80.   Du, Y., Seibenhener, M.L., Yan, J., Jiang, J., Wooten, M.C. (2015) aPKC phosphorylation of HDAC6 results in increased deacetylation activity. *PLoS One* **10**, e0123191.

81.   Pugacheva, E.N., Jablonski, S.A., Hartman, T.R., Henske, E.P., Golemis, E.A. (2007) HEF1-dependent Aurora A activation induces disassembly of the primary cilium. *Cell* **129**, 1351–63.

82.   Okuda, K., Ito, A., Uehara, T. (2015) Regulation of Histone Deacetylase 6 Activity via S-Nitrosylation. *Biol Pharm Bull* **38**, 1434–37.

83.   Zhang, M., Xiang, S., Joo, H.Y., Wang, L., Williams, K.A., Liu, W., Hu, C., Tong, D., Haakenson, J., Wang, C., Zhang, S., Pavlovicz, R.E., Jones, A., Schmidt, K.H., Tang, J., Dong, H., Shan, B., Fang, B., Radhakrishnan, R., Glazer, P.M., Matthias, P., Koomen, J., Seto, E., Bepler, G., Nicosia, S.V., Chen, J., Li, C., Gu, L., Li, G.M., Bai, W., et al. (2014) HDAC6 deacetylates and ubiquitinates MSH2 to maintain proper levels of MutSalpha. *Mol Cell* **55**, 31–46.

84.   Cohen, H.Y., Lavu, S., Bitterman, K.J., Hekking, B., Imahiyerobo, T.A., Miller, C., Frye, R., Ploegh, H., Kessler, B.M., Sinclair, D.A. (2004) Acetylation of the C terminus of Ku70 by CBP and PCAF controls Bax-mediated apoptosis. *Mol Cell* **13**, 627–38.

85.   Parmigiani, R.B., Xu, W.S., Venta-Perez, G., Erdjument-Bromage, H., Yaneva, M., Tempst, P., Marks, P.A. (2008) HDAC6 is a specific deacetylase of peroxiredoxins and is involved in redox regulation. *Proc. Natl. Acad. Sci. U. S. A.* **105**, 9633–38.

86.   Li, G.M. (2008) Mechanisms and functions of DNA mismatch repair. *Cell Res* **18**, 85–98.

87.   Edelbrock, M.A., Kaliyaperumal, S., Williams, K.J. (2013) Structural, molecular and cellular functions of MSH2 and MSH6 during DNA mismatch repair, damage signaling and other noncanonical activities. *Mutat Res* **743–744**, 53–66.

88.   Li, Y., Zhang, X., Polakiewicz, R.D., Yao, T.P., Comb, M.J. (2008) HDAC6 is required for epidermal growth factor-induced beta-catenin nuclear localization. *J Biol Chem* **283**, 12686–90.

89.   Jamieson, C., Sharma, M., Henderson, B.R. (2014) Targeting the beta-catenin nuclear transport pathway in cancer. *Semin Cancer Biol* **27**, 20–29.

90.   Youn, G.S., Lee, K.W., Choi, S.Y., Park, J. (2016) Overexpression of HDAC6 induces pro-inflammatory responses by regulating ROS-MAPK-NF-kappaB/AP-1 signaling pathways in macrophages. *Free Radic Biol Med* **97**, 14–23.

91.   Ran, J., Yang, Y., Li, D., Liu, M., Zhou, J. (2015) Deacetylation of alpha-tubulin and cortactin is required for HDAC6 to trigger ciliary disassembly. *Sci Rep* **5**, 12917.

92.   Zhang, L., Liu, S., Liu, N., Zhang, Y., Liu, M., Li, D., Seto, E., Yao, T.P., Shui, W., Zhou, J. (2015) Proteomic identification and functional characterization of MYH9, Hsc70, and DNAJA1 as novel substrates of HDAC6 deacetylase activity. *Protein Cell* **6**, 42–54.

93.   Betapudi, V. (2010) Myosin II motor proteins with different functions determine the fate of lamellipodia extension during cell spreading. *PLoS One* **5**, e8560.

94.   Sutoh, K. (1982) Identification of myosin-binding sites on the actin sequence. *Biochemistry (Mosc.)* **21**, 3654–61.

95.   Boyault, C., Gilquin, B., Zhang, Y., Rybin, V., Garman, E., Meyer-Klaucke, W., Matthias, P., Muller, C.W., Khochbin, S. (2006) HDAC6-p97/VCP controlled polyubiquitin chain turnover. *EMBO J* **25**, 3357–66.

96.   Boyault, C., Zhang, Y., Fritah, S., Caron, C., Gilquin, B., Kwon, S.H., Garrido, C., Yao, T.P., Vourc'h, C., Matthias, P., Khochbin, S. (2007) HDAC6 controls major cell response pathways to cytotoxic accumulation of protein aggregates. *Genes Dev* **21**, 2172–81.

97.   Pandey, U.B., Nie, Z., Batlevi, Y., McCray, B.A., Ritson, G.P., Nedelsky, N.B., Schwartz, S.L., DiProspero, N.A., Knight, M.A., Schuldiner, O., Padmanabhan, R., Hild, M., Berry, D.L., Garza, D., Hubbert, C.C., Yao, T.P., Baehrecke, E.H., Taylor, J.P. (2007) HDAC6 rescues neurodegeneration and provides an essential link between autophagy and the UPS. *Nature* **447**, 859–63.

98.   Blandino, G., Levine, A.J., Oren, M. (1999) Mutant p53 gain of function: differential effects of different p53 mutants on resistance of cultured cells to chemotherapy. *Oncogene* **18**, 477–85.

99.   Goh, A.M., Coffill, C.R., Lane, D.P. (2011) The role of mutant p53 in human cancer. *J Pathol* **223**, 116–26.

100.   Ryu, H.W., Shin, D.H., Lee, D.H., Choi, J., Han, G., Lee, K.Y., Kwon, S.H. (2017) HDAC6 deacetylates p53 at lysines 381/382 and differentially coordinates p53-induced apoptosis. *Cancer Lett* **391**, 162–71.

101.   Park, J.H., Kim, S.H., Choi, M.C., Lee, J., Oh, D.Y., Im, S.A., Bang, Y.J., Kim, T.Y. (2008) Class II histone deacetylases play pivotal roles in heat shock protein 90-mediated proteasomal degradation of vascular endothelial growth factor receptors. *Biochem Biophys Res Commun* **368**, 318–22.

102.   Subramanian, C., Jarzembowski, J.A., Opipari, A.W., Castle, V.P., Kwok, R.P. (2011) HDAC6 deacetylates Ku70 and regulates Ku70-Bax binding in neuroblastoma. *Neoplasia* **13**, 726–34.

103.   Zhang, Y., Kwon, S., Yamaguchi, T., Cubizolles, F., Rousseaux, S., Kneissel, M., Cao, C., Li, N., Cheng, H.L., Chua, K., Lombard, D., Mizeracki, A., Matthias, G., Alt, F.W., Khochbin, S., Matthias, P. (2008) Mice lacking histone deacetylase 6 have hyperacetylated tubulin but are viable and develop normally. *Mol Cell Biol* **28**, 1688–1701.

104.   Valenzuela-Fernandez, A., Alvarez, S., Gordon-Alonso, M., Barrero, M., Ursa, A., Cabrero, J.R., Fernandez, G., Naranjo-Suarez, S., Yanez-Mo, M., Serrador, J.M., Munoz-Fernandez, M.A., Sanchez-Madrid, F. (2005) Histone deacetylase 6 regulates human immunodeficiency virus type 1 infection. *Mol Biol Cell* **16**, 5445–54.

105.   Huo, L., Li, D., Sun, X., Shi, X., Karna, P., Yang, W., Liu, M., Qiao, W., Aneja, R., Zhou, J. (2011) Regulation of Tat acetylation and transactivation activity by the microtubule-associated deacetylase HDAC6. *J Biol Chem* **286**, 9280–86.

106.   Kiernan, R.E., Vanhulle, C., Schiltz, L., Adam, E., Xiao, H., Maudoux, F., Calomme, C., Burny, A., Nakatani, Y., Jeang, K.T., Benkirane, M., Van Lint, C. (1999) HIV-1 tat transcriptional activity is regulated by acetylation. *EMBO J* **18**, 6106–18.

107.   Tapia, M., Wandosell, F., Garrido, J.J. (2010) Impaired function of HDAC6 slows down axonal growth and interferes with axon initial segment development. *PLoS One* **5**, e12908.

108.   Zhang, F., Su, B., Wang, C., Siedlak, S.L., Mondragon-Rodriguez, S., Lee, H.G., Wang, X., Perry, G., Zhu, X. (2015) Posttranslational modifications of alpha-tubulin in alzheimer disease. *Transl Neurodegener* **4**, 9.

109.   Dompierre, J.P., Godin, J.D., Charrin, B.C., Cordelieres, F.P., King, S.J., Humbert, S., Saudou, F. (2007) Histone deacetylase 6 inhibition compensates for the transport deficit in Huntington's disease by increasing tubulin acetylation. *J Neurosci* **27**, 3571–83.

110.   Zhu, T., Zhao, D., Song, Z., Yuan, Z., Li, C., Wang, Y., Zhou, X., Yin, X., Hassan, M.F., Yang, L. (2016) HDAC6 alleviates prion peptide-mediated neuronal death via modulating PI3K-Akt-mTOR pathway. *Neurobiol Aging* **37**, 91–102.

111.   d'Ydewalle, C., Krishnan, J., Chiheb, D.M., Van Damme, P., Irobi, J., Kozikowski, A.P., Vanden Berghe, P., Timmerman, V., Robberecht, W., Van Den Bosch, L. (2011) HDAC6 inhibitors reverse axonal loss in a mouse model of mutant HSPB1-induced Charcot-Marie-Tooth disease. *Nat Med* **17**, 968–74.

112.   Dutcher, S.K. (2001) The tubulin fraternity: alpha to eta. *Curr Opin Cell Biol* **13**, 49–54.

113.   Little, M., Seehaus, T. (1988) Comparative analysis of tubulin sequences. *Comp Biochem Physiol B* **90**, 655–70.

114.   Krauhs, E., Little, M., Kempf, T., Hofer-Warbinek, R., Ade, W., Ponstingl, H. (1981) Complete amino acid sequence of beta-tubulin from porcine brain. *Proc Natl Acad Sci U A* **78**, 4156–60.

115.   Jacobs, M., Smith, H., Taylor, E.W. (1974) Tublin: nucleotide binding and enzymic activity. *J Mol Biol* **89**, 455–68.

116.   Maccioni, R., Seeds, N.W. (1977) Stoichiometry of GTP hydrolysis and tubulin polymerization. *Proc Natl Acad Sci U A* **74**, 462–66.

117.   Hendrickson, T.W., Yao, J., Bhadury, S., Corbett, A.H., Joshi, H.C. (2001) Conditional mutations in gamma-tubulin reveal its involvement in chromosome segregation and cytokinesis. *Mol Biol Cell* **12**, 2469–81.

118.   Wiese, C., Zheng, Y. (2000) A new function for the gamma-tubulin ring complex as a microtubule minus-end cap. *Nat Cell Biol* **2**, 358–64.

119.   Zheng, Y., Jung, M.K., Oakley, B.R. (1991) Gamma-tubulin is present in Drosophila melanogaster and Homo sapiens and is associated with the centrosome. *Cell* **65**, 817–23.

120.   Chang, P., Stearns, T. (2000) Delta-tubulin and epsilon-tubulin: two new human centrosomal tubulins reveal new aspects of centrosome structure and function. *Nat Cell Biol* **2**, 30–35.

121.   Vaughan, S., Attwood, T., Navarro, M., Scott, V., McKean, P., Gull, K. (2000) New tubulins in protozoal parasites. *Curr Biol* **10**, R258-9.

122.   McKean, P.G., Vaughan, S., Gull, K. (2001) The extended tubulin superfamily. *J Cell Sci* **114**, 2723–33.

123.   Ruiz, F., Krzywicka, A., Klotz, C., Keller, A., Cohen, J., Koll, F., Balavoine, G., Beisson, J. (2000) The SM19 gene, required for duplication of basal bodies in Paramecium, encodes a novel tubulin, eta-tubulin. *Curr Biol* **10**, 1451–54.

124.   Mandelkow, E.M., Mandelkow, E., Milligan, R.A. (1991) Microtubule dynamics and microtubule caps: a time-resolved cryo-electron microscopy study. *J Cell Biol* **114**, 977–91.

125.   Boukari, H., Sackett, D.L., Schuck, P., Nossal, R.J. (2007) Single-walled tubulin ring polymers. *Biopolymers* **86**, 424–36.

126.   Moores, C.A., Milligan, R.A. (2008) Visualisation of a kinesin-13 motor on microtubule end mimics. *J Mol Biol* **377**, 647–54.

127.   Mulder, A.M., Glavis-Bloom, A., Moores, C.A., Wagenbach, M., Carragher, B., Wordeman, L., Milligan, R.A. (2009) A new model for binding of kinesin 13 to curved microtubule protofilaments. *J Cell Biol* **185**, 51–57.

128.   Nogales, E., Wang, H.W., Niederstrasser, H. (2003) Tubulin rings: which way do they curve? *Curr Opin Struct Biol* **13**, 256–61.

129.   Watts, N.R., Sackett, D.L., Ward, R.D., Miller, M.W., Wingfield, P.T., Stahl, S.S., Steven, A.C. (2000) HIV-1 rev depolymerizes microtubules to form stable bilayered rings. *J Cell Biol* **150**, 349–60.

130.   Larsson, H., Wallin, M., Edstrom, A. (1976) Induction of a sheet polymer of tubulin by Zn2+. *Exp Cell Res* **100**, 104–10.

131.   Wolf, S.G., Mosser, G., Downing, K.H. (1993) Tubulin conformation in zinc-induced sheets and macrotubes. *J Struct Biol* **111**, 190–99.

132.   Kull, F.J., Sloboda, R.D. (2014) A slow dance for microtubule acetylation. *Cell* **157**, 1255–56.

133.   Bergen, L.G., Borisy, G.G. (1980) Head-to-tail polymerization of microtubules in vitro. Electron microscope analysis of seeded assembly. *J Cell Biol* **84**, 141–50.

134.   Sanchez, A.D., Feldman, J.L. (2016) Microtubule-organizing centers: from the centrosome to non-centrosomal sites. *Curr Opin Cell Biol* .

135.   Vertii, A., Hehnly, H., Doxsey, S. (2016) The Centrosome, a Multitalented Renaissance Organelle. *Cold Spring Harb Perspect Biol* **8**.

9

136. Hartman, J.J., Mahr, J., McNally, K., Okawa, K., Iwamatsu, A., Thomas, S., Cheesman, S., Heuser, J., Vale, R.D., McNally, F.J. (1998) Katanin, a microtubule-severing protein, is a novel AAA ATPase that targets to the centrosome using a WD40-containing subunit. *Cell* **93**, 277–87.

137. Kline-Smith, S.L., Walczak, C.E. (2002) The microtubule-destabilizing kinesin XKCM1 regulates microtubule dynamic instability in cells. *Mol Biol Cell* **13**, 2718–31.

138. Belmont, L.D., Mitchison, T.J. (1996) Identification of a protein that interacts with tubulin dimers and increases the catastrophe rate of microtubules. *Cell* **84**, 623–31.

139. Goedert, M., Crowther, R.A., Garner, C.C. (1991) Molecular characterization of microtubule-associated proteins tau and MAP2. *Trends Neurosci* **14**, 193–99.

140. Kuznetsov, S.A., Rodionov, V.I., Gelfand, V.I., Rosenblat, V.A. (1981) Microtubule-associated protein MAP1 promotes microtubule assembly in vitro. *FEBS Lett* **135**, 241–44.

141. Tokuraku, K., Katsuki, M., Nakagawa, H., Kotani, S. (1999) A new model for microtubule-associated protein (MAP)-induced microtubule assembly. The Pro-rich region of MAP4 promotes nucleation of microtubule assembly in vitro. *Eur J Biochem* **259**, 158–66.

142. Arnal, I., Wade, R.H. (1995) How does taxol stabilize microtubules? *Curr Biol* **5**, 900–908.

143. Hyman, A.A., Chretien, D., Arnal, I., Wade, R.H. (1995) Structural changes accompanying GTP hydrolysis in microtubules: information from a slowly hydrolyzable analogue guanylyl-(alpha,beta)-methylene-diphosphonate. *J Cell Biol* **128**, 117–25.

144. Gigant, B., Cormier, A., Dorleans, A., Ravelli, R.B., Knossow, M. (2009) Microtubule-destabilizing agents: structural and mechanistic insights from the interaction of colchicine and vinblastine with tubulin. *Top Curr Chem* **286**, 259–78.

145. Ponstingl, H., Krauhs, E., Little, M., Kempf, T. (1981) Complete amino acid sequence of alpha-tubulin from porcine brain. *Proc Natl Acad Sci U A* **78**, 2757–61.

146. Aillaud, C., Bosc, C., Peris, L., Bosson, A., Heemeryck, P., Van Dijk, J., Le Friec, J., Boulan, B., Vossier, F., Sanman, L.E., Syed, S., Amara, N., Coute, Y., Lafanechere, L., Denarier, E., Delphin, C., Pelletier, L., Humbert, S., Bogyo, M., Andrieux, A., Rogowski, K., Moutin, M.J. (2017) Vasohibins/SVBP are tubulin carboxypeptidases (TCPs) that regulate neuron differentiation. *Science* **358**, 1448–53.

147. Gundersen, G.G., Bulinski, J.C. (1986) Distribution of tyrosinated and nontyrosinated alpha-tubulin during mitosis. *J Cell Biol* **102**, 1118–26.

148. Peris, L., Wagenbach, M., Lafanechere, L., Brocard, J., Moore, A.T., Kozielski, F., Job, D., Wordeman, L., Andrieux, A. (2009) Motor-dependent microtubule disassembly driven by tubulin tyrosination. *J Cell Biol* **185**, 1159–66.

149. Liao, G., Gundersen, G.G. (1998) Kinesin is a candidate for cross-bridging microtubules and intermediate filaments. Selective binding of kinesin to detyrosinated tubulin and vimentin. *J Biol Chem* **273**, 9797–9803.

150. Reed, N.A., Cai, D., Blasius, T.L., Jih, G.T., Meyhofer, E., Gaertig, J., Verhey, K.J. (2006) Microtubule acetylation promotes kinesin-1 binding and transport. *Curr Biol* **16**, 2166–72.

151. Edde, B., Rossier, J., Le Caer, J.P., Desbruyeres, E., Gros, F., Denoulet, P. (1990) Posttranslational glutamylation of alpha-tubulin. *Science* **247**, 83–85.

152. Rudiger, M., Plessman, U., Kloppel, K.D., Wehland, J., Weber, K. (1992) Class II tubulin, the major brain beta tubulin isotype is polyglutamylated on glutamic acid residue 435. *FEBS Lett* **308**, 101–5.

153. Paturle-Lafanechere, L., Edde, B., Denoulet, P., Van Dorsselaer, A., Mazarguil, H., Le Caer, J.P., Wehland, J., Job, D. (1991) Characterization of a major brain tubulin variant which cannot be tyrosinated. *Biochemistry (Mosc.)* **30**, 10523–28.

154. Paturle-Lafanechere, L., Manier, M., Trigault, N., Pirollet, F., Mazarguil, H., Job, D. (1994) Accumulation of delta 2-tubulin, a major tubulin variant that cannot be tyrosinated, in neuronal tissues and in stable microtubule assemblies. *J Cell Sci* **107 (Pt 6)**, 1529–43.

155. Janke, C., Rogowski, K., Wloga, D., Regnard, C., Kajava, A.V., Strub, J.M., Temurak, N., van Dijk, J., Boucher, D., van Dorsselaer, A., Suryavanshi, S., Gaertig, J., Edde, B. (2005) Tubulin polyglutamylase enzymes are members of the TTL domain protein family. *Science* **308**, 1758–62.

156. Redeker, V., Levilliers, N., Schmitter, J.M., Le Caer, J.P., Rossier, J., Adoutte, A., Bre, M.H. (1994) Polyglycylation of tubulin: a posttranslational modification in axonemal microtubules. *Science* **266**, 1688–91.

157. Iftode, F., Clerot, J.C., Levilliers, N., Bre, M.H. (2000) Tubulin polyglycylation: a morphogenetic marker in ciliates. *Biol Cell* **92**, 615–28.

158. Song, Y., Kirkpatrick, L.L., Schilling, A.B., Helseth, D.L., Chabot, N., Keillor, J.W., Johnson, G.V., Brady, S.T. (2013) Transglutaminase and polyamination of tubulin: posttranslational modification for stabilizing axonal microtubules. *Neuron* **78**, 109–23.

159. Eipper, B.A. (1974) Properties of rat brain tubulin. *J Biol Chem* **249**, 1407–16.

160. Caron, J.M. (1997) Posttranslational modification of tubulin by palmitoylation: I. In vivo and cell-free studies. *Mol Biol Cell* **8**, 621–36.

161. Ozols, J., Caron, J.M. (1997) Posttranslational modification of tubulin by palmitoylation: II. Identification of sites of palmitoylation. *Mol Biol Cell* **8**, 637–45.

162. Ren, Y., Zhao, J., Feng, J. (2003) Parkin binds to alpha/beta tubulin and increases their ubiquitination and degradation. *J Neurosci* **23**, 3316–24.

163. Xiao, H., El Bissati, K., Verdier-Pinard, P., Burd, B., Zhang, H., Kim, K., Fiser, A., Angeletti, R.H., Weiss, L.M. (2010) Post-translational modifications to Toxoplasma gondii alpha- and beta-tubulins include novel C-terminal methylation. *J Proteome Res* **9**, 359–72.

164. Rosas-Acosta, G., Russell, W.K., Deyrieux, A., Russell, D.H., Wilson, V.G. (2005) A universal strategy for proteomic studies of SUMO and other ubiquitin-like modifiers. *Mol Cell Proteomics* **4**, 56–72.

165. Jordan, M.A., Ojima, I., Rosas, F., Distefano, M., Wilson, L., Scambia, G., Ferlini, C. (2002) Effects of novel taxanes SB-T-1213 and IDN5109 on tubulin polymerization and mitosis. *Chem Biol* **9**, 93–101.

166. Wong, C.C., Xu, T., Rai, R., Bailey, A.O., Yates, J.R., Wolf, Y.I., Zebroski, H., Kashina, A. (2007) Global analysis of posttranslational protein arginylation. *PLoS Biol* **5**, e258.

167. Walgren, J.L., Vincent, T.S., Schey, K.L., Buse, M.G. (2003) High glucose and insulin promote O-GlcNAc modification of proteins, including alpha-tubulin. *Am J Physiol Endocrinol Metab* **284**, E424-34.

168. Skultetyova, L., Ustinova, K., Kutil, Z., Novakova, Z., Pavlicek, J., Mikesova, J., Trapl, D., Baranova, P., Havlinova, B., Hubalek, M., Lansky, Z., Barinka, C. (2017)

Human histone deacetylase 6 shows strong preference for tubulin dimers over assembled microtubules. *Sci Rep* **7**, 11547.

169. L'Hernault, S.W., Rosenbaum, J.L. (1983) Chlamydomonas alpha-tubulin is posttranslationally modified in the flagella during flagellar assembly. *J Cell Biol* **97**, 258–63.

170. L'Hernault, S.W., Rosenbaum, J.L. (1985) Chlamydomonas alpha-tubulin is posttranslationally modified by acetylation on the epsilon-amino group of a lysine. *Biochemistry (Mosc.)* **24**, 473–78.

171. LeDizet, M., Piperno, G. (1987) Identification of an acetylation site of Chlamydomonas alpha-tubulin. *Proc Natl Acad Sci U A* **84**, 5720–24.

172. Piperno, G., Fuller, M.T. (1985) Monoclonal antibodies specific for an acetylated form of alpha-tubulin recognize the antigen in cilia and flagella from a variety of organisms. *J Cell Biol* **101**, 2085–94.

173. Piperno, G., LeDizet, M., Chang, X.J. (1987) Microtubules containing acetylated alpha-tubulin in mammalian cells in culture. *J Cell Biol* **104**, 289–302.

174. Kalebic, N., Sorrentino, S., Perlas, E., Bolasco, G., Martinez, C., Heppenstall, P.A. (2013) alphaTAT1 is the major alpha-tubulin acetyltransferase in mice. *Nat Commun* **4**, 1962.

175. Howes, S.C., Alushin, G.M., Shida, T., Nachury, M.V., Nogales, E. (2014) Effects of tubulin acetylation and tubulin acetyltransferase binding on microtubule structure. *Mol Biol Cell* **25**, 257–66.

176. Conacci-Sorrell, M., Ngouenet, C., Eisenman, R.N. (2010) Myc-nick: a cytoplasmic cleavage product of Myc that promotes alpha-tubulin acetylation and cell differentiation. *Cell* **142**, 480–93.

177. Ohkawa, N., Sugisaki, S., Tokunaga, E., Fujitani, K., Hayasaka, T., Setou, M., Inokuchi, K. (2008) N-acetyltransferase ARD1-NAT1 regulates neuronal dendritic development. *Genes Cells* **13**, 1171–83.

178. Creppe, C., Malinouskaya, L., Volvert, M.L., Gillard, M., Close, P., Malaise, O., Laguesse, S., Cornez, I., Rahmouni, S., Ormenese, S., Belachew, S., Malgrange, B., Chapelle, J.P., Siebenlist, U., Moonen, G., Chariot, A., Nguyen, L. (2009) Elongator controls the migration and differentiation of cortical neurons through acetylation of alpha-tubulin. *Cell* **136**, 551–64.

179. Akella, J.S., Wloga, D., Kim, J., Starostina, N.G., Lyons-Abbott, S., Morrissette, N.S., Dougan, S.T., Kipreos, E.T., Gaertig, J. (2010) MEC-17 is an alpha-tubulin acetyltransferase. *Nature* **467**, 218–22.

180. Shida, T., Cueva, J.G., Xu, Z., Goodman, M.B., Nachury, M.V. (2010) The major alpha-tubulin K40 acetyltransferase alphaTAT1 promotes rapid ciliogenesis and efficient mechanosensation. *Proc Natl Acad Sci U A* **107**, 21517–22.

181. Matsuyama, A., Shimazu, T., Sumida, Y., Saito, A., Yoshimatsu, Y., Seigneurin-Berny, D., Osada, H., Komatsu, Y., Nishino, N., Khochbin, S., Horinouchi, S., Yoshida, M. (2002) In vivo destabilization of dynamic microtubules by HDAC6-mediated deacetylation. *EMBO J* **21**, 6820–31.

182. Hubbert, C., Guardiola, A., Shao, R., Kawaguchi, Y., Ito, A., Nixon, A., Yoshida, M., Wang, X.F., Yao, T.P. (2002) HDAC6 is a microtubule-associated deacetylase. *Nature* **417**, 455–58.

183.   North, B.J., Marshall, B.L., Borra, M.T., Denu, J.M., Verdin, E. (2003) The human Sir2 ortholog, SIRT2, is an NAD+-dependent tubulin deacetylase. *Mol Cell* **11**, 437–44.
184.   Cho, Y., Cavalli, V. (2012) HDAC5 is a novel injury-regulated tubulin deacetylase controlling axon regeneration. *EMBO J* **31**, 3063–78.
185.   Castro-Castro, A., Janke, C., Montagnac, G., Paul-Gilloteaux, P., Chavrier, P. (2012) ATAT1/MEC-17 acetyltransferase and HDAC6 deacetylase control a balance of acetylation of alpha-tubulin and cortactin and regulate MT1-MMP trafficking and breast tumor cell invasion. *Eur J Cell Biol* **91**, 950–60.
186.   Szyk, A., Deaconescu, A.M., Spector, J., Goodman, B., Valenstein, M.L., Ziolkowska, N.E., Kormendi, V., Grigorieff, N., Roll-Mecak, A. (2014) Molecular basis for age-dependent microtubule acetylation by tubulin acetyltransferase. *Cell* **157**, 1405–15.
187.   Davenport, A.M., Collins, L.N., Chiu, H., Minor, P.J., Sternberg, P.W., Hoelz, A. (2014) Structural and functional characterization of the alpha-tubulin acetyltransferase MEC-17. *J Mol Biol* **426**, 2605–16.
188.   Dent, E.W., Callaway, J.L., Szebenyi, G., Baas, P.W., Kalil, K. (1999) Reorganization and movement of microtubules in axonal growth cones and developing interstitial branches. *J Neurosci* **19**, 8894–8908.
189.   Qiang, L., Yu, W., Liu, M., Solowska, J.M., Baas, P.W. (2010) Basic fibroblast growth factor elicits formation of interstitial axonal branches via enhanced severing of microtubules. *Mol Biol Cell* **21**, 334–44.
190.   Sudo, H., Baas, P.W. (2010) Acetylation of microtubules influences their sensitivity to severing by katanin in neurons and fibroblasts. *J Neurosci* **30**, 7215–26.
191.   Cai, D., McEwen, D.P., Martens, J.R., Meyhofer, E., Verhey, K.J. (2009) Single molecule imaging reveals differences in microtubule track selection between Kinesin motors. *PLoS Biol* **7**, e1000216.
192.   Dunn, S., Morrison, E.E., Liverpool, T.B., Molina-Paris, C., Cross, R.A., Alonso, M.C., Peckham, M. (2008) Differential trafficking of Kif5c on tyrosinated and detyrosinated microtubules in live cells. *J Cell Sci* **121**, 1085–95.
193.   Tran, A.D., Marmo, T.P., Salam, A.A., Che, S., Finkelstein, E., Kabarriti, R., Xenias, H.S., Mazitschek, R., Hubbert, C., Kawaguchi, Y., Sheetz, M.P., Yao, T.P., Bulinski, J.C. (2007) HDAC6 deacetylation of tubulin modulates dynamics of cellular adhesions. *J Cell Sci* **120**, 1469–79.
194.   Portran, D., Schaedel, L., Xu, Z., Théry, M., Nachury, M.V. (2017) Tubulin acetylation protects long-lived microtubules against mechanical aging. *Nat. Cell Biol.* **19**, 391–98.
195.   Xu, Z., Schaedel, L., Portran, D., Aguilar, A., Gaillard, J., Marinkovich, M.P., Thery, M., Nachury, M.V. (2017) Microtubules acquire resistance from mechanical breakage through intralumenal acetylation. *Science* **356**, 328–32.
196.   Cueva, J.G., Hsin, J., Huang, K.C., Goodman, M.B. (2012) Posttranslational acetylation of alpha-tubulin constrains protofilament number in native microtubules. *Curr Biol* **22**, 1066–74.
197.   Choudhary, C., Kumar, C., Gnad, F., Nielsen, M.L., Rehman, M., Walther, T.C., Olsen, J.V., Mann, M. (2009) Lysine acetylation targets protein complexes and co-regulates major cellular functions. *Science* **325**, 834–40.
198.   Chu, C.W., Hou, F., Zhang, J., Phu, L., Loktev, A.V., Kirkpatrick, D.S., Jackson, P.K., Zhao, Y., Zou, H. (2011) A novel acetylation of beta-tubulin by San modulates

microtubule polymerization via down-regulating tubulin incorporation. *Mol Biol Cell* **22**, 448–56.

199. Liu, N., Xiong, Y., Li, S., Ren, Y., He, Q., Gao, S., Zhou, J., Shui, W. (2015) New HDAC6-mediated deacetylation sites of tubulin in the mouse brain identified by quantitative mass spectrometry. *Sci Rep* **5**, 16869.

200. Wagner, F.F., Olson, D.E., Gale, J.P., Kaya, T., Weiwer, M., Aidoud, N., Thomas, M., Davoine, E.L., Lemercier, B.C., Zhang, Y.L., Holson, E.B. (2013) Potent and selective inhibition of histone deacetylase 6 (HDAC6) does not require a surface-binding motif. *J Med Chem* **56**, 1772–76.

201. Furumai, R., Komatsu, Y., Nishino, N., Khochbin, S., Yoshida, M., Horinouchi, S. (2001) Potent histone deacetylase inhibitors built from trichostatin A and cyclic tetrapeptide antibiotics including trapoxin. *Proc Natl Acad Sci U A* **98**, 87–92.

202. Guardiola, A.R., Yao, T.P. (2002) Molecular cloning and characterization of a novel histone deacetylase HDAC10. *J Biol Chem* **277**, 3350–56.

203. Haggarty, S.J., Koeller, K.M., Wong, J.C., Grozinger, C.M., Schreiber, S.L. (2003) Domain-selective small-molecule inhibitor of histone deacetylase 6 (HDAC6)-mediated tubulin deacetylation. *Proc Natl Acad Sci U A* **100**, 4389–94.

204. Schemies, J., Sippl, W., Jung, M. (2009) Histone deacetylase inhibitors that target tubulin. *Cancer Lett* **280**, 222–32.

205. Butler, K.V., Kalin, J., Brochier, C., Vistoli, G., Langley, B., Kozikowski, A.P. (2010) Rational design and simple chemistry yield a superior, neuroprotective HDAC6 inhibitor, tubastatin A. *J Am Chem Soc* **132**, 10842–46.

206. Santo, L., Hideshima, T., Kung, A.L., Tseng, J.C., Tamang, D., Yang, M., Jarpe, M., van Duzer, J.H., Mazitschek, R., Ogier, W.C., Cirstea, D., Rodig, S., Eda, H., Scullen, T., Canavese, M., Bradner, J., Anderson, K.C., Jones, S.S., Raje, N. (2012) Preclinical activity, pharmacodynamic, and pharmacokinetic properties of a selective HDAC6 inhibitor, ACY-1215, in combination with bortezomib in multiple myeloma. *Blood* **119**, 2579–89.

207. Wang, H., Byun, Y., Barinka, C., Pullambhatla, M., Bhang, H.E., Fox, J.J., Lubkowski, J., Mease, R.C., Pomper, M.G. (2010) Bioisosterism of urea-based GCPII inhibitors: Synthesis and structure-activity relationship studies. *Bioorg Med Chem Lett* **20**, 392–97.

208. Pardridge, W.M. (2005) The blood-brain barrier: bottleneck in brain drug development. *NeuroRx* **2**, 3–14.

209. Kozikowski, A.P., Zhang, J., Nan, F., Petukhov, P.A., Grajkowska, E., Wroblewski, J.T., Yamamoto, T., Bzdega, T., Wroblewska, B., Neale, J.H. (2004) Synthesis of urea-based inhibitors as active site probes of glutamate carboxypeptidase II: efficacy as analgesic agents. *J Med Chem* **47**, 1729–38.

210. Plechanovova, A., Byun, Y., Alquicer, G., Skultetyova, L., Mlcochova, P., Nemcova, A., Kim, H.J., Navratil, M., Mease, R., Lubkowski, J., Pomper, M., Konvalinka, J., Rulisek, L., Barinka, C. (2011) Novel substrate-based inhibitors of human glutamate carboxypeptidase II with enhanced lipophilicity. *J Med Chem* **54**, 7535–46.

211. Mlcochova, P., Plechanovova, A., Barinka, C., Mahadevan, D., Saldanha, J.W., Rulisek, L., Konvalinka, J. (2007) Mapping of the active site of glutamate carboxypeptidase II by site-directed mutagenesis. *FEBS J* **274**, 4731–41.

212. Pavlicek, J., Ptacek, J., Cerny, J., Byun, Y., Skultetyova, L., Pomper, M.G., Lubkowski, J., Barinka, C. (2014) Structural characterization of P1'-diversified urea-based inhibitors of glutamate carboxypeptidase II. *Bioorg Med Chem Lett* **24**, 2340–45.

213. Yamamoto, T., Kozikowski, A., Zhou, J., Neale, J.H. (2008) Intracerebroventricular administration of N-acetylaspartylglutamate (NAAG) peptidase inhibitors is analgesic in inflammatory pain. *Mol Pain* **4**, 31.

214. Feng, J.F., Van, K.C., Gurkoff, G.G., Kopriva, C., Olszewski, R.T., Song, M., Sun, S., Xu, M., Neale, J.H., Yuen, P.W., Lowe, D.A., Zhou, J., Lyeth, B.G. (2011) Post-injury administration of NAAG peptidase inhibitor prodrug, PGI-02776, in experimental TBI. *Brain Res* **1395**, 62–73.

215. Rais, R., Vavra, J., Tichy, T., Dash, R.P., Gadiano, A.J., Tenora, L., Monincova, L., Barinka, C., Alt, J., Zimmermann, S.C., Slusher, C.E., Wu, Y., Wozniak, K., Majer, P., Tsukamoto, T., Slusher, B.S. (2017) Discovery of a para-Acetoxy-benzyl Ester Prodrug of a Hydroxamate-Based Glutamate Carboxypeptidase II Inhibitor as Oral Therapy for Neuropathic Pain. *J Med Chem* **60**, 7799–7809.

216. Ferraris, D.V., Majer, P., Ni, C., Slusher, C.E., Rais, R., Wu, Y., Wozniak, K.M., Alt, J., Rojas, C., Slusher, B.S., Tsukamoto, T. (2014) delta-Thiolactones as prodrugs of thiol-based glutamate carboxypeptidase II (GCPII) inhibitors. *J Med Chem* **57**, 243–47.

217. Lapi, S.E., Wahnishe, H., Pham, D., Wu, L.Y., Nedrow-Byers, J.R., Liu, T., Vejdani, K., VanBrocklin, H.F., Berkman, C.E., Jones, E.F. (2009) Assessment of an 18F-labeled phosphoramidate peptidomimetic as a new prostate-specific membrane antigen-targeted imaging agent for prostate cancer. *J Nucl Med* **50**, 2042–48.

218. Mallari, J.P., Choy, C.J., Hu, Y., Martinez, A.R., Hosaka, M., Toriyabe, Y., Maung, J., Blecha, J.E., Pavkovic, S.F., Berkman, C.E. (2004) Stereoselective inhibition of glutamate carboxypeptidase by organophosphorus derivatives of glutamic acid. *Bioorg Med Chem* **12**, 6011–20.

219. Dannoon, S., Ganguly, T., Cahaya, H., Geruntho, J.J., Galliher, M.S., Beyer, S.K., Choy, C.J., Hopkins, M.R., Regan, M., Blecha, J.E., Skultetyova, L., Drake, C.R., Jivan, S., Barinka, C., Jones, E.F., Berkman, C.E., VanBrocklin, H.F. (2016) Structure-Activity Relationship of (18)F-Labeled Phosphoramidate Peptidomimetic Prostate-Specific Membrane Antigen (PSMA)-Targeted Inhibitor Analogues for PET Imaging of Prostate Cancer. *J Med Chem* **59**, 5684–94.

220. Kelly, J.M., Taylor, M.C., Horn, D., Loza, E., Kalvinsh, I., Bjorkling, F. (2012) Inhibitors of human histone deacetylase with potent activity against the African trypanosome Trypanosoma brucei. *Bioorg Med Chem Lett* **22**, 1886–90.

221. Zhang, L., Wang, X., Li, X., Zhang, L., Xu, W. (2014) Discovery of a series of hydroximic acid derivatives as potent histone deacetylase inhibitors. *J Enzyme Inhib Med Chem* **29**, 582–89.

222. Tykvart, J., Schimer, J., Barinkova, J., Pachl, P., Postova-Slavetinska, L., Majer, P., Konvalinka, J., Sacha, P. (2014) Rational design of urea-based glutamate carboxypeptidase II (GCPII) inhibitors as versatile tools for specific drug targeting and delivery. *Bioorg Med Chem* **22**, 4099–4108.

223. Ganguly, T., Dannoon, S., Hopkins, M.R., Murphy, S., Cahaya, H., Blecha, J.E., Jivan, S., Drake, C.R., Barinka, C., Jones, E.F., VanBrocklin, H.F., Berkman, C.E. (2015) A high-affinity [(18)F]-labeled phosphoramidate peptidomimetic PSMA-targeted inhibitor for PET imaging of prostate cancer. *Nucl Med Biol* **42**, 780–87.

224.   Tolmachev, V., Feldwisch, J., Lindborg, M., Baastrup, B., Sandstrom, M., Orlova, A. (2011) Influence of an aliphatic linker between DOTA and synthetic Z(HER2:342) Affibody molecule on targeting properties of the (111)In-labeled conjugate. *Nucl Med Biol* **38**, 697–706.

225.   Nedrow, J.R., Latoche, J.D., Day, K.E., Modi, J., Ganguly, T., Zeng, D., Kurland, B.F., Berkman, C.E., Anderson, C.J. (2016) Targeting PSMA with a Cu-64 Labeled Phosphoramidate Inhibitor for PET/CT Imaging of Variant PSMA-Expressing Xenografts in Mouse Models of Prostate Cancer. *Mol Imaging Biol* **18**, 402–10.

226.   Chopra, A. (2004) in *Molecular Imaging and Contrast Agent Database (MICAD)* (Bethesda (MD)).

227.   Rowe, S.P., Gage, K.L., Faraj, S.F., Macura, K.J., Cornish, T.C., Gonzalez-Roibon, N., Guner, G., Munari, E., Partin, A.W., Pavlovich, C.P., Han, M., Carter, H.B., Bivalacqua, T.J., Blackford, A., Holt, D., Dannals, R.F., Netto, G.J., Lodge, M.A., Mease, R.C., Pomper, M.G., Cho, S.Y. (2015) (1)(8)F-DCFBC PET/CT for PSMA-Based Detection and Characterization of Primary Prostate Cancer. *J Nucl Med* **56**, 1003–10.

228.   Cho, S.Y., Gage, K.L., Mease, R.C., Senthamizhchelvan, S., Holt, D.P., Jeffrey-Kwanisai, A., Endres, C.J., Dannals, R.F., Sgouros, G., Lodge, M., Eisenberger, M.A., Rodriguez, R., Carducci, M.A., Rojas, C., Slusher, B.S., Kozikowski, A.P., Pomper, M.G. (2012) Biodistribution, tumor detection, and radiation dosimetry of 18F-DCFBC, a low-molecular-weight inhibitor of prostate-specific membrane antigen, in patients with metastatic prostate cancer. *J Nucl Med* **53**, 1883–91.

229.   Lupold, S.E., Hicke, B.J., Lin, Y., Coffey, D.S. (2002) Identification and characterization of nuclease-stabilized RNA molecules that bind human prostate cancer cells via the prostate-specific membrane antigen. *Cancer Res* **62**, 4029–33.

230.   Rockey, W.M., Huang, L., Kloepping, K.C., Baumhover, N.J., Giangrande, P.H., Schultz, M.K. (2011) Synthesis and radiolabeling of chelator-RNA aptamer bioconjugates with copper-64 for targeted molecular imaging. *Bioorg Med Chem* **19**, 4080–90.

231.   Kahn, D., Austin, J.C., Maguire, R.T., Miller, S.J., Gerstbrein, J., Williams, R.D. (1999) A phase II study of [90Y] yttrium-capromab pendetide in the treatment of men with prostate cancer recurrence following radical prostatectomy. *Cancer Biother Radiopharm* **14**, 99–111.

232.   Ruggiero, A., Holland, J.P., Hudolin, T., Shenker, L., Koulova, A., Bander, N.H., Lewis, J.S., Grimm, J. (2011) Targeting the internal epitope of prostate-specific membrane antigen with 89Zr-7E11 immuno-PET. *J Nucl Med* **52**, 1608–15.

233.   Alt, K., Wiehr, S., Ehrlichmann, W., Reischl, G., Wolf, P., Pichler, B.J., Elsasser-Beile, U., Buhler, P. (2010) High-resolution animal PET imaging of prostate cancer xenografts with three different 64Cu-labeled antibodies against native cell-adherent PSMA. *Prostate* **70**, 1413–21.

234.   Pfob, C.H., Ziegler, S., Graner, F.P., Kohner, M., Schachoff, S., Blechert, B., Wester, H.J., Scheidhauer, K., Schwaiger, M., Maurer, T., Eiber, M. (2016) Biodistribution and radiation dosimetry of (68)Ga-PSMA HBED CC-a PSMA specific probe for PET imaging of prostate cancer. *Eur J Nucl Med Mol Imaging* **43**, 1962–70.

235.   Gourni, E., Canovas, C., Goncalves, V., Denat, F., Meyer, P.T., Maecke, H.R. (2015) (R)-NODAGA-PSMA: A Versatile Precursor for Radiometal Labeling and Nuclear Imaging of PSMA-Positive Tumors. *PLoS One* **10**, e0145755.

236.   Benesova, M., Schafer, M., Bauder-Wust, U., Afshar-Oromieh, A., Kratochwil, C., Mier, W., Haberkorn, U., Kopka, K., Eder, M. (2015) Preclinical Evaluation of a Tailor-Made DOTA-Conjugated PSMA Inhibitor with Optimized Linker Moiety for Imaging and Endoradiotherapy of Prostate Cancer. *J Nucl Med* **56**, 914–20.

237.   Rosano, G.L., Ceccarelli, E.A. (2014) Recombinant protein expression in Escherichia coli: advances and challenges. *Front Microbiol* **5**, 172.

238.   Schultz, B.E., Misialek, S., Wu, J., Tang, J., Conn, M.T., Tahilramani, R., Wong, L. (2004) Kinetics and comparative reactivity of human class I and class IIb histone deacetylases. *Biochemistry (Mosc.)* **43**, 11083–91.

239.   Lai, M.J., Huang, H.L., Pan, S.L., Liu, Y.M., Peng, C.Y., Lee, H.Y., Yeh, T.K., Huang, P.H., Teng, C.M., Chen, C.S., Chuang, H.Y., Liou, J.P. (2012) Synthesis and biological evaluation of 1-arylsulfonyl-5-(N-hydroxyacrylamide)indoles as potent histone deacetylase inhibitors with antitumor activity in vivo. *J Med Chem* **55**, 3777–91.

240.   Bergman, J.A., Woan, K., Perez-Villarroel, P., Villagra, A., Sotomayor, E.M., Kozikowski, A.P. (2012) Selective histone deacetylase 6 inhibitors bearing substituted urea linkers inhibit melanoma cell growth. *J Med Chem* **55**, 9891–99.

241.   Skoge, R.H., Dolle, C., Ziegler, M. (2014) Regulation of SIRT2-dependent alpha-tubulin deacetylation by cellular NAD levels. *DNA Repair Amst* **23**, 33–38.

242.   Nam, H.J., Kang, J.K., Kim, S.K., Ahn, K.J., Seok, H., Park, S.J., Chang, J.S., Pothoulakis, C., Lamont, J.T., Kim, H. (2010) Clostridium difficile toxin A decreases acetylation of tubulin, leading to microtubule depolymerization through activation of histone deacetylase 6, and this mediates acute inflammation. *J Biol Chem* **285**, 32888–96.

243.   Schaedel, L., John, K., Gaillard, J., Nachury, M.V., Blanchoin, L., Thery, M. (2015) Microtubules self-repair in response to mechanical stress. *Nat Mater* **14**, 1156–63.

244.   Yajima, H., Ogura, T., Nitta, R., Okada, Y., Sato, C., Hirokawa, N. (2012) Conformational changes in tubulin in GMPCPP and GDP-taxol microtubules observed by cryoelectron microscopy. *J Cell Biol* **198**, 315–22.

245.   Ly, N., Elkhatib, N., Bresteau, E., Pietrement, O., Khaled, M., Magiera, M.M., Janke, C., Le Cam, E., Rutenberg, A.D., Montagnac, G. (2016) alphaTAT1 controls longitudinal spreading of acetylation marks from open microtubules extremities. *Sci Rep* **6**, 35624.